Vortex Flow and Vortex Breakdown
Above a Delta Wing in
High Subsonic Flow:
an experimental investigation

Vortex Flow and Vortex Breakdown Above a Delta Wing in High Subsonic Flow:

an experimental investigation

PROEFSCHRIFT

ter verkrijging van de graad van doctor aan de
Technische Universiteit Delft, op gezag van de
Rector Magnificus Prof. ir. K.F. Wakker,
in het openbaar te verdedigen ten overstaan van een commissie,
door het college van Dekanen aangewezen,
op vrijdag 14 juni 1996 te 16.00 uur

door

Sharon Rose DONOHOE
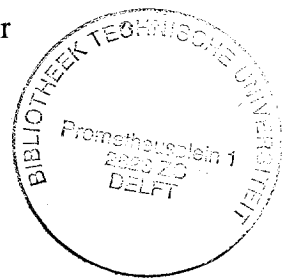
Master of Science in Engineering, Aeronautical and Astronautical Engineering
geboren te Santa Barbara, Californië, Verenigde Staten van Amerika

Dit proefschrift is goedgekeurd door de promotor:

Prof. dr. ir. P.G. Bakker

Samenstelling promotiecommissie:

Rector Magnificus, voorzitter

Prof. dr. ir. P.G. Bakker,	TU Delft, promotor
Ir. W.J. Bannink,	TU Delft, toegevoedg promotor
Prof. dr. R.C. Nelson,	Univ. of Notre Dame, Verenigde Staten van Amerika
Prof. dr. ir. G.J. van Heijst,	TU Eindhoven
Prof. dr. ir. L. van Wijngaarden,	Universiteit Twente
Prof. dr. ir. H.W.M. Hoeijmakers,	TU Delft
Ir. A. Elsenaar,	NLR, Amsterdam

For Mom and Dad

"Now with the wisdom of years I try to figure things out
and the only people I fear are those that never have doubts."

- Billy Joel, *"Shades of Grey"*
Album: River of Dreams
Columbia Records, 1993

Table of Contents

List of Symbols

AR	wing aspect ratio
	($AR = \frac{4}{\tan \Lambda} = 0.933$ in current study)
C_L	wing center line
C_p	static pressure coefficient $\left(C_p = \frac{2(p - p_\infty)}{\gamma p_\infty M_\infty^2} \right)$
C_p^*	critical pressure coefficient (i.e. $M = 1.0$)
$\overline{-C_p}$	averaged negative surface pressure coefficient
L	length of integration path along parallel bundle of light in Schlieren system
LDA	laser doppler anemometry
LDV	laser doppler velocimetry
M	Mach number
N_z'	number of five-hole probe traverses neglected in SRV simulation
P	total pressure
P_{bd}	port breakdown location
Re, Re_{c_r}	Reynolds number based on the root chord
S_{bd}	starboard breakdown location
T	temperature
b	wingspan (111.9 mm in current study)
c_l	lift coefficient
c_r	root chord (120 mm in current study)
f	focal length of parabolic mirror (150 mm in current study)
n	refractive index of light ($n \approx 1$ in air)
p	pressure
p_p	pitot pressure

q	dynamic pressure
$r.p.m.$	(revolutions/minute)
t	time
x, y, z	cartesian coordinate system
x, ϕ, r	cylindrical coordinate system (see Figure 1.7)
z_h	integration path length in SRV simulations
α_{cr}	angle of attack at which vortex breakdown appears at the wing trailing edge
γ	ratio of specific heats ($\gamma = 1.4$ for air at standard atmospheric conditions)
κ	Gladstone-Dale constant ($\kappa \approx 0.23 \cdot 10^{-3} \ m^3/kg$ for air at standard atmospheric conditions)
μ	dynamic viscosity
ν	kinematic viscosity
ω	vorticity
ρ	density
Λ	leading edge sweep angle
$\underline{\Omega}$	vorticity vector
Φ	swirl angle $\left(\arctan \frac{V_\theta}{V_x} \right)$; flow roll angle (see Figure 4.2)
Θ	flow pitch angle (see Figure 4.2)

Subscripts:

N	flow component normal to wing leading edge
le	local distance to the leading edge
m	model fixed Cartesian coordinate system (see Figure 6.39)
min	minimum value of flow quantity
p	probe fixed Cartesian coordinate system (see Figure 4.2)
t	wind tunnel fixed Cartesian coordinate system (see Figure 6.39)
tot	total isentropic stagnation value of flow property
∞	free stream value of flow property

1

Introduction

In order to achieve an attractive balance between supersonic cruise performance and maneu-
verability at high subsonic speeds, combat aircraft designers are often led to utilize the bene-
fits of highly swept slender wings or delta wings. In order to obtain their high maneuverabil-
ity, these aircraft utilize the non-linear lift component created by the powerful rotating flow
existing on the lee-side of a delta wing when operating at angle of attack. The first aircraft de-
signed to exploit this non-linear lift component became operational in the 1960's. The Anglo-
French Concorde remains the only highly swept-wing commercial transport aircraft to date,
but many high-performance fighter type aircraft have been designed and flown. Examples
include fighter aircraft such as the United States Navy F-18 and Air Force F-16, the French
Mirage 2000, the European Tornado and several aircraft of the former Soviet Union. Recent
successes with the American/German X-31 fighter aircraft illustrate the performance bene-
fits which can be obtained by harnessing the powerful separated lee-side flow field [Erickson
1995].

Yet, while many delta wing or highly swept wing aircraft have been designed since the
1960's, research on delta wings has continued. Extensive experimental, theoretical and nu-
merical research has been done on the leading edge vortex system of delta wings. Most stud-
ies have focused, however, on incompressible and low Reynolds number flows. The *Inter-
national Vortex Flow Experiment on Euler Code Validation*, a large international effort in-
volving institutes in the Netherlands, Germany, Sweden and the United States, was carried
out between 1983 and 1987. This effort, as its name implies, was intended to supply an ex-
perimental data base for validation of Euler method simulations of delta wing flows in the
transonic/supersonic flow regime [Elsenaar 1987]. This study concluded that many questions
regarding the properties and geometry of the leading edge vortices of a delta wing in a high
subsonic free stream remained unresolved.

An important motivation for research on delta wings is the unpredictable and unsteady
nature of the delta wing flow field at high angle of attack. The flow will yield increasing lift

1

with increasing angle of attack until the point where vortex *breakdown* or vortex *bursting* occurs. Vortex breakdown was described by Lambourne and Bryer [1961] as "a structural change from a strong regular spiral motion to a weaker turbulent motion". A water tunnel visualization of vortex breakdown above a delta wing at 20° angle of attack is shown in Figure 1.1. The dramatic change of nature of the flow field following vortex breakdown can pro-
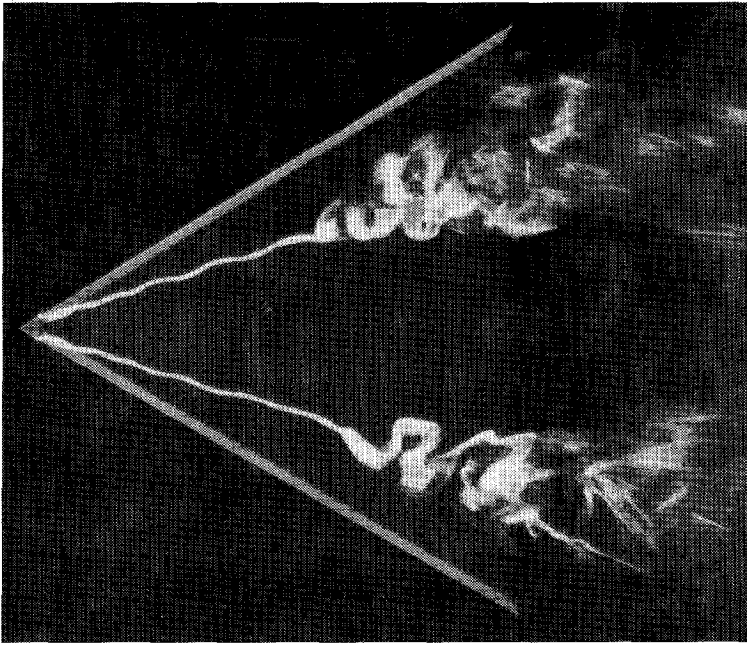
Figure 1.1: Vortex breakdown above a delta wing in a water tunnel at 20° angle of attack [Werlé 1960].

duce control problems for an aircraft. Vortex breakdown can cause a strong nose-up pitching moment and an asymmetry of vortex breakdown with respect to the fuselage can produce strong rolling moments. The unsteady nature of the flow field beyond the point of breakdown may also lead to fatigue problems for control surfaces impacted by the flow [Wentz 1987]. While the vortex breakdown phenomenon has been studied for almost four decades, a generally accepted theory of its basic physical mechanisms has yet to be defined. Vortex breakdown becomes particularly complex in the high subsonic flow regime where compressibility effects such as shock waves are present in the flow field. In his recent survey of the last forty years of vortex breakdown research, Délery admits that despite its importance for high speed flight "the question of shock/vortex interaction and shock-induced breakdown" remains "a largely unexplored field" [1994].

The current study considers the vortex flow about a delta wing in the high subsonic flow regime. The remainder of this introduction describes the basic physical characteristics of leading edge vortices above a delta wing and provides a brief review of the history of vortex breakdown research to date. The specific objectives of the current investigation are presented in Section 1.3.

1.1   Properties of the Leading Edge Vortex

Because most research has been carried out in the incompressible and low Reynolds number flow regime, the understanding of the vortex flow above a delta wing resulting mainly from these investigations will be presented in the discussion below. Characteristics of the flow field unique to the high subsonic flow regime, the focus of the current investigation, will be emphasized where relevant.

1.1.1   Geometry of the Flow Field

Figure 1.2 illustrates the complicated vortical flow field typically found above a simple flat-plate sharp leading edge delta wing operating at moderately high angle of attack and its associated surface pressure distribution. The flow, initially attached to the windward side of the wing, turns outward toward the leading edge where, unable to negotiate the sharp leading edge, it separates. This separated flow combines with the boundary layer departing from the lee-side of the wing to form a viscous shear layer. This shear layer, under the influence of the pressure gradients existing on the lee-side of the wing and its own vorticity, rolls up into a vortex type structure. The entrained flow will reattach to the upper surface of the wing at A_1 and move outwards beneath the primary vortex core towards the leading edge. A local surface pressure maximum will exist at A_1 due to the stagnation of the flow at this point (see inset of Figure 1.2). In contrast, a local surface pressure minimum will exist beneath the primary vortex core as a result of the acceleration of the flow through the "throat" formed between the primary vortex and the upper surface of the wing. Encountering an adverse pressure gradient outboard of the primary vortex core, the flow may again separate at S_2 and form a secondary vortex. This process may repeat itself, forming a third or tertiary vortex inboard of the secondary vortex core for certain configurations. The tertiary vortex is not illustrated in Figure 1.2. The lift resulting from low pressure produced above the surface of the wing by this rotational field is commonly referred to as vortex lift. The presence of the secondary vortex and the boundary layer may influence the location of the pressure minimum associated with the primary vortex such that it is not located exactly below the location of the primary vortex core. Similarly, the pressure minimum associated with the secondary and tertiary vor-

A: Surface Reattachment
S: Surface Separation
vc: Vortex Core
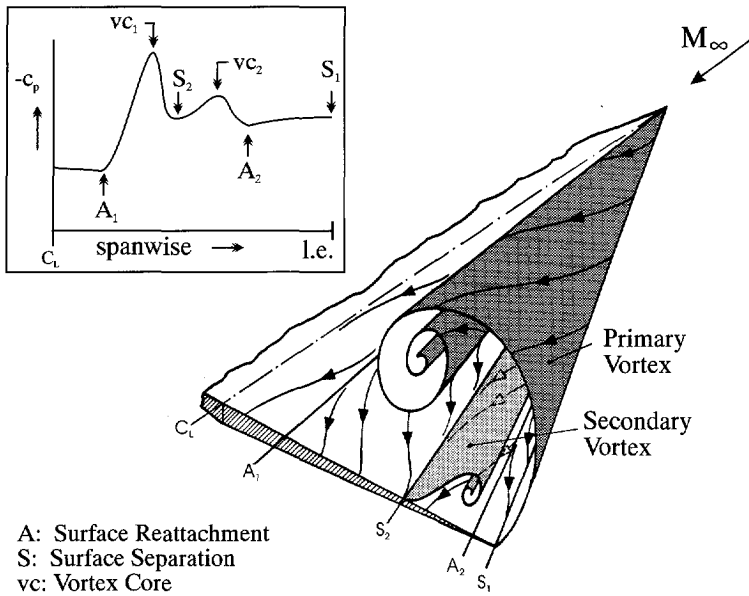
Figure 1.2: Characteristic lee side flow field of a sharp leading edge delta wing at intermediate angle of attack and its corresponding surface pressure distribution.

tices may be displaced due to the influence of the boundary layer and the presence of the other vortices above the wing.

Leading edge vortex research has concentrated on the primary vortex due to the less significant size and strength of the secondary and tertiary vortices. The most important function of the latter vortices is their influence on the location of the primary vortex. The core of the primary vortex will tend to be displaced upwards and inwards as a function of the size of the secondary vortex. In low speed flows the secondary separation location is found to be Reynolds number dependent. This dependence is attributed to the importance of the state of the boundary layer of the reattached flow on its capacity to resist the adverse pressure gradient as it moves outboard beneath the primary vortex. While experimental investigations suggest the presence of a cross-flow shock wave embedded beneath the primary vortex for certain configurations in the high subsonic flow regime [Muylaert 1980; Boersen and Elsenaar 1987] (see Figure 1.3), definitive evidence of its existence has yet to be obtained [Elsenaar et al. 1988]. Erickson [1991] suggested, however, that the insensitivity of the secondary separation location to Reynolds number, which he observed for free stream Mach numbers exceeding 0.8, is due to the shock-induced nature of the secondary vortex formation in that flow regime. The oil flow visualization results obtained by Erickson exhibited a large angle
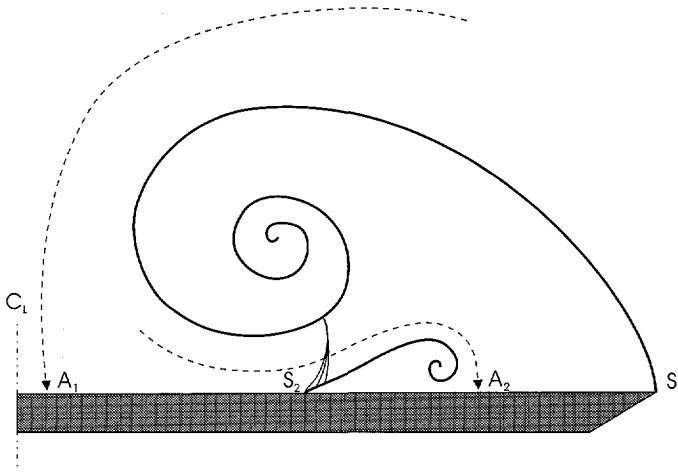
Figure 1.3: Illustration of embedded cross-flow shock wave.

existing between the oil surface flow lines leading to the secondary separation line and the secondary separation line itself. Erickson considered this large angle between the two lines to be indicative of a shock-induced flow separation.

1.1.2 Internal Structure of the Leading Edge Vortex

The first investigation of the internal structure of leading edge vortices was made by Earnshaw [1961]. This investigation was carried out using a 5-hole probe above a delta wing of aspect ratio one with a free stream velocity of $100\ ft/sec$. Earnshaw concluded that the vortex could best be described as consisting of three separate regions; the outer shear layer or vortex sheet, a vortex core and a viscous sub-core (see Figure 1.4). This initial description of the leading edge vortex structure has since been supported by, among others, the various researchers discussed below.

   The outer shear layer of the vortex, formed when the flow separates at the sharp leading edge, transports the vorticity emanating from the boundary layers on both the upper and lower surfaces of the wing as well as that generated by the separation itself. Two different types of vortical substructures embedded in the vortex sheet have also been observed. These include a temporally periodic structure [GadelHak and Blackwelder 1985; Lowson 1988; Reynolds and Abtahi 1989] and a stationary vortex-cell structure [Squire et al. 1961; Lowson 1988; Reynolds and Abtahi 1989]. The temporally periodic structure has been observed to be highly sensitive to disturbances in the flow field [Lowson 1988]. The steady vortical structures in the streamwise direction were investigated in a detailed five-hole probe study by Washburn and
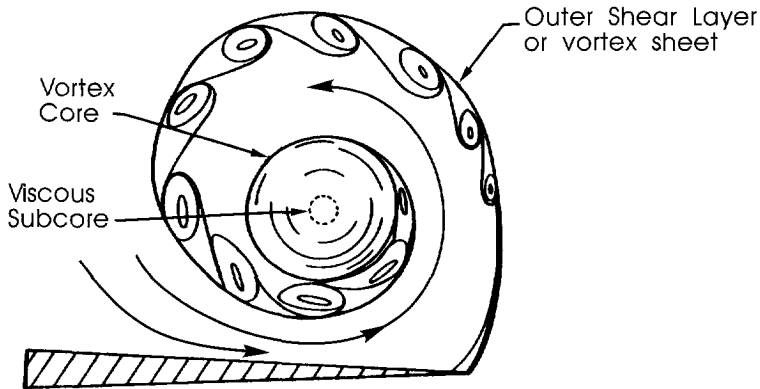
Figure 1.4: Internal divisions of a leading edge vortex [Payne 1987].

Visser [1994a]. They concluded that the existence of these vortices results from an instability similar to the cross-flow instability in a swept wing boundary layer.

Earnshaw defined the vortex core as a region where the free shear-layer has diffused to such an extent that its spiral structure can no longer be detected. The size of the vortex core was found by Earnshaw to be approximately 30% the local semi-span. In the viscous sub-core large total pressure losses and high velocity gradients were observed. Earnshaw found this region to have a diameter of approximately 5% of the local semi-span. Early theoretical models, such as that developed by Hall [1961] discussed below, made use of these various regions by assuming the vortex core to be rotational, inviscid and conical except in the viscous subcore itself.

Earnshaw also observed a "jet-like" axial velocity profile about the vortex axis. A "jet-like" axial velocity profile implies a profile where the velocity along the axis of the vortex is a local maximum, higher than the free stream value, at the axis of the vortex core (i.e. $r = 0$). Figure 1.5a illustrates a characteristic jet-like velocity profile. Axial velocities along the axis of the vortex were found to be as high as 2.3 times that of the free stream velocity. The magnitude of circumferential velocities in the vortex sub-core were found to be nearly equivalent to the magnitude of the free stream velocity. The jet-like axial velocity profile, high circumferential velocities and total pressure loss in the subcore have been confirmed by numerous researchers since Earnshaw's initial observations. Figure 1.6 illustrates the velocity components in the vortex core measured in an hot-wire survey by Nelson and Visser [1991].

Hall [1961] developed a model for the structure of the core of the vortex based on Earnshaw's measurements. This model assumed a continuous and rotational flow field in which viscous diffusion is confined to a relatively slender subcore. The conical inviscid outer so-

a) jet-like axial velocity profile   b) wake-like axial velocity profile
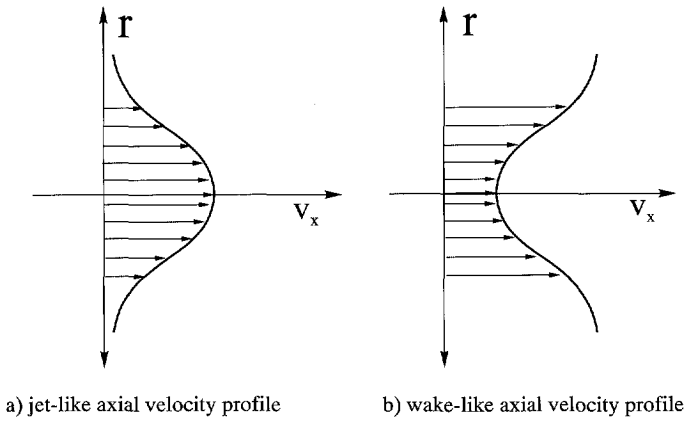
Figure 1.5: Illustration of jet-like and wake-like axial velocity profiles.
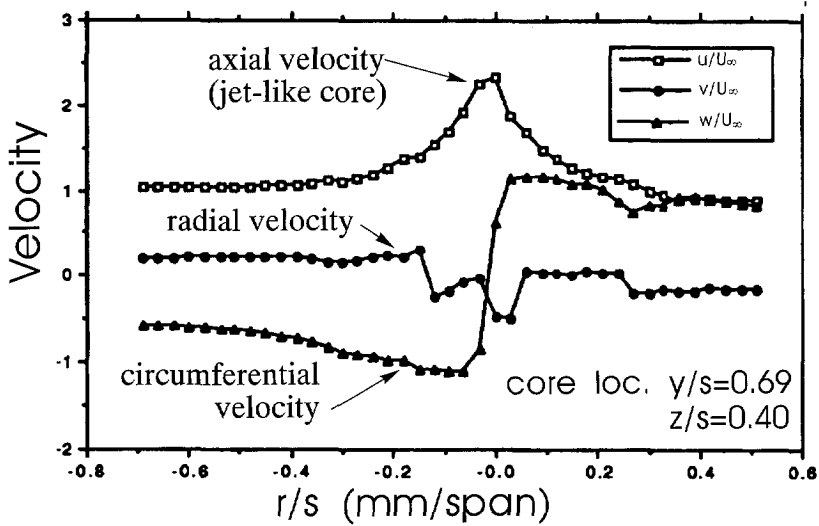
Figure 1.6: Velocity components along a horizontal traverse through the vortex core, $\Lambda = 70°$, $\alpha = 20°$, $x/c = 0.5$, $Re = 2.5 \cdot 10^5$ [Nelson and Visser 1991].

lution is matched to the viscous subcore through a boundary layer type region. Similar to experimental observations, Hall's model yielded high axial velocities about the vortex axis or a "jet-like"axial velocity profile. Hall explained this phenomenon as being a consequence of the axial velocity induced by the circumferential vorticity component ω_ϕ in the axisymmetric vortex model he applied (see Figure 1.7). The cylindrical vorticity components are
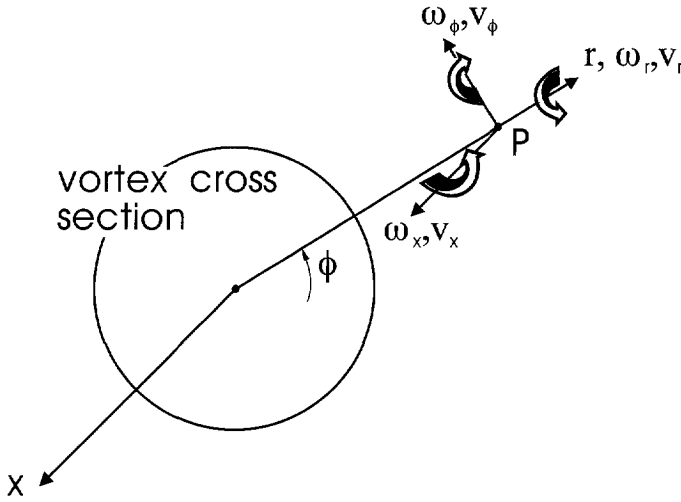
Figure 1.7: Cylindrical coordinate system and vorticity components

defined as:

$$\omega_r = \left(\frac{1}{r} \frac{\partial v_x}{\partial \phi} - \frac{\partial v_\phi}{\partial x} \right) \tag{1.1}$$

$$\omega_\phi = \left(\frac{\partial v_r}{\partial x} - \frac{\partial v_x}{\partial r} \right) \tag{1.2}$$

$$\omega_x = \left(-\frac{1}{r} \frac{\partial v_r}{\partial \phi} + \frac{v_\phi}{r} + \frac{\partial v_\phi}{\partial r} \right) \tag{1.3}$$

It is indeed possible to see from Equations 1.1-1.3 that the axial velocity profile in the radial direction (i.e. $\frac{\partial v_x}{\partial r}$) is only influenced by the circumferential vorticity component ω_ϕ.

In the high subsonic flow regime, initial Laser Doppler Velocimetry (LDV) measurements of the vortex core found a "wake-like" axial velocity profile instead of the anticipated jet-like profile observed at lower speeds [Vorropoulos and Wendt 1983]. A wake-like profile

is defined as one in which the flow along the vortex core is a local velocity minimum, less than the free stream value, at the vortex core (see Figure 1.5b). These measurements were later determined to be unreliable, however, due to the inability of the LDV flow particles to follow the high accelerations present in the vortex core [Falatyn 1987]. The jetting nature of the vortex core in the high subsonic flow regime has since been confirmed via five-hole probe measurements [Houtman and Bannink 1987].

1.1.3   Shock Waves and other Compressibility Effects

An early investigation of the leading edge vortices of delta wings in high speed flow was conducted by L.C. Squire et al. [1961]. This study, which emphasized supersonic flow conditions, found increasing Mach number to cause a flattening of the primary vortices and the formation of conical shock waves above the vortices at high Mach numbers and angles of attack. The component of non-linear lift resulting from the vortical flow above the wing was found to decrease with increasing Mach number. Erickson et al. [1989] similarly noted a decreasing lift with increasing Mach number in the supersonic flow regime, but found the opposite trend in the high subsonic flow regime. Stanbrook and Squire [1964] investigated the effect of free stream Mach number M_∞ and angle of attack α on the geometry of the leading edge vortices. This study established a relationship between the flow angle α_N perpendicular to the leading edge of the wing and the Mach number M_N and the flow field topology above the lee-side of the wing, where

$$M_N = M_\infty \cdot \sqrt{1 - \sin^2 \Lambda \cdot \cos^2 \alpha} \tag{1.4}$$

and

$$\alpha_N = \tan^{-1}\left(\frac{\tan \alpha}{\cos \Lambda}\right) \tag{1.5}$$

where Λ is the leading edge sweep angle. Miller and Wood [1984] applied these definitions to develop the diagram for classifying the flow about thin delta wings shown in Figure 1.8. The location of the boundaries in this figure are defined by the Reynolds number, as well as geometric parameters such as leading edge radius, thickness-to-chord ratio, taper ratio, etc. This diagram only considers a cross flow, however, and does not take into consideration trailing edge effects and possible vortex breakdown. But, the classifications do provide an indication of the anticipated cross-flow pattern sufficiently far upstream of the trailing edge.

A unique aspect of the vortex flow above a delta wing in the high subsonic flow regime is the presence of a terminating or trailing edge shock wave system. These shock waves attest
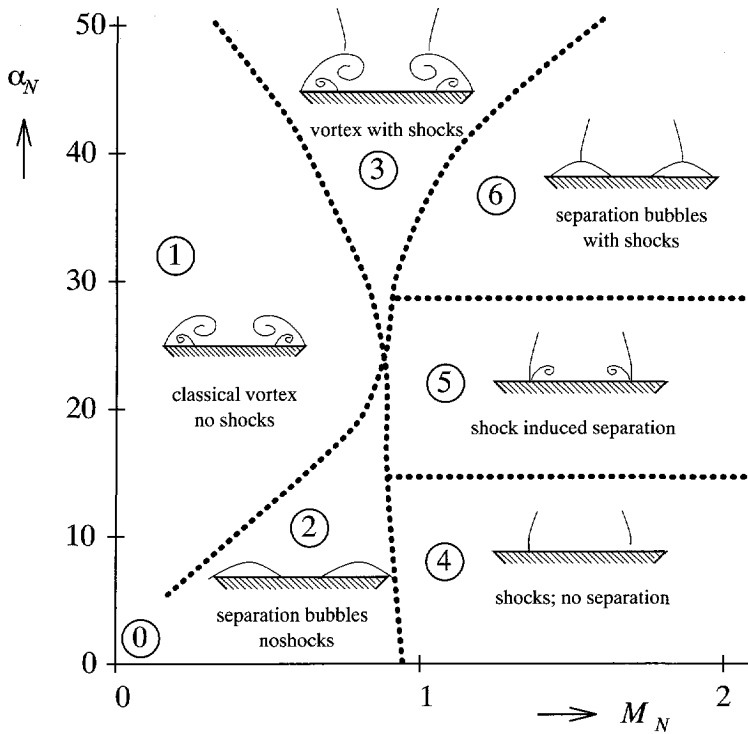
Figure 1.8: Classification of leeward flow patterns over thin delta wings [Miller and Wood 1984].

to the presence of a supersonic flow pocket above the leeward surface of the delta wing. Terminating shock waves have been observed by numerous researchers [Lambourne and Bryer 1961; Muylaert 1980; Bannink and Houtman 1987; Schrader et al. 1988]. Figure 1.9 is an image of a trailing edge shock wave visualized by a side view transmission Schlieren system. An unsteadiness in this shock system has also been observed, but an attempt by Schrader et al. [1988] to define a dominant frequency for these fluctuations was inconclusive. The span-wise distribution of this system and its influence on the leading edge vortices themselves has also yet to be defined.

1.1.4   Progress in Modelling the Leading Edge Vortex System

Of initial efforts made in simulating the effects of the leading edge vortices on wing performance in the 1960's, Polhamus' [1966] model was a noted success. This model is based on an empirical analogy between the vortex lift and the leading edge suction associated with the potential flow about the leading edge. While Polhamus' model provided a reasonable prediction of the total suction force it did not provide any detailed information on the flow
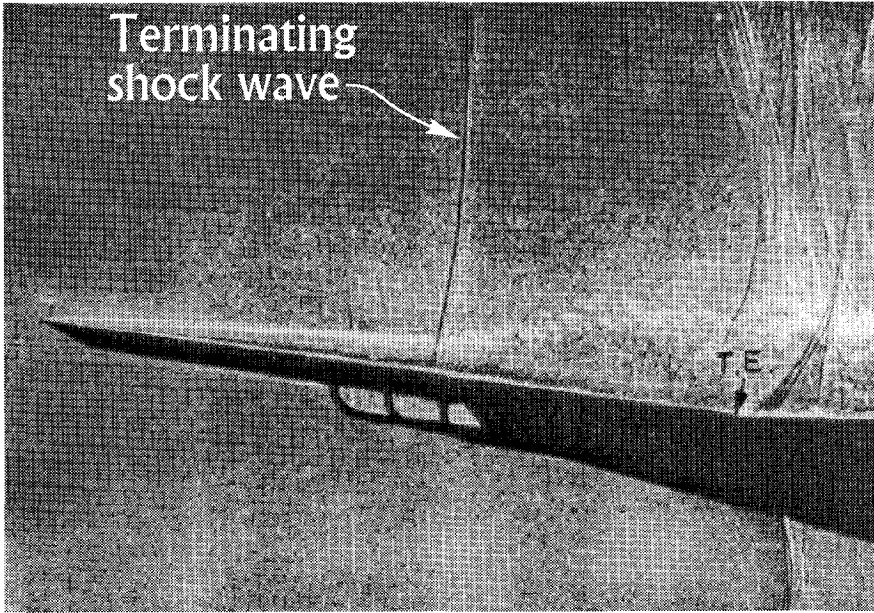
Figure 1.9: Side-view Schlieren visualization of a trailing edge shock wave interacting with vortex breakdown, $M_\infty = 0.9$, $\alpha = 10°$ [Lambourne and Bryer 1961].

field. Throughout the 1970's various panel and vortex-lattice methods were developed to calculate this three-dimensional vortical flow field. The improved capabilities of computers in the 1980's led, however, to the development of Euler methods based on the Euler equations capable of computing the flow field about more complex flow configurations than was previously feasible. A detailed description of the development and limitations of these various algorithms is provided by Hitzel and Schmidt [1984].

While Euler methods are capable of mimicking flow separation at a sharp leading edge, the secondary and tertiary separations from the smooth upper surface can not be captured. Solutions of the laminar three-dimensional Navier-Stokes equations for the flow about a delta wing at angle of attack have, in contrast, successfully modelled these vortices [Rizzetta and Shang 1984; Fujii and Schiff 1989]. Unfortunately, high grid resolution is necessary to capture these viscous effects [Ekaterinaris and Schiff 1990b]. Requisite computational grid resolution results in high computational costs which render Navier-Stokes methods not yet practical for common use.

1.2   Vortex Breakdown

Vortex breakdown above the lee-side of a delta wing was first visualized in a water tunnel by Werlé [1954]. Figure 1.1 illustrates how the highly organized vortical structure being shed from the leading edge of the wing ends abruptly at approximately 50% of the chord. As mentioned above, the consequences of this phenomenon for an aircraft operating at high angle of attack can be significant. Several comprehensive reviews regarding progress in vortex breakdown research have been published [Hall 1972; Leibovich 1978; Escudier 1988; Délery 1994]. A brief overview of significant conclusions is provided below. It should be noted, however, that much of the information obtained on the vortex breakdown phenomenon has been obtained through the investigation of axisymmetric vortices confined in a tube and not a free vortex over a wing. Delta wing vortices are fed with vorticity along the entire length of the wing, are exposed to a longitudinal pressure gradient and are not fully axisymmetric. Emphasis is given in the discussion below to investigations specifically focusing on vortex breakdown above delta wings. While most information over vortex breakdown has been obtained through experimental or theoretical studies, progress has been made recently in numerically simulating the phenomenon.

1.2.1   Observations in Vortex Breakdown

Werlé's [1954] initial observation of vortex breakdown over a delta wing was soon confirmed by Peckham and Atkinson [1957]. A relationship between sweep angle of the leading edge and angle of attack with the chord-wise location of breakdown was identified by both Peckham [1958] and Elle [1958]. They found that an increase in incidence or a decrease of effective sweep (i.e. increase in aspect ratio, $AR = (4/\tan\Lambda)$) moved the burst point upstream. Lambourne and Bryer [1961] identified two unique types of vortex breakdown, bubble and spiral mode, which are illustrated in Figure 1.10. The bubble mode is characterized by an axisymmetric expansion of the vortex about the vortex core. In the case of spiral breakdown the core is noted to exhibit an abrupt kink in the subcore followed by a spiralling motion of the vortex subcore about its original axis for several rotations before dispersing into large scale turbulence. Lambourne and Bryer noted, however, that the bubble breakdown was "observed only occasionally and for short duration" in comparison with the spiral mode. Benjamin [1967] suggested that the spiral breakdown mode is a secondary phenomenon which manifests itself after the initial bubble breakdown has appeared. The bubble-mode of breakdown has indeed been shown experimentally to precede the spiral-mode of breakdown for low speed flow about a delta wing with increasing angle of attack by both Payne and Nelson [1985] and Ayoub and McLachlan [1987]. Numerical three-dimensional
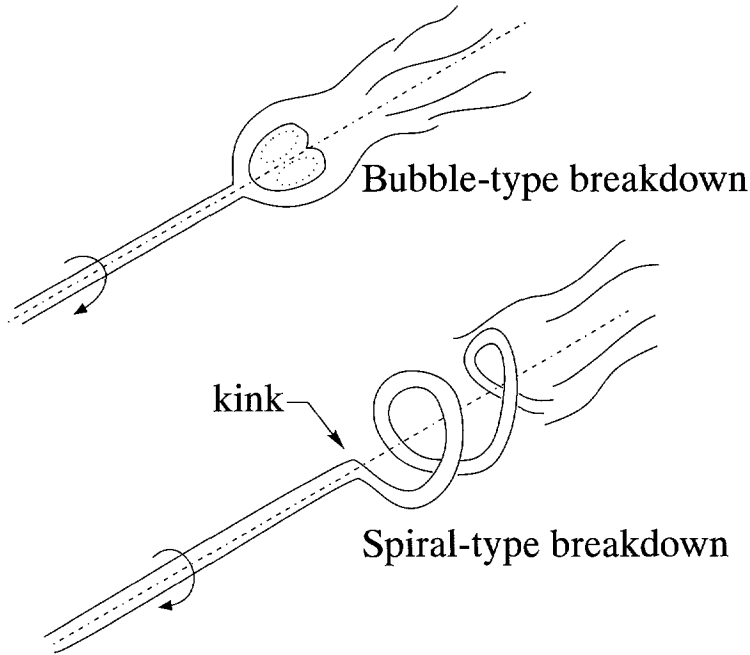
Figure 1.10: Illustration of bubble and spiral vortex breakdown modes.

Navier-Stokes calculations by Weimer et al. [1994] of an axisymmetric free vortex embedded in an axial decelerated flow, similarly, simulated a transition from the bubble to spiral breakdown mode. An experimental investigation of vortex breakdown of an axisymmetric vortex, on the other hand, lead Backstein and Staufenbiel [1994] to conclude that the spiral breakdown mode can better be described as a "smooth transition from a slightly disturbed straight vortex to a spiral shape" than an actual "breakdown" of the vortex structure in the presence of sufficiently low adverse pressure gradient. This "smooth transition" is in conflict with the numerical results of Weimer et al. [1994] mentioned above. This controversy is summarized by Délery [1994] in his conclusion that while "different types of breakdown (spiral and bubble types) seem to exist", "this point is subject to controversy".

Vortex breakdown is further noted to be an unsteady phenomenon which can better be described by a breakdown region than a breakdown point [McKernan and Nelson 1983]. Elsenaar and Hoeijmakers [1991] noted that while vortex breakdown is characterized by a broadening of the vortex structure and often accompanied by the "onset of unsteadiness and turbulence in the vortical flow region", a "global strong circulatory flow pattern does persist".

Numerous parametric studies have been carried out investigating the effect of such factors as angle of incidence, Reynolds number, leading edge sweep angle and shape, trailing edge

shape and compressibility on vortex breakdown. The influence of the wind tunnel itself on the vortex breakdown has also been evaluated. The major conclusions from these studies are presented below.

Angle of Attack: The tendency of the vortex breakdown location to move forward with increasing angle of attack (i.e. increasing adverse pressure gradient), initially noted by Lambourne and Bryer [1961], has since been supported by many researchers.

Reynolds Number: Reynolds number has been shown to have only a weak effect on vortex breakdown location for sharp leading edge delta wings at high angle of attack [Erickson 1982; Roos and Kegelman 1990]. Erickson attributed this to the influence of potential flow effects at high angle of attack where the vortical flow field emanating from a sharp leading edge dominates the flow field. At lower angle of attack the vortex core is more significantly influenced by the presence of the upper surface boundary layer. Significant Reynolds number effects were also noted by Erickson for wings with "round leading edges, deflected flaps, thick sections, etc., where leading-edge flow separation is delayed and a salient edge of separation does not exist."

Wing Camber: Lambourne and Bryer [1961] observed that vortex breakdown moved downstream with increasing wing camber. This delay in the appearance of vortex breakdown was attributed to the decreased longitudinal pressure gradient associated with the increased camber of the wing profile.

Leading Edge Sweep: The initial observations by Peckham [1958] and Elle [1958] that increased sweep angle delays the appearance of vortex breakdown above the wing have since been supported by numerous researchers. The delay of breakdown with increasing sweep angle is attributed to the decreasing vortex strength associated with the increasing wing sweep angle [Hemsch and Luckring 1990]. Wentz and Kohlman [1971] conducted a study of various delta wings ranging in leading edge sweep angle from $45°$ to $85°$ and found that a higher sweep angle corresponded with a higher angle of attack (α_{cr}) at which vortex breakdown first occurred above the wing up until $\Lambda = 75°$. Beyond $\Lambda = 75°$ Wentz and Kohlman observed the initial appearance of breakdown above the wing at a constant angle of attack. This independence of breakdown characteristics from sweep angle at high sweep angle has not been confirmed, however, by other researchers [Skow and Erickson 1982].

Wentz and Kohlman [1971] also noted that in the subsonic flow regime, for delta wings with a leading edge sweep angle of less than $70°$, the appearance of vortex breakdown above

the wing did not correspond with c_{lmax}, but c_{lmax} was reached only in the post-breakdown regime. A similar trend is observed in the post-breakdown force measurements of Erickson et al. [1989] in the high subsonic regime.

Shape of Leading Edge Profile: The influence of the shape of the leading edge profile on burst location, even in the case of a thin wing with a sharp leading edge, was first noted by Earnshaw [1964]. This observation was supported by Kegelman and Roos [1989] in a study examining a variety of both curved profiles and bevelled sharp leading edge profiles. Significant differences in the angle of attack at which vortex breakdown appeared above the wing as well as its upstream progression with increasing angle of attack were observed for the various profiles. These differences were attributed to the variation in the location of leading edge separation and the strength of the resulting vortex for the various leading edge profiles. Bevelled sharp leading edge profiles oriented with the sharp leading edge windward were noted to produce a stronger leading edge vortex and result in a lower critical angle of attack (i.e. the angle of attack where vortex breakdown first appears above the wing).

Trailing Edge Influence: In the above mentioned study using various delta wing planforms Wentz and Kohlman [1971] also examined the influence of the trailing edge on vortex breakdown. Comparing a plain 70° sweep delta wing with a diamond and arrow planform revealed no significant differences in breakdown characteristics (see Figure 1.11). This observation concurs with Earnshaw's [1964] earlier conclusion that apex sweep is more important than trailing edge sweep in determining vortex breakdown.

a) plain profile   b) diamond profile   c) arrow profile
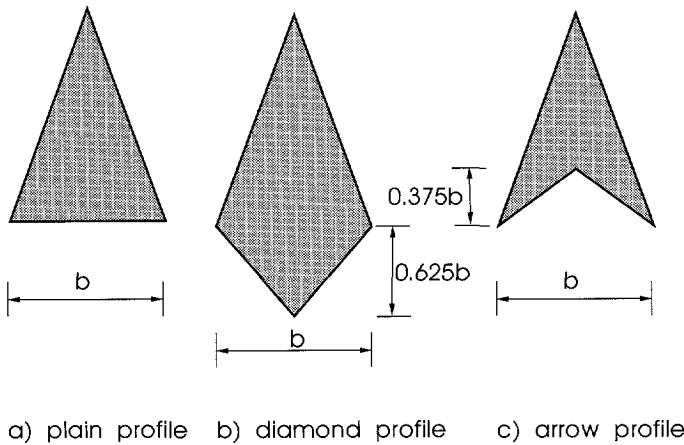
Figure 1.11: Delta wing planforms examined by Wentz and Kohlman [1971].

Mach Number and Compressibility: In the incompressible flow regime the breakdown position is found to move gradually forward from the trailing edge with increasing angle of attack. In the high subsonic or compressible regime, in contrast, breakdown has been observed to jump suddenly forward from the trailing edge to as far forward as 50% of the root chord with just a slight increase in angle of attack upon reaching a critical angle of attack [Muylaert 1980]. The significant loss of lift and nose down pitching moment resulting from this sudden flow "transition" have been demonstrated via both force balance measurements [Muylaert 1980; Erickson et al. 1989] and surface pressure measurements [Elsenaar and Hoeijmakers 1991].

Another unique aspect of vortex breakdown in the high subsonic flow regime is the terminating shock wave system interacting with the vortices. While these shocks can exist both with and without vortex breakdown present above the wing, their presence is believed to have a strong influence on the vortex breakdown phenomenon. The transition from a single trailing edge shock to a two shock system (located at approximately 50% and 90% of the chord) at the occurrence of vortex breakdown has been observed by numerous researchers [Muylaert 1980; Bannink et al. 1989; Elsenaar and Hoeijmakers 1991]. It is not yet clear whether the vortex breakdown causes the double-shock structure or if the vortex breakdown is initiated by the formation of the second shock.

Wind tunnel influences: Increasing free stream turbulence levels has been shown to lead to premature vortex breakdown as well as an increased unsteadiness in the breakdown location [Washburn 1992]. Support blockage will tend to encourage breakdown if it occurs in the path of the vortex. Wind tunnel wall interference, on the other hand, has been shown to increase the effective camber of the wing and, thereby, delay breakdown [Weinberg 1992].

1.2.2 Theories on Mechanisms of Vortex Breakdown

Although some progress has been made in defining the origin of vortex breakdown since Werlé's initial observations, the physical mechanisms of vortex breakdown remain a controversial topic. The presence of an adverse pressure gradient and/or surpassing a critical swirl intensity are two conditions which have been generally recognized as promoting vortex breakdown [Délery 1994]. Swirl intensity is characterized by the ratio of the circumferential velocity (v_ϕ) to the axial velocity (v_x) near the vortex core (see Figure 1.7). Three traditional classes of analytical theories on the genesis of vortex breakdown which have emerged include the concept of the critical state, the quasi-cylindrical approach and consideration of hydrodynamic instabilities. A relatively new approach to the investigation of vortex breakdown is the examination of vorticity dynamics. The numerical simulation of vortex breakdown with

the Navier-Stokes equations has also been recently shown to be possible in certain cases. A brief summary of progress to date for each of these various approaches to vortex breakdown analysis is presented below. In many of these studies the simplified case of an isolated vortex in a tube has been studied in place of the delta wing leading edge vortex.

Critical State or Wave Theory: H.B. Squire [1960] proposed the theory that when a long standing wave can be supported by a vortex, small disturbances coming from downstream can propagate in the upstream direction and initiate vortex breakdown. Squire defined *supercritical* flow as flow which could not support a standing wave and *subcritical* flow as flow which could support such a wave. Squire showed theoretically for a cylindrical inviscid flow that the transition from the supercritical to subcritical flow state can be brought about by increasing the swirl of the vortex. Swirl is typically quantified for axisymmetric vortices, or near the core of leading edge vortices, by the helix angle $\Phi = \arctan(\frac{v_\phi}{v_x})$, where v_ϕ is the local circumferential velocity component and v_x is the local axial component. Délery et al. [1987] investigated the relationship between swirl intensity, adverse pressure gradient and vortex breakdown using laser doppler anemometry (LDA) for a vortex generated by a $75°$ delta wing and fed into a two dimensional variable pressure duct. They noted that provided sufficient swirl is present the vortex would breakdown even in the absence of an adverse pressure gradient. This trend is illustrated in Figure 1.12. In this case the swirl intensity was defined as the
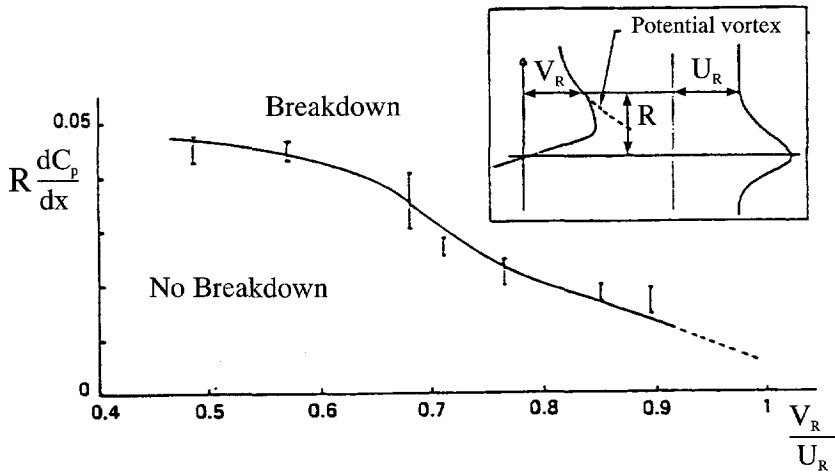
Figure 1.12: Influence of swirl intensity on the requisite adverse pressure gradient to induce vortex breakdown [Délery et al. 1987].

ratio between the circumferential and axial velocity components at the point where the cir-

cumferential velocity distribution departs from the potential vortex distribution (see inset of Figure 1.12). The critical state theory is further supported by the tendency mentioned above for vortex breakdown to be delayed by increasing sweep angle. Increased sweep angle will decrease the rate at which the strength or swirl of a vortex increases along the length of the leading edge and thereby inhibit its breakdown.

The original wave theory of H.B. Squire was criticised by Benjamin [1962] because the group velocity of his standing waves is directed downstream and, thus, incapable of propagating disturbances upstream. Benjamin considered breakdown to be a transition between two *conjugate* states where in the critical state the vortex can support axisymmetric standing waves. Benjamin concluded, similar to Squire, however, that the critical condition was reached with sufficient swirl.

Randall and Leibovich [1973] developed a variant of the wave theory first proposed by H.B. Squire in their trapped wave model of vortex breakdown. In the model they proposed the forward propagation of finite amplitude waves was halted by a viscous dissipation at the point of vortex breakdown. A self-admitted weakness of this theory is its reliance on viscous dissipation. The role of Reynolds number and viscosity in the breakdown process is generally accepted to be small (see discussion on page 14). In an extension of this trapped wave theory Darmofal and Murman [1994] illustrated via axisymmetric, viscous, incompressible Navier-Stokes simulations of swirling flows in a variable area pipe, that vortex breakdown results when a subcritical flow goes through a process of wave-focusing, allowing disturbances to amplify. In an analogy with shock wave formation they noted that: "A flow which is 'accelerating' through the critical condition will not breakdown since wave-focusing cannot occur (similar to a compressible flow expanding through sonic conditions)."

Quasi-Cylindrical Theory: Quasi-cylindrical vortex breakdown theory was first investigated by Gartshore [1962; 1963]. This theory can be considered comparable with that of using the boundary layer equations to estimate the location of surface flow separation. In boundary layer calculations, the solution will fail as flow separation is approached and this failure is considered an indication of imminent separation. Similarly, as the point of breakdown is approached the streamlines diverge rapidly, large axial gradients develop and the quasi-cylindrical approximation fails. Calculations reveal that solution breakdown coincide with the occurrence of vortex breakdown in some cases [Hall 1967]. This method of vortex breakdown investigation is, of course, limited to investigating the flow prior to the appearance of vortex breakdown.

Hydrodynamic Instabilities: The importance of hydrodynamic instabilities to vortex break-down was first proposed by Jones [1960] and Ludwieg [1961]. Ludwieg suggested that as a result of an existing instability, disturbance waves are amplified and the vortex develops an asymmetry, finally leading to breakdown. Essentially stability analysis allows the amplification or decay of infinitesimal disturbances imposed on the flow to be investigated. The vortex breakdown examined in this way is analogous with a laminar-turbulent transition. While asymmetric streamwise velocity distributions preceding vortex breakdown, measured both with a five-hole probe [Payne et al. 1987] and a Laser Doppler Velocimetry system [Kegelman and Roos 1989], support the hydrodynamic instability analysis, this approach is considered to be incomplete. Several weaknesses in the instability theory are described by Escudier [1988]. Hydrodynamic instability theory is not able to capture, via the gradual propagation of instabilities it proposes, the dramatic transition nature of the vortex breakdown observed in experiments . Also, instability theory can not account for the fluctuation between spiral and bubble vortex breakdown modes observed experimentally [Escudier and Zehnder 1982].

Vorticity Dynamics: The consideration of vorticity dynamics in the investigation of vortex breakdown was first introduced in the theoretical work of Brown and Lopez [1990]. Their work identified the existence of negative azimuthal vorticity ω_ϕ (see Figure 1.7) as an essential feature in the vortex breakdown process. They showed that the presence of a negative azimuthal vorticity initiated a positive feedback mechanism which led to the ultimate stagnation of the vortex core and, thus, vortex breakdown. Further investigations into the role of vorticity dynamics in vortex breakdown have since been made [Nelson and Visser 1991; Darmofal 1993; Brücker and Althaus 1995]. Nelson and Visser conducted a low speed ($U_\infty = 10m/s$) hot-wire study of a delta wing vortex and observed that the azimuthal vorticity did indeed become negative as breakdown was approached. Darmofal conducted a theoretical and computational study of an incompressible axisymmetric vortex. He concluded that the presence of an adverse pressure gradient causes a divergence of stream surfaces, which tilts the axial vorticity into the azimuthal direction, leading to a further decrease of the axial velocity by amplifying the axial pressure gradient which, through continuity, further increases the radial outflow. Brücker and Althaus, similarly, concluded from their particle tracking velocimetry investigations of vortex breakdown in a cylindrical tube that positive feed-back resulting from vorticity dynamics is the "key-mechanism leading to vortex breakdown."

Numerical Simulation of Vortex Breakdown The importance of viscosity in the vortex breakdown phenomenon is an issue of continuing debate. Nonetheless, Hitzel et al. [1987] have simulated the flow preceding and beyond vortex breakdown using the time-dependent

Euler equations. The results do reflect certain aspects of experimentally observed vortex breakdown (i.e. total pressure losses and reversed flow in the core). Because this pressure loss can not be explained theoretically questions remain regarding the influences of grid density and numerical viscosity. The initial appearance of vortex breakdown compares well with experimental observations, but the results tend to diverge rapidly with further increasing angle of attack [Hitzel 1988; Agrawal et al. 1991]. The likely explanation of this divergence is the increasing importance of viscosity in the flow field beyond the point of vortex breakdown.

Three dimensional Navier-Stokes simulations of the flow about delta wings at high angle of attack have been able to identify both spiral and bubble-type breakdown modes [Thomas et al. 1987; Kandil and Chuang 1988; Hartwich et al. 1988; Fujii and Schiff 1989]. Ekaterinaris and Schiff [1990a] noted that with increasing angle of attack the appearance of bubble-breakdown preceded that of spiral-breakdown. These results are comparable with those of Weimer et al. [1994] discussed above for an axisymmetric free vortex where the bubble-breakdown mode preceded the spiral-mode. A prohibitively fine computational grid is necessary, however, to capture the small-scale details of the flow in the breakdown region [Ekaterinaris and Schiff 1990b].

1.3   Objectives of Current Investigation

While extensive research has been done to investigate the vortical flow about delta wings, certain fundamental questions remain unanswered. This is particularly true in the high subsonic flow regime where the effects of compressibility play an important role. Specific questions include the geometry of the terminating shock wave system and its influence on the vortex breakdown process. The presence of embedded cross-flow shock waves has yet to be confirmed experimentally and the possible influence of these shock waves on the lee-side flow field evaluated. The structure of the vortex throughout the breakdown process itself in this flow regime is unknown. And, finally, the applicability of various theories on vortex breakdown mechanisms, developed for the incompressible flow regime, to the high subsonic flow regime is unclear.

The motivation for the current study is to examine some of these questions. The flow field which will be considered is that of a flat-plate, 65° sweep, bevelled sharp leading edge delta wing in a high subsonic free stream. While a rounded leading edge is of more practical interest, the sharp leading edge is selected for its simplicity and suitability for use in comparison with inviscid numerical calculations. The current study is experimental in nature and will examine the flow field using a variety of qualitative and quantitative investigative techniques. The techniques applied include several conventional measurement and visualization

techniques. The inability of available measurement and visualization techniques to capture the unsteady and three-dimensional aspects of the flow field, however, motivated the development of the surface reflective visualization (SRV) system. The SRV technique is developed and validated in the course of the present study. While the majority of the work presented in this report is experimental, concurrent numerical work being done in the High Speed Aerodynamics Laboratory of the Delft University of Technology will be presented where appropriate for comparison purposes.

An overview of the method of approach used for investigating the various questions outlined above is presented in Chapter 2. In Chapter 3 the various measurement systems and techniques used in the current study are described in detail together with a discussion of measurement quality. The five-hole probe measurement technique is discussed separately in Chapter 4 as the intrusive nature of this measurement technique make its data quality analysis more complex. The development and validation of the surface reflective visualization system SRV technique are discussed in Chapter 5. The geometry and other interesting aspects of the vortex system observed in the current investigation, both with and without vortex breakdown present above the wing, are presented in Chapter 6. Finally, conclusions and future prospects are given in Chapter 7.

2
Project Overview

The major objectives of this investigation of the vortical flow field above a flat-plate, 65°
sweep, sharp leading edge delta wing in a high subsonic free stream are to:

- define the geometry of the vortical flow system above a delta wing for a variety of combinations of free stream Mach number and angle of attack in the high subsonic flow regime

- investigate the behavior of embedded cross-flow shock waves

- examine the structure of the vortex throughout the breakdown process in the high subsonic flow regime

- define the geometry of the terminating shock wave system and its interaction with the vortex breakdown process

- determine the applicability of the vorticity dynamics theory on vortex breakdown, developed for the incompressible flow regime, in the high subsonic flow regime

In pursuit of these objectives various experimental techniques are utilized. The advantages
and limitations of these various investigative techniques are discussed below. The testing program, specifying which measurement techniques are applied at various combinations of free
stream Mach number and angle of attack, is presented in Section 2.3. The rationale behind
the selection of this particular measurement program is also discussed.

2.1 Conventional Measurement Techniques

Conventional investigative techniques used in this study include oil surface flow visualizations, surface pressure measurements, five-hole probe measurements and optical transmission
flow field visualizations. These various techniques are useful in evaluating specific aspects
of the flow field. Surface separation and reattachment lines are defined using the oil surface

flow visualization technique. Figure 2.1 illustrates a characteristic oil flow streak pattern for the flow over a sharp leading edge delta wing with no vortex breakdown occurring above the wing. The termination of the organized vortical structure caused by vortex breakdown can also be identified via the oil flow surface visualization technique. A characteristic oil flow pattern when vortex breakdown is present above the wing is shown in Figure 2.2.
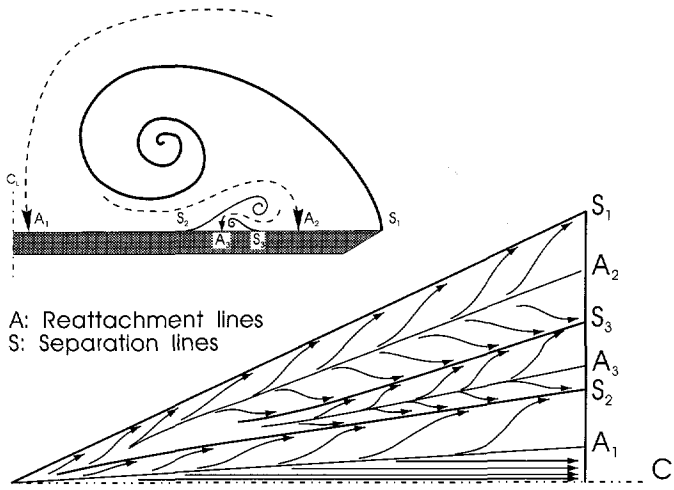
Figure 2.1: Characteristic oil flow surface pattern and cross-section of the associated vortical flow field.
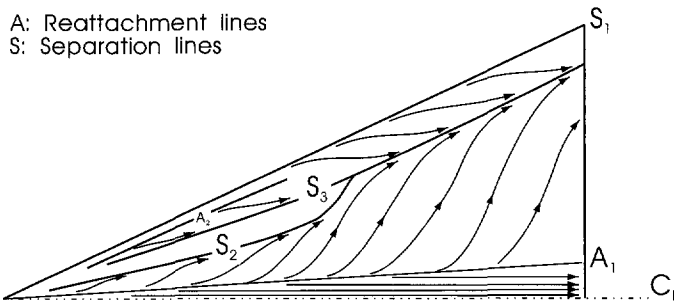
Figure 2.2: Characteristic oil flow surface pattern associated with vortex breakdown occurring above the wing.

The lee-side surface pressure distribution also gives some indication of the location of surface flow separation and reattachment lines. More importantly, however, the surface pressure measurements illustrate the influence of large scale variations in the vortex system, such as vortex breakdown, on the surface pressure distribution and vortex lift. While, the time av-

erage nature of the surface pressure measurements limits their usefulness in tracing the unsteady vortex breakdown process itself, they do provide some indication of the termination of an organized vortex structure.

Five-hole probe measurements allow quantitative information to be obtained in the flow field. The five-hole probe measurements have the disadvantage, however, of being intrusive on the flow field and ineffective once vortex breakdown has taken place. The presence of the five-hole probe in the flow field may, in fact, induce vortex breakdown. Five-hole probe measurements are viable, therefore, only well before the point of incipient vortex breakdown (i.e. low angle of attack and free stream Mach number).

The optical transmission flow visualization technique can provide an *instantaneous* view of the flow field both with and without vortex breakdown present above the wing, but remains limited to a side-view perspective of the flow field integrated over the full width of the test section. This integration process makes it impossible to determine the spanwise extent of various phenomena and conceals asymmetries between the port and starboard leading edge vortex systems.

Therefore, while the above mentioned techniques are useful in evaluating certain aspects of the flow field, they also have significant limitations. The inability of these conventional measurement techniques to capture the three-dimensional and unsteady features of the flow field associated with vortex breakdown above a delta wing in the high subsonic flow regime provided the incentive to develop the surface reflective visualization system discussed below.

2.2   The Surface Reflective Visualization System

The surface reflective visualization (SRV) system provides a new perspective on the flow field above a flat-plate delta wing in the high subsonic flow regime. The SRV system yields a plan-view Schlieren image of the flow field above the delta wing. By incorporating a high speed camera and spark light source into this system it is possible to obtain *instantaneous* images of the rapidly fluctuating flow field. Embedded cross-flow shock waves and the spanwise distribution of the terminating shock wave system can both be visualized via the SRV system. This new perspective allows the symmetry of the two leading edge vortices both before and beyond the point of vortex breakdown to be examined. The SRV system further permits the vortex breakdown process itself to be visualized. While many smoke, laser sheet and dye visualizations have been made of vortex breakdown in the low speed flow regime, clear visualizations of vortex breakdown in the high subsonic compressible flow regime are not yet available.

The original nature of the SRV system necessitated an extensive system analysis study

to determine the proper interpretation of the resulting images. In this analysis study an algorithm is applied to both an experimental and a numerical data base which simulates the optical SRV system. The simulated-SRV images resulting from this procedure are compared with actual SRV images to gain insight into the actual flow field. Details on the SRV system and this analysis study are provided in Chapter 5.

While the SRV system has many advantages, it does not provide quantitative flow field information, knowledge of the flow on the model surface nor a complete definition of the three-dimensional flow field. Information obtained via the conventional techniques described above complement the SRV images, therefore, in defining the complex three-dimensional flow field existing above the delta wing.

2.3   Testing Matrix

2.3.1   Overview of the Measurement Program

Three different Mach numbers ($M_\infty = 0.6, 0.7$ and 0.8) and four different angles of attack ($\alpha = 10°, 15°, 18°$ and $20°$) are examined in the current study. These cases are selected to be representative of flows both with and without terminating shock waves and both exhibiting and not exhibiting vortex breakdown above the wing. In some cases tests have been made with certain techniques outside this matrix of Mach numbers and angles of attack to gain additional insight into the flow field. In this study the Reynolds number and Mach number do not vary independently due to the use of a nominally constant stagnation pressure ($200 kPa$) and stagnation temperature ($280 \pm 10 K$) for all experiments. The nominal Reynolds number associated with each of the free stream Mach numbers is shown in Table 2.1.

The various measurement techniques applied for specific $M_\infty - \alpha$ combinations are also shown in Table 2.1. Surface pressure measurements, transmission flow field visualizations with the Schlieren knife edge aligned parallel with the free stream flow, oil surface flow visualizations and SRV visualizations with the Schlieren knife edge aligned parallel with the free stream flow are performed for all combinations of the testing matrix. The five-hole probe measurements are carried out only at $\alpha = 10°$ and $\alpha = 15°$ because no vortex breakdown is observed above or behind the wing at these angles of attack. As mentioned above, five-hole probe measurements are no longer viable beyond the point of incipient vortex breakdown due to interference effects and calibration difficulties. The Schlieren knife edge orientation perpendicular to the free stream flow in the transmission flow visualizations and SRV images is applied only at higher combinations of Mach number and angle of attack because preliminary investigations indicated that the terminating shock wave system, best visualized with this Schlieren knife orientation, is only present for these combinations. While surface

Meas. Type	$M_\infty = 0.6$ $(Re_{cr} = 3.2\cdot10^6)$				$M_\infty = 0.7$ $(Re_{cr} = 3.6\cdot10^6)$				$M_\infty = 0.8$ $(Re_{cr} = 4.0\cdot10^6)$			
	$10°$	$15°$	$18°$	$20°$	$10°$	$15°$	$18°$	$20°$	$10°$	$15°$	$18°$	$20°$
5_{hp}	X	X							X	X		
SP	X	X	X	X	X	X	X	X	X	X	X	X
T_h	X	X	X	X	X	X	X	X	X	X	X	X
T_v							X	X		X	X	X
O	X	X	X	X	X	X	X	X	X	X	X	X
SRV_h	X	X	X	X	X	X	X	X	X	X	X	X
SRV_v			X	X		X	X	X		X	X	X

5_{hp}:   Five-hole probe measurements

SP: Surface pressure measurements

T_h: Transmission Schlieren visualization with Schlieren knife edge parallel to free stream flow

T_v: Transmission Schlieren visualization with Schlieren knife edge perpendicular to free stream flow

O: Oil surface flow visualization

SRV_h: SRV images with Schlieren knife edge parallel to root chord and free stream flow (i.e. zero yaw angle)

SRV_v: SRV images with Schlieren knife edge perpendicular to root chord and free stream flow (i.e. zero yaw angle)

Table 2.1: Outline of measurement techniques used in test matrix.

pressure measurements and oil flow visualizations are performed when vortex breakdown is present above the wing in the current study (i.e. $\alpha = 18°$ and $\alpha = 20°$), interpretations of the average flow field information provided by these techniques must be made with care. The flow field is known to be unsteady in the presence of vortex breakdown and direct comparison of average measurements with *instantaneous* visualizations is not possible. More specific details on the objectives and scope of the five-hole probe and surface pressure measurement programs are provided below.

2.3.2 Five-hole Probe Measurement Program

A five-hole probe measurement program is carried out to obtain quantitative information in the flow field. Measurements are made both above the delta wing and in its wake in order to trace the development of the flow field prior to vortex breakdown. In the high subsonic flow regime vortex breakdown is known to jump suddenly from the trailing edge to well forward on the wing upon reaching the trailing edge. Measurements are made, therefore, in the

wake of the wing in order to trace a more gradual development of the flow field preceding the appearance of vortex breakdown.

Measurements are conducted in two spanwise planes above the wing surface oriented perpendicular to the wing upper surface and in two planes behind the wing oriented perpendicular to the free stream flow direction (See Figure 2.3). The orientation of the planes is selected
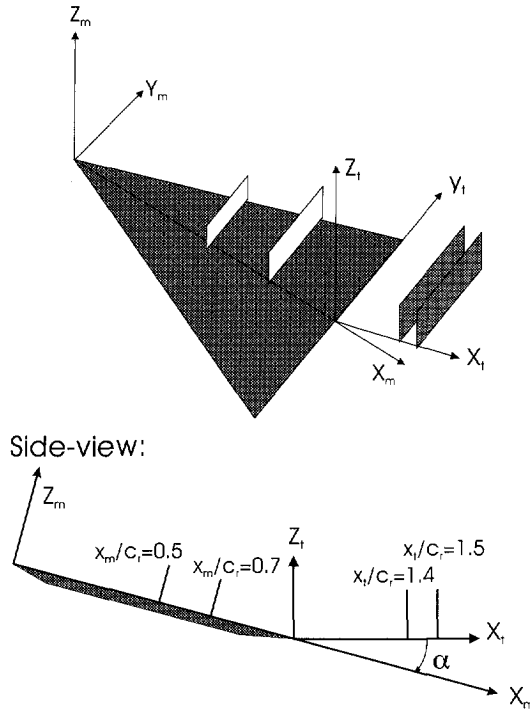
Figure 2.3: Illustration of body fixed Cartesian coordinate system m, tunnel coordinate system t and 5-hole probe measurement planes.

in order to most closely capture the vortical nature of the flow or the vortex cross-flow plane. The vortical flow field is observed to have a nearly conical geometry above the wing surface and to realign itself with the free stream beyond the trailing edge. The relevant grid spacing for each of the measurement planes is shown in Tables 2.2 and 2.3. All planes are made up of a square measurement grid (i.e. $\Delta y = \Delta z$) with N_z traverses in the z_m direction and N_y measurement positions in the spanwise direction y_m. The step size Δ in the measurement planes located above the wing is equivalent to 1.8% of the local semi-span. The step size Δ for the measurement planes behind the wing is equivalent to 3.6% of the wing semi-span. These values of Δ are selected to capture the anticipated conical geometry of the flow above the wing and its Cartesian orientation in the wake of the wing. Each of the measurement

Meas. Plane No.	M_∞ [1]	α [°]	(x_m/c_r) [1]	N_z [1]	N_y [1]	Step Size Δ [mm]
1	0.6	10	0.5	14	37	0.5
2	0.6	10	0.7	14	37	0.7
3	0.8	10	0.5	14	37	0.5
4	0.8	10	0.7	13	33	0.7
5	0.6	15	0.5	18	40	0.5
6	0.6	15	0.7	18	41	0.7
7	0.8	15	0.5	18	40	0.5
8	0.8	15	0.7	18	41	0.7
9	0.8	10	0.7	13	33	1.4
10	0.8	10	0.72	14	37	0.72

Table 2.2: Five-hole probe measurement grids above the wing.

Meas. Plane No.	M_∞ [1]	α [°]	(x_t/c_r) [1]	N_z [1]	N_y [1]	Step Size Δ [mm]
11	0.6	10	0.4	12	17	2.0
12	0.6	10	0.5	12	17	2.0
13	0.8	10	0.4	12	17	2.0
14	0.8	10	0.5	12	19	2.0
15	0.6	15	0.4	12	20	2.0
16	0.6	15	0.5	12	20	2.0
17	0.8	15	0.4	11	20	2.0
18	0.8	15	0.5	12	20	2.0

Table 2.3: Five-hole probe measurement grids in the wake of the wing.

planes listed in Tables 2.2 and 2.3, thus, represents a unique combination of Mach number, angle of attack, x_m or x_t position and grid spacing.

2.3.3 Surface Pressure Measurement Program

Surface pressure measurements are made at several $M_\infty - \alpha$ combinations in addition to those listed in Table 2.1. These combinations include $\alpha = 0°, 5°$ and $19°$ at $M_\infty = 0.6, 0.7$ and 0.8. The lower angles of attack are examined to trace the development of the surface pressure distribution with increasing angle of attack. The condition of $\alpha = 19°$ is examined in order to gain additional insight into the influence of vortex breakdown on the wing performance.

Three different models are used for the surface pressure measurements. Three models are

required due to the unfeasibility of containing the requisite pressure lines for a large number of pressure ports inside one delta wing. The pressure tap distribution of the three models is shown in Figure 2.4 and listed in Table 2.4. A total of 156 ports are present on the three models, with 135 of these being unique. A certain number of ports are repeated, or located on more than one model, to insure the comparability of test results made with the three models at nominally similar test conditions. The consistency of the test results for the three models is discussed further in Section 3.3.

   The three models are each designed to capture different aspects of the flow field. Model 1, with a dense distribution of pressure ports in the span-wise direction at 70% of the root chord, is designed to examine the span-wise surface pressure distribution. Model 2 measures the pressure distribution along the root chord as well as along three separate rays extending from 70% to 90% of the rood chord. These ray-wise ports near the trailing edge are selected to monitor the trailing edge influence on the pressure distribution as well as that of vortex breakdown. On the third model pressure ports are distributed along several conical rays extending from 40% to 65% of the root chord. These ports are chosen to examine the change in span-wise pressure distribution with increasing x_m-station.

model 1

model 2

model 3

models 1,2,3
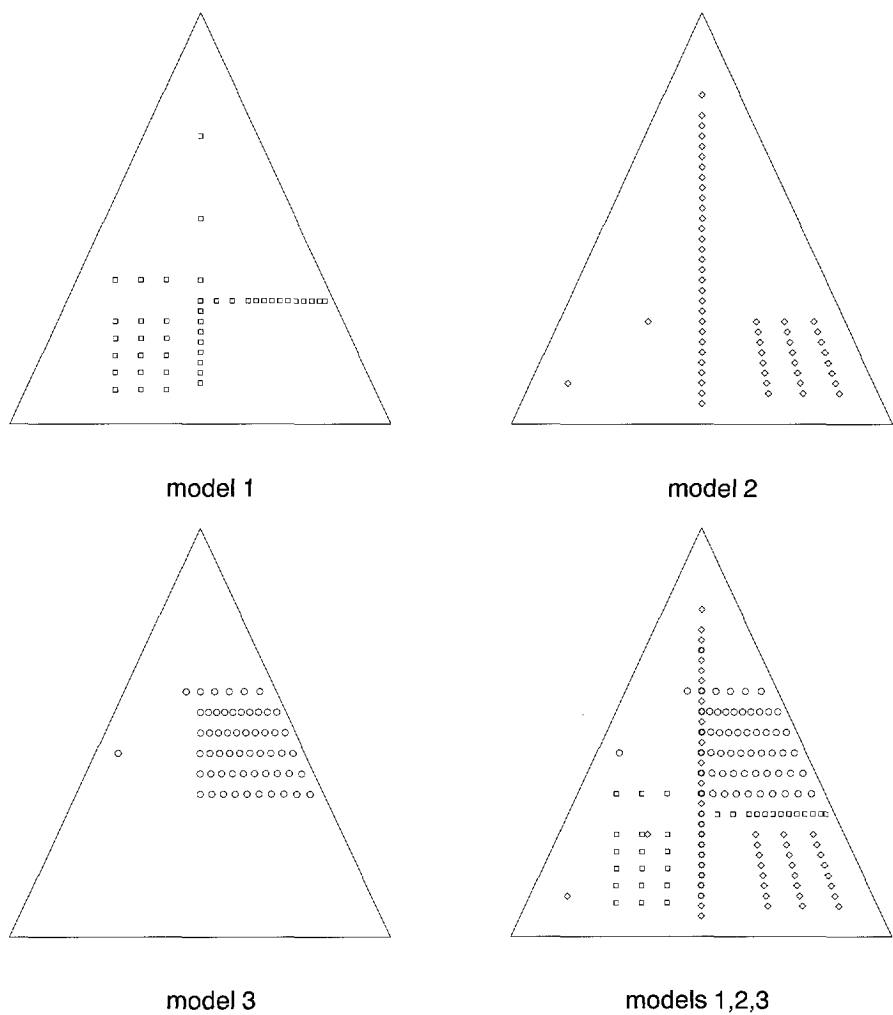
Figure 2.4: Surface pressure tap locations for the surface pressure models.

Table 2.4: Model coordinates of the surface pressure orifices.

port	model 1		model 2		model 3	
no.	x_m [mm]	y_m [mm]	x_m [mm]	y_m [mm]	x_m [mm]	y_m [mm]
1.	36.00	0.00	24.00	0.00	48.00	0.00
2.	60.00	0.00	30.00	0.00	48.00	4.20
3.	78.00	0.00	33.00	0.00	48.00	8.46
4.	84.00	0.00	36.00	0.00	48.00	12.86
5.	87.00	0.00	39.00	0.00	48.00	17.47
6.	90.00	0.00	42.00	0.00	54.00	0.00
7.	93.00	0.00	45.00	0.00	54.00	2.36
8.	96.00	0.00	48.00	0.00	54.00	4.72
9.	99.00	0.00	51.00	0.00	54.00	7.11
10.	102.00	0.00	54.00	0.00	54.00	9.52
11.	105.00	0.00	57.00	0.00	54.00	11.97
12.	108.00	0.00	60.00	0.00	54.00	14.47
13.	84.00	4.67	63.00	0.00	54.00	17.03
14.	84.00	9.33	66.00	0.00	54.00	19.65
15.	84.00	14.00	69.00	0.00	54.00	22.37
16.	84.00	16.33	72.00	0.00	60.00	0.00
17.	84.00	18.67	75.00	0.00	60.00	2.62
18.	84.00	21.00	78.00	0.00	60.00	5.25
19.	84.00	23.33	81.00	0.00	60.00	7.90
20.	84.00	25.67	84.00	0.00	60.00	10.58
21.	84.00	28.00	87.00	0.00	60.00	13.30
22.	84.00	30.33	90.00	0.00	60.00	16.08
23.	84.00	32.67	93.00	0.00	60.00	18.92
24.	84.00	35.00	96.00	0.00	60.00	21.84
25.	84.00	36.50	99.00	0.00	60.00	24.85
26.	78.00	-10.00	102.00	0.00	66.00	0.00
27.	90.00	-10.00	105.00	0.00	66.00	2.88
28.	95.00	-10.00	108.00	0.00	66.00	5.77
29.	100.00	-10.00	111.00	0.00	66.00	8.69
30.	105.00	-10.00	114.00	0.00	66.00	11.64

Table 2.4: Model coordinates of the surface pressure orifices.

port	model 1		model 2		model 3	
no.	x_m [mm]	y_m [mm]	x_m [mm]	y_m [mm]	x_m [mm]	y_m [mm]
31.	110.00	-10.00	90.00	15.87	66.00	14.63
32.	78.00	-17.50	93.00	16.40	66.00	17.69
33.	90.00	-17.50	96.00	16.93	66.00	20.81
34.	95.00	-17.50	99.00	17.46	66.00	24.02
35.	100.00	-17.50	102.00	17.99	66.00	27.34
36.	105.00	-17.50	105.00	18.51	72.00	0.00
37.	110.00	-17.50	108.00	19.04	72.00	3.14
38.	78.00	-25.00	111.00	19.57	72.00	6.30
39.	90.00	-25.00	90.00	24.12	72.00	9.48
40.	95.00	-25.00	93.00	24.92	72.00	12.70
41.	100.00	-25.00	96.00	25.72	72.00	15.96
42.	105.00	-25.00	99.00	26.53	72.00	19.29
43.	110.00	-25.00	102.00	27.33	72.00	22.70
44.			105.00	28.14	72.00	26.21
45.			108.00	28.94	72.00	29.82
46.			111.00	29.74	48.00	-4.20
47.			90.00	32.76	66.00	-24.02
48.			93.00	33.85	78.00	0.00
49.			96.00	34.94	78.00	3.40
50.			99.00	36.03	78.00	6.82
51.			102.00	37.13	78.00	10.27
52.			105.00	38.22	78.00	13.75
53.			108.00	39.31	78.00	17.29
54.			111.00	40.40	78.00	20.90
55.			90.00	-15.87	78.00	24.59
56.			108.00	-39.31	78.00	28.39
57.					78.00	32.31

3

Measurement Systems and Data Quality Analysis

In this chapter relevant experimental systems and equipment are discussed. Measurement accuracy, repeatability and possible sources of measurement error for each of these measurement techniques are also considered. The five-hole probe measurement technique and surface reflective visualization system are discussed separately in Chapters 4 and 5, respectively. The five-hole probe technique is discussed separately because it is an intrusive measurement technique which requires more extensive data quality analysis than the non intrusive techniques discussed in the current chapter. The surface reflective visualization technique is discussed independently because it is a new technique and, therefore, requires an extensive system analysis to support the interpretation of the resulting images.

3.1 Wind Tunnel

All experiments are performed in the TST-27 transonic/supersonic wind tunnel located in the High Speed Aerodynamics Laboratory of the Department of Aerospace Engineering of the Delft University of Technology in the Netherlands. The TST-27 wind tunnel, shown in Figure 3.1, is a "blow-down" type wind tunnel with a test section 28 cm wide and with a height varying from 25 cm to 27 cm depending on the Mach number. Test Mach numbers range from 0.5 to 0.9 in the subsonic regime and from 1.2 to 4.0 in the supersonic regime. Subsonic and transonic Mach numbers are controlled using a variable choke section in the outlet diffuser. This choke forms a sonic throat which prevents disturbances from propagating upstream into the test section. Small deviations of the Mach number during a run are corrected by an automated control system which finely adjusts this choke [Bannink and Bakker 1983]. Supersonic Mach numbers are set by means of a continuously variable throat and flexible upper and lower walls. Separate modules downstream of the test section allow the use of the
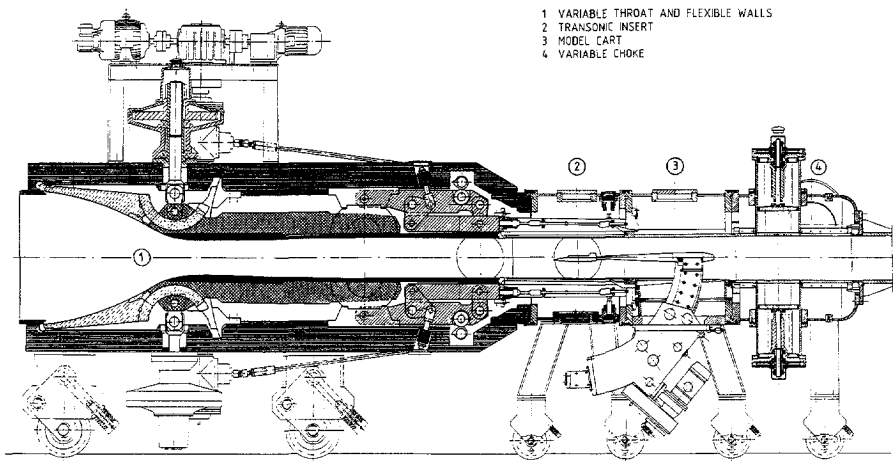
Figure 3.1: TST-27 transonic/supersonic wind tunnel.

wind tunnel in several configurations.

Two test section configurations are used in the current study. These include a transonic slotted wall test section and a solid wall test section with cross sections of $28 \times 25.3 \ cm^2$ and $28 \times 26 \ cm^2$, respectively. The transonic test section, having slotted upper and lower walls and designed in order to minimize wind tunnel wall effects [van Oort 1986], is inserted downstream of the solid wall test section (see Figure 3.1). Use of this test section allows combinations of Mach number and higher angle of attack to be tested in the high subsonic flow regime than is otherwise possible. Most tests in this study are made in the solid wall test section, however, in order to provide more comparable test conditions for tests made with the model supported on a sting and the SRV tests, which require the model to be mounted on the side wall of the test section. Either of two different model carts are used to support the model on the sting. One of these carts is equipped with an angle of attack mechanism for automated adjustment of the model incidence (see Figure 3.1). The other cart has a stationary sting support and a three dimensional automated traverse mechanism used for supporting the five-hole probe (see Figure 3.2). There are $29.5 \ cm$ and $25 \ cm$ diameter windows in the side walls of the solid wall and transonic test sections, respectively, to allow visual access while testing. Some data obtained using the slotted wall test section are presented in this report, but only at combinations of lower Mach number and smaller angle of attack, where flow differences between the two test environments are not significant.

Dried air with a relative humidity ratio of $4.1 \cdot 10^{-6}$ (i.e. dew point temperature of $-45^{\circ}C$)
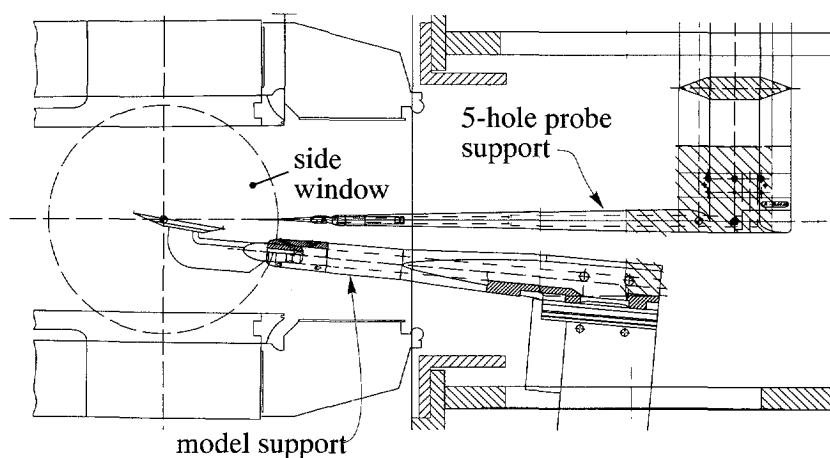
Figure 3.2: Model support cart equipped with a three-dimensional traverse mechanism.

is supplied from a $300\ m^3$ pressure vessel having a maximum pressure of $4.5\ MPa$. In the tests in the high subsonic regime of the current investigation the Mach number remains constant during a run within a range of ± 0.002. The temperature of the air in the stagnation chamber varies during a run within a range of $\pm 10K$ as a function of the atmospheric temperature and how recently warm air was pumped into the storage tank via the compressors. No separate heating system is currently in use with the TST-27 wind tunnel.

3.2   Models and Supports

All models used in this study are flat-plate delta wings with a bevelled sharp leading edge, $65°$ leading edge sweep, chord length of $120\ mm$ and an aspect ratio of 1.87. The bevel angle to the leading and trailing edges from the underside of the wing is $30°$. The model is supported during testing by either a sting or side-wall support. The thickness of the model including the plate which connects it to the support is $10\ mm$. Unique aspects of the various models used for particular types of tests are discussed below in conjunction with the relevant measurement systems.

The delta wing is supported on a sting during side-view transmission flow field visualizations, oil flow visualizations, surface pressure measurements and five-hole probe measurements in order to allow side-view optical access of the model while the wind tunnel is running (see Figure 3.3). The sting support also allows easy adjustment of the angle of attack and, in the case of surface pressure measurements, houses the pressure lines leading from the model to the pressure transducers located outside the tunnel. The side-view access provided by the

sting is particularly useful during five-hole probe measurements as it allows the flow to be monitored during testing to determine whether the probe is significantly interfering with the flow field (i.e. initiating vortex breakdown).
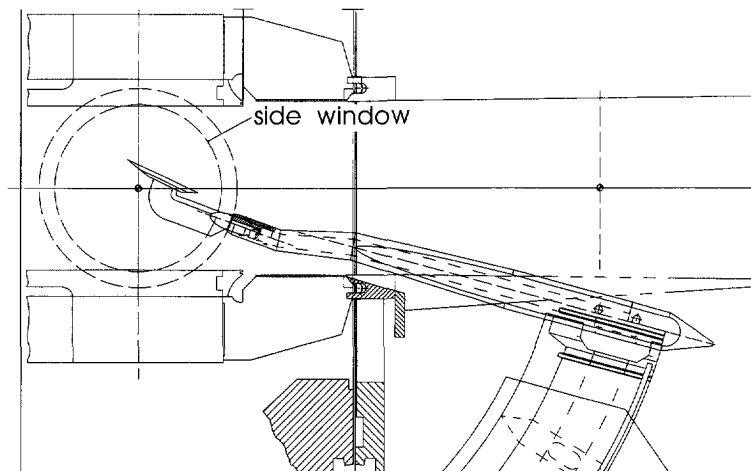
Figure 3.3: Side-view of sting support.

The side-wall support is shown in Figure 3.4. This support is designed to provide the high stiffness necessary for the optical SRV system and a minimum of support interference. The angle of attack is adjusted by placing or removing blocks, machined to a specific angle, between the support and the tunnel wall. The support alone yields $20°$ angle of attack. The mirrored upper surface SRV model is glued to the upper surface of the side-wall support to provide more uniform heat transfer during a run and, thus, prevent optical distortion. For this reason, two side-wall supports are constructed and one support is used exclusively for the SRV tests.

Surface oil flow and five-hole probe tests are performed in the solid wall test section with both the sting and side-wall support configurations to check the comparability of the two support configurations. The surface oil flow tests show the secondary flow separation lines to be comparable for the two support configurations. The presence of vortex breakdown above the wing is also found to be consistent for both support configurations except in the cases exhibiting asymmetric vortex breakdown (see Section 6.3). The latter is not surprising, however, because then the oil flow can not provide an accurate representation of this flow field above the surface of the wing due to the flow's highly unsteady nature. Various tests with the same support and $M_\infty - \alpha$ combination also exhibit vortex breakdown on either the port side of the wing, starboard side of the wing or not at all. Though the flow is also unsteady in the
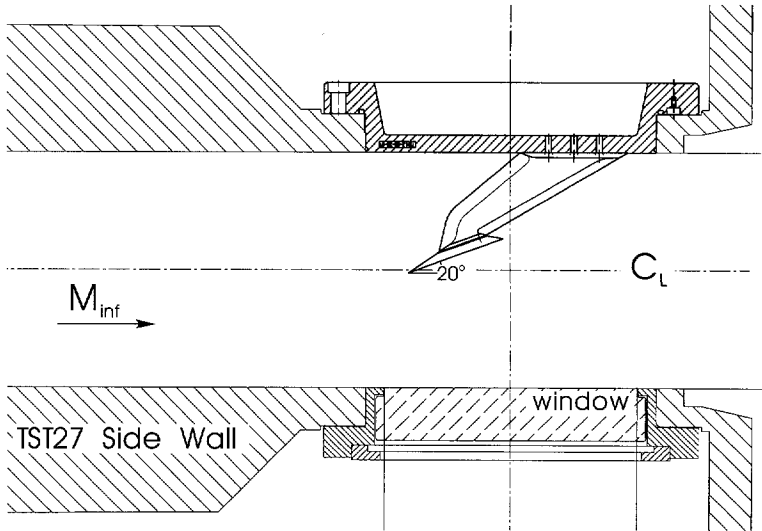
Figure 3.4: Top-view of side-wall support.

case of symmetric vortex breakdown, the oil flow patterns are found to be more repeatable. The drying of the oil also has a significant influence on the final flow pattern. Beyond a certain period of time during a given run the oil will dry in place and prevent it from following further flow fluctuations.

Five hole probe tests are made with the model supported both on the sting and the side-wall support to examine the consistency of the primary vortex core location above the wing for the two support configurations. In the current investigation the primary vortex core location is defined as the location of $(p_{tot})_{min}$ in each of the five-hole probe measurement planes (for further discussion see Section 4.5.2). These tests show that the spanwise location of the vortex core remains the same within 2% of the local semi-span and the normal distance to the wing surface within 4% of the local semi-span when $(x_m/c_r) = 0.7$ (see Table 3.1). The

M_∞	Side-wall support		Sting support	
	$\left(\dfrac{y_m}{y_{le}}\right)$	$\left(\dfrac{z_m}{y_{le}}\right)$	$\left(\dfrac{y_m}{y_{le}}\right)$	$\left(\dfrac{z_m}{y_{le}}\right)$
0.6	0.68	0.22	0.66	0.19
0.8	0.60	0.22	0.61	0.18

Table 3.1: Comparison of primary vortex core location (i.e. $(p_{tot})_{min}$) when $\alpha = 15°$ and $(x_m/c_r) = 0.7$ for measurements made with side-wall and sting supports.

larger discrepancy in normal distance to the wing can be explained by the inability to cor-

rect for dynamic vertical displacement of the side-wall supported model and the probe itself when the wind tunnel is on due to lack of side-view visual access in this configuration. Only top-view visual access of the model is available in the side-wall support configuration. A dynamic vertical position correction is made in the case of the model supported on the sting and is found to be a maximum of 0.5 mm vertical deflection downward of the probe when in the vicinity of the wing upper surface and a maximum of 0.5 mm vertical deflection upwards of the wing apex when $M_\infty = 0.8$ and $\alpha = 15°$. Deflections are noted to be less at combinations of lower Mach number and smaller angle of attack.

3.3   Surface Pressure Measurements

As mentioned in Section 2.3.3, three different models are necessary for the surface pressure measurements due to the impossibility of containing the pressure lines for all the desired pressure ports inside one delta wing. The combined pressure tap distribution of the three models is shown in Figure 3.5. As mentioned in Section 2.3.3, a certain number of ports on the three
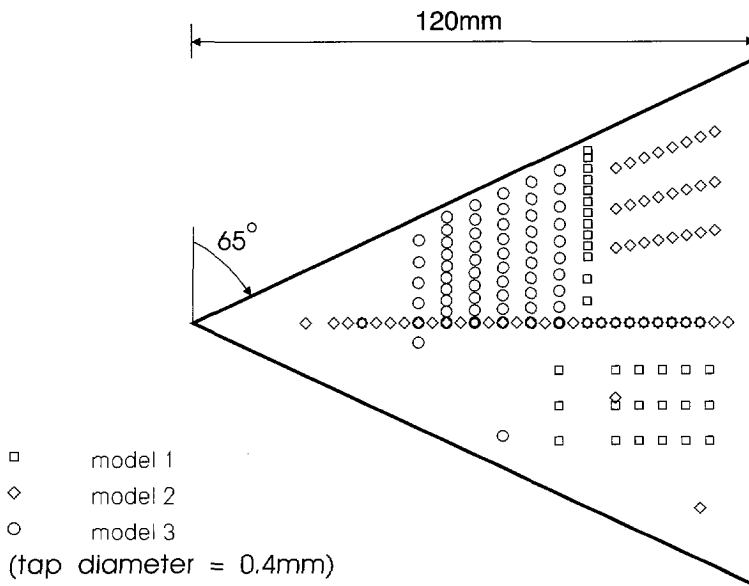
Figure 3.5: Combined pressure tap distribution of all three models.

models are repeated, particularly along the root chord, in order to establish compatibility between tests made at nominally identical test conditions. Two pressure ports are mirrored on either side of the root chord on models 2 and 3 in order to examine the symmetry of the flow field about the root chord. The diameter of the pressure taps is 0.4 mm. The pressure lines

are connected to two pressure scanning valves. Due to the relatively long pressure lines (approximately $2\ m$) and the use of pressure scanning valves, surface pressures measurements are limited to average values (measurement time $\approx 300\ msec$).

Contour plots are a useful tool for obtaining a more global perspective on the surface pressure distribution on the surface of a model. Because the distribution of the pressure orifices in the current investigation is neither regular nor dense some preliminary data processing is necessary to create useful contour plots. First the data of the three models are superimposed on one side of the wing to provide a higher data density. The symmetry of the surface pressures about the root chord is checked by comparing the mirrored pressure taps of models 2 and 3 mentioned above and is found to be quite good even for configurations experiencing asymmetric vortex breakdown above the wing ($|\Delta c_p|_{max} < 0.1$). While the models of identical design were machined with a geometric accuracy of $\pm 0.1\ mm$, small differences in the pressure distribution are apparent at the same nominal Mach number and angle of attack. Before superimposing the data, the pressure distributions along the centerline are compared and the incidence slightly varied until the curves of the three models match satisfactorily (the nominal incidence differing by a maximum of $0.2°$). The displacements caused by aerodynamic loading have been measured and found to be less than $0.4°$ for the most extreme condition (i.e. Mach 0.8 at $20°$ incidence).

To generate a grid from the irregularly distributed data points the Delaunay triangulation method [Weatherill 1990] is applied via implementation of the software package $Tecplot$[1]. The resulting unstructured mesh contains 147 nodes and 216 triangular elements and is illustrated on the starboard side of the wing in Figure 3.6. The foremost taps on the centerline ($0.2 \leq (x_m/c_r) \leq 0.40$) are not included in the data grid because of the lack of corresponding spanwise information at these chordwise locations. A more complete delta wing image is obtained by mirroring the grid about the centerline.

3.4   Oil Surface Flow Visualizations

The oil used in producing the surface flow visualizations is white in color and consists of a mixture of 30 g of *Shell Tellus 29* oil, 19 g of titanium dioxide powder and 4 drops of *Shell T40* detergent (oleic acid). A base layer of oleic acid is also applied as a primer to the model to ease the flow of the oil during testing. Two models are used for oil flow visualization testing. Both of these models are painted black in order to provide maximum contrast with the white oil mixture. The only difference between the two models is that one is suitable for use with the sting support and the other is for use with the side-wall support. Tests made with the

---

[1]A product of Amtec Engineering, Inc., P.O. Box 3633, Bellevue, WA 98009-3633 USA
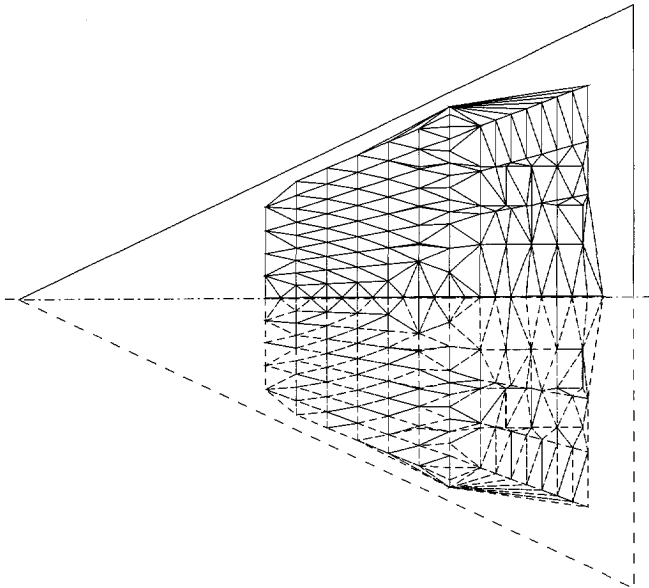
Figure 3.6: Unstructured mesh on one half of the wing (solid) and its reflection (dotted)

model mounted on the sting are conducted both in the transonic test section and in the solid wall test section. The sting support allows side-view transmission visualizations to be made while the tunnel is running. Testing in the transonic slotted wall test section is done so that the oil flow can be observed on the lee-side of the model while the tunnel is running via an optical probe extending into the plenum of the wind tunnel and aligned between two slots (see Figure 3.7). Tests are done with the model mounted on the side-wall support to insure the compatibility between the oil surface flow visualizations and the SRV images.

An important limitation of the surface oil flow visualization technique is that the pattern left on the model at the end of the run represents an integrated effect of the surface shear distribution over the entire course of the run (i.e. including both the starting and stopping of the wind tunnel). Another difficulty of the oil flow technique is the tendency of the oil to dry during the run and no longer respond to changes in the surface shear stress. For these reasons it is important to observe the oil during the course of the run to ensure both that the oil has not become too dry and that the surface flow pattern is not significantly distorted during the tunnel shut-down process. Generous application of the oleic acid primer helps inhibit rapid drying of the oil onto the surface of the model during testing.
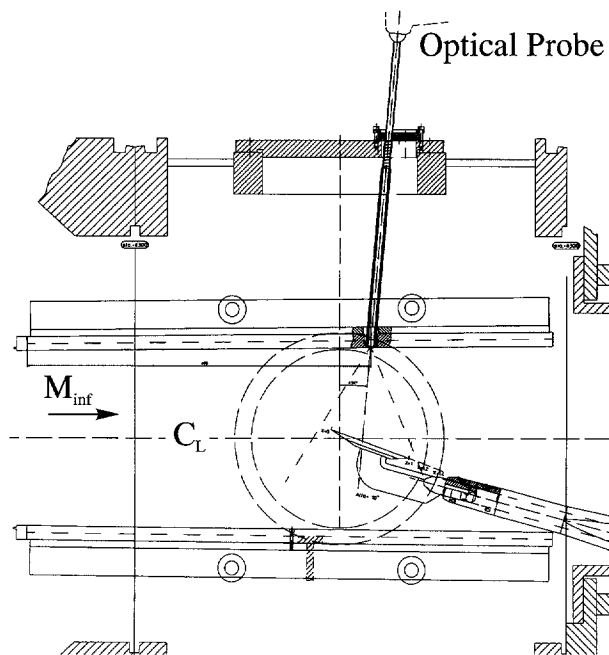
Figure 3.7: Side-view of transonic slotted wall test section with optical probe.

3.5 Transmission Flow Field Visualizations

The side-view transmission Schlieren system used in this study has parabolic mirrors as its main optical component [Holder and North 1963]. Various types of cameras and lighting configurations are used to capture different aspects of the flow field. Continuous lighting by a Schlieren arc lamp combined with a standard camera or video camera is sufficient to capture an image of the average flow field (exposure time $\approx 20\ msec$). In order to obtain sharp images of the highly fluctuating terminating shock wave system and the flow field structure associated with vortex breakdown, however, a high speed camera and a spark light source are required.

An Impulsphysik Strobodrum camera is used in this study to record the flow field at higher frequencies than is possible with standard commercial video cameras (normally rated at $50\ Hz$ in Europe). This camera is operated by first winding $35\ mm$ film tightly around the inner drum of the camera, bringing the inner drum up to rotational speed (maximum $3000\ r.p.m.$), opening the shutter of the camera in the dark wind tunnel hall and exposing images in quick succession (maximum $4.5\ kHz$) with a spark light source (see Figure 3.8).

The spark light source used in this study, a Fischer-R138 Nanolite, provides an expo-
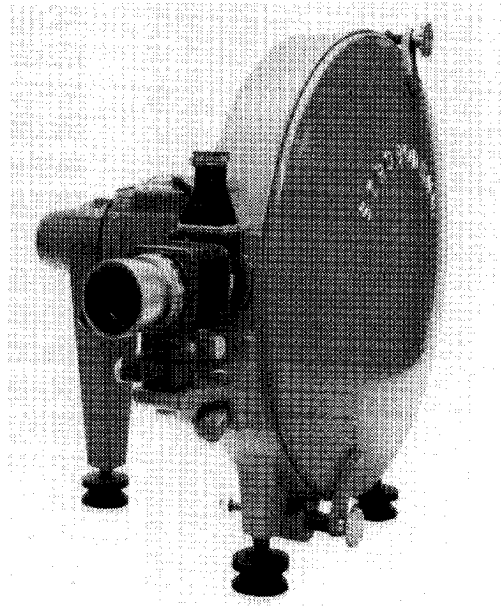
Figure 3.8: Impulsphysik high speed Strobodrum camera.

sure time of approximately $20\ nsec$ at a maximum frequency of $10\ kHz$. Initial tests were made with the spark discharging in air. However, when additional illumination was found to be necessary for the SRV system, a chamber was built to surround the spark and filled with Xenon. According to manufacturer's information, housing the spark in a Xenon chamber can be expected to provide nine times more illumination as compared to the spark discharge in air. Although the quantitative improvement of the Xenon chamber on the light source is not measured in the current study, the resulting qualitative improvement in the SRV images is very apparent. The spark light source can be used either in combination with the high speed camera to obtain a limited number of exposures at high frequency (76 images in the optical configuration used in the current study) or synchronized with a digital CCD video camera to obtain *instantaneous* images at a lower frequency over the entire course of a wind tunnel run ($\approx 2\ min$).

4

Five-hole Probe Measurements

The five-hole probe measurements are an important facet of the current investigation as only they provide information on the quantitative flow properties (flow angle, local Mach number and total pressure) within the vortical flow field above and behind the delta wing. This measurement technique has the disadvantage, however, of being "intrusive" or disturbing the flow field it is intended to measure. The vortical flow field above a delta wing is particularly sensitive to disturbances resulting from the presence of obstacles in the flow field [Lambourne and Bryer 1961]. The large pressure, density and velocity gradients characteristically present in the vortical flow field above a delta wing also lead to inaccuracies in the probe measurements as the five-hole probe is calibrated in a uniform free stream. An exact assessment of the accuracy of the five-hole probe measurements is not possible as no other independent data on the flow properties in the flow field is available. The accuracy of the probe measurements in a uniform free stream flow is investigated, however. In order to gain some insight into the reliability of the five-hole probe measurements in the vortical flow field the compatibility of the five-hole probe measurements with other "non intrusive" measurements in the same flow field is evaluated. These "non intrusive" measurements include surface pressure measurements, surface oil flow visualizations and side-view transmission Schlieren images. The surface pressure measurements and surface oil flow visualizations are not truly non intrusive as the requisite presence of surface pressure taps and a thin layer of oil on the model surface for each of these techniques, respectively, will disturb the upper surface boundary layer to some extent.

4.1   Probe Geometry and Configuration:

The non-nulling spherical five-hole probe used in this investigation and its calibration procedure were developed by Houtman and Bannink [1989] specifically for application in transonic flow fields. The hemi-spherical head of the probe is 1.6 mm in diameter and the five pressure taps are 0.2 mm in diameter (see Figure 4.1). The five-hole probe is mounted on

an xyz traverse mechanism providing a minimum step length of 0.01 mm. To improve the
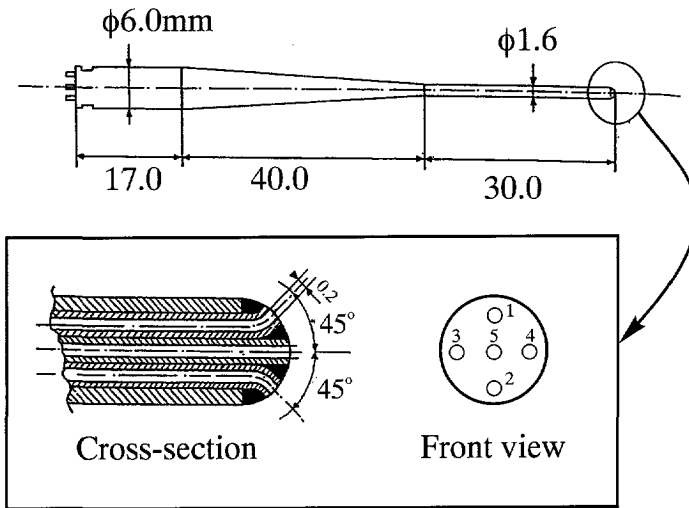
Figure 4.1: Five-hole probe geometry.

time response of the five-hole probe, five Endevco 8507-15 miniature piezoresistive pressure transducers[1] are installed in the probe support inside the wind tunnel at a distance of approximately 10 cm from the head of the probe. The pressure transducers were previously located outside of the tunnel at a distance of approximately 2 m from the head of the probe. The increased proximity of the pressure transducers to the probe head significantly decreases the measurement time requirement at each point and, thus, allows the use of finer and more extensive measurement grids than was previously feasible.

4.2   Probe Calibration

The flow at a particular point in a steady three-dimensional flow is characterized by five independent parameters: the direction of the flow (given by two angles), the Mach number, the total pressure and total temperature. The relation between the measured pressures on the surface of the five-hole probe and these flow properties are obtained via calibration coefficients. Three independent calibration coefficients are developed which are based on potential flow and Newtonian flow theory about a sphere in the incompressible and supersonic flow regimes, respectively. An important criterion in the selection of these calibration coefficients is that

---

[1] A product of Endevco, Rancho Viejo Road, San Juan Capistrano, CA 92675 USA, tel: (714)493-8181.

they should be sensitive to a change in the flow quantity to which they are related and less sensitive to changes in the other quantities.

4.2.1 Theoretical Pressure Distribution and Flow Conditions

Beginning with a right-handed Cartesian coordinate system with its x_p axis aligned along the probe center, the free stream flow direction relative to the probe can be defined in two ways (see Figure 4.2). The flow can be defined in terms of the angle of attack α in the $x_p - z_p$
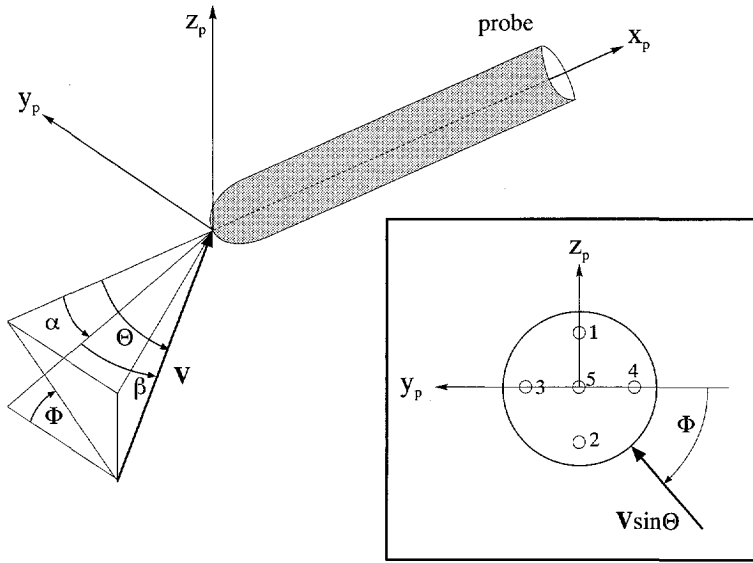
Figure 4.2: Flow angles relative to five-hole probe.

plane and the sideslip angle β in the plane containing the velocity vector and the y_p axis or in terms of the pitch angle Θ with respect to the probe center line and the roll angle Φ in the $y_p - z_p$ plane. These two sets of flow angles can be related to each other via the relations

$$\tan \alpha = \tan \Theta \sin \Phi \qquad (4.1)$$

$$\tan \beta = \frac{\sin \Theta \cos \Phi}{\sqrt{1 - \sin^2 \Theta \cos^2 \Phi}} \qquad (4.2)$$

when $0 \leq \Theta \leq (\pi/2)$ and $0 \leq \Phi < 2\pi$. The pressure distribution on the surface of the probe can be described theoretically as a function of the angle between the surface normal and the free stream flow direction θ. The angle θ can be defined at each of the five pressure ports on the

probe via the relation:

$$\cos\theta_i = \cos\Theta\cos\delta_i + \sin\Theta\sin\delta_i(\cos\Phi\sin\phi_i - \sin\Phi\cos\phi_i) \qquad (4.3)$$

where the angles δ_i, the angle between the normal to the surface and the probe center line, and ϕ_i, the roll angle in the $y_p - z_p$ plane, define the geometric position of the orifice (see Figure 4.3). Substituting δ_i and ϕ_i for the various pressure orifices and noting that $\delta_1 =$

Figure 4.3: Angles defining free stream flow relative to pressure orifice.

$\delta_2 = \delta_3 = \delta_4 = \delta$ and $\delta_5 = 0°$ for the probe used in the current investigation, the following relations are obtained:

$$\begin{aligned}
\cos\theta_1 &= \cos\Theta\cos\delta - \sin\Theta\sin\Phi\sin\delta \\
\cos\theta_2 &= \cos\Theta\cos\delta + \sin\Theta\sin\Phi\sin\delta \\
\cos\theta_3 &= \cos\Theta\cos\delta - \sin\Theta\cos\Phi\sin\delta \qquad (4.4) \\
\cos\theta_4 &= \cos\Theta\cos\delta + \sin\Theta\cos\Phi\sin\delta \\
\cos\theta_5 &= \cos\Theta
\end{aligned}$$

Now, assuming that the flow about the probe can be described by the theory for flow about

a sphere, the pressure distribution about the probe in the incompressible flow regime can be described according to incompressible potential flow theory by the relation:

$$c_{p_i} = 1 - \frac{9}{4} \sin^2 \theta_i \tag{4.5}$$

Equation 4.5 can be written in terms of the pitot pressure p_p, which is equal to the stagnation pressure in the incompressible flow regime, such that:

$$\frac{p_i}{p_p} = 1 - \frac{9}{4} \left(1 - \frac{p_\infty}{p_p}\right) \sin^2 \theta_i \tag{4.6}$$

For high-supersonic and hypersonic flow the pressure distribution about a sphere can be described using modified Newtonian theory such that:

$$c_{p_i} = c_{p_{max}} \cos^2 \theta_i = \frac{p_p - p_\infty}{q_\infty} \cos^2 \theta_i \tag{4.7}$$

Rewriting this expression in the same form as Equation 4.6 yields:

$$\frac{p_i}{p_p} = 1 - \left(1 - \frac{p_\infty}{p_p}\right) \sin^2 \theta_i \tag{4.8}$$

Here the pitot pressure p_p is equal to the stagnation pressure downstream of the normal shock wave located in front of the probe. The flow about the probe head can, thus, be described both in the incompressible and high supersonic flow regimes by the equation:

$$\frac{p_i}{p_p} = 1 - F \sin^2 \theta_i \tag{4.9}$$

where

$$F = \begin{cases} \frac{9}{4} \left(1 - \frac{p_\infty}{p_p}\right) & \text{when } M = 0, \\ \left(1 - \frac{p_\infty}{p_p}\right) & \text{when } M \gg 1 \end{cases} \tag{4.10}$$

Supposing that F is only dependent on the Mach number, Equation 4.9 can be applied in the entire Mach number range.

From Equation 4.9 it is possible to derive a relationship between the five measured pressures and the various flow quantities (i.e. flow angle, Mach number, total pressure and total temperature). The ratio between the pressure differences of the two opposite pairs of pressure orifices yields a direct relationship with the roll angle Φ. This relationship is developed

from Equations 4.4 and 4.9 such that:

$$\frac{p_2 - p_1}{p_4 - p_3} = \tan \Phi \tag{4.11}$$

In order to develop a relation for the pitch angle Θ the variation of α (or β) at a constant β (or α) yields a variation in the pressure difference between two opposite orifices $p_2 - p_1$ (or $p_4 - p_3$). A relationship can be obtained, therefore, which is mainly dependent on the pitch angle Θ and on the Mach number (via F) such that:

$$R = \sqrt{\left(\frac{p_2 - p_1}{p_p}\right)^2 + \left(\frac{p_4 - p_3}{p_p}\right)^2} = 4F \sin \delta \cos \delta |\sin \theta \cos \theta| \tag{4.12}$$

To eliminate the Mach number dependent function F, a relation similar to the formula for dynamic pressure is introduced:

$$S = \frac{p_5}{p_p} - \sum_{i=1}^{4} \frac{p_i}{4p_p} = F sin^2\delta \left(1 - \frac{3}{2} sin^2\Theta\right) \tag{4.13}$$

Dividing R of Equation 4.12 by S of 4.13 yields:

$$Q = \frac{R}{S} = \frac{\sqrt{\left(\frac{p_2 - p_1}{p_p}\right)^2 + \left(\frac{p_4 - p_3}{p_p}\right)^2}}{\frac{p_5}{p_p} - \sum_{i=1}^{4} \frac{p_i}{4p_p}} \tag{4.14}$$

In terms of the flow angles Θ and δ, Q can be described as:

$$Q = \begin{cases} \dfrac{4 \tan \Theta}{\tan \delta(1 - \frac{1}{2} \tan^2 \Theta)} & \text{for } n\pi \leq \Theta \leq n\pi + \frac{\pi}{2}; n = 0, 1, 2 \dots, \\[3mm] \dfrac{-4 \tan \Theta}{\tan \delta(1 - \frac{1}{2} \tan^2 \Theta)} & \text{for } n\pi + \frac{\pi}{2} \leq \Theta \leq (n+1)\pi; n = 0, 1, 2 \dots \end{cases} \tag{4.15}$$

Solving 4.15 for Θ gives:

$$\tan \Theta = \frac{1}{Q \tan \delta} \left(-4 \pm \sqrt{16 + 2Q^2 \tan^2 \delta}\right) \tag{4.16}$$

where in the region $0 \leq \Theta \leq \frac{\pi}{2}$ the $+$ sign is valid when $Q \geq 0$ and the $-$ sign is valid when $Q < 0$. The angle Θ can be eliminated from Equation 4.13 by substituting in Equation 4.9

with $i = 5$ as $\theta_5 = \Theta$:

$$\frac{p_5}{p_p}\left(1 - \frac{3}{2}\sin^2\delta\right) - \sum_{i=1}^{4}\frac{p_i}{4p_p} = \sin^2\delta\left(F - \frac{3}{2}\right) \tag{4.17}$$

where F and the pitot pressure p_p remain unknown. In order to eliminate p_p Equations 4.12 and 4.16 are substituted into Equation 4.9. This results in an expression for the pitot pressure, such that:

$$p_p = p_5 + \frac{p_5 - \sum_{i=1}^{4}\frac{p_i}{4}}{\sin^2\delta}\left(-1 \pm \sqrt{1 + \frac{1}{8}Q^2\tan^2\delta}\right) \tag{4.18}$$

Substituting Equation 4.18 into Equation 4.17 yields a relation for F, previously assumed to be a function of only the Mach number, where

$$F = \frac{p_5\left(1 - \frac{3}{2}\sin^2\delta\right) - \sum_{i=1}^{4}\frac{p_i}{4}}{p_5\sin^2\delta + \left(p_5 - \sum_{i=1}^{4}\frac{p_i}{4}\right)\left(-1 \pm \sqrt{1 + \frac{1}{8}Q^2\tan^2\delta}\right)} + \frac{3}{2} \tag{4.19}$$

4.2.2 Selection of Calibration Coefficients

In order to define the flow conditions about the probe three independent calibration coefficients are necessary (two for the flow angle and one for the Mach number). While these coefficients can be developed theoretically, the discrepancy between the theoretical and the real pressure distribution about the probe requires that the probe also be calibrated at series of flow angles and Mach numbers. When measuring in an unknown flow field the flow quantities are determined as a function of these calibration coefficients via an interpolation procedure. The selection of calibration coefficients which are nearly linearly dependent on only one of the flow quantities increases the accuracy of this procedure.

The three calibration coefficients which are selected are C_Φ, C_Θ and C_M, which are almost linearly dependent on the roll angle Φ, pitch angle Θ and Mach number, respectively. The flow angle coefficients are taken from Equations 4.11 and 4.16 directly such that:

$$C_\Phi = \tan^{-1}\left(\frac{p_2 - p_1}{p_4 - p_3}\right) \tag{4.20}$$

and

$$C_\Theta = \tan^{-1}\left[\frac{1}{Q\tan\delta}(-4 \pm \sqrt{16 + 2Q^2\tan^2\delta})\right] \tag{4.21}$$

where Q is defined in Equation 4.15, the $+$ sign is valid for $Q \geq 0$ and the $-$ sign for $Q < 0$. The flow coefficients C_α and C_β can be derived via Equations 4.1 and 4.2, respectively, such that:

$$C_\alpha = \tan^{-1}(\tan C_\Theta \sin C_\Phi) \tag{4.22}$$

$$C_\beta = \tan^{-1}\left(\frac{\sin C_\Theta \cos C_\Phi}{\sqrt{1 - \sin^2 C_\Theta \cos^2 C_\Phi}}\right) \tag{4.23}$$

While the exact relationship between F and the Mach number is unknown, F is assumed to be a function of only the Mach number. For this reason the definition of C_M is taken from Equation 4.19 such that:

$$C_M = \frac{p_5\left(1 - \frac{3}{2}\sin^2\delta\right) - \sum_{i=1}^{4}\frac{p_i}{4}}{\sum_{i=1}^{4}\frac{p_i}{4} - p_5\cos^2\delta \pm \left(p_5 - \sum_{i=1}^{4}\frac{p_i}{4}\right)\sqrt{1 + \frac{1}{8}Q^2\tan^2\delta}} + \frac{3}{2} \tag{4.24}$$

In order to determine the total pressure the pitot pressure is first calculated from Equation 4.18. In the supersonic flow regime the total pressure is calculated from the pitot pressure according to the relationship for total pressure loss through a normal shock wave:

$$\frac{p_p}{p_t} = \left(\frac{\gamma+1}{2\gamma M^2 - (\gamma-1)}\right)^{\frac{1}{\gamma-1}} \cdot \left(\frac{(\gamma+1)M^2}{2 + (\gamma-1)M^2}\right)^{\frac{\gamma}{\gamma-1}} \tag{4.25}$$

This theoretically derived total pressure is corrected for actual flow conditions via a calibration in which:

$$p_t = \frac{p_t}{p_p}(M) \cdot \frac{p_{p_{th}}}{C_{pt}} \tag{4.26}$$

where $\frac{p_t}{p_p}(M)$ is the reciprocal of Equation 4.25 and $p_{p_{th}}$ is calculated from Equation 4.18. The correction coefficient for the total pressure can, thus, be written as:

$$\begin{aligned}
C_{pt} &= \frac{p_{p_{th}}}{p_{t_{meas}}} \cdot \frac{p_t}{p_p}(M) \tag{4.27}\\[2mm]
&= \frac{p_5 + \left(p_5 - \sum_{i=1}^{4}\frac{p_i}{4}\right)\left(-1 \pm \sqrt{1 + \frac{1}{8}Q^2\tan^2\delta}\right)\cdot\sin^{-2}\delta}{p_{t_{meas}}} \cdot \frac{p_t}{p_p}(M)
\end{aligned}$$

In the calibration of the five-hole probe the Mach number and two flow angles Φ and Θ are varied independently. It is, therefore, useful to define a coordinate system in C_M, C_Φ,

C_Θ space such that the flow properties can be described as:

$$M = f_1(C_M, C_\Phi, C_\Theta)$$
$$\Phi = f_2(C_M, C_\Phi, C_\Theta) \qquad (4.28)$$
$$\Theta = f_3(C_M, C_\Phi, C_\Theta)$$

The correction coefficient for the total pressure can also be expressed as a function of C_M, C_Φ and C_Θ such that:

$$C_{pt} = f_4(C_M, C_\Phi, C_\Theta) \qquad (4.29)$$

4.2.3 Calibration Procedure

The calibration matrix of the current investigation consists of 37 different roll angles Φ at 10 different pitch angles Θ for each of seven different free stream Mach numbers. The roll angle Φ is varied from 0 to 360° with an increment of 10° (see Table 4.1). The pitch angle Θ is

M_∞ [1]	Θ [°]	Φ [°]
0.55 0.77 0.85 1.16 1.3 1.5 1.76	$0 \le \Theta \le 45, \Delta = 7.5°$ $45 \le \Theta \le 60, \Delta = 5°$	$0 \le \Phi \le 360, \Delta = 10°$

Table 4.1: Five-hole probe calibration matrix.

varied from 0 to 45° with an increment of 7.5° and from 45 to 60° with an increment of 5°. The smaller increment at the higher pitch angles is used to improve the accuracy of the calibration at these flow angles where flow separation is present. The free stream Mach numbers calibrated include 0.55, 0.7, 0.85, 1.16, 1.3, 1.5 and 1.76. From the calibration data 2590 points in the C_M, C_Φ, C_Θ space are calculated which correspond with the relevant combinations of Mach number, roll angle and pitch angle where they were obtained. The value of C_{pt} at each point defines the total pressure correction at that point.

Figure 4.4 illustrates the variation of C_M with Θ for various free stream Mach numbers when $\Phi = 50°$ and $\Phi = 90°$. The value of C_M is noted not to be completely independent of
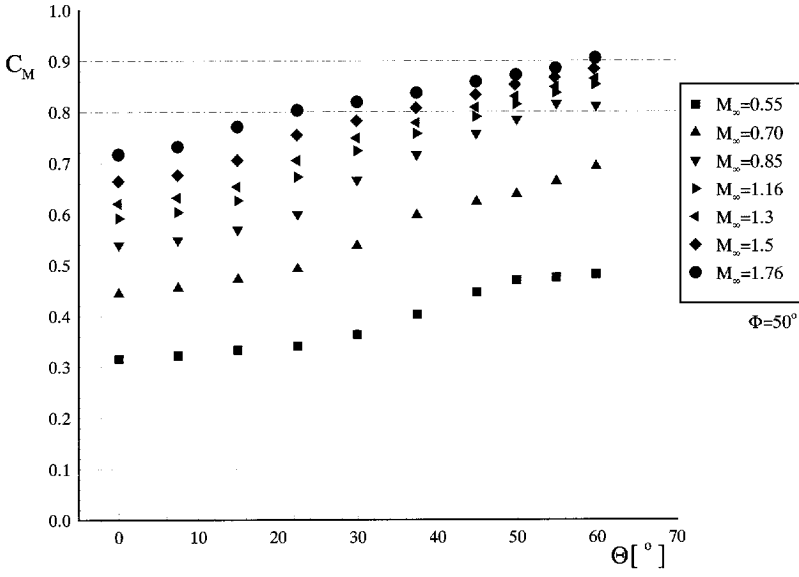
(a) $\Phi = 50°$
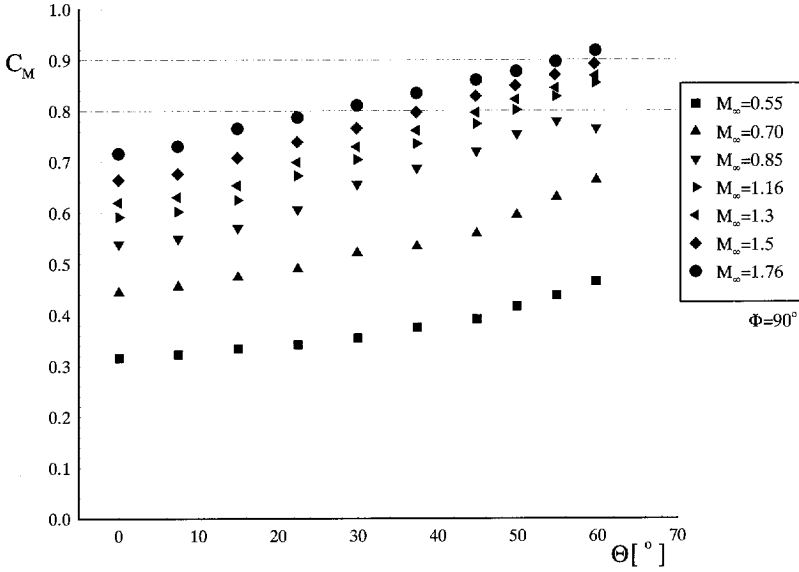
(b) $\Phi = 90°$

Figure 4.4: Variation of C_M with Θ for various Mach numbers at $\Phi = 50°$ and $\Phi = 90°$.

Θ and Φ.

Figure 4.5 illustrates the variation of C_Θ with Mach number at various values of Θ when $\Phi = 50°$ and $\Phi = 90°$. When $0° \leq \Theta \leq 37.5°$, the value of C_Θ, calculated from the probe measurements via Equation 4.21, is noted to be nearly independent of Mach number and Φ. The actual values of C_Θ also correspond well with the actual values of Θ in this range (i.e. $|C_\Theta - \Theta| \leq 2°$). The discrepancy between the theoretically calculated value of C_Θ and the actual value increases, however, for large values of Θ. This is to be expected as flow separation, a viscous effect neglected in the calibration theory, significantly influences the pressure distribution at large values of Θ.

The variation of C_Φ with Θ for several Mach numbers at $\Phi = 50°$, $70°$ and $90°$ is illustrated in Figure 4.6. The corresponding values of C_Φ vary between Φ and $(\Phi - 10°)$ over the full range of Mach number and Θ investigated.

The total pressure correction versus Θ for the full range of Mach numbers when $\Phi = 50°$ and $\Phi = 90°$ is illustrated in Figure 4.7. The pitot pressure correction factor, calculated from the measured pressures via Equation 4.27, is no more than 8% for the full range of Mach numbers and pitch angles investigated. The advantage of using the derived calibration coefficient C_{pt} as opposed to, for example, the total pressure estimated by pressure port number five (i.e. p_5) is illustrated in Figure 4.8. While this pressure port provides a good estimation of the total pressure at small Θ, the correction factor increases with increasing pitch angle. The correction at large pitch angles is as large as 60% of the actual pitot pressure.
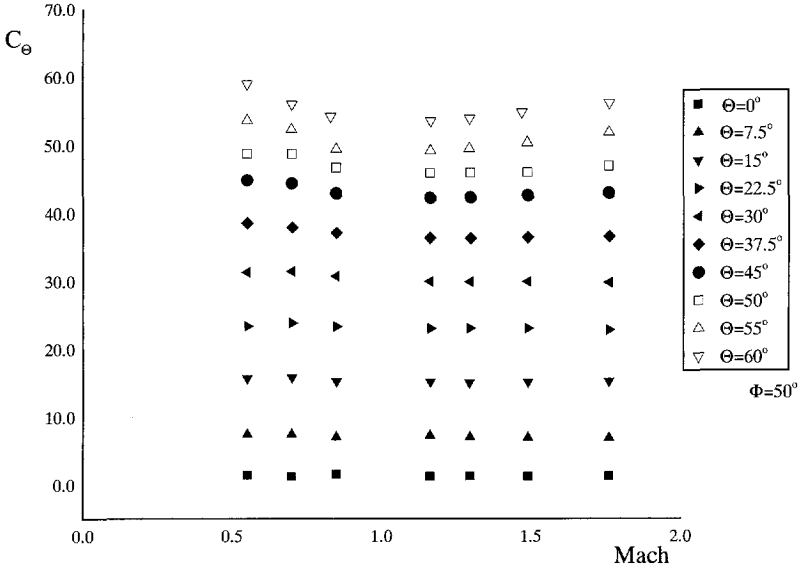
(a) $\Phi = 50°$
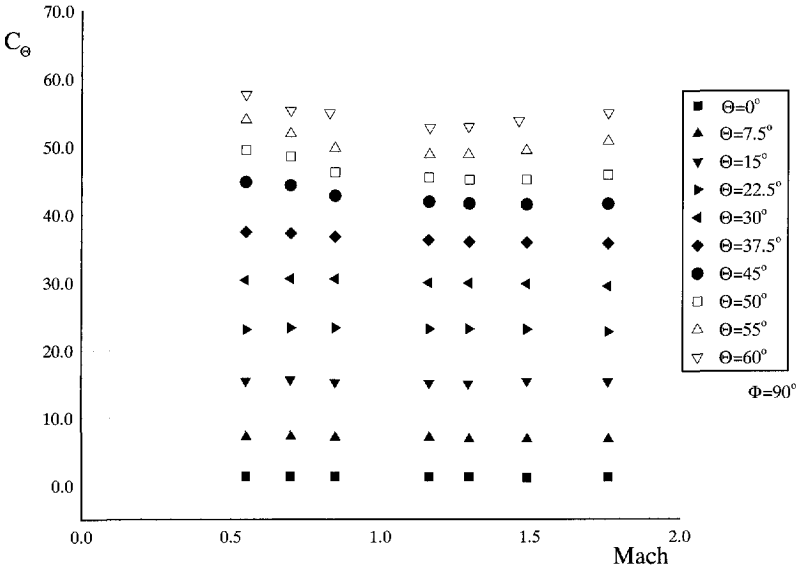
(b) $\Phi = 90°$

Figure 4.5: Variation of C_Θ with Mach number for various Θ at $\Phi = 50°$ and $\Phi = 90°$.
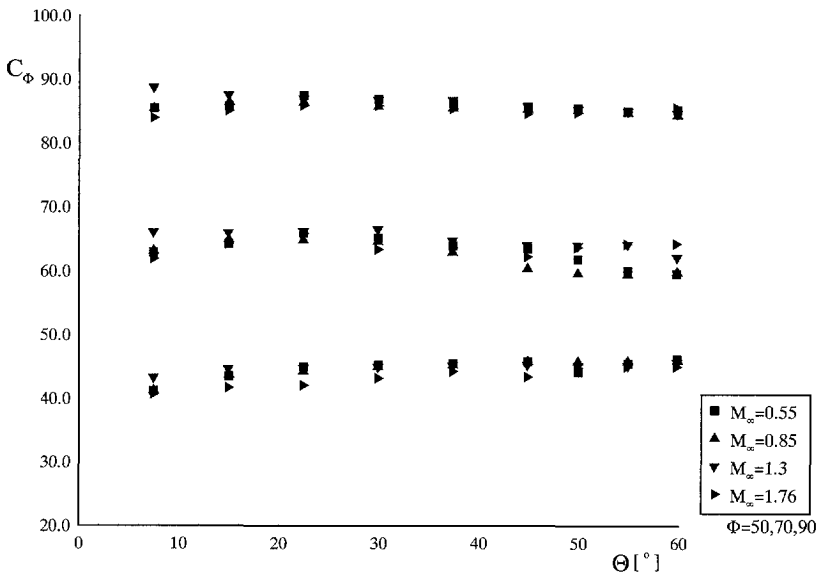
Figure 4.6: Variation of C_Φ with Θ for various Mach numbers.
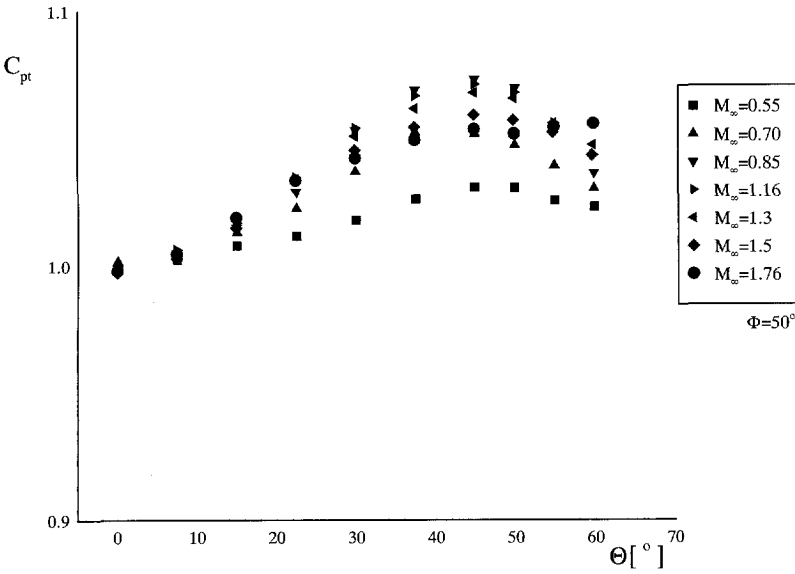
(a) $\Phi = 50°$
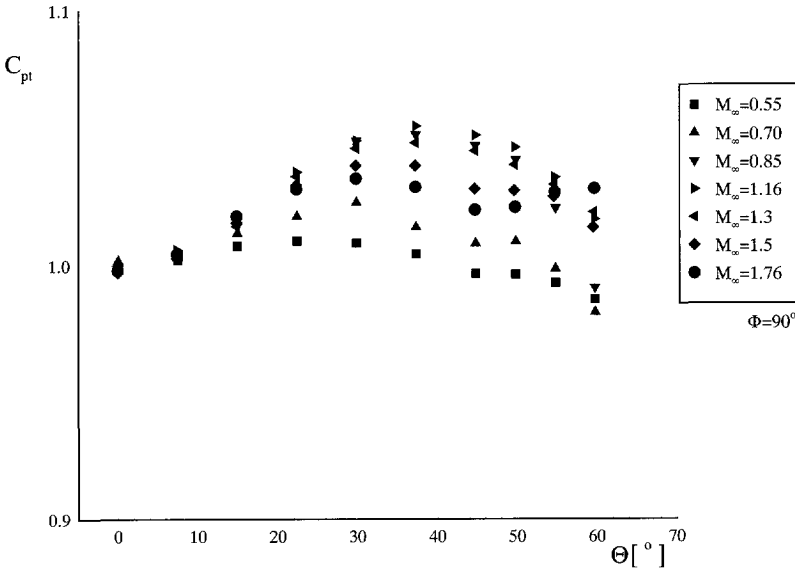
(b) $\Phi = 90°$

Figure 4.7: Variation of C_{pt} with Θ for various Mach numbers at $\Phi = 50°$ and $\Phi = 90°$.
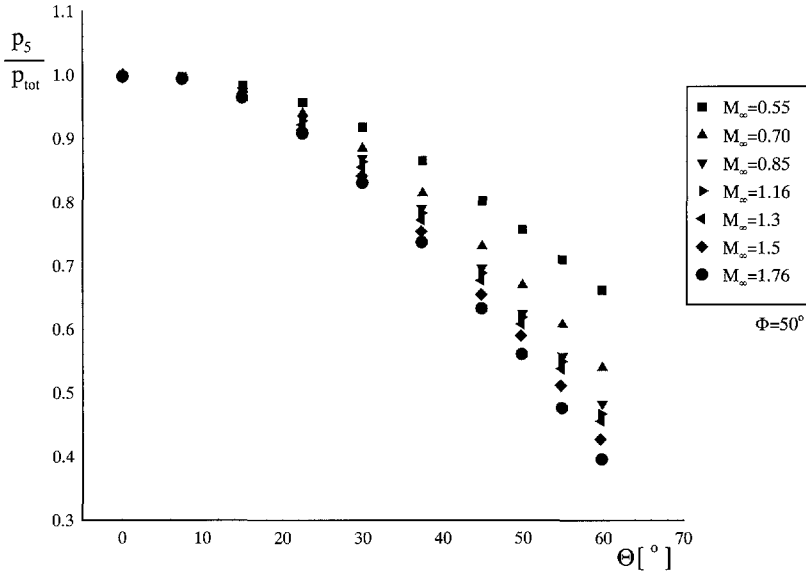
(a) $\Phi = 50°$
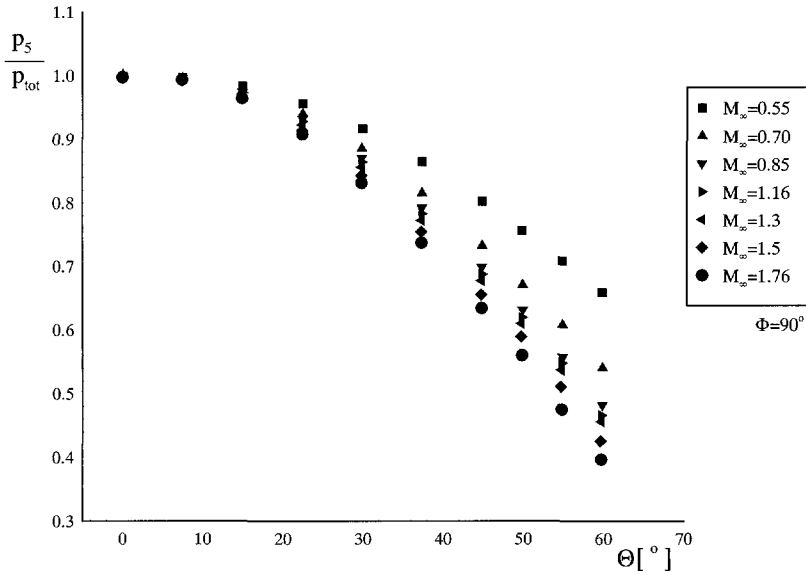
(b) $\Phi = 90°$

Figure 4.8: Variation of (p_5/p_{tot}) with Θ for various Mach numbers at $\Phi = 50°$ and $\Phi = 90°$.

4.2.4 Data Processing

In order to determine the flow quantities in an unknown flow field an interpolation of the calibration data is required. Functions are commonly developed which are expressed as polynomials of the form:

$$A = \sum_{i=0}^{I} \sum_{j=0}^{J} \sum_{k=0}^{K} \alpha_{ijk} C_M^i C_\Theta^j C_\Phi^k \tag{4.30}$$

where A is any of the quantities Mach number, Θ, Φ or C_{pt}. A common approach is to derive polynomial expressions valid for the entire calibration range, or for various specific regions defined by the maximum pressure in one of the orifices [Everett et al. 1985]. This technique requires the use of higher order polynomials. At high pitch angles the inaccuracy of this approach increases significantly, however, due to the nonlinear effects of flow separation and shock waves. In the current investigation polynomial expressions are developed which are valid only in a very limited region in the vicinity of some calibration points [Voerman 1976]. This local three-dimensional look-up algorithm significantly increases the accuracy of the probe measurements when large flow angles are present.

4.3 Probe Measurements in a Uniform Free Stream:

In addition to the calibration matrix mentioned above, a series of tests is performed with the probe in a uniform flow field at specific roll angles, pitch angles and free stream Mach numbers to evaluate the accuracy of the probe calibration. The Mach numbers selected are between the Mach numbers of the calibration matrix. The conditions at which tests are performed are listed in Table 4.2. High flow angles are emphasized in these tests as the nonlinear behavior of the calibration coefficients at high flow angle decreases the accuracy of the interpolation procedure when high flow angles are present.

The Mach number calculated via the five hole probe measurements and the actual free stream Mach number in the wind tunnel for each of the control tests are illustrated in Figure 4.9. The discrepancy between the calculated and actual value of Mach is, indeed, noted to be largest for the largest flow angles Θ at each Mach number. The root mean square of the error in Mach number ($\Delta M = M_\infty - M_{cal}$) over the relevant range of Θ and Φ for each specific Mach number is found to be less than 0.03 (see Table 4.3).

The calculated value of Θ for each of the control tests is shown in Figure 4.10. Again, the discrepancy between the actual and calculated value of Θ is noted to be greatest at the highest pitch angles. This discrepancy is limited, however, to no more than 0.9°. The root mean square of this discrepancy for all the control tests made at each specific Mach number

M_∞ [1]	Θ [°]	Φ [°]
0.8	35.3 47.96 58.12	0.0, 4.7, 9.5, 14.6, 19.7, 24.6
1.39	42.24 44.75 47.25 49.75 52.25 54.7 57.18	(46, 60, 75, 90)
1.67	45 50 55 60	(45, 60, 75, 90)

Table 4.2: Five-hole probe calibration control measurements.
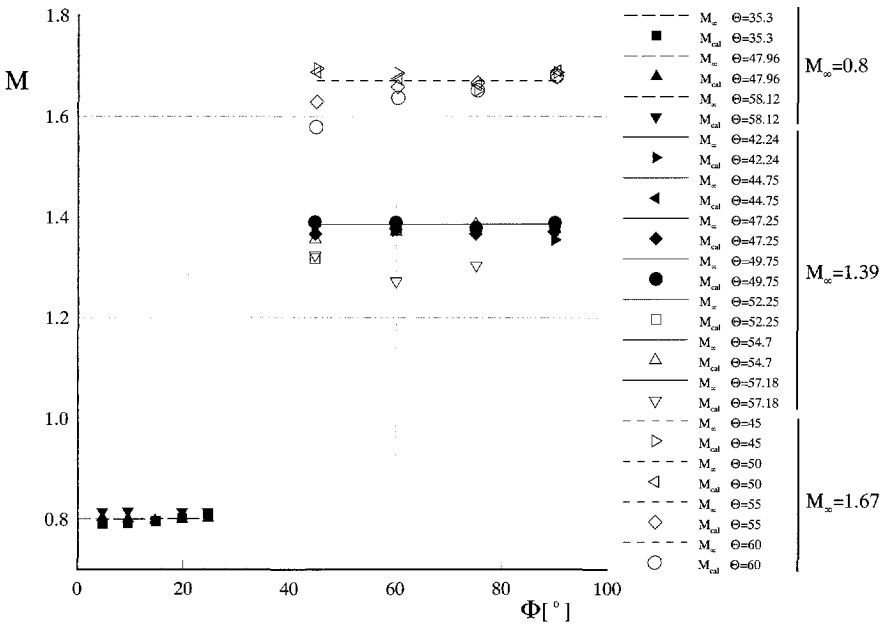
Figure 4.9: Mach number accuracy at various Θ and Φ.

M_∞	ΔM_{RMS}	$\Delta\Theta_{RMS}$	$\Delta\Phi_{RMS}$	$\Delta\left(\dfrac{p_t}{p_{tot}}\right)_{RMS}$
0.8	0.013	0.16°	0.48°	0.004
1.39	0.021	0.24°	0.46°	0.004
1.67	0.021	0.21°	0.36°	0.009

Table 4.3: Root mean square of error in flow quatities for calibration control tests.
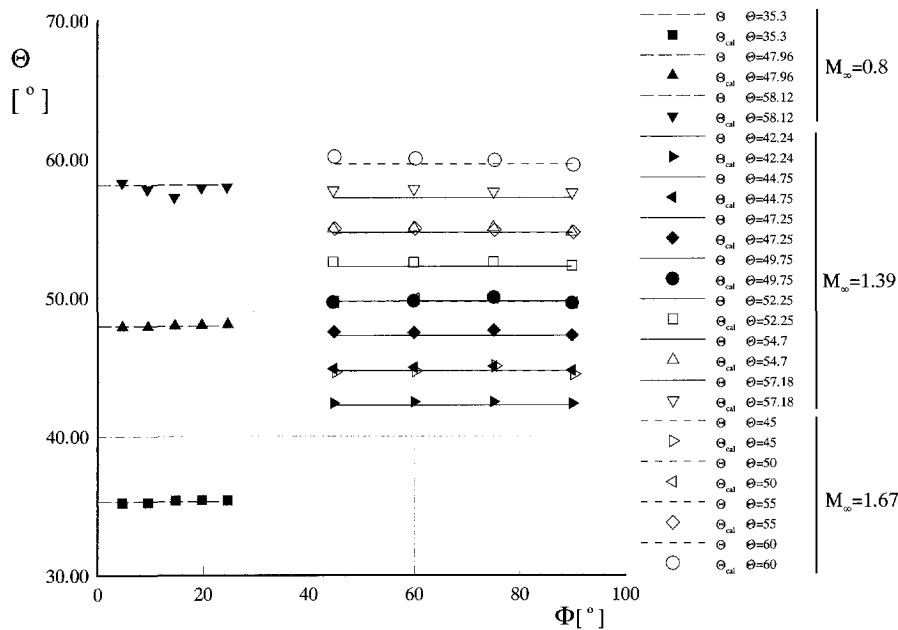
Figure 4.10: Calculated and actual flow pitch angles Θ_{cal} and Θ.

is, however, less than $0.3°$ (see Table 4.3).

The calculated value of roll angle versus actual roll angle for the various control tests is illustrated in Figure 4.11. The maximum discrepancy in Φ is $1.3°$ and the root mean square of the error is less than $0.5°$ for all Mach numbers investigated.
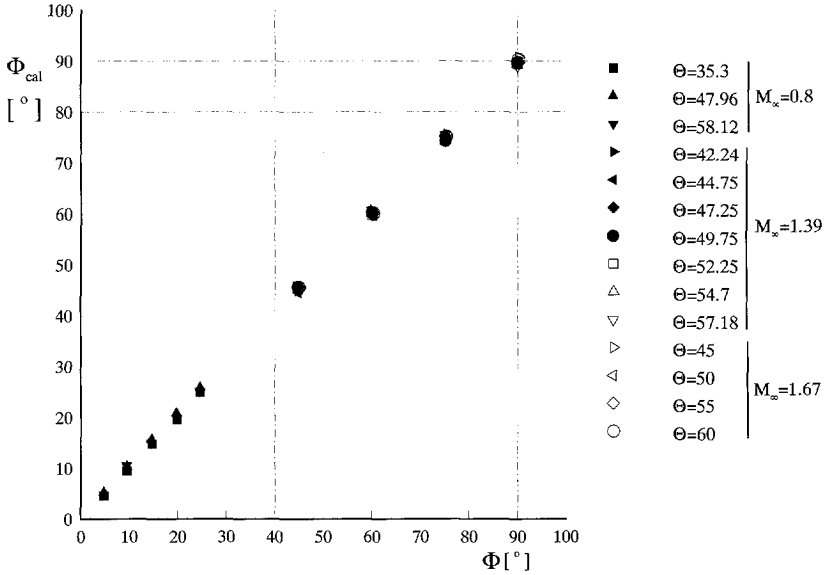
Figure 4.11: Calculated and actual flow roll angles Φ_{cal} and Φ.

Figure 4.12 illustrates the ratio of the calculated total pressure to the actual total pressure for the control measurements. The maximum discrepancy of the calculated total pressure value is less than 4% of the actual value while the root mean square of the discrepancy at each of the Mach numbers tested is less than 1% of the actual value. Again, the largest discrepancy is observed at the largest pitch angles.

These tests illustrate, therefore, the excellent accuracy of the five-hole probe measurements in a uniform free stream with a pitch angle up to $60°$. This accuracy can be attributed to the selection of appropriate calibration coefficients and the local three-dimensional look-up algorithm applied. Unfortunately, the accuracy of probe measurements above the delta wing is not the same as that for measurements in a uniform free stream. Probe/flow field interference effects and the accuracy of the five-hole probe measurements in the vortical flow field are considered in the following discussion.
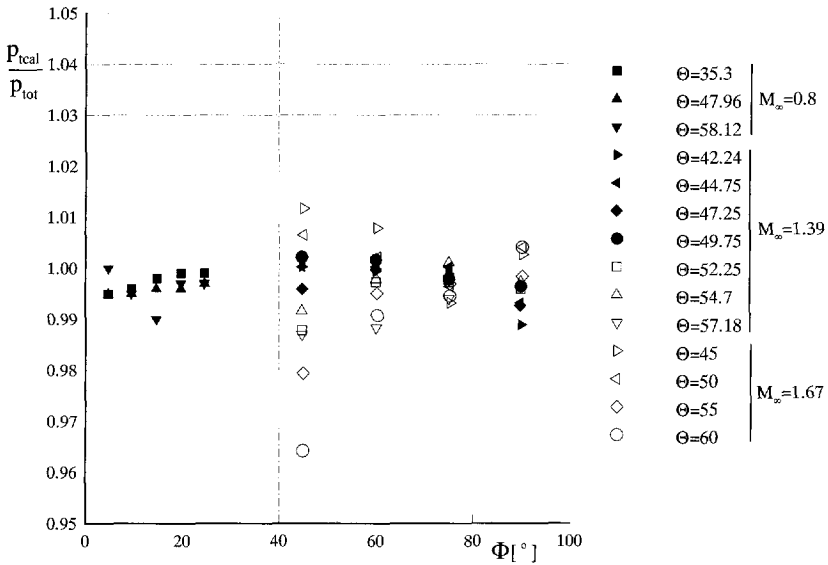
Figure 4.12: Ratio of calculated total pressure to actual total pressure.

4.4 Probe Interference Effects

The presence of the probe in the vortical flow field will disturb the flow to a certain extent and the presence of the wing in the vicinity of the probe will influence the flow about the probe itself. The errors associated with these phenomena are referred to as interference effects. Early investigations by Lambourne and Bryer [1961] observed the influence of bodies or obstructions introduced along the core of the vortex on the vortex stability (i.e. with or without vortex breakdown). They also found that the influence of the obstruction depends not only on the size of the obstruction, but also on its proximity to the natural burst location. Flow fields which are more prone to vortex breakdown are also, therefore, more sensitive to disturbances placed in the flow field.

Figure 4.13 illustrates the relative position and size of the probe in the measurement field. While this five-hole probe is specifically designed to be as small as practically feasible, the diameter of the probe is noted to be relatively large in comparison with the model being investigated. The diameter of the probe is equivalent to 5.7% of the local semi-span when $(x_m/c_r) = 0.5$ and 2.9% of the wing semi-span at the trailing edge.

The flow field is monitored via a side-view transmission Schlieren system during testing to observe the influence of the probe on the flow field. Due to the presence of the undisturbed

(a) Top-view

(b) Side-view
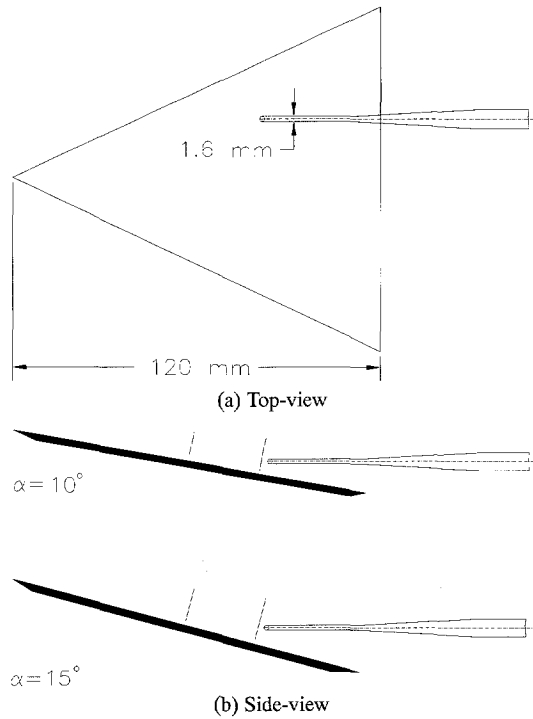
Figure 4.13: Illustration of relative size of the five-hole probe, delta wing and measurement planes above the wing.

vortex on the port side of the wing, however, the exact state of the starboard vortex where the measurements are being made is obscured. The probe is noted to shake significantly when in the vicinity of the wing upper surface and near the center of the primary vortex. This effect is most extreme at the combination of highest angle of attack ($15°$) and largest free stream Mach number (0.8). The increased interference at higher angle of attack and Mach number is consistent with the observation by Lambourne and Bryer that the proximity of incipient vortex breakdown location influences the amount of flow interference which results from obstructions in the flow field. The tendency for a vortex to breakdown is known to increase with increasing Mach number and angle of attack (see Section 1.2.1).

4.5 Analysis of Five-hole Probe Measurements

The characteristic lee side vortical flow field of a sharp leading edge delta wing at angle of attack, introduced in Chapter 1, is illustrated in Figure 4.14. Significant total pressure losses
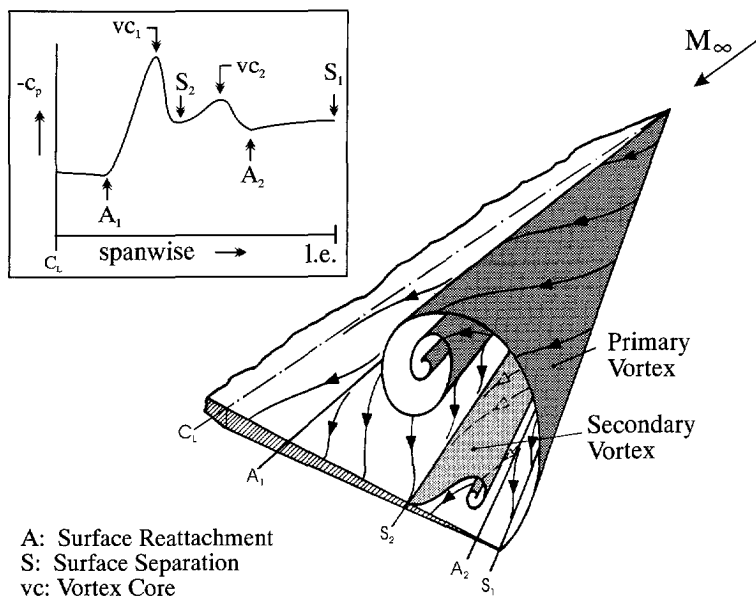
Figure 4.14: Characteristic lee side vortical flow field of a sharp leading edge delta wing at angle of attack and its corresponding surface pressure distribution.

are anticipated in the vicinity of the core of the primary and secondary vortices [Earnshaw 1961; Payne 1987]. As illustrated in the inset of Figure 4.14, local static pressure minima are anticipated on the surface of the wing beneath the primary and secondary vortices [Erickson 1991]. In the following discussion the compatibility of the data obtained via five-hole probe measurements in the current investigation with these anticipated flow characteristics is evaluated. Data obtained in the current investigation via non intrusive measurement techniques (i.e. surface pressure measurements and flow visualizations) are also considered in this analysis.

In order to illustrate the cross-flow velocity components above the wing a local right-handed Cartesian reference system x_c, y_c, z_c, with the origin at P_c is introduced (see Figure 4.15). In this coordinate system the x_c axis coincides with the conical ray OP_c and the y_c axis, perpendicular to the axial ray x_c, is parallel with the upper surface of the wing. The point P_c is the location of minimum total pressure in the local five-hole probe measurement
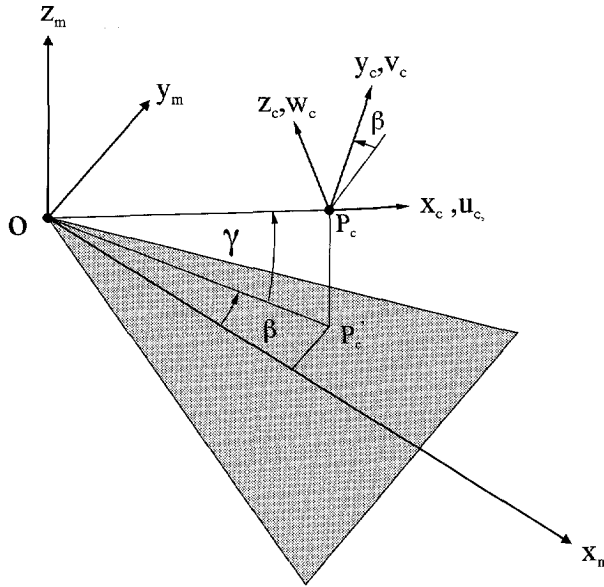
Figure 4.15: Illustration of relevant axial and cross-flow velocity components above (u_c, v_c, w_c) the wing.

plane, which is assumed to be the approximate location of the primary vortex core. Implicit in this assumption is the assumption that the core of the primary vortex is aligned with the conical ray OP_c. The cross-flow velocity components v_c, w_c above the wing are, thus, contained in the plane perpendicular to the conical ray OP_c. The selection of this coordinate system to illustrate the cross-flow velocity components is based on the observed conical trajectory of the primary vortex above the wing which will be discussed in Section 6.1.1.

4.5.1   Total Pressure and Cross-flow Velocity

The total pressure distribution and cross-flow velocity vectors at $(x_m/c_r) = 0.7$ for several combinations of Mach number and angle of attack are shown in Figures 4.16 and 4.17, respectively. The five-hole probe measurement grid is superimposed as dots onto the contour plots in Figure 4.16, for reference purposes. The spanwise location of the secondary separation line at $(x_m/c_r) = 0.7$, taken from the surface oil flow visualizations, is also indicated in these figures.

In Figure 4.17 the velocity vectors are noted to be oriented counter clockwise about the minimum total pressure and to be oriented clockwise outboard of the secondary separation position for each of the combinations of Mach number and angle of attack illustrated. The location of absolute minimum total pressure in Figure 4.16 can, thus, be suspected to coincide
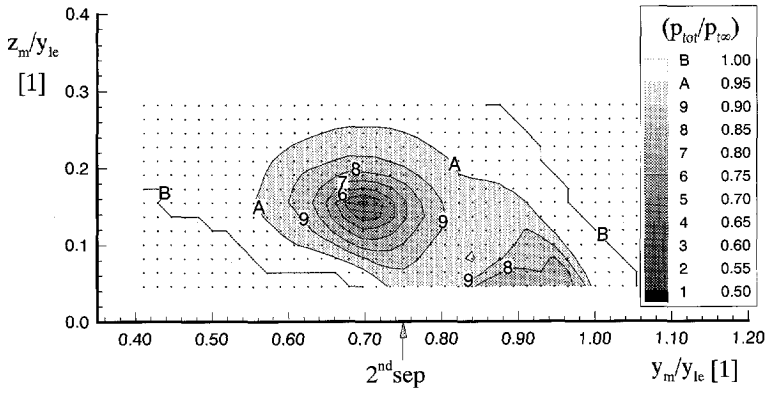
(a) $M_\infty = 0.6$, $\alpha = 10°$
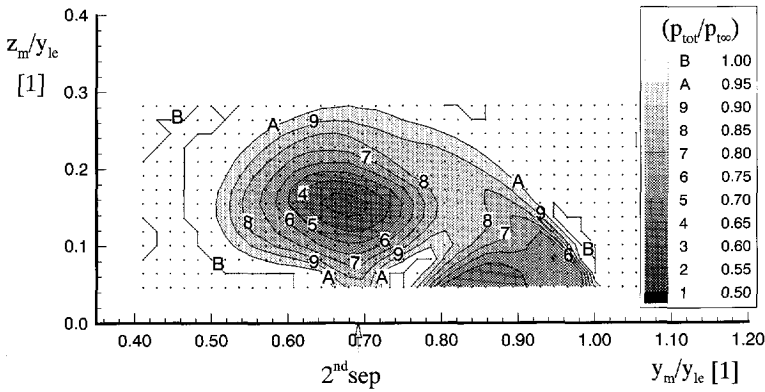
(b) $M_\infty = 0.8$, $\alpha = 10°$
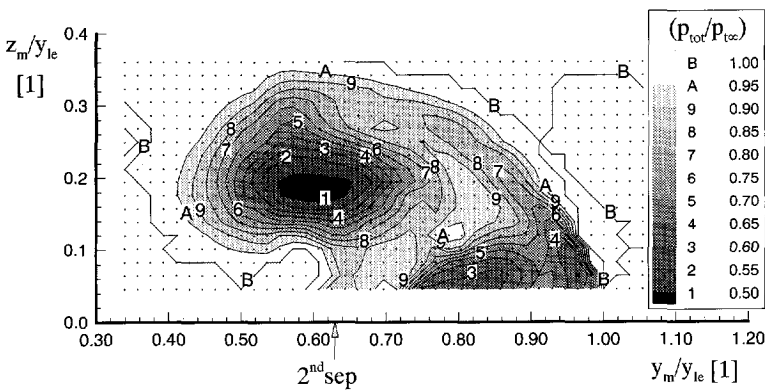
(c) $M_\infty = 0.8$, $\alpha = 15°$

Figure 4.16: Total pressure distribution, $(x_m/c_r) = 0.7$.
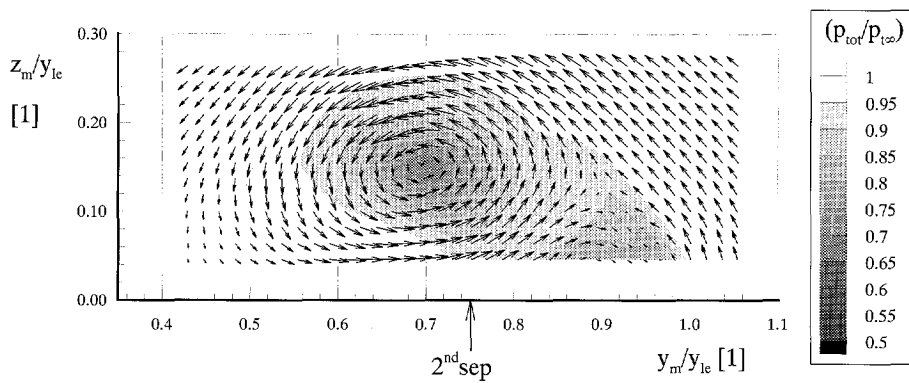
(a) $M_\infty = 0.6$, $\alpha = 10°$
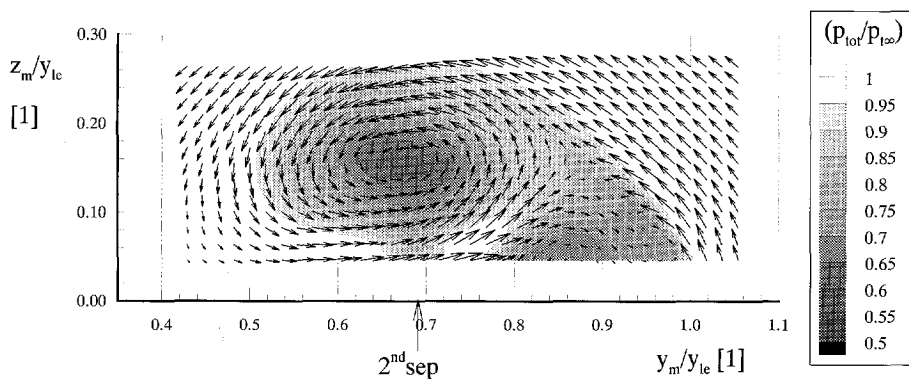
(b) $M_\infty = 0.8$, $\alpha = 10°$
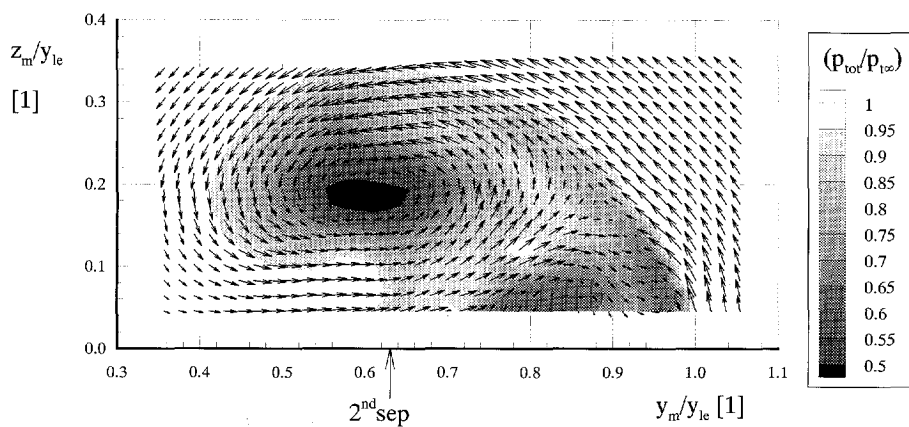
(c) $M_\infty = 0.8$, $\alpha = 15°$

Figure 4.17: Total pressure distribution with superimposed cross-flow velocity direction (v_c, w_c), $(x_m/c_r) = 0.7$.

with the primary vortex core for each $M_\infty - \alpha$ combination. The area of decreased total pressure outboard of the secondary separation line in Figure 4.16 can be associated with the secondary vortex. The increasing total pressure loss with increasing Mach number and angle of attack is consistent with expectations. Increasing Mach number and angle of attack will increase the amount of shear (velocity gradient) in the shear layer emanating from the leading edge and lead to increased total pressure losses.

The spanwise total pressure gradient observed below the primary vortex in the vicinity of the secondary separation line when $M_\infty = 0.8$ and $\alpha = 15°$ (Figure 4.16c) may be associated with an embedded cross-flow shock. The static pressure measurements on the surface of the model at $(x_m/c_r) = 0.7$ (see Figure 4.18) do indicate that the flow is supersonic in this region (i.e. $C_p < C_p^*$). For further discussion on the embedded cross-flow shock wave see Section 6.1.2.
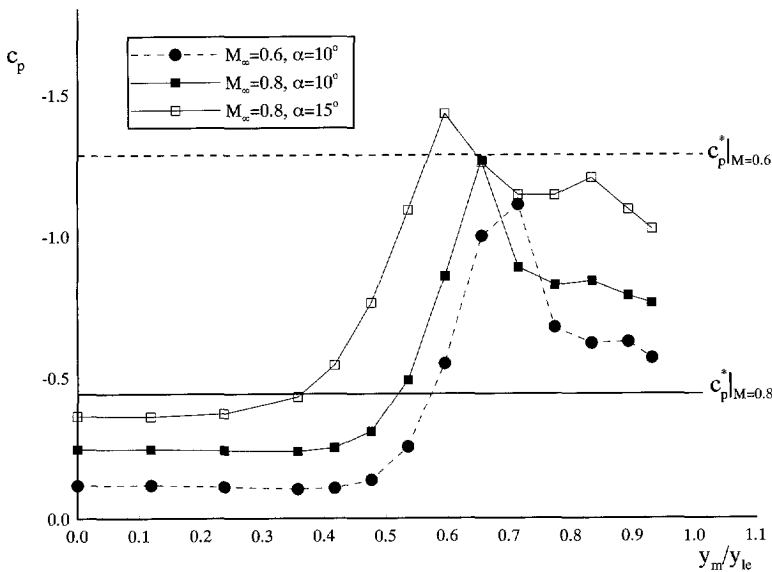
Figure 4.18: Spanwise surface pressure distribution at $(x_m/c_r) = 0.7$.

While it is not possible to examine the quantitative accuracy of the cross-flow velocity vector, the orientation of this vector can be examined for consistency with the anticipated cross-flow velocity pattern (see, for example, Figure 4.14) and the surface oil flow visualizations. The orientation of the cross-flow vectors about the regions of total pressure loss representing the primary and secondary vortices is consistent with the anticipated cross-flow

velocity distribution. The change in orientation of the vectors beneath the primary vortex from approximately parallel with the wing surface to slightly upward at the same spanwise location as the secondary separation line in oil flow visualizations also supports the viability of the cross-flow velocity vector orientation.

4.5.2 Defining Location of Primary Vortex Core

The location of the primary vortex core is defined in the current study as the location of minimum total pressure in each of the five-hole probe measurement planes. In order to investigate the viability of this definition the height of the primary vortex core above the surface of the wing can also be estimated from side-view transmission Schlieren images configured such that the Schlieren knife edge is aligned parallel with the free stream flow. As further discussed in Section 5.1, Schlieren images illustrate a component of the density gradient existing perpendicular to a parallel light bundle integrated over the path of the bundle. The component which is illustrated is that which is perpendicular to the orientation of the Schlieren knife edge. By aligning the Schlieren knife edge parallel with the free stream flow, the density gradient perpendicular to the free stream, integrated over the width of the test section, is illustrated.

In the case of a sustained vortex (i.e. jet-like axial velocity profile about the core), the primary vortex core can be expected to coincide with the location of minimum density. Thus, the height of the primary vortex core above the wing can be estimated from a transmission Schlieren image (see, for example, Figure 4.19) as the conical ray which separates the region of decreasing integrated-density moving away from the upper surface of the wing (black coloration) and increasing integrated-density gradient (white). This line of separation is illustrated in Figure 4.19 for the combination $M_\infty = 0.8$ and $\alpha = 10°$.

Table 4.4 lists the height of the primary vortex core above the wing (z_m/y_{le}) as deter-

M_∞	$\left(\frac{x_m}{c_r}\right)$	$\alpha = 10°$		$\alpha = 15°$	
		$\left(\frac{z_m}{y_{le}}\right)_{trans}$	$\left(\frac{z_m}{y_{le}}\right)_{5hp}$	$\left(\frac{z_m}{y_{le}}\right)_{trans}$	$\left(\frac{z_m}{y_{le}}\right)_{5hp}$
0.6	0.5	0.16	0.16	0.22	0.21
	0.7		0.16		0.19
0.8	0.5	0.14	0.16	0.18	0.19
	0.7		0.16		0.18

Table 4.4: Comparison of primary vortex core position above wing determined via five-hole probe measurements (5hp) and transmission Schlieren images (trans).

mined via the minimum total pressure location in the five-hole probe measurement planes
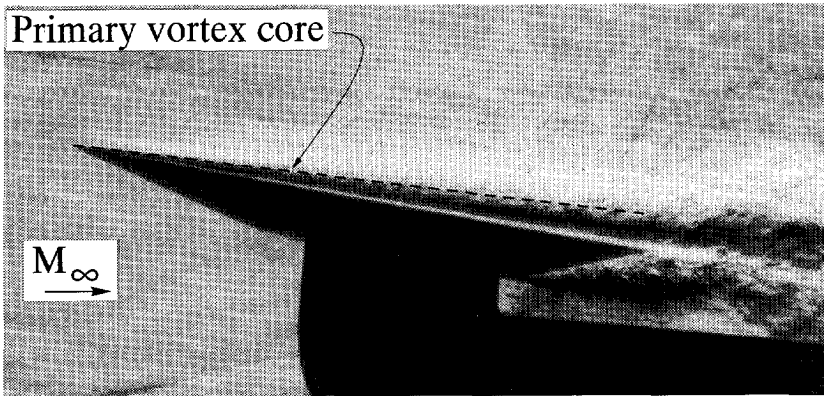
Figure 4.19: Side-view transmission Schlieren image illustrating approximate location of primary vortex core, $M_\infty = 0.8$ and $\alpha = 10°$.

M_∞	$\left(\frac{x_m}{c_r}\right)$	$\alpha = 10°$		$\alpha = 15°$	
		$(p_{tot})_{min}$	$2^{nd}sep.$	$(p_{tot})_{min}$	$2^{nd}sep.$
0.6	0.5	0.72	0.76	0.66	0.67
	0.7	0.70	0.75	0.66	0.71
0.8	0.5	0.66	0.68	0.63	0.63
	0.7	0.68	0.69	0.61	0.63

Table 4.5: Spanwise location of minimum total pressure from five-hole probe measurements and secondary separation line from oil flow visualizations.

and via the side-view Schlieren images. The height of the primary vortex core above the surface of the wing determined via both techniques is noted to be very similar in all cases, differing by no more than 3% of the local semi-span. This similarity illustrates the consistency between the five-hole probe measurements in the vicinity of the primary vortex core with the side-view transmission images. Unfortunately, it is not possible to estimate the primary vortex core location behind the wing optically due to the presence of the trailing edge vortex system at approximately the same height as the primary vortex core.

The definition of the location of minimum total pressure as the primary vortex core location can also be examined for consistency with the oil flow visualizations. Because the secondary vortex separation is a consequence of the adverse pressure gradient outboard of the primary vortex core, the secondary separation line can be expected to be located outboard of the primary vortex core. In Table 4.5 the location of the secondary separation line is, indeed, noted to be coincident with or outboard of $(p_{tot})_{min}$ in all cases.

4.5.3 Static Pressure Measurements in Vicinity of Wing Surface

While it is possible to measure very close to the wing upper surface with the five-hole probe, these measurements are particularly vulnerable to interference effects. In order to measure beneath the primary vortex core itself the probe passes through the core of the primary vortex downstream of the measurement plane (see Figure 4.13b). The magnitude of these interference effects is illustrated by comparing the static pressures measured by the five-hole probe just above the wing surface with the surface pressure measurements. In Figures 4.20, 4.21 and 4.22 the distribution of the static pressure coefficient C_p at $(x_m/c_r) = 0.7$ is illustrated together with the surface pressure measurements at $(x_m/c_r) = 0.7$ for several combinations of free stream Mach number and angle of attack. The value of C_p in the five-hole probe measurement planes is based on the static pressure calculated from the locally measured Mach number and total pressure via the isentropic flow relation:

$$p = p_{tot}\left(1 + \frac{\gamma - 1}{2}M^2\right)^{\frac{-\gamma}{(\gamma-1)}} \tag{4.31}$$

The surface pressure measurements reveal a significantly different C_p distribution than the five-hole probe measurements made in the vicinity of the wing upper surface. In Figure 4.20b the surface pressure measurements are noted to exhibit a lower value of minimum C_p at a more inboard location than in the five-hole probe measurements just above the wing surface. The discrepancy between the static pressure measurements just above the wing surface and the surface pressure measurements is even more significant in Figures 4.21b and 4.22b. In both of these figures the static pressures just above the wing surface indicate large regions of positive C_p while the surface pressures indicate only negative values of C_p. The high pressures measured beneath the primary vortex are particularly *suspect* as a static pressure minimum and large flow accelerations are anticipated in this region.

It is interesting to note that the location of minimum C_p in the surface pressure measurements coincides with the spanwise location of $(p_{tot})_{min}$ measured by the five-hole probe within the grid spacing of two measurement techniques. As mentioned in Section 1.1.1, the spanwise location of the primary vortex core can be expected to correspond with a local minimum of the static pressure distribution when viscous effects are neglected. Thus, the correspondence between the location of minimum C_p in the surface pressure measurements and $(p_{tot})_{min}$ supports the premise that the minimum total pressure location measured by the five-hole probe is a legitimate definition of the primary vortex core location.
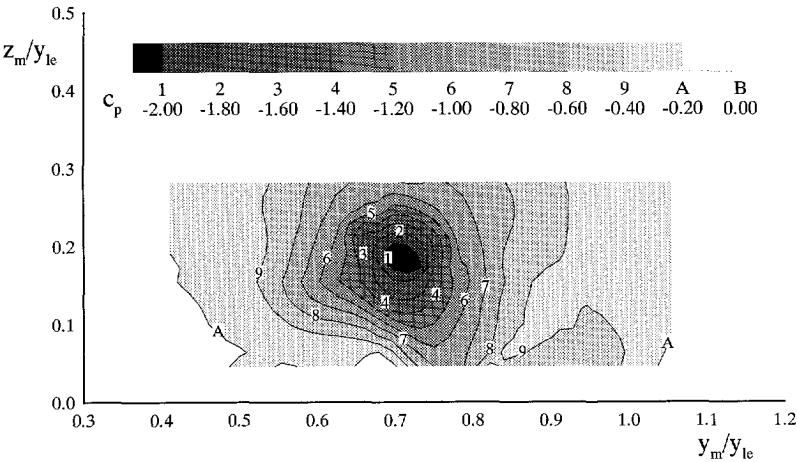
(a) C_p distribution
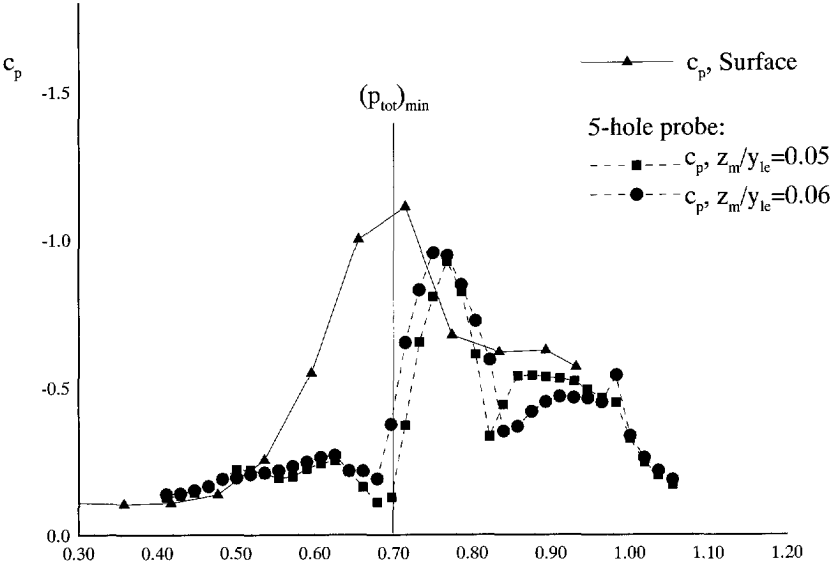
(b) Spanwise C_p distribution on and near surface of wing.

Figure 4.20: $M_\infty = 0.6$, $\alpha = 10°$ and $(x_m/c_r) = 0.7$.
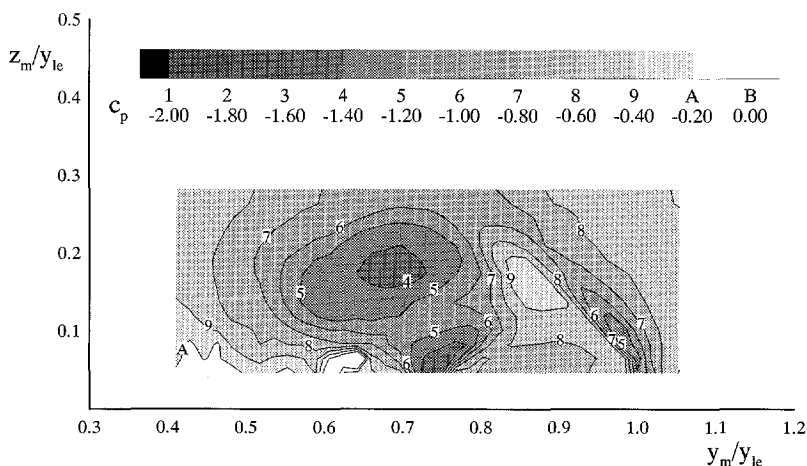
(a) C_p distribution
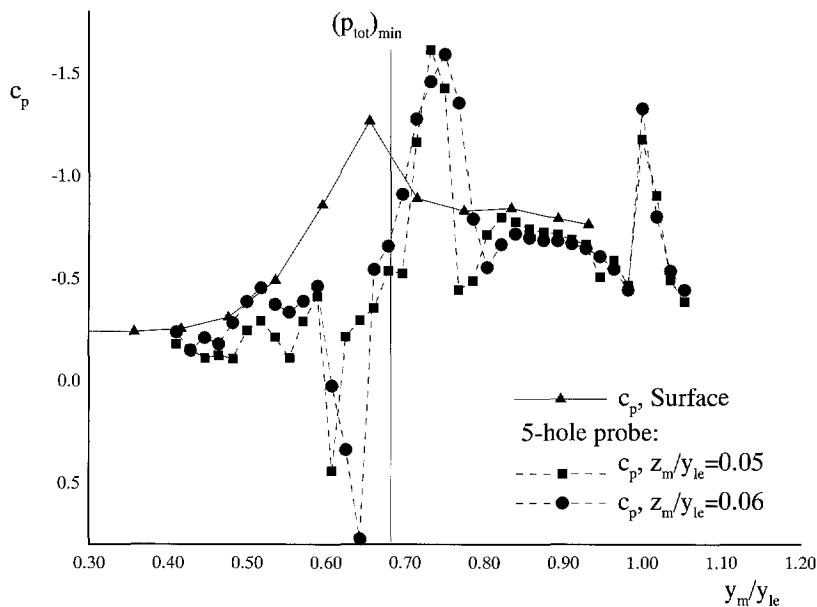
(b) Spanwise C_p distribution on and near surface of wing.

Figure 4.21: $M_\infty = 0.8$, $\alpha = 10°$ and $(x_m/c_r) = 0.7$.
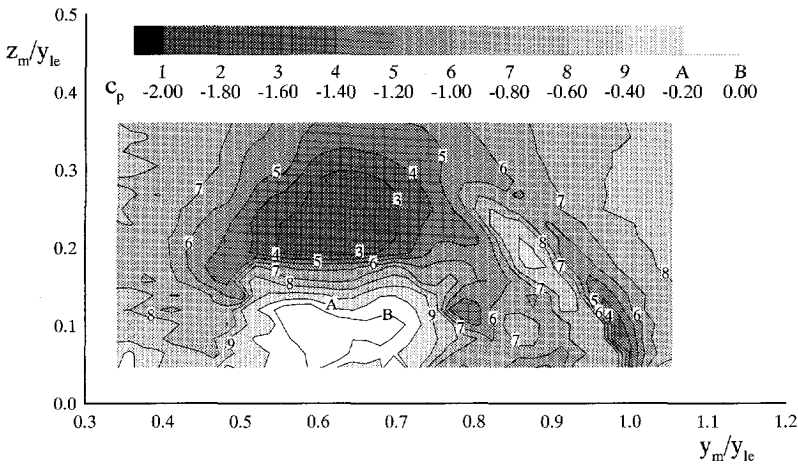
(a) C_p distribution
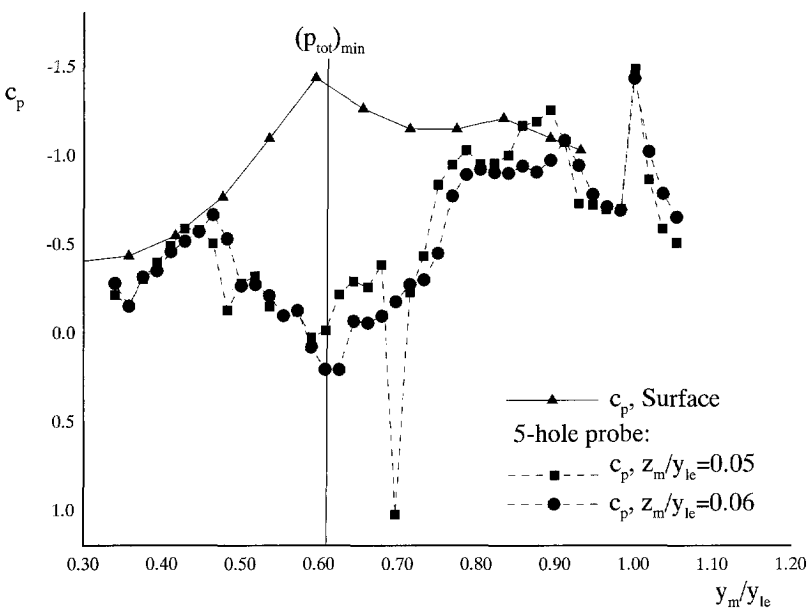
(b) Spanwise C_p distribution on and near surface of wing.

Figure 4.22: $M_\infty = 0.8$, $\alpha = 15°$ and $(x_m/c_r) = 0.7$.

4.6   Conclusions

The five-hole probe used in the current investigation is found to provide good accuracy in measuring the Mach number (±0.02), flow angle ($\pm1°$) and total pressure ($\pm1\%$) in a uniform free stream in both the subsonic and supersonic flow regimes. The five-hole probe measurements are suspected to be significantly less accurate, however, when measuring the vortical flow above the delta wing investigated in the current study. While the orientation of the cross-flow velocity vectors and the total pressure measurements are consistent with the anticipated delta wing flow field and non intrusive measurement data, the static pressure measurements in the vicinity of the wing are not. The position of primary vortex core as defined by $(p_{tot})_{min}$ in the five-hole probe measurements is found to be consistent with the transmission Schlieren images, oil flow visualizations and surface pressure measurements.

5

The Surface Reflective Visualization (SRV) System

The surface reflective visualization (SRV) system, described in this chapter, is a derivative of a double-pass Schlieren system [Holder and North 1963]. The definitive characteristic of the SRV system is that the upper surface of the model is itself a flat mirror and a component of the optical system. This system allows a top-view image of the flow field above the model to be obtained. This top-view perspective is particularly useful in the current study for gaining understanding of the three-dimensional flow field above the delta wing. The non intrusive and high speed nature of the SRV technique make it suitable for visualizing flow fields both with and without vortex breakdown present above the wing.

The SRV system is a new technique which has been developed in the course of the current investigation. Because the SRV system yields a two-dimensional image of the three-dimensional flow field above the delta wing, the interpretation of these images is not straight forward. To gain insight into the proper interpretation of the SRV images an SRV system analysis study is performed. In this study "simulated-SRV" images are produced from both a numerically generated flow solution above the delta wing under consideration and an experimentally measured flow field above the relevant delta wing in the TST-27 wind tunnel. The simulated-SRV images are examined to define the appearance of such phenomena as the primary vortex core and embedded cross-flow shock waves on the final image.

5.1 The Schlieren Concept

By definition, a Schlieren system produces a two-dimensional image of a component of the density gradient existing perpendicular to a parallel light bundle integrated over the path of the bundle. The component of the density gradient which is visualized is determined by the orientation of the Schlieren knife edge. Specifically, the change in illumination at a location

(x, y) in a Schlieren image relative to that of the undisturbed image is described by the relation

$$\frac{\Delta I}{I}(x, y) \propto \int_0^L \frac{\partial}{\partial y} n(x, y, z) dz, \tag{5.1}$$

where the refractive index n is linearly coupled to the density via the relation

$$n = 1 + \kappa \rho, \tag{5.2}$$

the Schlieren knife edge is in the $x - y$ plane parallel to the x-axis and the z-axis is aligned with the path of the parallel light bundle. The integral taken from 0 to L follows the path of the bundle of light. The Gladstone-Dale constant κ is a characteristic of the gas through which the light passes which is a weak function of the light wavelength and nearly independent of pressure and temperature under moderate physical conditions [Vest 1979]. The Gladstone-Dale constant is equal to $0.23 \cdot 10^{-3}$ (m^3/kg) for air at atmospheric conditions (temperature 293K and pressure 0.1 MPa) in the visible light spectrum [Merzkirch 1987]. The value of the Gladstone-Dale constant for a given gas is either estimated from molecular data or determined experimentally. The determination of this value becomes problematic in situations where combustion is present or where real-gas effects are important [Williams 1993].

5.2   SRV System Configuration

Similar to the transmission visualization system discussed in Section 3.5, the SRV system is configured such that the light source is projected, via a parabolic mirror, as a parallel bundle of light into the test section. In the SRV system, however, this bundle is projected along a path perpendicular to the upper surface of the model (see Figure 5.1), and not perpendicular to the side window of the test section as in the transmission visualization case. Because the upper surface of the model is a mirror, the light is reflected back along nominally the same path to the parabolic mirror, folded via a flat mirror and brought to focus on the image plane of the camera.

In order to obtain sufficient light for the photos it is necessary to place a tiny flat mirror at the junction of the outgoing and returning light bundles. Initially a splitter mirror was used at this location, but preliminary tests revealed that due to large light losses at the junction point (50% from the incident bundle and 50% from the returning bundle) use of the high speed camera was infeasible. To solve this problem, a tiny mirror was introduced at the junction point and the parabolic mirror and flat mirror were adjusted such that the light bundle passed
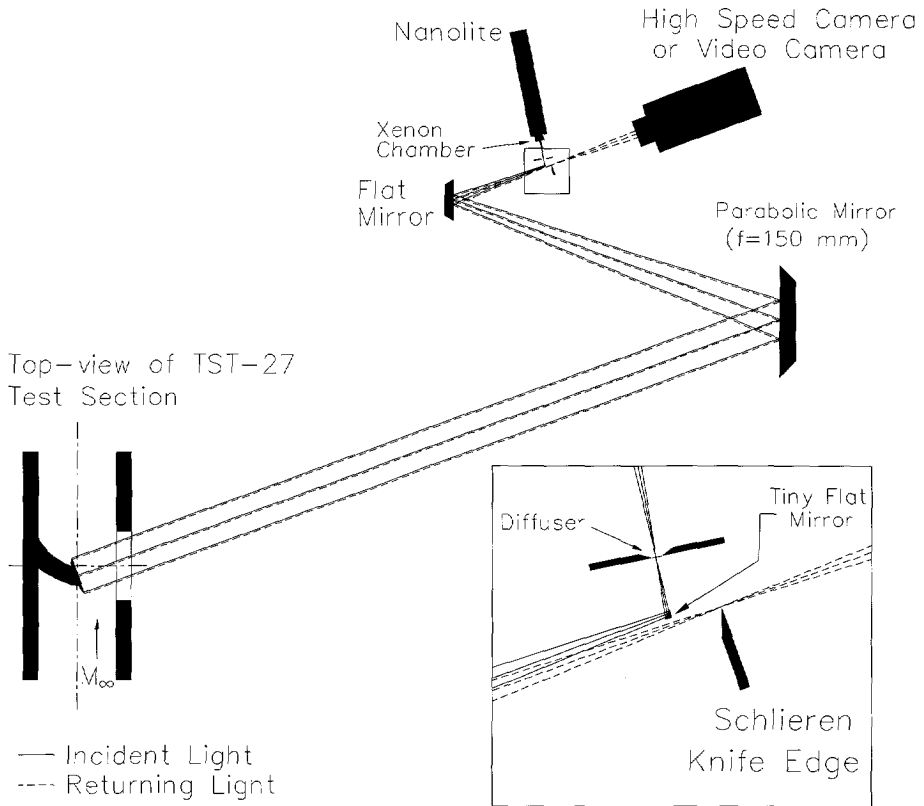
Figure 5.1: Surface Reflective Visualization (SRV) System Configuration

just next to the tiny mirror on its return path. The displacement of the returning light bundle, caused by the introduction of the tiny mirror, results in a divergence angle of 0.08° at the model surface between the incident and returning bundles of light. While there were initial concerns that this divergence would seriously decrease the sharpness of the resulting images, this was found not to be the case.

The addition of the Xenon chamber encasing the spark light source, discussed in Section 3.5, improved the quality of the SRV images by allowing a optical diffuser to be placed in front of the light source. The presence of this diffuser decreases the variation in spark location inherent in the spark light source and, thus, stabilizes the position of the focal point of the returning bundle of light on the Schlieren knife edge. The spark fluctuations in preliminary tests (prior to the addition of the Xenon chamber) resulted in a highly irregular basis illumination level I (see Equation 5.1) as the basis illumination of the image is determined by the position of the returning light bundle on the Schlieren knife edge. This variation in basis

illumination made it difficult to obtain a proper exposure for the film and made comparison of different Schlieren images problematic.

The mirrored upper surface of the SRV model is formed by machining a steel model to a mirror finish with an accuracy of ± 0.003 mm. The leading edge is slightly curved, however, as a result of the polishing process. The light color of the starboard leading edge and dark color of the port leading edge seen in Figure 5.2, a Schlieren image made of the model in the tunnel with no flow, is a result of this curvature. The scratches on the upper surface of the model, while very apparent in this SRV image with no flow over the wing, are a result of the polishing process and are of negligible physical depth.
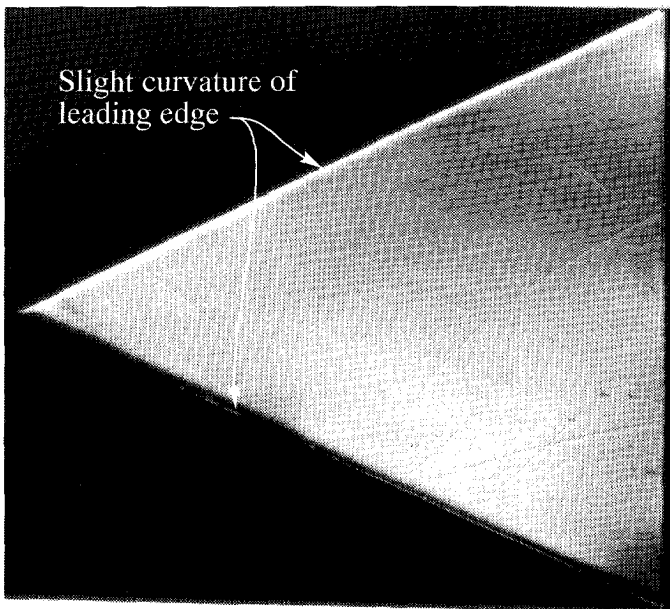
Figure 5.2: SRV image made of the model with no flow in the wind tunnel and the Schlieren knife edge aligned parallel with the root chord.

In an SRV optical system configuration commonly used in this study, the knife edge is aligned parallel with the root chord of the model (the x_m axis) or the free stream flow direction and the path of the light approaches the model surface perpendicularly along the z_m axis (See Figure 5.3). Images produced with this configuration illustrate the distribution of the spanwise density gradient integrated along a path perpendicular to the model surface. In the SRV system the light passes through the flow above the upper surface of the wing twice, along nominally the same path. The integration path length L in Equation 5.1 is, therefore, the sum of the incident and returning light paths. An example of an image produced with this
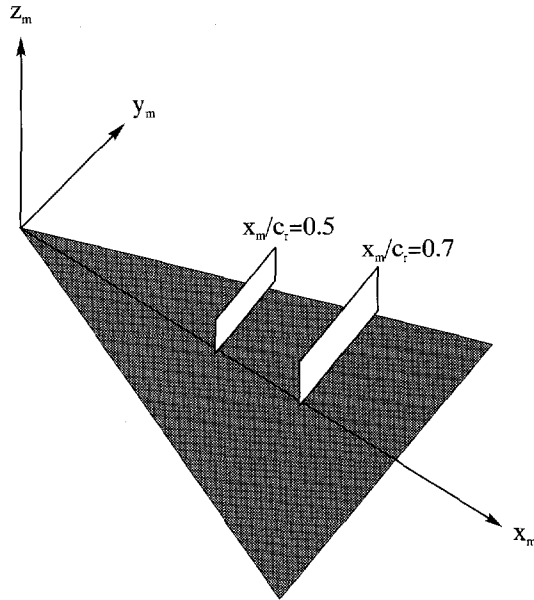
Figure 5.3: Illustration of model-fixed Cartesian coordinate system and applicable 5-hole probe measurement planes for simulated-SRV study.

optical configuration is shown in Figure 5.4. The gradients in the spanwise direction of the inboard half of the primary vortices are represented by the light and dark colored bands on the port and starboard sides of the wing, respectively. The dark lines intersecting the chord at approximately 80% and 90% of the root chord represent the terminating shock wave system. Theoretically, the terminating shock wave system, exhibiting density gradients mainly in the chord-wise direction, should not be visualized by a Schlieren system with the knife edge aligned parallel with the free stream. The reason that these shock waves are visualized is the presence of the tiny flat mirror at the junction of the outgoing and returning light bundles. Shock waves causing a large deflection of the light, due to their strength or extent along the path of the light, will cause the light to deflect outside the path of the returning bundle and impact the tiny mirror. The tiny mirror functions, thus, as an effective Schlieren knife edge oriented perpendicular to the root chord when large deflections of the light occur.

The distribution of the chord-wise density gradient, integrated along a path perpendicular to the model surface, can be produced by aligning the Schlieren knife edge perpendicular to the root chord (i.e. parallel with the y_m axis). This configuration is particularly useful in examining flow configurations exhibiting a terminating shock wave system. An example of an SRV image produced with this system configuration is shown in Figure 5.5. This combi-
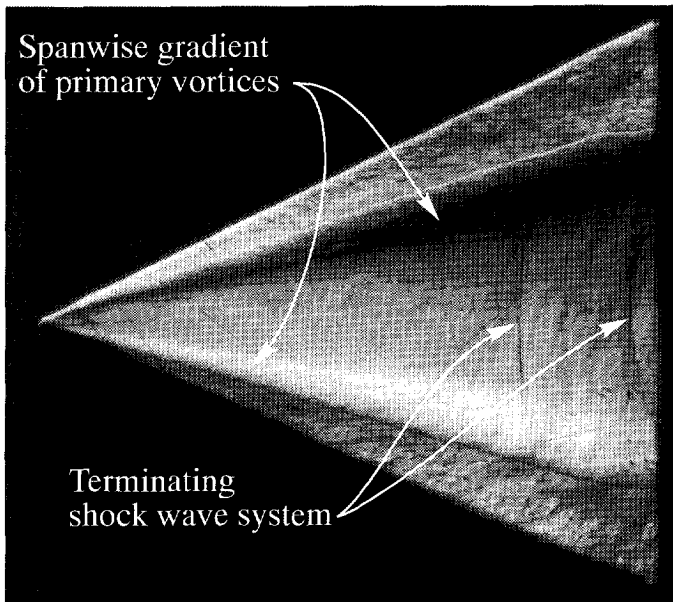
Figure 5.4: SRV image produced with the Schlieren knife edge aligned parallel with the root chord, $M_\infty = 0.8, \alpha = 15°$.
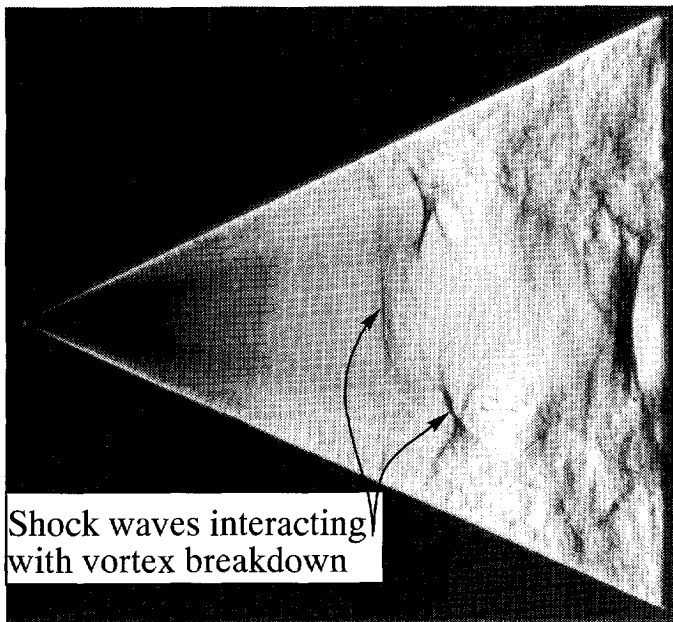
Figure 5.5: SRV image produced with the Schlieren knife edge aligned perpendicular to the root chord, $M_\infty = 0.8, \alpha = 20°$.

nation of angle of attack and Mach number exhibits shock waves interacting with the vortex breakdown structure. The near uniform darkening of the first 30% of the model is, unfortunately, due to a slight deflection of the model tip due to the aerodynamic forces acting on the wing.

5.3   SRV System Analysis

As mentioned above, Schlieren images represent an integrated gradient of the refractive index perpendicular to a light bundle along the path of that bundle. For a highly three-dimensional flow, gradients in the refractive index caused by flow phenomena along the line of sight may interfere with each other in the integration process. This makes it difficult to determine the presence and the extent of phenomena such as shock waves and vortices in an unknown flow field. In order to interpret the SRV images of the vortical flow field above a delta wing in a high subsonic free stream obtained in the current investigation the optical SRV system is modelled, via a numerical algorithm, and applied to two defined vortical flow fields. The first flow field is defined by numerically calculating the vortical flow field about the delta wing via the three-dimensional Euler equations. The second flow field is defined via five-hole probe measurements of the flow field above the delta wing in the wind tunnel.

The motivation for applying the simulated-SRV system to both a numerically calculated flow field and an experimentally measured field is that each field captures or models specific aspects of the actual flow field being visualized which the other does not. The flow field numerically calculated via the three-dimensional Euler equations models the embedded cross-flow shock waves, but does not capture viscous aspects of the flow field such as the secondary vortices. The Euler calculations also yield information in the entire flow field around the wing which allows the simulation of complete SRV images.

The data obtained experimentally via the five-hole probe capture the influence of the secondary vortex system, but are incomplete near the upper surface of the model where probe-surface interference problems make measurements infeasible. The inability to measure in the vicinity of the upper surface with the five-hole probe makes it impossible to determine the presence or extent of embedded cross-flow shock waves beneath the primary vortices with this technique. Another limitation of the experimental technique is that the time intensive nature of five-hole probe measurements restricts the amount of data which can practically be obtained above the model. For this reason only cross-sections of an SRV image can be produced from the experimental measurement data and not an entire image.

SRV simulations are performed for the free stream Mach numbers of 0.6 and 0.8 at $10°$ and $15°$ angle of attack. These particular $M_\infty - \alpha$ combinations are selected for several

reasons. Five-hole measurements are not possible once vortex breakdown becomes incipient above the wing. These combinations of M_∞ and α do not exhibit breakdown above or behind the wing in the wind tunnel. These combinations of free stream Mach number and angle of attack also provided a series of flows with increasing complexity. When $M_\infty = 0.6$ and $\alpha = 10°$ neither vortex breakdown nor embedded cross-flow shock waves are present above the wing. When $M_\infty = 0.8$, $\alpha = 10°$, embedded cross flow shocks are observed in the numerical calculations of the flow field. Finally, when $\alpha = 15°$ both embedded cross-flow shock waves and a phenomenon considered similar to vortex breakdown in some respects (i.e. solution breakdown) are present in the numerical flow solution. Again, no vortex breakdown is observed above or behind the wing in the experimental wind tunnel measurements for any of these $M_\infty - \alpha$ combinations.

5.3.1   Simulated-SRV Images of Numerically Calculated Flow Field

Numerical Simulation

The numerical simulations presented in this dissertation are conducted by E.M. Houtman at the High Speed Aerodynamics Laboratory of the Delft University of Technology. For reference purposes a short description of the numerical simulation method is provided below. See Houtman and Bannink [1991] for a more detailed description of the numerical technique.

The computational method is based on a finite volume discretization of the three-dimensional conservation law form of the Euler equations. The Euler equations represent the conservation of mass, momentum and energy for an inviscid, non-heat conducting calorically perfect gas in the absence of external forces and heating. The spatial discretization of the Euler equations makes use of the flux difference splitting approach following Roe [1981], whereby physical propagation properties are taken into account to some extent. The calculation of the fluxes at the cell faces is done according to van Leer's MUSCL (Monotone Upstream-centered Schemes for Conservation Laws) approach with flux limiting, which provides second order accuracy. The system of discretized equations is solved by a nonlinear multigrid full approximation scheme (FAS), with a Collective Gauss-Seidel relaxation procedure acting as smoothing method.

In order to obtain a close resemblance with the experimental investigations, the flow simulations are performed on a computational mesh representing the delta wing in the TST-27 wind tunnel. The wing support in the wind tunnel is not included in the model geometry. The grid has an H-O topology, and covers only a half-space due to the symmetry of the flow problem. The number of grid cells is $196,608$, with 96 cells in chordwise direction, 64 cells in spanwise direction and 32 cells between the model surface and the walls of the wind tunnel.

The surface grid along with the grid in the symmetry plane and some cross-planes is shown in Figure 5.6. The grid is conical on the surface, thus, preserving good resolution near the apex.
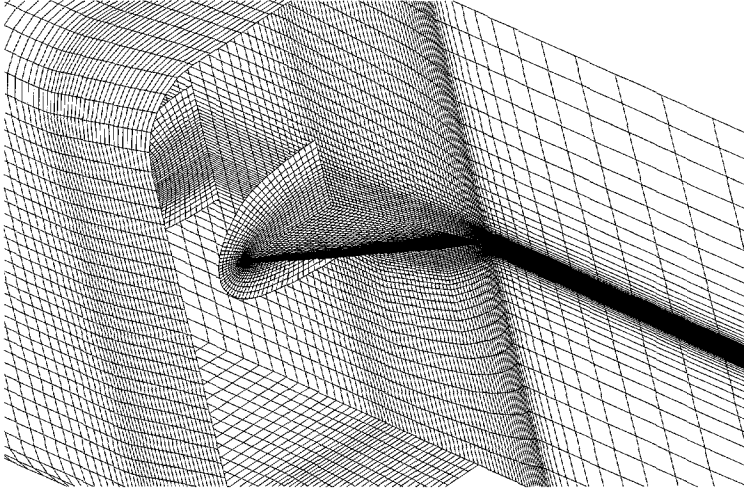
Figure 5.6: Computational grid.

Numerical calculations of the flow field about the delta wing yield solutions with a shear layer emanating from the sharp leading edge which rolls up into a leading edge vortex that agree with experiments, except for the absence of secondary and tertiary separations and their effects. For $\alpha = 15°$ a phenomenon exhibiting some similarities with vortex-breakdown occurs. These solutions are characterized by an "unsteady" region near the vortex core at the trailing edge where the flow is directed upstream and solution convergence is not obtained. The angle of attack at which this phenomenon occurs in the numerical simulations is less than the angle of attack for which vortex breakdown is observed in experiments (approximately 18°).

Schlieren Simulation Algorithm

The construction of the Schlieren images from the numerical flow solution consists of two steps. The first step includes integration of the refractive-index gradient along the line of sight according to Equation 5.1. The second step consists of post-processing the integrals to produce the desired Schlieren image. The post-processing allows such parameters as the desired Schlieren knife edge direction and the sensitivity (i.e. the value of ΔI associated with a given integrated-density gradient) of the Schlieren system to be adjusted. In an actual Schlieren system the optical sensitivity is a function of the Gladstone-Dale constant and the

position of the Schlieren knife edge in the light bundle at the focal plane of the parabolic mirror. When, as in the case of the current investigation, the Schlieren knife edge is positioned to block half of the light bundle, the amount of decreasing illumination associated with a gradient displacing the light bundle onto the Schlieren knife edge is equivalent to the amount of increased illumination associated with an integrated density gradient displacing the light bundle above the Schlieren knife edge. In the case of the numerically simulated images the sensitivity is assigned such that the full-scale of available gray scales (0 to 256) is utilized. This numerical simulation technique is an extension of a technique previously developed by Lanen and Houtman [1992] to generate interferogram images from a numerical flow solution.

From Equation 5.2 it follows that the refractive-index can be replaced by the density ρ, which is one of the quantities available in the computed flow solution. The actual light path is bent due to refractive-index gradients. Formally this path through the flow field should be traced, and the refractive index gradient (or density gradient) should be integrated along this path, but this is a very time intensive procedure computationally. The computational complexity can be reduced considerably by approximating the light path by a straight line perpendicular to the image plane. This approximation will not have a significant influence on the final simulated-SRV image if the intersection of the simulated-SRV line of sight with the image plane at the wing surface is not significantly displaced from the line of sight of the actual SRV images.

A concept sketch of the difference between the assumed straight light path and the actual light path through the vortical flow field is illustrated in Figure 5.7. The curvature of the actual SRV line of sight is shown in the solid black lines, while the dotted lines indicate that followed in the integration path of the simulated-SRV images. The path of the returning light, after being reflected from upper surface of the model, is illustrated by the light rays penetrating the mirror surface of the delta wing and continuing through the mirrored image of the vortex system on the other side of the image plane. The curvature of the line of sight in the actual SRV system has been exaggerated for illustration purposes. The difference between the intersection of the simulated-SRV line of sight and the actual SRV line of sight with the image plane defines the geometric inaccuracy of the simulated images. This discrepancy can be estimated by assuming a constant $(\partial\rho/\partial y)$ throughout the vortical flow field and calculating the deflection of the light ray passing through the field.

Consider an analogous situation illustrated in Figure 5.8 where a light ray is shown passing through a wind tunnel test section where a density gradient $(d\rho/dh)$ is present and where ρ is only a function of h. Assuming the deflection of the ray is sufficiently small and that the density along the ray can be assumed to be that present at the height h_1 where the light ray enters the test section. The deflection angle ϵ, or gradient (dh/ds), of the light path s can

Incident Light

Mirror Surface
of Delta Wing

A_1 S_2 A_2 S_1

- - ► Simulated-SRV line of sight

── ► Actual SRV line of sight

Returning Light
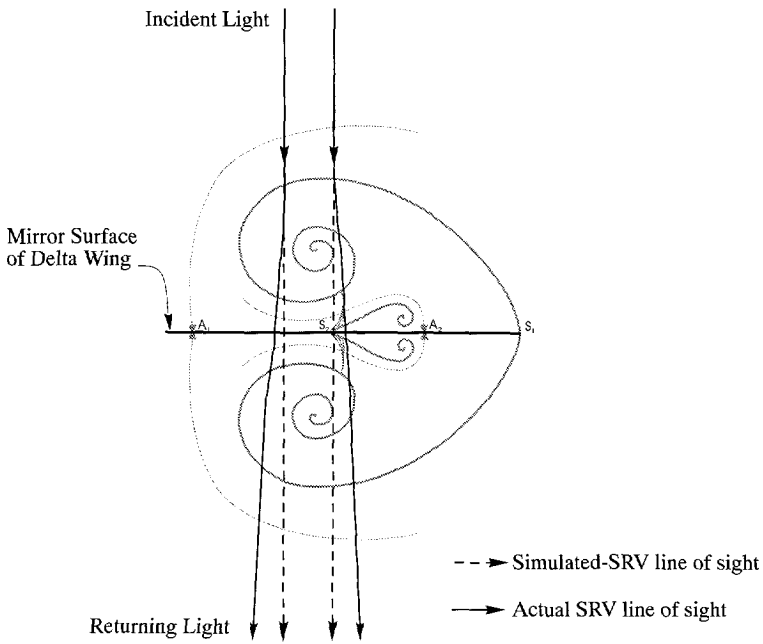
Figure 5.7: Schematic view of simulated-SRV line of sight and actual SRV line of sight through the vortical flow field.

h

δ

$\varepsilon(W)$

h_1

s

W
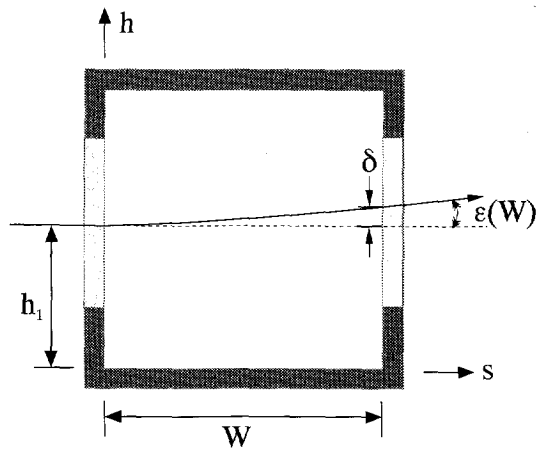
Figure 5.8: Refraction of light ray passing through a wind tunnel test section with a constant value of $(\partial\rho/\partial h)$ through the width of the test section W.

then be calculated via the relation:

$$\epsilon(s) = \int_0^s \left(\frac{1}{n} \frac{dn}{dh} \right)_{h_1} ds \tag{5.3}$$

where,

$$n = 1 + \kappa\rho, \tag{5.4}$$

[Liepmann and Roshko 1957]. Now, assuming that the gradient $(d\rho/dh)$ is constant, the deflection angle ϵ can be described by the relation:

$$\epsilon(s) = \left(\frac{s\kappa}{1 + \kappa\rho} \left(\frac{d\rho}{dh} \right) \right)_{h_1} \tag{5.5}$$

The parabolic nature of the light path s implied in Equation 5.5 (i.e. ϵ varies linearly with s) allows the discrepancy δ between the two lines of sight exiting the test section to be defined as:

$$\delta = \frac{W\epsilon}{2} = \left(\frac{W^2\kappa}{2(1 + \kappa\rho)} \left(\frac{d\rho}{dy} \right) \right)_{h_1} \tag{5.6}$$

In the case of the current investigation the constant density gradient $(\partial\rho/\partial y)$ assumed throughout the flow field is that present in the vicinity of the embedded cross-flow shock wave present when $M_\infty = 0.8$ and $\alpha = 15°$ (see Figure 5.9). This value represents the maximum $(\partial\rho/\partial y)$ present in the relevant numerical flow solutions and will, thus, yield the maximum geometric discrepancy. Twice the height of the vortical flow field above the wing is taken as the length of the path W because the actual line of sight will pass through the vortical field twice. The discrepancy between the simulated and actual lines of sight at the model surface is found to be $17.6 \cdot 10^{-6}$ m when $M_\infty = 0.8$, $\alpha = 15°$, $[(\partial\rho/\rho_\infty)/(\partial y/y_{le})] = 3.5$ and $W = 2 \cdot 0.4 y_{le}$. This discrepancy is less than a tenth of a percent of the local semi-span. Because the chordwise gradients in the vortical flow field are significantly smaller than the spanwise gradients in the absence of terminating shock waves (see Section 6.2), the geometric discrepancy between the simulated and actual line of sight will be less than this in the chordwise direction. The geometric inaccuracy of the simulated-SRV images resulting from the estimation of the line of sight as a straight line can, thus, be considered negligible.

In order to evaluate integrals along straight lines through a discrete field, an algorithm has been written which calculates the values of the appropriate integrand at certain points, after which the integration is performed according the trapezoidal rule. This process is schemat-
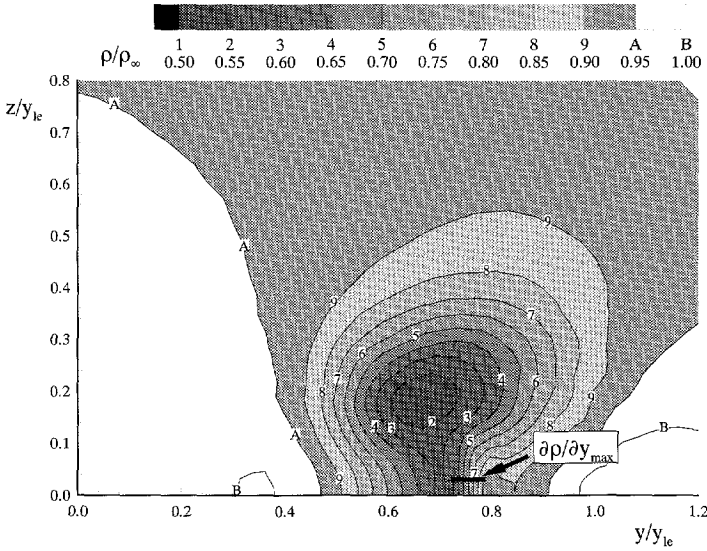
Figure 5.9: Numerically calculated density distribution in cross-flow plane $(x_m/c_r) = 0.7$ when $M_\infty = 0.8$ and $\alpha = 15°$.

ically shown in Figure 5.10. The Euler method uses a grid with hexahedral cells. For the interpolation procedure, each computational cell is subdivided into five tetrahedrals. The integration procedure follows a path along subsequent cell faces of the tetrahedrals. The intersection of the light path with the cell face is determined and the density is calculated via a linear interpolation between the known density values at the nodes of the triangular cell face (see Figure 5.10).

A further simplification in the simulation process is made by the changing the order of the differentiation and the integration in Equation 5.1 such that:

$$\int_0^L \frac{\partial \rho(y;z)}{\partial y} dz = \frac{\partial}{\partial y} \int_0^L \rho(y;z) dz \tag{5.7}$$

where ρ has again been substituted for the refractive index n. In this way, first an integration of the density for the desired flow field is performed, which yields the two-dimensional distribution of the integrated-density at the image plane. This simplification is advantageous because the height above the wing of the various points of integration (i.e. the intersection of the line of integration with the cell faces) for two adjacent rays is not necessarily equivalent. The continuous calculation of the density gradient perpendicular to the light throughout the field would require additional interpolations in order to determine the adjacent density val-
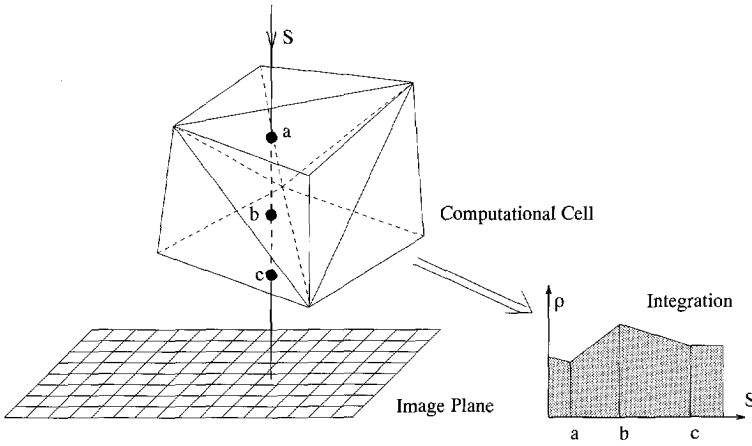
Figure 5.10: Schematic view of density integration through numerical flow field.

ues. This simplification does not affect the accuracy of the simulation, however, as the rule
of Leibnitz:

$$\frac{d}{ds}\int_0^{g(s)} F(\xi;s)d\xi = \int_0^{g(s)} \frac{\partial F}{\partial s}d\xi + F\{g(s);s\}\frac{dg}{ds} \tag{5.8}$$

becomes:

$$\frac{d}{ds}\int_0^{g(s)} F(\xi;s)d\xi = \int_0^{g(s)} \frac{\partial F}{\partial s}d\xi \tag{5.9}$$

when $g(s)$, as in the case of Equation 5.7, is a constant.

The two-dimensional density distribution, obtained via the integration through the flow
field along a ray perpendicular to the upper surface of the model, is used by image process-
ing software to construct a Schlieren image. This is done by differentiation of the integrated-
density field in a direction normal to the desired Schlieren knife-edge orientation. The inten-
sity pattern is proportional to the gradient of the integrated-density (see Equation 5.1). The
creation of Schlieren images is implemented as a module in the visualization package AVS[1],
such that direction of the Schlieren knife-edge and the intensity level can be adjusted inter-
actively.

---

[1]A product of Advanced Visual Systems, 300 Fifth Ave., Waltham, MA 02154

Results

A simulated-SRV image, when $M_\infty = 0.6, \alpha = 10°$ and with the Schlieren knife-edge aligned parallel to the root chord, is shown in Figure 5.11a . The corresponding cross-sections of the integrated-density and spanwise integrated-density gradient at $(x_m/c_r) = 0.70$ are shown in the Figure 5.11b. The position of the vortex core indicated both in the top-view SRV image and the cross-section is obtained by an algorithm which determines the location of minimal total pressure in a large number of cross-planes. The vortex core location is noted to coincide with the spanwise location of a transition from lightening to darkening of the SRV image in Figure 5.11a. This effect can also be seen in the spanwise distribution of the integrated-density gradient in Figure 5.11b as the gradient (indicated by the dashed line) passes through zero very close to the primary vortex core location. When $M_\infty = 0.6$ and $\alpha = 10°$, embedded shock waves do not appear in the computed flow field solution.

The simulated-SRV image and corresponding cross-sections of the integrated-density and spanwise integrated-density gradient at $(x_m/c_r) = 0.70$ when $M_\infty = 0.8, \alpha = 10°$ are shown in Figure 5.12. The primary vortex core location is, again, superimposed on these images. It is interesting to note that in this case the location of the primary vortex core is slightly more inboard $(\Delta(y_m/y_{le}) \approx 0.02)$ than the minimum value of the integrated-density or the location where the y-derivative of the integrated-density passes through zero. This discrepancy suggests that the primary vortex when $M_\infty = 0.8, \alpha = 10°$ is less axisymmetric than that at $M_\infty = 0.6, \alpha = 10°$. The magnitude of the integrated-density gradients are also noted to be larger in this higher Mach number case as a result of the increased density variations present.

The spanwise distribution of pressure and conical Mach number show that a very weak cross-flow shock is formed just outboard of the position of the primary vortex core when $M_\infty = 0.8$ and $\alpha = 10°$. The conical Mach number is based on the velocity component normal to the local conical ray. This shock formation is also visible in the simulated-SRV image of Figure 5.12a, where just outboard of the primary vortex core a weak black and a white line are visible at the port side and starboard sides of the wing, respectively. The location of the embedded cross-flow shock wave at the model surface, determined by examination of the conical Mach number distribution on the surface, is superimposed on the cross-section shown in Figure 5.12b. This shock wave location is noted to nearly coincide with a local peak in the spanwise integrated-density gradient on the starboard side of the wing (i.e. when $(y_m/y_{le}) > 0$).

Figure 5.13 illustrates the simulated-SRV image and corresponding cross-sections of the integrated-density and spanwise integrated-density gradient at $(x_m/c_r) = 0.70$ when $M_\infty = 0.8, \alpha = 15°$. Again, the location of the primary vortex core and embedded cross-flow shock
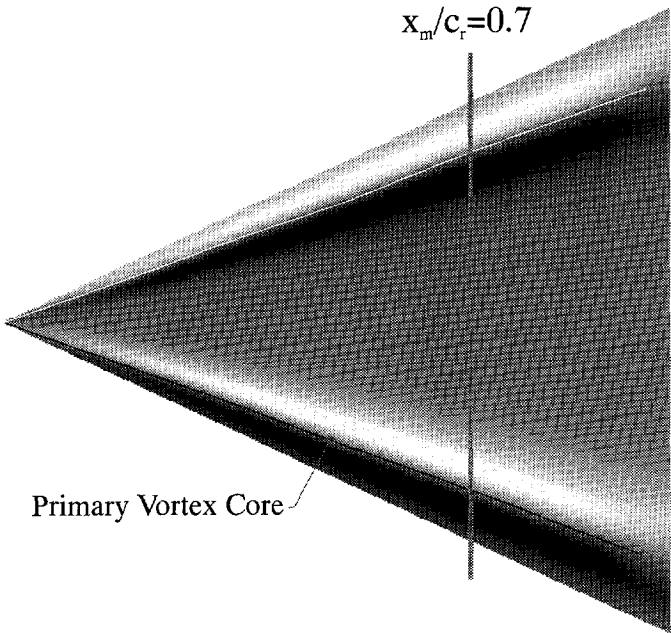
(a) Numerical simulated-SRV Image, Schlieren knife edge parallel with root chord
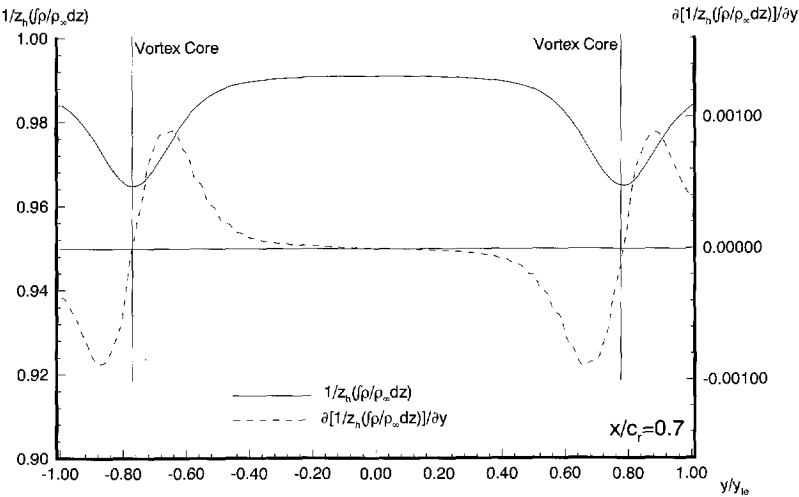
(b) Spanwise distribution of integrated-density and density gradient, $(x_m/c_r) = 0.70$

Figure 5.11: $M_\infty = 0.6$, $\alpha = 10°$
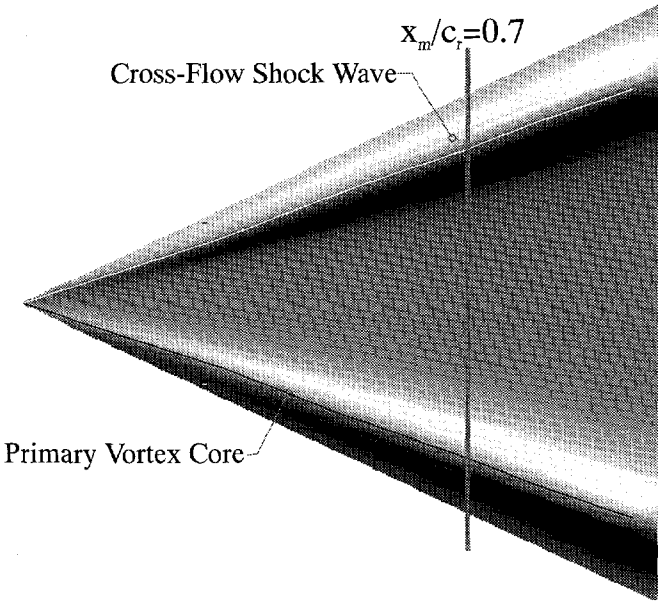
(a) Numerical simulated-SRV Image, Schlieren knife edge parallel with root chord
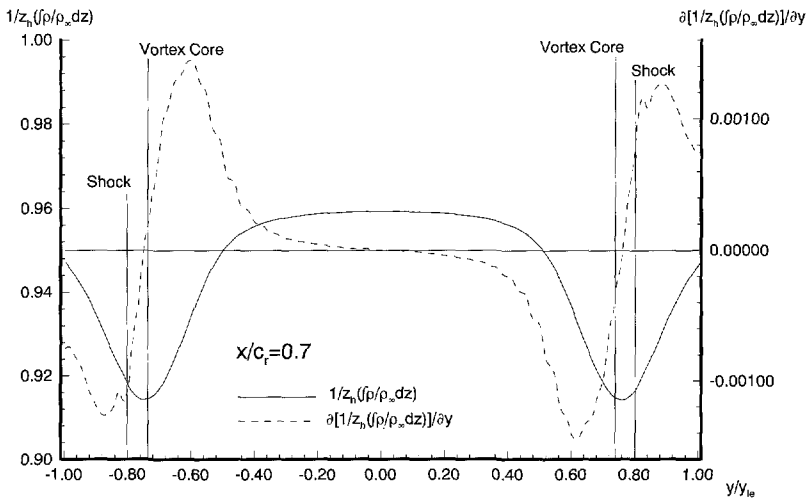
(b) Spanwise distribution of integrated-density and spanwise integrated-density gradient, $(x_m/c_r) = 0.70$

Figure 5.12: $M_\infty = 0.8$, $\alpha = 10°$
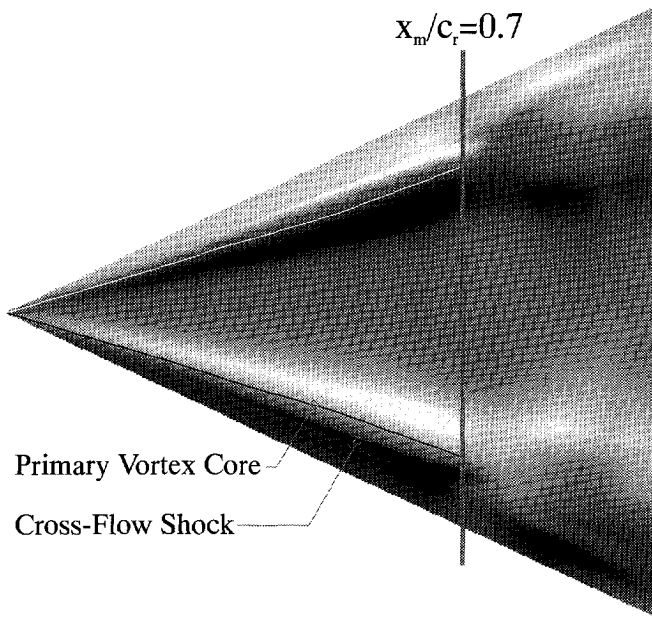
$$x_m/c_r=0.7$$

Primary Vortex Core

Cross-Flow Shock

(a) Numerical simulated-SRV Image, Schlieren knife edge parallel with root chord
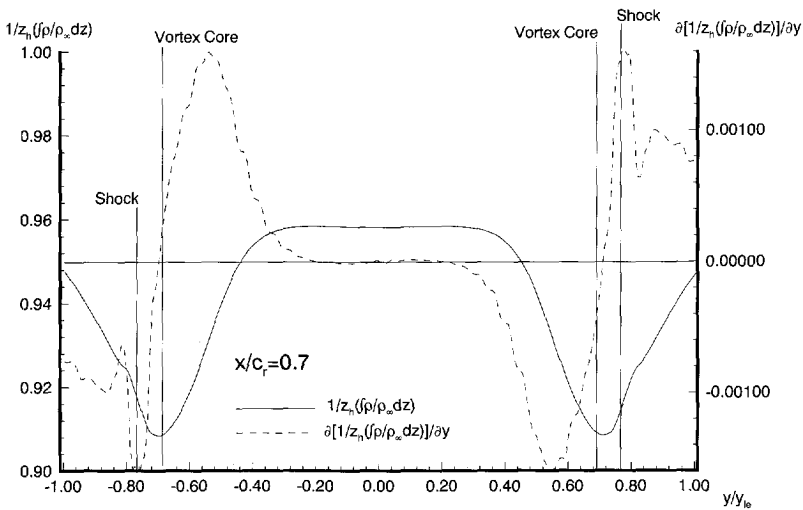
(b) Spanwise distribution of integrated-density and spanwise integrated-density gradient, $(x_m/c_r) = 0.70$

Figure 5.13: $M_\infty = 0.8$, $\alpha = 15°$

wave are superimposed in these images. A cross section of the conical Mach number distribution together with the direction of the conical (cross-flow) velocity is shown in Figure 5.14. Between the vortex core and the surface a region of supersonic cross-flow exists, which is
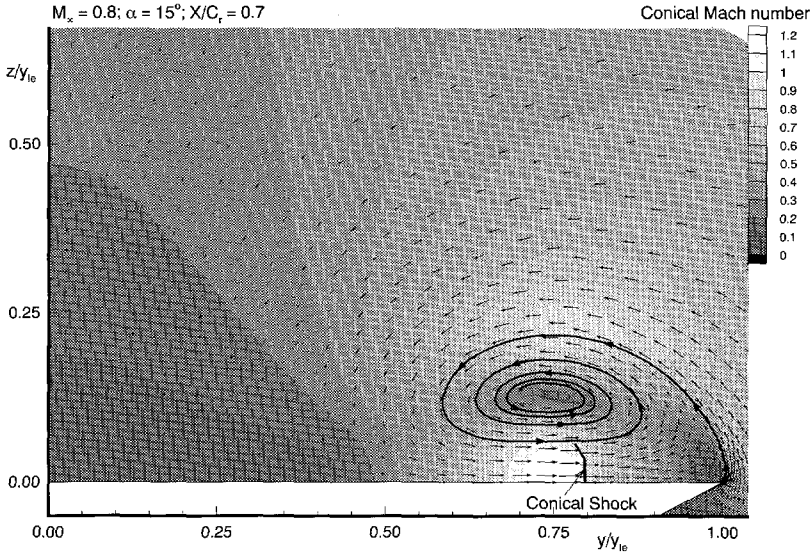
Figure 5.14: Distribution of conical Mach number, $M_\infty = 0.8$, $\alpha = 15°$, $(x_m/c_r) = 0.7$

terminated by the indicated conical shock. A stronger embedded cross-flow shock wave is present when $M_\infty = 0.8$ and $\alpha = 15°$ than in the case of $M_\infty = 0.8$ and $\alpha = 10°$. In the spanwise distribution of the spanwise integrated-density gradient shown in Figure 5.13b, a significant local peak is indeed visible on the starboard side of the wing which corresponds with the location of the embedded cross-flow shock wave. The embedded cross-flow shock waves are clearly visible in the simulated-SRV image of Figure 5.13a upstream of the "vortex breakdown" (i.e. $(x_m/c_r) \leq 0.7$). Downstream of the point of "vortex breakdown" the shock ceases to exist due to the decreased circumferential velocities.

5.3.2   Simulated-SRV Images of Experimentally Measured Flow Field

Five-hole Probe Measurements

As discussed in Chapter 4, the five-hole probe measurements in the vortical flow field above the delta wing define the local Mach number and total pressure distribution in each measurement plane. This information is used to calculate the distribution of the local density to free

stream density ratio, assuming a constant total enthalpy, via the relation,

$$\frac{\rho}{\rho_\infty} = \frac{p_t}{p_{t\infty}} \left(\frac{1 + \frac{\gamma-1}{2}M_\infty^2}{1 + \frac{\gamma-1}{2}M^2} \right)^{\frac{1}{\gamma-1}} \tag{5.10}$$

Five-hole probe measurements are made in two different spanwise planes perpendicular to the upper surface of the delta wing for each $M_\infty - \alpha$ combination examined. These planes are located at $(x_m/c_r) = 0.5$ and $(x_m/c_r) = 0.7$ and have a grid spacing of $0.5\ mm$ and $0.7\ mm$, respectively (See Figure 5.3). An additional measurement plane, with a grid spacing of $1.4\ mm$, is also examined at $M_\infty = 0.8$, $\alpha = 15°$ and $(x_m/c_r) = 0.7$ to examine the influence of the grid spacing on the simulation results and to provide a more complete picture of the flow characteristics in the spanwise plane. Details on the specific grid dimensions are found in Table 2.2 on Page 28.

Schlieren Simulation Algorithm

As previously mentioned, it is not possible to simulate a complete two-dimensional SRV image from the five-hole probe measurements in the same manner as for the numerical flow solution due to the limitation of measuring the flow in only two span-wise planes at each $M_\infty - \alpha$ combination. From the density distribution, however, cross-sections of simulated-SRV images with the knife edge aligned parallel with the root chord can be calculated in a manner similar to that used for the numerical flow solutions. This is done by calculating the spanwise component of the integrated-density gradient for each of the five-hole probe measurement planes. As in the simulation algorithm applied to the numerical flow solution, local values of (ρ/ρ_∞) are first integrated along a path perpendicular to the wing. This process is illustrated schematically in Figure 5.15. A characteristic experimentally determined density distribution above the wing is shown in Figure 5.16 for reference purposes. In the calculation of integrated-density values several traverses close to the wing surface are omitted due to clear evidence of wing/probe interference (i.e. positive C_p values just above the wing surface). The number of traverses omitted is indicated in the relevant graphics by the variable N_z'. The spanwise gradient of the integrated-density is calculated from the spanwise distribution of the integrated-density via a finite-difference discretization. As in the simulated-SRV images of the numerical flow solutions, the gradient of integrated-density is related to the illumination which is represented in an actual Schlieren image when the Schlieren knife edge is aligned parallel with the root chord.
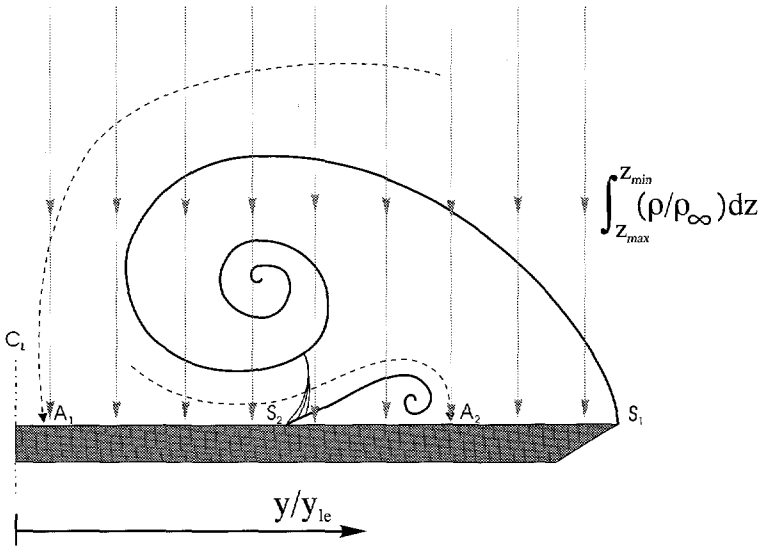
Figure 5.15: Illustration of integration path perpendicular to upper surface through the five-hole probe measurement grid.
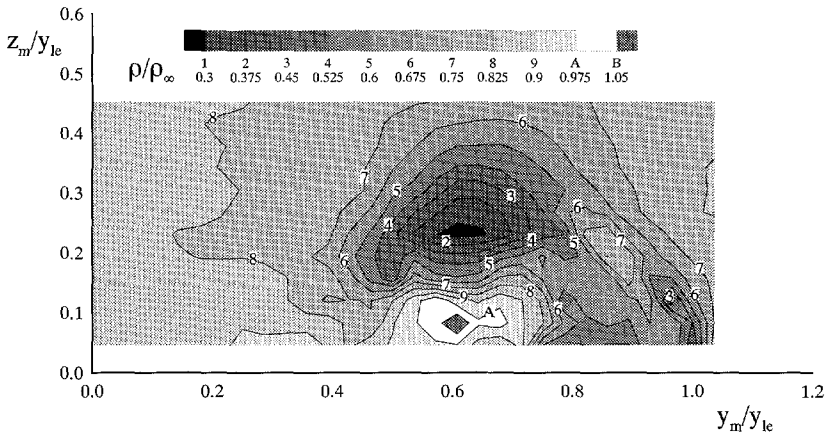
Figure 5.16: Density distribution when $(x_m/c_r) = 0.7$, $\alpha = 15°$ and $M_\infty = 0.8$.

Results

In the results discussed below the location of the primary vortex core, defined as the location of minimum total pressure in the five-hole probe measurement plane, is used as a point of reference in interpreting the simulated-SRV results. Figure 5.17 illustrates a characteristic total pressure distribution above the wing. Total pressure losses are noted to be significant in the shear layer emanating from the leading edge, about the primary vortex core and in the vicinity of the secondary vortex. The primary vortex core location for each of the measurement planes above the wing are listed in Table 5.1 for reference purposes.
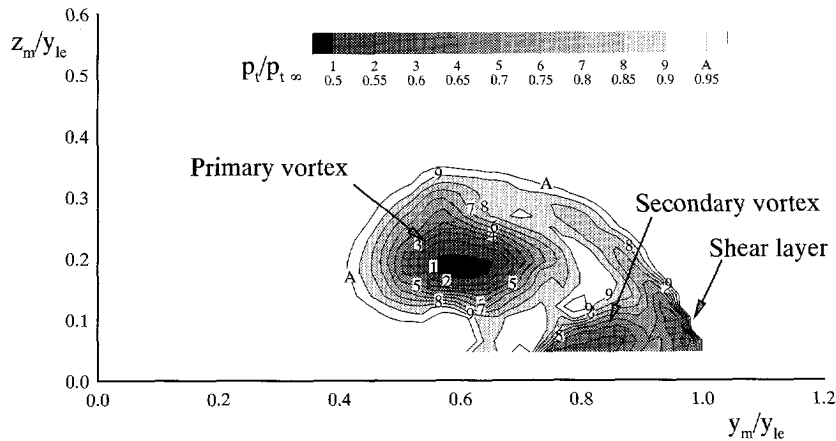
Figure 5.17: Total pressure distribution when $(x_m/c_r) = 0.7$, $\alpha = 15°$ and $M_\infty = 0.8$.

M_∞	$\left(\dfrac{x_m}{c_r}\right)$	$\alpha = 10°$		$\alpha = 15°$	
		$\left(\dfrac{y_m}{y_{le}}\right)$	$\left(\dfrac{z_m}{y_{le}}\right)$	$\left(\dfrac{y_m}{y_{le}}\right)$	$\left(\dfrac{z_m}{y_{le}}\right)$
0.6	0.5	0.72	0.16	0.66	0.21
	0.7	0.70	0.16	0.66	0.19
0.8	0.5	0.66	0.16	0.63	0.19
	0.7	0.68	0.16	0.61	0.18

Table 5.1: Location of primary vortex core (i.e. $(p_{tot})_{min}$) determined via five-hole probe measurements.

Figure 5.18 illustrates the spanwise distribution of both the integrated-density and the spanwise gradient of the integrated-density at $(x_m/c_r) = 0.5$ and $(x_m/c_r) = 0.7$ when $M_\infty = 0.6$ and $\alpha = 10°$. The minimum integrated-density and zero value of the spanwise integrated-density gradient are located slightly outboard of the primary vortex core.

(a) $(x_m/c_r) = 0.50$

(b) $(x_m/c_r) = 0.70$
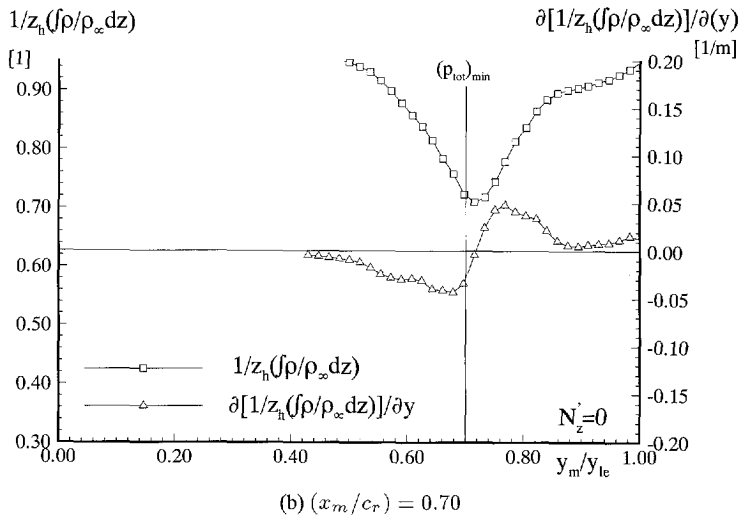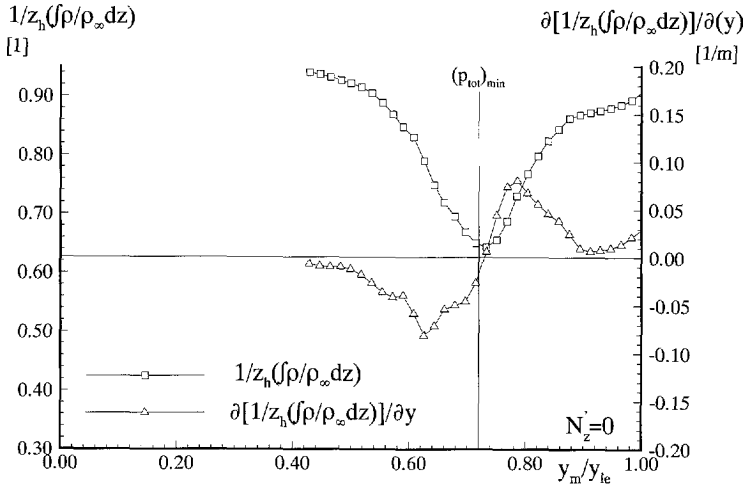
Figure 5.18: Spanwise distribution of integrated-density and spanwise integrated-density gradient, $M_\infty = 0.6$, $\alpha = 10°$.

Figure 5.19 illustrates the spanwise distribution of both the integrated-density and the spanwise gradient of the integrated-density at $(x_m/c_r) = 0.5$ and $(x_m/c_r) = 0.7$ when $M_\infty = 0.6$ and $\alpha = 15°$. In this image, similar to the case of $M_\infty = 0.6$ and $\alpha = 10°$, the minimum integrated-density and zero value of the spanwise gradient of the integrated-density both occur outboard of the primary vortex core location. At $(x_m/c_r) = 0.70$ the difference between the primary vortex core location and the zero value of the spanwise gradient of the integrated-density is approximately 2% of the local semi-span when $M_\infty = 0.6$, $\alpha = 10°$ and approximately 5% of the local semi-span when $M_\infty = 0.6$, $\alpha = 15°$. An explanation of this difference at the two angles of attack is likely the increased influence of the presence of the secondary vortex at the higher angle of attack. The integrated-density can be expected to decrease in the vicinity of the primary vortex in the outboard direction up to the location of the primary vortex core and increase beyond this point. Similarly, the integrated-density can be expected to decrease in the vicinity of the secondary vortex in the outboard direction up until the location of the secondary vortex core and increase beyond this point. This effect is visible in the density distributions of measurement planes at $(x_m/c_r) = 0.70$ for both angles of attack at $M_\infty = 0.6$ in Figure 5.20. The decreasing integrated-density in the direction of the leading edge resulting from the secondary vortex is more significant when $\alpha = 15°$ than in the case of $\alpha = 10°$.

Figure 5.21 illustrates the spanwise distribution of both the integrated-density and the spanwise gradient of the integrated-density at $(x_m/c_r) = 0.5$ and $(x_m/c_r) = 0.7$ when $M_\infty = 0.8$ and $\alpha = 15°$. In the case of $(x_m/c_r) = 0.7$ these data are presented for both the fine and coarse measurement grid cases. While the minimum integrated-density is significantly less in the case of the fine grid than for the coarser grid, the spanwise location of the minimum value remains the same. The lower integrated-density minimum in the fine grid case can be attributed to the presence of more measurement points in the vicinity of the vortex core where the density is significantly less than in the surrounding flow. The location of the minimum integrated-density is nearly coincident with the primary vortex core location at both $(x_m/c_r) = 0.50$ and $(x_m/c_r) = 0.70$. This is likely a result of the need to remove data in the vicinity of the wing upper surface at this $M_\infty - \alpha$ combination ($N_z' = 3$ and 5 at $(x_m/c_r) = 0.50$ and $(x_m/c_r) = 0.70$, respectively) due to probe/surface interference. The removal of these measurements in the vicinity of the wing upper surface significantly reduces the influence of the secondary vortex on the integrated-density values.
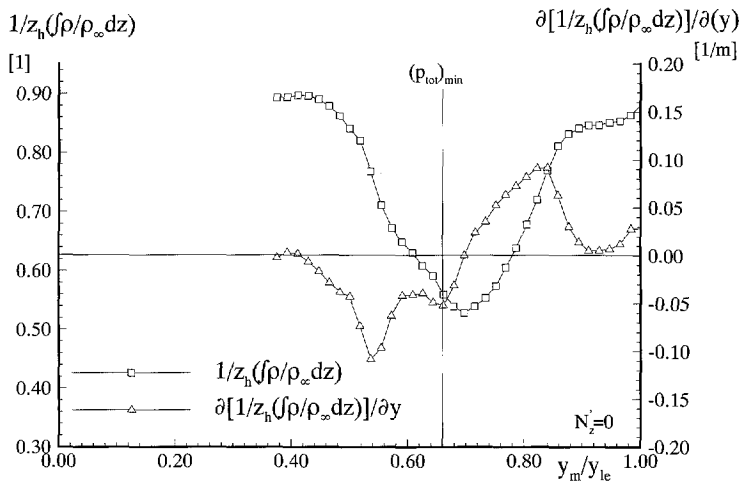
(a) $(x_m/c_r) = 0.50$
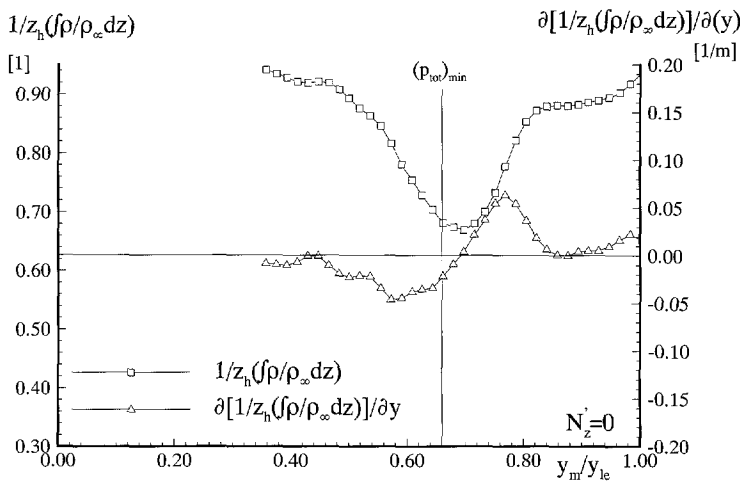
(b) $(x_m/c_r) = 0.70$

Figure 5.19: Spanwise distribution of integrated-density and spanwise integrated-density gradient, $M_\infty = 0.6$, $\alpha = 15°$.

(a) $M_\infty = 0.6$, $\alpha = 10°$

(b) $M_\infty = 0.6$, $\alpha = 15°$
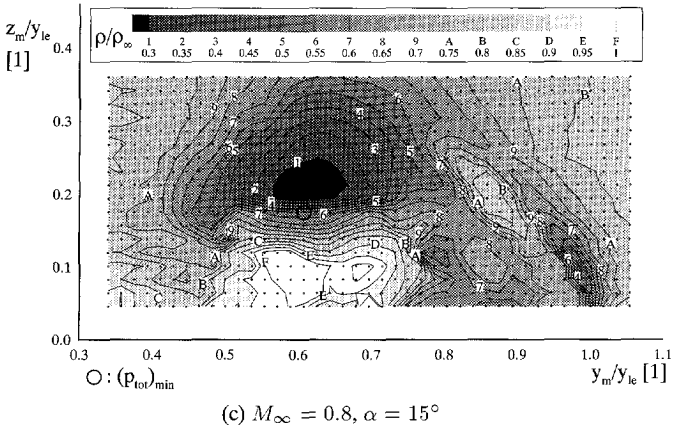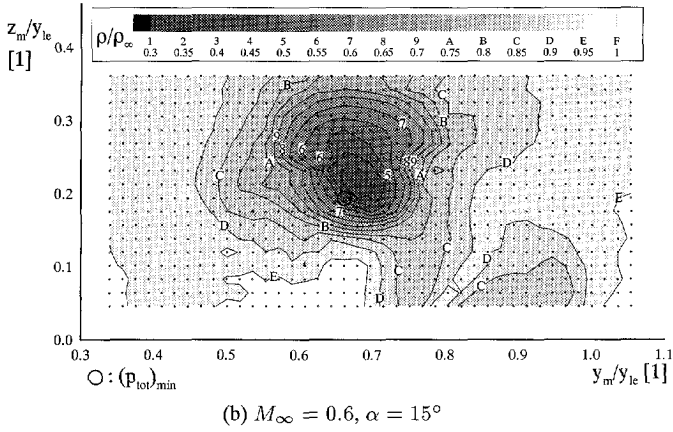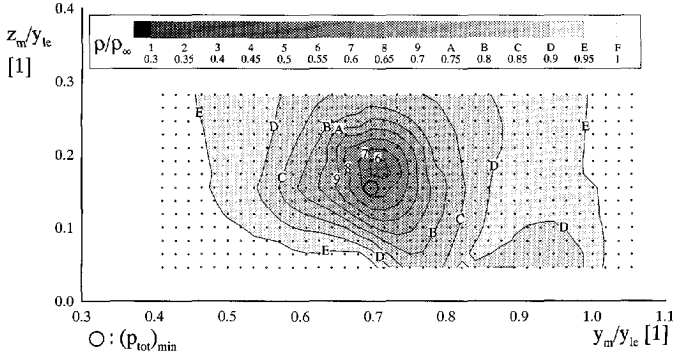
(c) $M_\infty = 0.8$, $\alpha = 15°$

Figure 5.20: Density distribution at $(x_m/c_r) = 0.70$ with superimposed measurement grid.

(a) $(x_m/c_r) = 0.50$

(b) $(x_m/c_r) = 0.70$
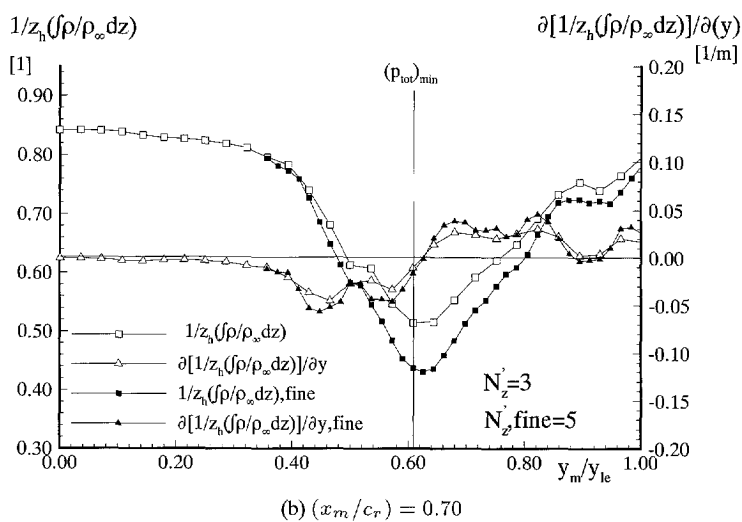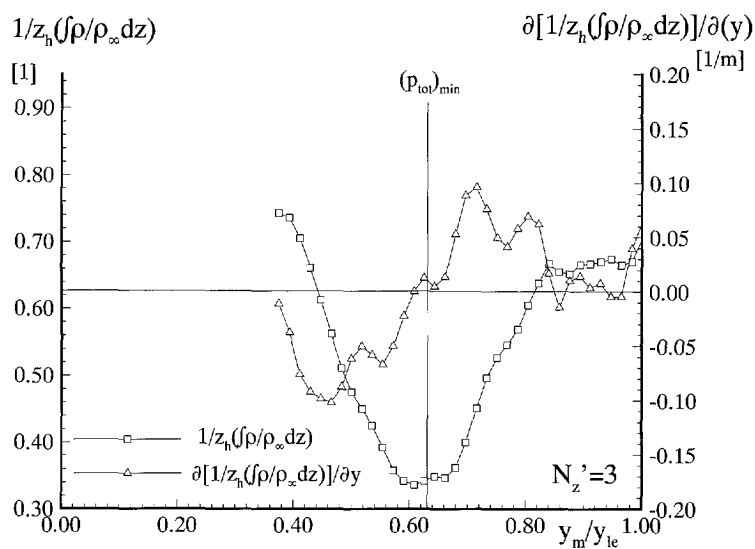
Figure 5.21: Spanwise distribution of integrated-density and spanwise integrated-density gradient, $M_\infty = 0.8$, $\alpha = 15°$.

5.3.3 Analysis of Actual SRV Images

In Figure 5.22 an actual SRV image when $M_\infty = 0.6$ and $\alpha = 10°$ is shown together with a cross section of the illumination level of this image at $(x_m/c_r) = 0.7$. These illumination levels are determined by first optically scanning the photographic SRV image to create a digital image of the photo and then extracting the desired cross section from this digital image. The lowest illumination level (0) corresponds with the color black and the highest illumination level (256) corresponds with the color white. These illumination levels correspond theoretically with the spanwise gradient of the integrated-density calculated in the simulated-SRV images discussed above. Average SRV images (exposure time 4 $msec$) are digitized, when available, to remove noise and unsteady aspects of the flow field visible in *instantaneous* images made with the spark light source (exposure time ≈ 20 $nsec$).

In Figure 5.22 the primary vortex core, defined as the minimum total pressure location in each five-hole probe measurement plane, is noted to intersect the illumination curve on the starboard side of the wing (i.e. when $(y_m/y_{le}) > 0$) approximately halfway between its minimum and maximum illumination level. On the port side of the wing this is also true, but the illumination curve is less smooth on the port side of the wing. The "noise" on the port side of the wing can be attributed to scratches on the model surface, which are more visible in the light colored region on the port side of the wing. The location of the primary vortex core approximately halfway between the minimum and maximum illumination levels is consistent with its location approximately halfway between the minimum and maximum values of spanwise integrated-density gradient observed in the simulated-SRV cross sections from both the numerical flow solution (see Figure 5.11b) and the five-hole probe data field (see Figure 5.18b).

In Figure 5.23 an actual SRV image at $M_\infty = 0.6$ and $\alpha = 15°$ is shown together with a cross section of the illumination values at $(x_m/c_r) = 0.7$. It is interesting to note that the location of the vortex core on the spanwise distribution of the illumination coincides with the edge of the intensity plateau on both sides of the wing. This is in contrast with the case of $M_\infty = 0.6$, $\alpha = 10°$, where the location of the primary vortex core coincides with a region of steadily increasing illumination (on the starboard side of the wing) approximately half way between the minimum and maximum values. In the simulated-SRV image cross section generated from the five-hole probe measurements, a similar behavior is observed. The zero value of the spanwise integrated-density gradient is further outboard of the primary vortex core location in the case of $M_\infty = 0.6$, $\alpha = 15°$ (see Figure 5.19b) than in the case of $M_\infty = 0.6$, $\alpha = 10°$ (see Figure 5.18b). The presence of the secondary vortex is, again, likely responsible for this effect.

In Figure 5.24 an actual SRV image at $M_\infty = 0.8$ and $\alpha = 15°$ is shown together with
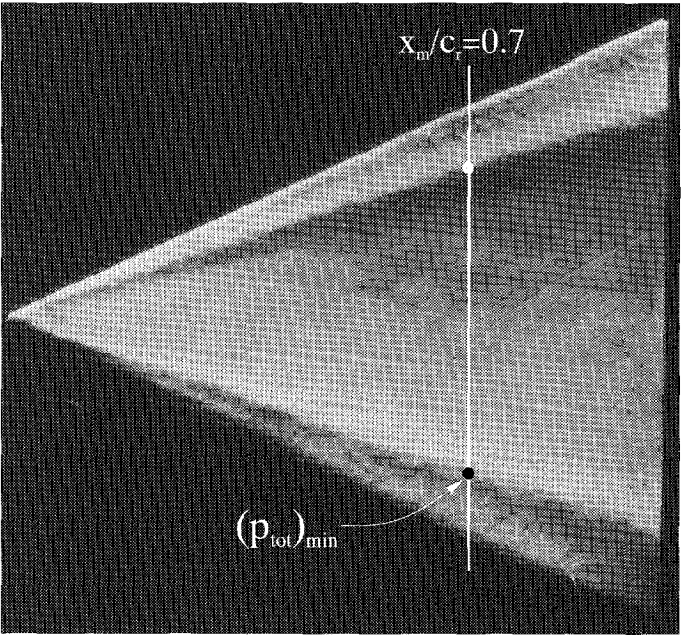
(a) SRV image (exposure time $\approx 20 \; nsec$) with the Schlieren knife edge aligned parallel with the root chord
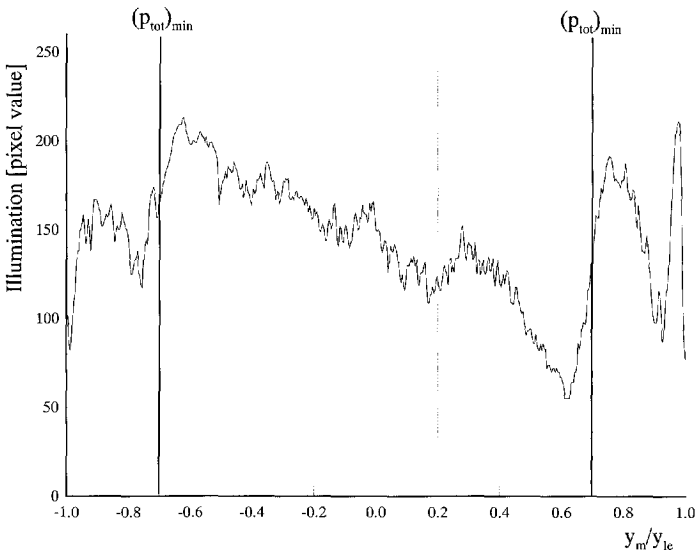
(b) pixel value or illumination distribution at $(x_m/c_r) = 0.7$

Figure 5.22: $M_\infty = 0.6, \; \alpha = 10°$
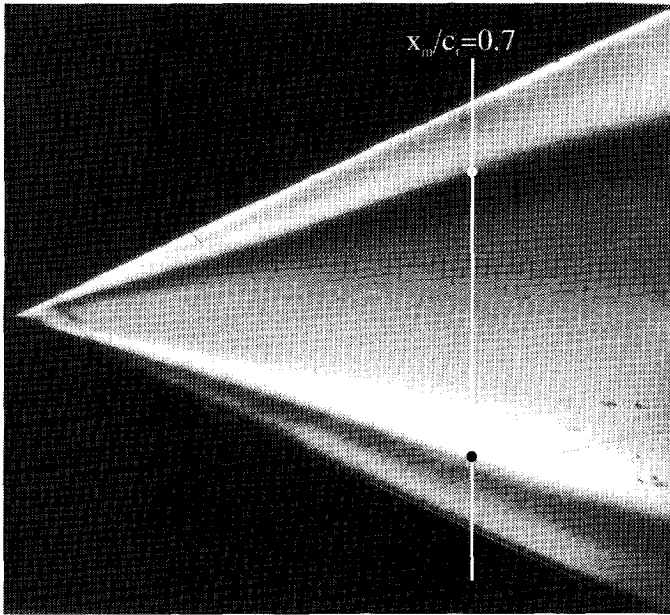
(a) Average SRV image (exposure time $4msec$) with the Schlieren knife edge aligned parallel with the root chord
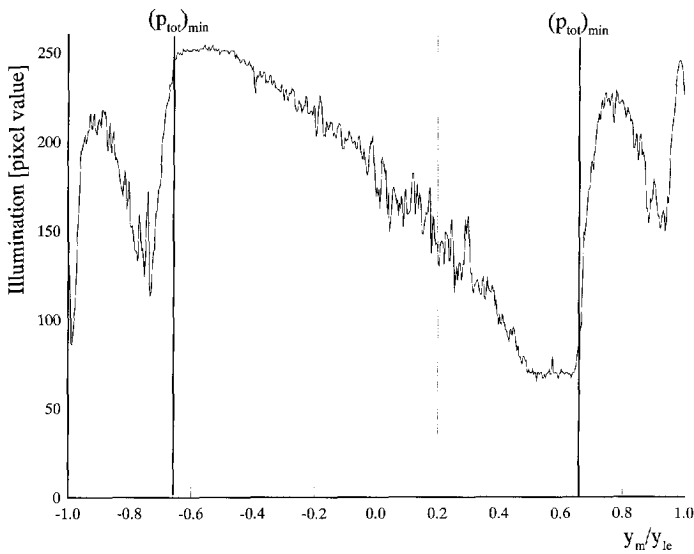
(b) pixel value or illumination distribution at $(x_m/c_r) = 0.7$

Figure 5.23: $M_\infty = 0.6$, $\alpha = 15°$

a cross section of the illumination values at $(x_m/c_r) = 0.7$. On the starboard side of the wing the primary vortex core is noted, as in the case of $M_\infty = 0.6$, $\alpha = 15°$, to coincide with the edge of a plateau of minimum pixel values or the outboard edge of the black band visible in Figure 5.24a. A spike in the illumination level is visible outboard of the primary vortex core on the starboard side of the wing in Figure 5.24b which corresponds with the white line visible in Figure 5.24a. The appearance of this line on the SRV image outboard of the primary vortex core appears very similar to the image of the embedded cross-flow shock in the simulated-SRV image of Figure 5.13a. The peak in the illumination level visible in the spanwise distribution of Figure 5.24b also looks very similar to the peak observed in the spanwise gradient of the integrated-density seen in Figure 5.13b. These similarities suggest that the sharp lines observed in Figure 5.24a do indeed correspond with the presence of an embedded cross-flow shock wave on the upper surface of the wing.

5.3.4 Conclusions

The SRV system analysis study illustrates that due to the presence of the secondary vortex below the primary vortex it is not possible to determine the exact location of the primary vortex core directly from the SRV images. The similarities between the simulated-SRV imaging of embedded cross-flow shock waves present in the numerical flow solutions with lines present in the actual SRV image suggest that these lines also represent embedded cross-flow shock waves present on the upper surface of the wing. It is interesting to note that Schlieren images obtained in experiments with vortex breakdown present above the wing (see Section 6.3) strongly resemble the "vortex breakdown" shown in the simulated-SRV image of the numerical solution in Figure 5.13a.
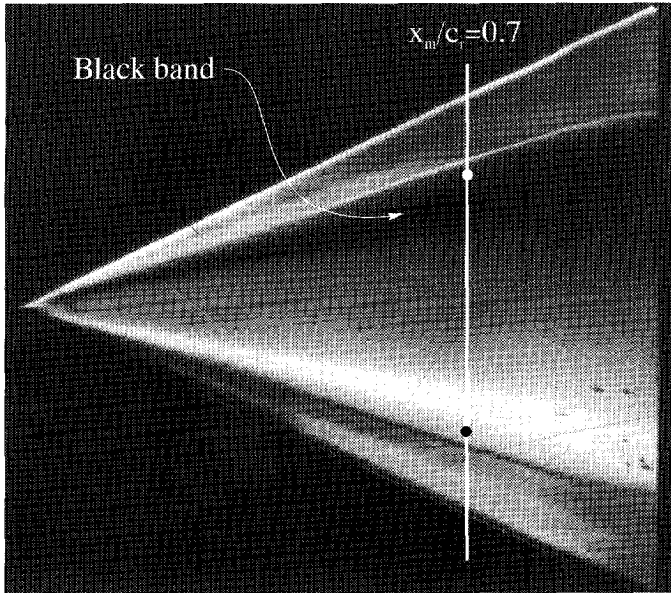
(a) Average SRV image (exposure time $4\ msec$) with the Schlieren knife edge aligned parallel with the root chord
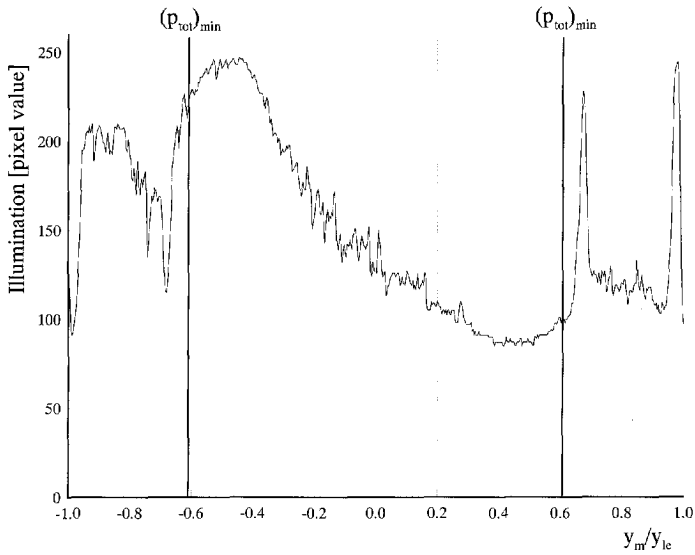
(b) pixel value or illumination distribution at $(x_m/c_r) = 0.7$

Figure 5.24: $M_\infty = 0.8$, $\alpha = 15°$

6

Discussion

Various observations regarding the flow field about the sharp leading edge delta wing investigated in the current study are discussed in this chapter. First the organized vortex structure and surface flow geometry of $M_\infty - \alpha$ combinations not exhibiting vortex breakdown above the wing are examined. Next, characteristics of the complex flow field associated with the $M_\infty - \alpha$ combinations exhibiting vortex breakdown above the wing are presented. In Section 6.4, the average surface pressure distribution is examined for the various $M_\infty - \alpha$ combinations of the test matrix in order to evaluate the importance of large scale flow variations, such as vortex breakdown, on the wing performance. Finally, the development with increasing streamwise station of the axial velocity distribution and in-plane vorticity vectors are examined in order to evaluate the vorticity dynamics theory of vortex breakdown in Section 6.5.

6.1 Geometry of the Lee-side Vortex System

According to the diagram developed by Miller and Wood [1984] (see Figure 6.1), all $M_\infty - \alpha$ combinations of the current study can be expected to exhibit the "classical vortex" topology sufficiently upstream of the trailing edge. Table 6.1 lists the corresponding values of M_N and α_N for the various $M_\infty - \alpha$ combinations of the current investigation. All cases considered in this study do, indeed, exhibit primary, secondary and tertiary vortices over the leading 50% of the wing. The Miller and Wood diagram is developed exclusively for cross-flow conditions, however, where trailing edge effects and vortex breakdown are not present (see Section 1.1). The presence of the trailing edge and its associated pressure rise are found to have a significant influence on the flow field in the current study.

The status of the leading edge vortex system (i.e. with or without vortex breakdown occurring above the wing) for the various $M_\infty - \alpha$ combinations is shown in Table 6.2. At 10° and 15° angle of attack, no vortex breakdown (NB) is observed above the wing for any of the free stream Mach numbers examined. Only symmetric vortex breakdown (SymB) is
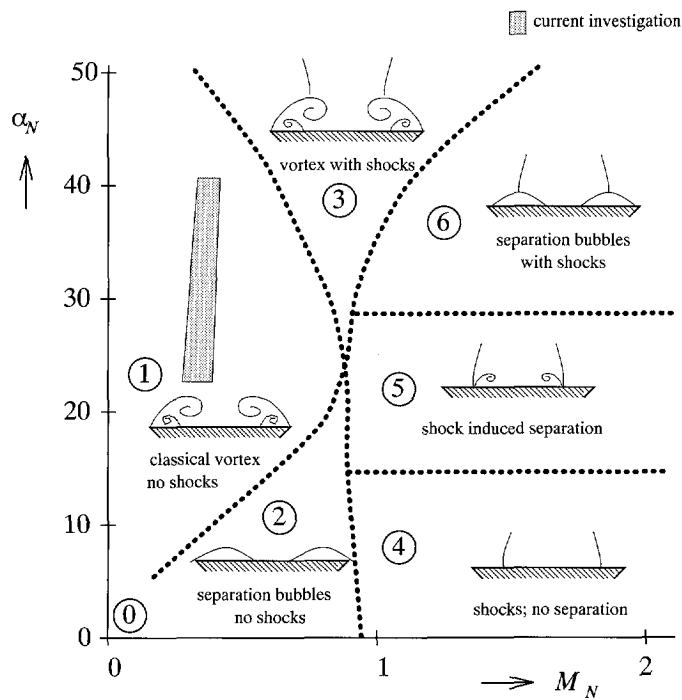
Figure 6.1: Classification of leeward flow patterns over thin delta wings. [Miller and Wood 1984].

α	α_N	M_N		
		$M_\infty = 0.6$	$M_\infty = 0.7$	$M_\infty = 0.8$
10	22.6	0.27	0.32	0.36
15	32.4	0.29	0.33	0.39
18	37.6	0.30	0.36	0.41
20	40.7	0.33	0.39	0.44

Table 6.1: Corresponding values of M_N and α_N for $M_\infty - \alpha$ configurations of the current investigation.

M_∞	Angle of Attack			
	10°	15°	18°	20°
0.6	NB	NB	NB	SymB
0.7	NB	NB, TS	AsymB, TS	SymB, TS
0.8	NB, TS	NB, TS	AsymB, TS	SymB, TS

(NB: No vortex breakdown; AsymB: Asymmetric vortex breakdown; SymB: Symmetric vortex breakdown; TS: terminating shock wave system observed)

Table 6.2: The state of the leading edge vortex system for each of the $M_\infty - \alpha$ configurations considered.

observed for the case of $M_\infty = 0.6$, while both symmetric and asymmetric breakdown are observed for the free stream Mach numbers of 0.7 and 0.8 at different angles of attack. The $M_\infty - \alpha$ combinations which exhibit a terminating shock wave system (TS), a trailing edge effect unique to the high subsonic flow regime, are also indicated in Table 6.2. For the case of $M_\infty = 0.6$, no terminating shock waves appear above the wing at any of the angles of attack investigated, while at $M_\infty = 0.7$ and $M_\infty = 0.8$, these shock waves first appear at 15° and 10° angle of attack, respectively.

Geometric characteristics of the flow cases not exhibiting vortex breakdown above the wing are discussed in the current section. The geometry and nature of the surface flow separation and reattachment lines as well as the geometry of the vortices themselves are considered. In this discussion only the primary and secondary vortex systems are considered. Although a tertiary vortex system is also present, its smaller size and circulation limit its influence on the overall flow field. $M_\infty - \alpha$ combinations which do exhibit vortex breakdown above the wing are discussed in Section 6.3.

6.1.1 Primary Vortices

Defining the geometry and trajectory of the primary vortex is important due to the large contribution of the primary vortex to vortex lift and the influence which it can have on the pressure distribution over control surfaces in its vicinity. Also, obstructions such as control surfaces located in the path of the primary vortex can cause premature breakdown of the vortex system and lead to large scale flow fluctuations and loss of lift [Lambourne and Bryer 1961].

Surface Flow Topology: The primary vortex separation occurs at the sharp leading edge in all $M_\infty - \alpha$ combinations of the current investigation. An inboard displacement of the primary reattachment line is observed, however, with increasing angle of attack. While it is difficult to locate this line precisely on the oil flow images, the primary reattachment appears
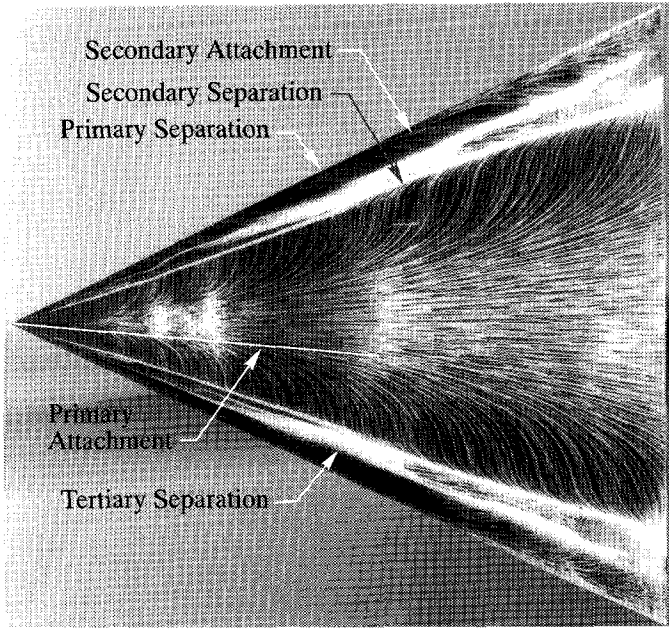
Figure 6.2: Oil surface flow visualization, $\alpha = 15°$, $M_\infty = 0.6$.

to move inboard from approximately $(y_m/y_{le}) = 0.35$ when $\alpha = 10°$ to $(y_m/y_{le}) = 0.10$ when $\alpha = 20°$ for all Mach numbers considered. A characteristic oil surface flow visualization image is shown in Figure 6.2 with the approximate location of primary reattachment indicated. The primary reattachment line is defined in this study as the ray extending from the apex along which the oil on the inboard side moves downstream towards the trailing edge while on its outboard side the oil traces curve outboard towards the leading edge and the secondary separation line. While the primary reattachment line is not necessarily truly conical, particularly in the vicinity of the trailing edge and beyond vortex breakdown, it is approximately conical over the first 50% of the model where the ray is defined.

An inboard movement of the local spanwise pressure maximum with increasing angle of attack is observed in the surface pressure measurements. Such a local spanwise pressure maximum can be expected at the location of primary reattachment (see Figure 1.2). In Figure 6.3a a local spanwise maximum in the surface pressure distribution is observed for the case of $M_\infty = 0.6$ and 15° angle of attack. This local maximum moves inboard to coincide with the root chord at 20° angle of attack (see Figure 6.3b). It is not possible to define the exact location of the primary reattachment from the surface pressure measurements due to a combination of boundary layer dissipation effects and insufficient pressure tap distribution
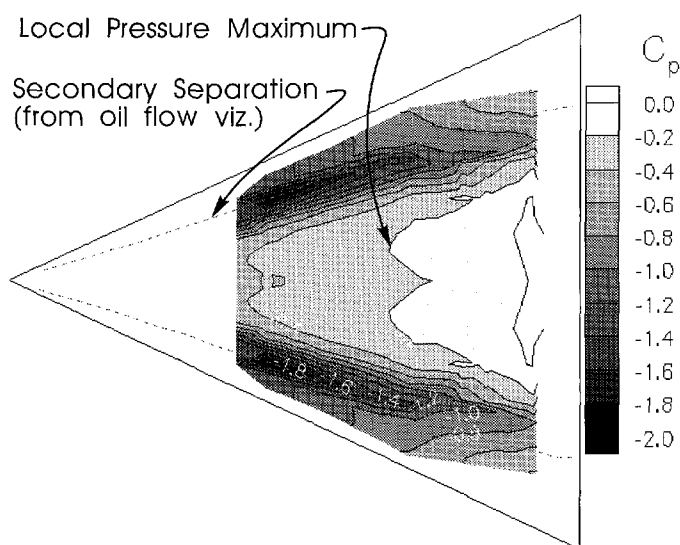
(a) $\alpha = 15°$
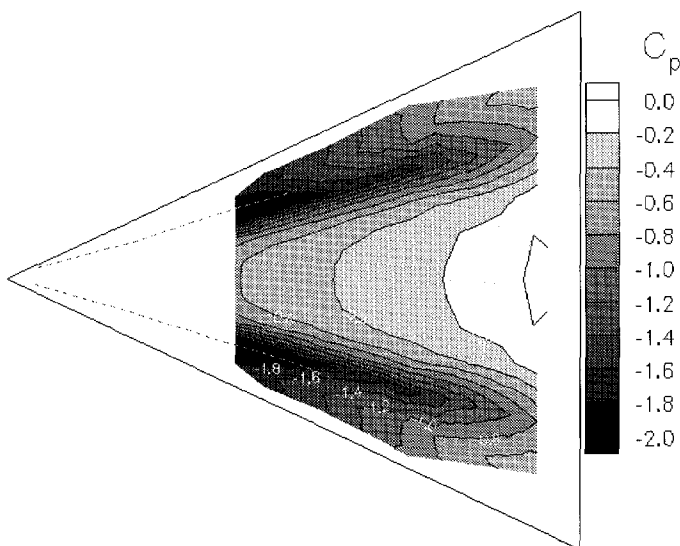
(b) $\alpha = 20°$

Figure 6.3: Surface pressure distributions at $M_\infty = 0.6$ and two angles of attack.

density. The inboard movement of the pressure maximum with angle of attack is consistent, however, with the inboard movement of the primary reattachment line with increasing angle of attack which is observed in the oil surface flow visualizations.

Vortex Geometry: In this investigation the location of the center of the primary vortex core in each of the five-hole probe measurement planes is defined as the location of the minimum total pressure (see Section 4.5.2). The total pressure distribution in a spanwise plane above the wing and a spanwise plane behind the wing at $10°$ angle of attack and two free stream Mach numbers are shown in Figures 6.4 and 6.5, respectively.   Above the wing the total pressure loss in the vortex core and shear layer are noted to be higher in the case of $M_\infty = 0.8$ than for $M_\infty = 0.6$. The total pressure loss associated with the secondary vortex is also visible outboard of the primary vortex in the cross-sectional pressure distribution above the wing . The total pressure loss outboard of the primary vortex behind the wing is attributed to the trailing edge vortex which has been shown by Hummel [1979] to "absorb" the rapidly decaying secondary vortex beyond the trailing edge. The secondary vortex above the wing and the trailing edge vortex behind the wing are discussed further in Sections 6.1.2 and 6.1.4, respectively.

   The primary vortex core location for each of the 5-hole measurement planes of the current investigation are presented in Table 6.3. The coordinate systems used in presenting the

Above Wing

M_∞	$\left(\frac{x_m}{c_r}\right)$	$\left(\frac{y_m}{y_{le}}\right)$ $\alpha=10°$	$\left(\frac{z_m}{y_{le}}\right)$	$\left(\frac{y_m}{y_{le}}\right)$ $\alpha=15°$	$\left(\frac{z_m}{y_{le}}\right)$
0.6	0.5	0.72	0.16	0.66	0.21
	0.7	0.70	0.16	0.66	0.19
0.8	0.5	0.66	0.16	0.63	0.19
	0.7	0.68	0.16	0.61	0.18

Behind Wing

M_∞	$\left(\frac{x_t}{c_r}\right)$	$\left(\frac{2y_t}{b}\right)$ $\alpha=10°$	$\left(\frac{2z_t}{b}\right)$	$\left(\frac{2y_t}{b}\right)$ $\alpha=15°$	$\left(\frac{2z_t}{b}\right)$
0.6	1.4	0.82	0.22	0.72	0.29
	1.5	0.82	0.22	0.72	0.29
0.8	1.4	0.79	0.14	0.72	0.23
	1.5	0.79	0.18	0.72	0.26

Table 6.3: Primary vortex core location determined via five-hole probe measurements.
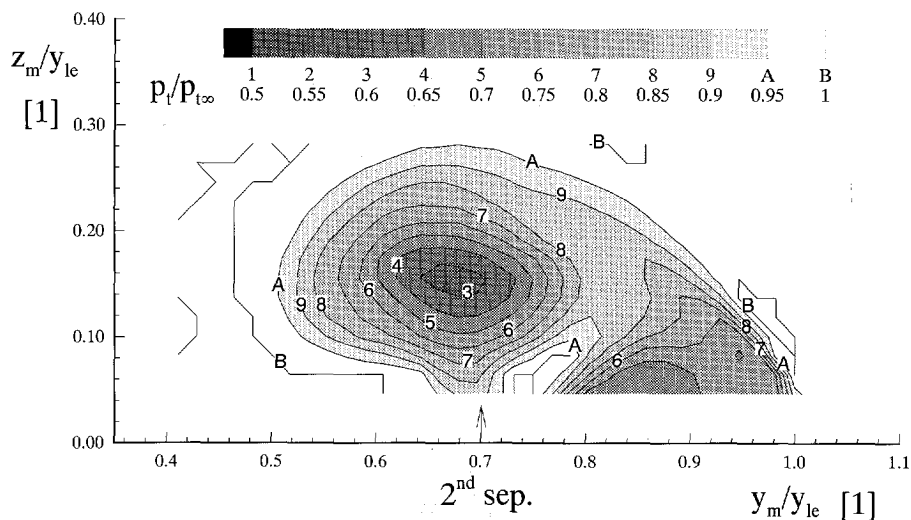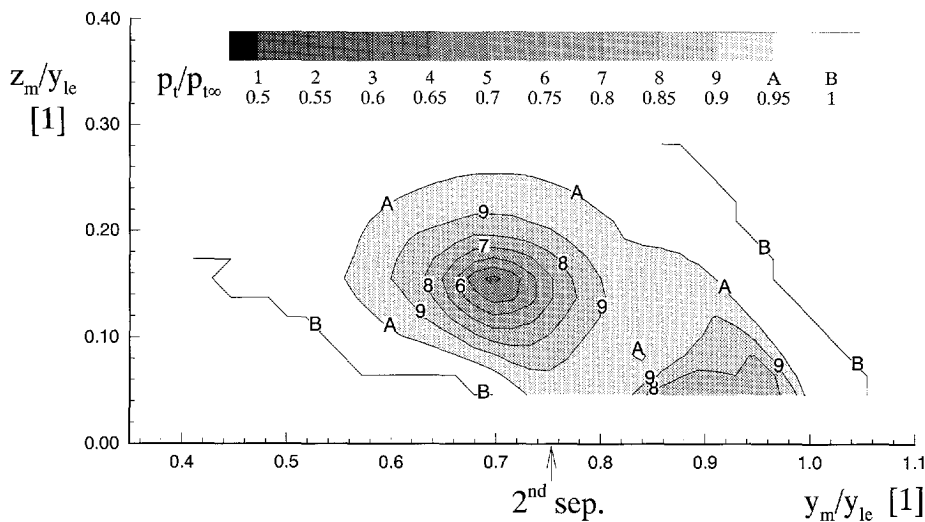
(a) $M_\infty = 0.6$

(b) $M_\infty = 0.8$

Figure 6.4: Total pressure distributions above the wing when $(x_m/c_r) = 0.7$ and $\alpha = 10°$.
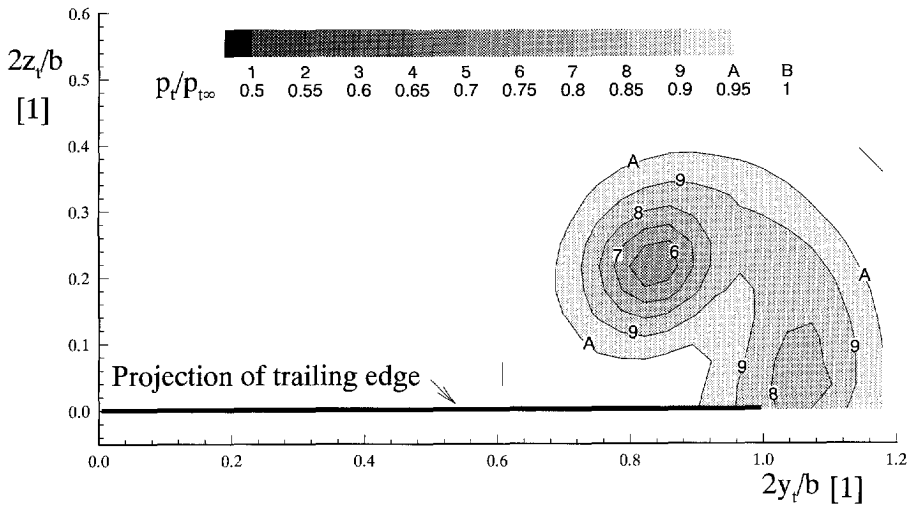
(a) $M_\infty = 0.6$
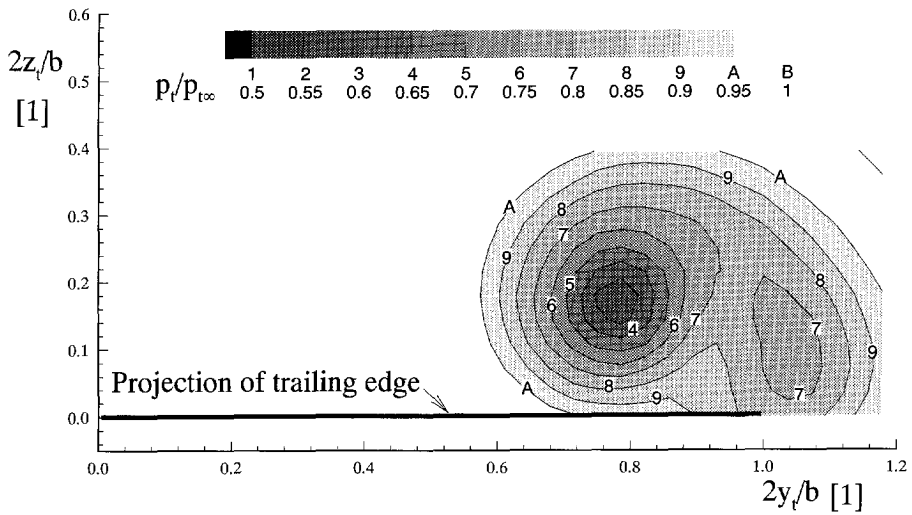
(b) $M_\infty = 0.8$

Figure 6.5: Total pressure distributions behind the wing when $(x_t/c_r) = 0.5$ and $\alpha = 10°$.
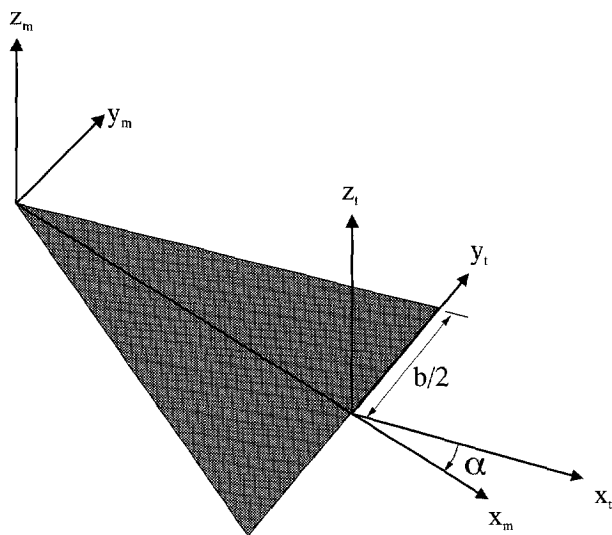
Figure 6.6: Illustration of body fixed Cartesian coordinate system m and tunnel fixed coordinate system t.

results above and behind the wing are shown in Figure 6.6. The coordinate system m used to present the results above the wing is fixed on the model. The primary vortex core location is presented in terms of (y_m/y_{le}) and (z_m/y_{le}) (i.e. the conical coordinates). The wake coordinate system t is consistent with the wind tunnel coordinate system, but its origin is translated to the root chord line intersection with the trailing edge of the model. The primary vortex core location in the wake of the wing is presented in terms of $(2y_t/b)$ and $(2z_t/b)$ or in Cartesian coordinates (b is the span of the delta wing).

The primary vortex core is noted to move inboard with both increasing angle of attack and Mach number. The vortex core is observed to move upward with increasing angle of attack relative to the model surface or wind tunnel centerline for the measurements above and behind the wing, respectively. The effect of Mach number on the vertical position is negligible within the resolution of the measurement grid. At each $M_\infty - \alpha$ combination the primary vortex core is noted to maintain a nearly constant location between the two measurement planes above the wing in conical coordinates and between the two measurement planes behind the wing in Cartesian coordinates. The uncertainty of the (y_m/y_{le}) and (z_m/y_{le}) locations is ± 0.01, or one percent of the local semi-span, as a result of the grid spacing. The location of the vortex core (i.e. $(p_{tot})_{min}$) behind the wing in terms of $(2y_t/b)$ and $(2z_t/b)$ is accurate within the range of ± 0.02 or two percent of the trailing edge half-span. The conical and quasi-two-dimensional geometry of the vortex structure above and behind the wing, respec-
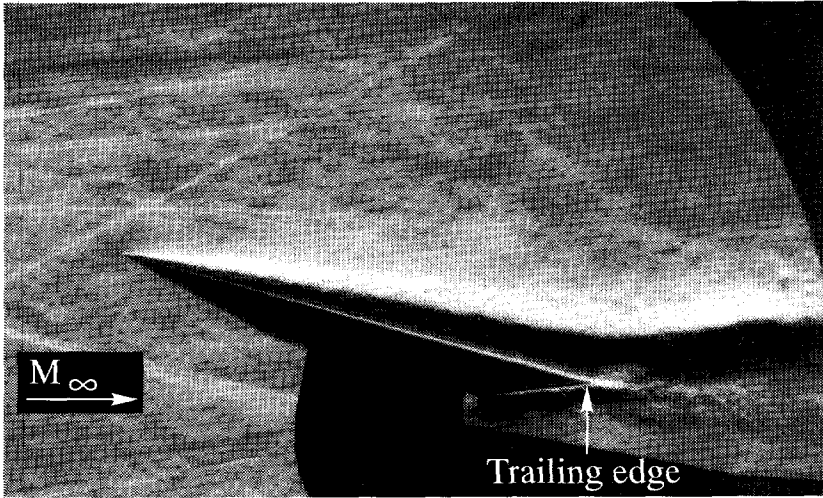
Figure 6.7: Side-view transmission Schlieren flow visualization image, Schlieren knife edge parallel with free stream, $M_\infty = 0.6$, $\alpha = 15°$.

tively, is also observed qualitatively in the side-view transmission flow visualization image of Figure 6.7. The vortex system appears to follow a ray extending from the apex of the wing up until the trailing edge where it turns in the direction of the free stream.

The inboard movement of the primary vortex core with increasing Mach number and angle of attack is also manifest in the surface pressure measurements. The spanwise location of minimum C_p when $(x_m/c_r) = 0.7$ is shown in Figure 6.8 for various $M_\infty - \alpha$ combinations. The $(C_p)_{min}$ location is determined via a cubic spline of the C_p values for each $M_\infty - \alpha$ combination (see Figure 6.9). The maximum error in this value, defined by the spacing of the pressure ports in this region, is $\pm 3\%$ of the local semi-span. The minimum pressure location is observed to move inboard with increasing angle of attack. The highest free stream Mach number also exhibits the most inboard location at a given angle of attack. The location of minimum C_p can be expected to correspond approximately with the spanwise location of the primary vortex core. The exact location of $(C_p)_{min}$ may be displaced slightly outboard, however, as a result of the presence of the secondary vortex. The spanwise location of the primary vortex core, again taken from the five hole probe measurements above the wing, is also indicated for several $M_\infty - \alpha$ combinations in Figure 6.8. The uncertainty of this position, defined by the measurement grid spacing, is $\pm 1\%$ of the local semi-span. The location of the minimum total pressure is noted to coincide with the location of $(C_p)_{min}$ within the grid resolution of the two measurement techniques.
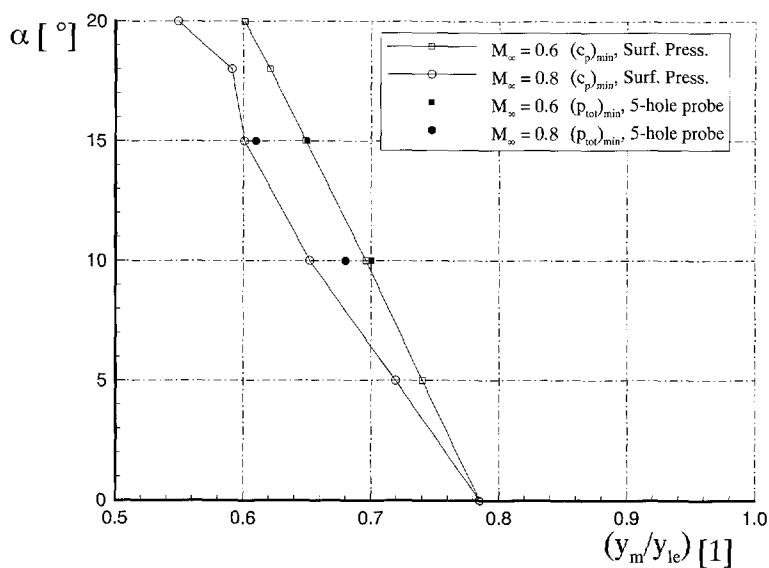
Figure 6.8: Spanwise location minimum C_p from surface pressure measurements and minimum p_{tot} from five-hole probe measurements, $(x_m/c_r) = 0.70$.
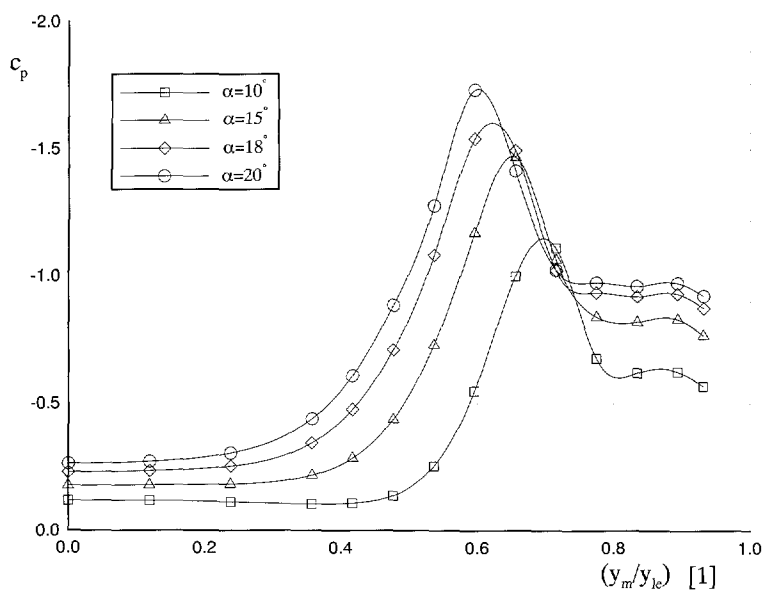
Figure 6.9: Spanwise distribution of C_p, $(x_m/c_r) = 0.70$ and $M_\infty = 0.6$.

6.1.2   Secondary Vortices

The secondary vortex is an important feature of the vortical flow field due to its contribution
to the vortex lift component as well as its influence on the location of the primary vortex.
Increasing the size of the secondary vortex will displace the primary vortex core upwards
and inwards.

Surface Flow Topology: The secondary separation line is sharply defined in the oil flow vi-
sualization images (see Figure 6.10a). Three different types of the secondary separation lines
are observed in the current study. The type of secondary separation line observed for each
of the $M_\infty - \alpha$ combinations of the test matrix is shown in Table 6.4. These three different

M_∞	Re_{c_r}	Angle of Attack			
		10°	15°	18°	20°
0.6	$3.2 \cdot 10^6$	A	C	C	B (SymB)
0.7	$3.6 \cdot 10^6$	C	C	B (AsymB)	B (SymB)
0.8	$4.0 \cdot 10^6$	C	B	B (AsymB)	B (SymB)
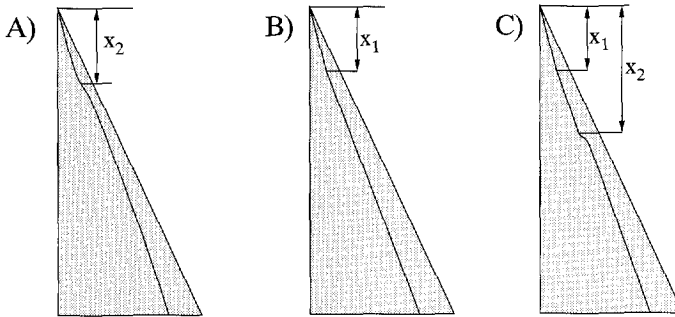
Table 6.4: Secondary separation line classification for the various configurations of the test matrx.

types were originally defined by Bannink et al. [1989]. Type A separation is characterized by
a gradual outboard curvature of the secondary separation line at the streamwise location x_2.
Type B separation, on the other hand, is characterized by a sharp outboard "kink" of the sec-
ondary separation line at the streamwise location x_1. Type C secondary separation exhibits
both a kink of the secondary separation line at x_1 as well as an outboard curvature of the line
further downstream at x_2.

   Type A secondary separation is observed only for the case of $M_\infty = 0.6$, $\alpha = 10°$, in the
current study (see Figure 6.11). The outboard displacement of the secondary separation line
is generally understood as indicative of transition from laminar to turbulent of the boundary
layer moving outboard beneath the primary vortex and its, thereby, increased ability to resist
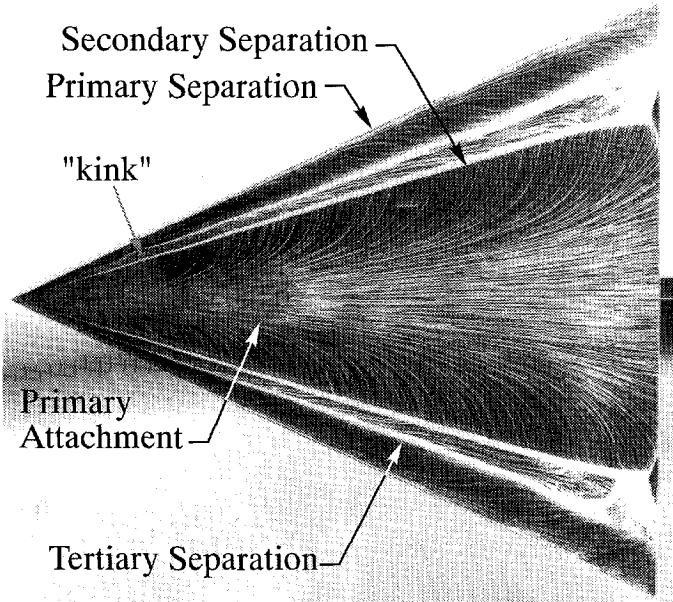
(a) Oil flow surface visualization image (type B secondary separation)
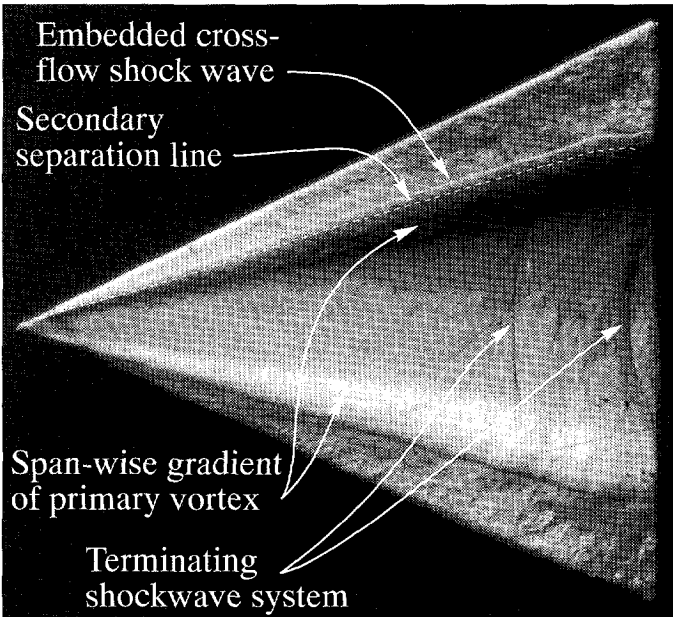
(b) SRV image, Schlieren knife edge parallel with root chord

Figure 6.10: Flow visualizations, $M_\infty = 0.8$, $\alpha = 15°$.
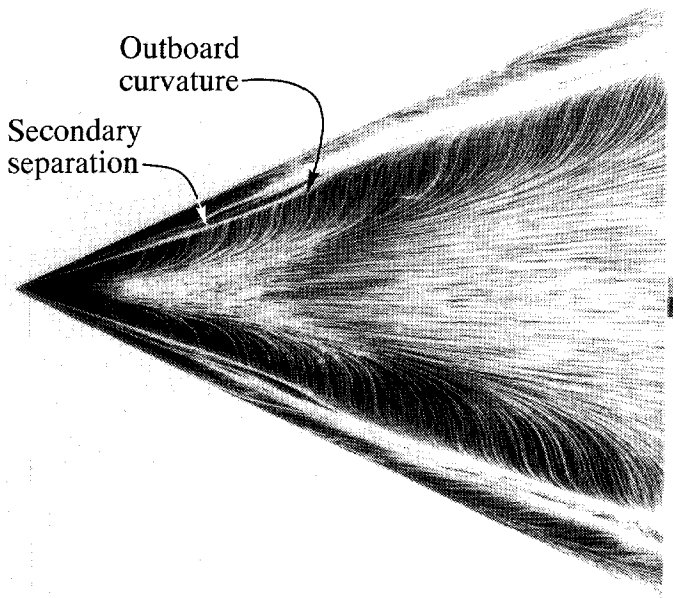
Figure 6.11: Oil flow surface visualization image (type A secondary separation), $M_\infty = 0.6$, $\alpha = 10°$.

the adverse pressure gradient present outboard of the primary vortex core (see Figure 1.2). The position of this outboard curvature and the position of the secondary separation line itself were, indeed, observed by Earnshaw and Lawford [1964] to be Reynolds number dependent in the low speed regime. Visser and Washburn [1994b] noted a trend of decreasing (x_2/c_r) for increasing angle of attack and velocity for a variety of flat plate delta wings in the low speed regime. In this study Visser and Washburn established a tentative relationship between the circulation of the vortex and the location of "transition" or outboard curvature of the secondary separation line. Naarding and Verhaagen [1988] observed that Re_t (Reynolds number at the location of outboard curvature on the wing) was not independent of the wind tunnel velocity but tended to increase with speed.

Type B separation is observed for the highest combinations of angle of attack and Mach number in the current study (see Figure 6.10a). The streamwise location of the characteristic kink, or abrupt outboard movement of the secondary separation line, is observed to correspond approximately with the initial appearance of the embedded cross-flow shock wave in the corresponding SRV images. A possible explanation of the presence of the outboard kink is that the appearance of the cross-flow shock wave has a stabilizing effect on the boundary layer. Such a phenomenon has been noted by Délery [1985] in the case of turbulent boundary
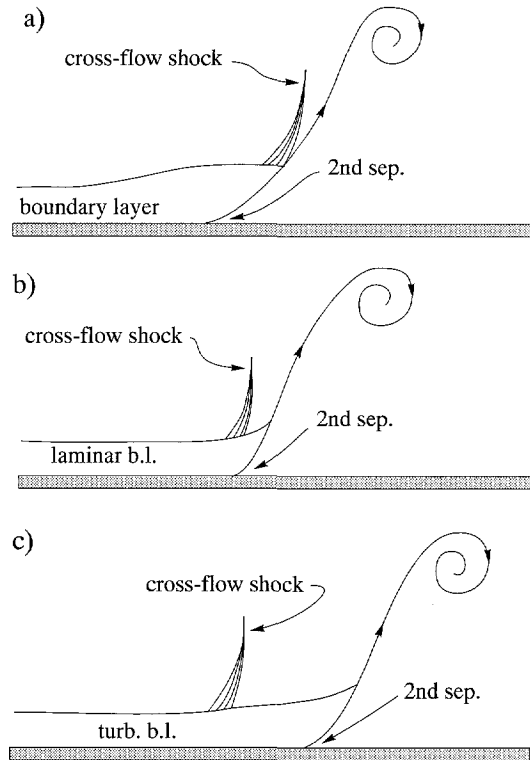
Figure 6.12: Relative embedded cross-flow shock wave and secondary separation location.

layers. Délery explained this effect as being due to the increased mixing caused by the presence of an incident shock wave which increases the momentum of the boundary layer and, thus, inhibits its tendency to separate. The boundary layer on the first half of the delta wing is likely laminar, however, which makes the function of such a mechanism unclear.

Another interesting aspect of the SRV image shown in Figure 6.10b, where the superimposed secondary separation line is taken from the oil flow visualization image of Figure 6.10a, is that the secondary separation line is located inboard, or effectively upstream, of the embedded cross-flow shock wave (see Figure 6.12a). Such a shock-wave/surface-separation geometry is representative of a shock-wave/boundary-layer interaction, where the pressure rise induced by a shock wave will propagate upstream in the subsonic boundary layer and induce flow separation. Separation "upstream" of the cross-flow shock wave does indeed appear only in the highest Mach number cases. The inboard movement of the location of the secondary separation (y_{m_1}/y_{le}) relative to the cross-flow shock wave (y_{m_2}/y_{le}) with increasing angle of attack and Mach number shown in Table 6.5 illustrates the increasing influence of

α :	$M_\infty = 0.6$				$M_\infty = 0.7$				$M_\infty = 0.8$			
	$10°$	$15°$	$18°$	$20°$	$10°$	$15°$	$18°$	$20°$	$10°$	$15°$	$18°$	$20°$
$\left(\frac{x_1}{c_r}\right)\cdot 100$	-	19	19	19	30	19	19	19	30	20	19	20
$\left(\frac{x_2}{c_r}\right)\cdot 100$	31	48	50	-	49	63	-	-	66	-	-	-
$\left(\frac{y_{m_1}}{y_{le}}\right)\cdot 100$	76	69	67	64	70	67	64	64	68	64	62	61
$\left(\frac{y_{m_2}}{y_{le}}\right)\cdot 100$	-	68	68	69	66	70	69	70	68	69	68	70

$\left(\frac{x_1}{c_r}\right)$: chordwise location of the S2-line kink (oil flow visualizations)

$\left(\frac{x_2}{c_r}\right)$: chordwise location of the S2-line outboard shift (oil flow visualizations)

$\left(\frac{y_{m_1}}{y_{le}}\right)$: spanwise location of the S2-line at $\left(\frac{x_m}{c_r}\right) = 0.45$ (oil flow visualizations)

$\left(\frac{y_{m_2}}{y_{le}}\right)$: spanwise location of the cross-flow shock signature at $\left(\frac{x_m}{c_r}\right) = 0.45$ (SRV)

Table 6.5: Measured locations of characteristic secondary separation features.

the embedded cross-flow shock wave on the secondary separation line. Erickson [1991] considered a high angle of incidence of the oil flow traces intersecting the separation line to be indicative of shock-induced separation. The high angle of interception of the oil flow lines approaching the secondary separation line in Figure 6.10a, an $M_\infty - \alpha$ combination exhibiting embedded cross-flow shock waves, as compared to those approaching the separation line in Figure 6.11, an $M_\infty - \alpha$ combination not exhibiting an embedded cross-flow shock wave, supports Erickson's interpretation.

Type C separation is a hybrid of Type A and Type B secondary separation modes. An outboard kink is observed to coincide approximately with the appearance of the embedded cross-flow shock wave in a manner similar to Type B separation and an outboard curvature is observed downstream of this point in a manner similar to Type A separation (see Figure 6.13a). The chord-wise location of the outboard curvature (x_2/c_r) is seen in Table 6.5 to increase with increasing angle of attack and Mach number. This is in contrast with the trend of decreasing (x_2/c_r) for increasing angle of attack and velocity observed in the low speed regime by Visser and Washburn [1994b] mentioned above. The influence of the boundary layer state (i.e. laminar, turbulent, transitional) on the outboard curvature location (x_2/c_r) is not investigated as the state of the boundary layer on the surface of the delta wing is not determined within the scope of the current investigation.

Upstream of the outboard curvature of the separation line at x_2, the cross-flow shock wave is located coincidentally or slightly outboard of the secondary separation line (see Figure 6.12b). Downstream of this point the cross-flow shock is located inboard of the separation line (see Figure 6.12c). The outboard curvature is, again, attributed to transition of the
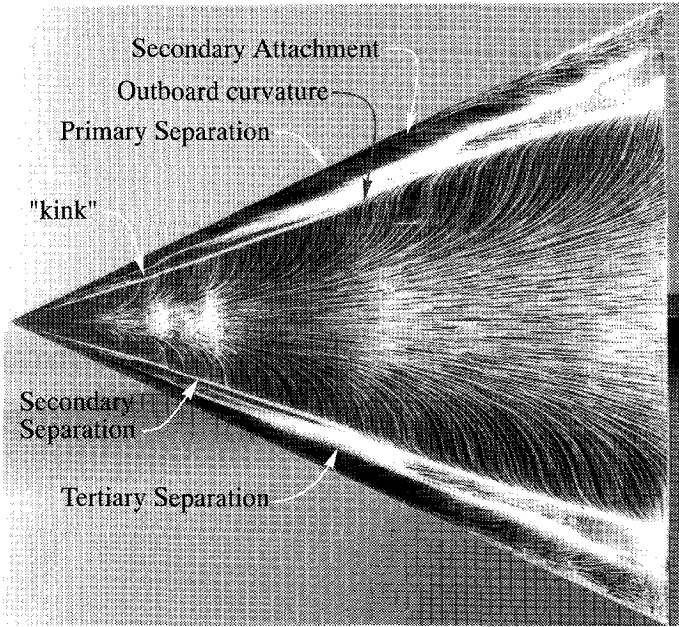
(a) Oil flow surface visualization (type C secondary separation)
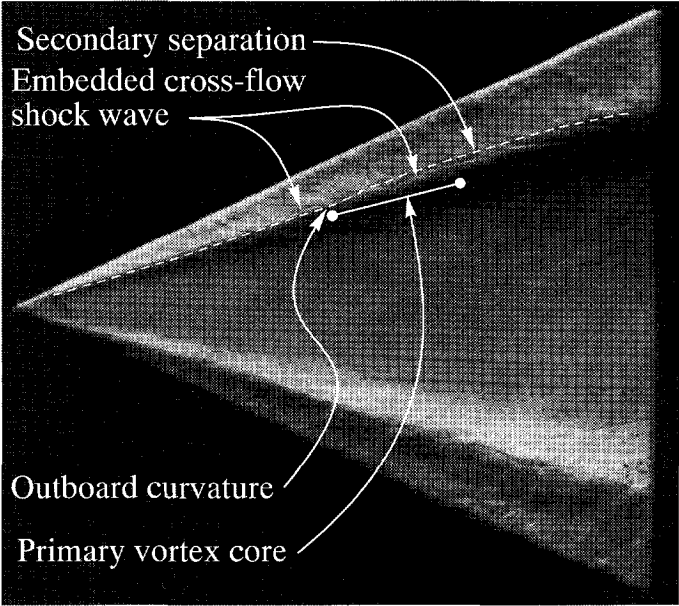
(b) SRV image, Schlieren knife edge parallel with root chord

Figure 6.13: Flow visualizations, $M_\infty = 0.6$, $\alpha = 15°$.

boundary layer from laminar to turbulent moving outboard beneath the primary vortex. It appears that transition of the boundary layer provides the boundary layer sufficient momentum to pass through the cross-flow shock wave and separate only outboard of this shock wave or effectively downstream of the cross-flow shock wave.

In is interesting to note that the secondary separation line classification progresses from Type A to Type C and finally to Type B with increasing Mach number and/or angle of attack in Table 6.4. This trend suggests an increasing influence of the embedded cross-flow shock wave on the separation process with increasing Mach number and angle of attack. The observed geometric relationship between the secondary separation line and the embedded cross-flow shock wave, when present, for the three classifications is illustrated in Figure 6.14. No embedded cross-flow shock wave is observed for the only case of Type A secondary separation in this investigation ($M_\infty = 0.6$, $\alpha = 10°$) . For this case the upper surface boundary layer approaching the secondary separation line upstream of x_2 can be assumed to be laminar and turbulent downstream of x_2.

An embedded cross-flow shock wave is observed in the SRV images for all $M_\infty - \alpha$ combinations exhibiting Type C separation (see Table 6.5). This shock wave, with its origin at approximately x_1, is outboard (i.e. downstream) of the secondary separation line upstream of x_2 and inboard (i.e. upstream) of the secondary separation line downstream of x_2. While the state of the upper surface boundary layer (i.e. laminar, transitional or turbulent) is not determined in this investigation, it is hypothesized that the transition of the boundary layer from laminar to turbulent provides it sufficient momentum to navigate the pressure rise associated with the embedded cross-flow shock wave downstream of x_2.

The state of the boundary layer downstream of x_1 in the case of Type B separation, on the other hand, is more difficult to hypothesize. The secondary separation line remains inboard or upstream of the embedded cross-flow shock for the entire length of the wing downstream of the approximate origin of this shock wave at x_1. It is unlikely that the boundary layer remains laminar over the entire length of the wing considering the relatively high Reynolds numbers for which Type B separation is observed. The strength of the embedded cross-flow shock wave is more likely so high at the combinations of high Mach number and angle of attack at which Type B separation is observed that the status of the boundary layer is no longer an significant factor in the separation process. Again, the mechanism whereby the appearance of the embedded cross-flow shock wave at x_1 causes an outboard displacement of the separation line S_2 remains unclear.

Vortex Geometry: The increasing influence of the secondary vortex on the flow field with increasing angle of attack and Mach number is apparent in both the surface pressure measure-

outboard
curvature

S_2

T

L

A_1

C_L

X_2

L: laminar boundary layer
T: turbulent boundary layer

(a) Type A

embedded cross-
flow shock wave

S_2

kink

L

A_1

C_L

X_1

L: laminar boundary layer

(b) Type B

embedded cross-
flow shock wave

S_2

outboard
curvature

kink

T

L

A_1

C_L

X_1

X_2

L: laminar boundary layer
T: turbulent boundary layer

(c) Type C
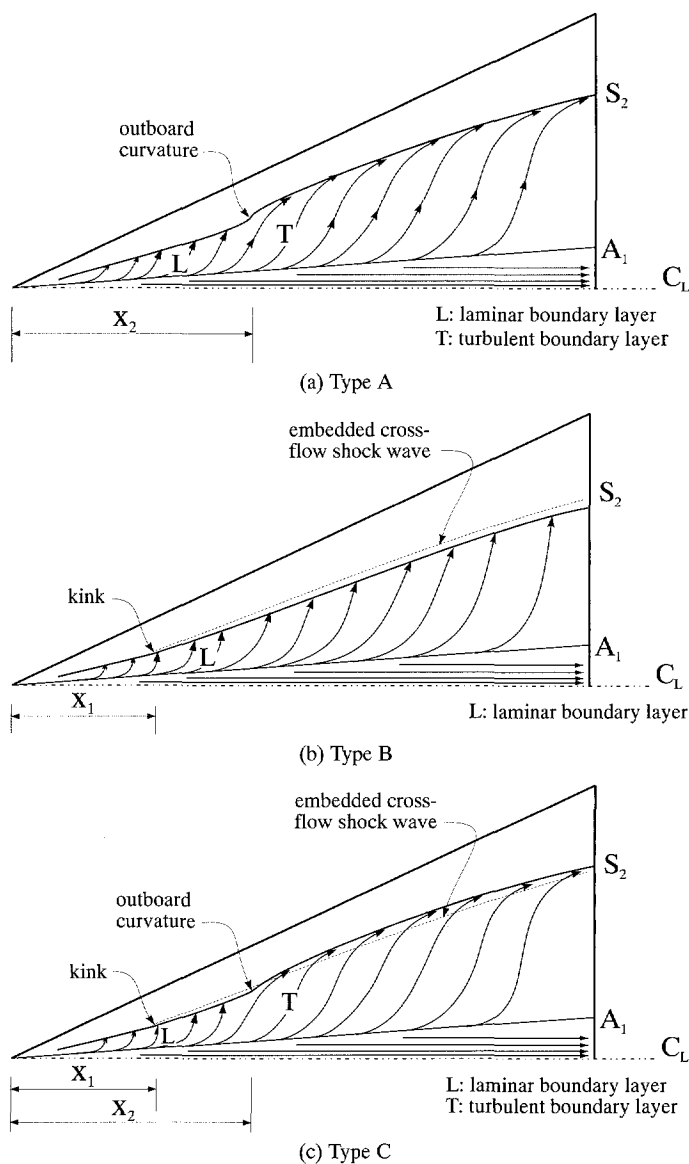
Figure 6.14: Characteristic secondary separation lines (taken from oil surface flow visualizations) and embedded cross-flow shock wave geometries (taken from SRV images) for the three secondary separation line classifications A, B and C.

ments and the flow field measurements. The surface pressure distributions for several com-
binations of Mach number and angle of attack at $(x_m/c_r) = 0.7$ are shown in Figure 6.15.
While the minimum measured C_p value when $\alpha = 15°$ (solid symbols) is nearly the same for
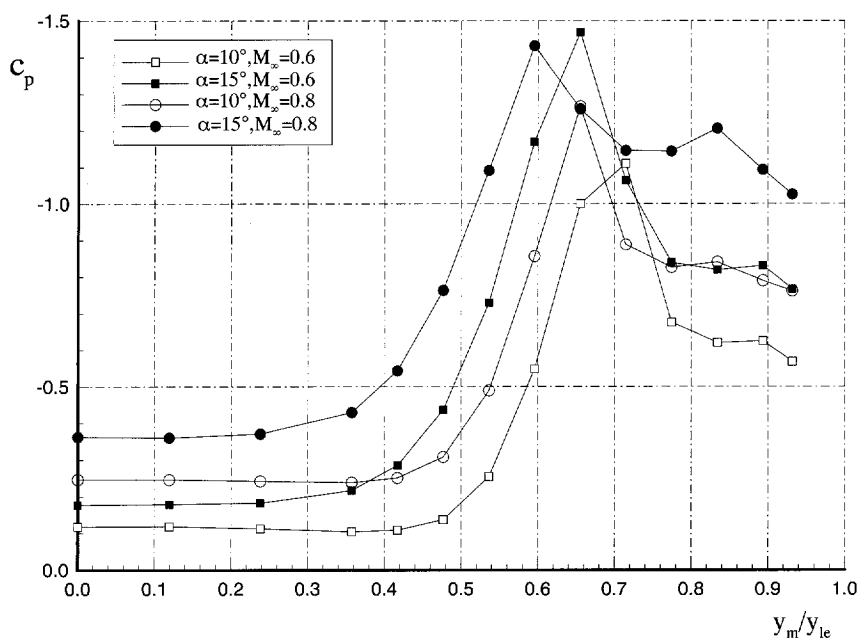
Figure 6.15: Spanwise pressure distribution at $(x_m/c_r) = 0.7$ for various Mach numbers and angles
of attack.

the $M_\infty = 0.6$ and $M_\infty = 0.8$ cases, the pressure rises significantly moving outboard of this
minimum value in the $M_\infty = 0.6$ case while for the $M_\infty = 0.8$ case the value of C_p remains
low. This low C_p value outboard of the $(C_p)_{min}$ in the case of $M_\infty = 0.8$ is attributed to
the influence of the secondary vortex. Similarly, in both Mach number cases, the increase in
pressure (or rise in C_p) outboard of $(C_p)_{min}$ is higher for the case of $\alpha = 10°$ than when
$\alpha = 15°$. This behavior is indicative of the increasing influence of the secondary vortex on
the surface pressure distribution with increasing angle of attack.

The inboard movement of the primary vortex with increasing angle of attack and free
stream Mach number seen in Figure 6.8 is also a result of the increasing influence of the sec-
ondary vortex. The higher total pressure loss associated with the secondary vortex and the
increased extent of the secondary vortex for the case of $M_\infty = 0.8$ as compared with a free
stream Mach number of 0.6 are seen in the total pressure contour plots of Figure 6.4.

6.1.3 Terminating Shock Wave System

Application of the SRV system provides a unique top-view perspective on the terminating shock wave system and its interaction with the leading edge vortex system. As mentioned in Section 1.1.3, previous observations of this shock wave system have been limited to a side-view perspective and were, therefore, unable to define the spanwise distribution of the shock wave system. A typical side-view image of the terminating shock wave system is shown in Figure 6.16 when $M_\infty = 0.8$, $\alpha = 15°$. In the current section the terminating shock wave
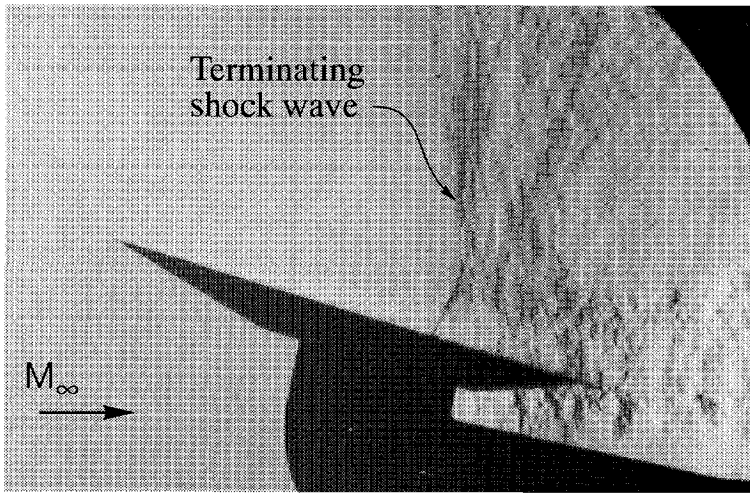
Figure 6.16: Side-view transmission Schlieren image with Schlieren knife edge oriented perpendicular to the free stream, $M_\infty = 0.8$, $\alpha = 15°$.

system existing in the presence of a sustained vortex system is discussed. The terminating shock wave system existing in the presence of vortex breakdown is discussed in Section 6.3.

Table 6.2 shows that the terminating shock wave system exists in the presence of a sustained vortex system when $\alpha = 10°$, $M_\infty = 0.8$ and at $\alpha = 15°$ when $M_\infty = 0.7$ and 0.8. A top-view perspective of this shock wave system is shown in the SRV images of Figure 6.17 for this same $M_\infty - \alpha$ combination. In Figure 6.17a the Schlieren knife edge is oriented perpendicular to the root chord, thus, illuminating the chordwise density gradients integrated over a path nominally perpendicular to the upper surface of the wing. This orientation is effective for illustrating the chordwise gradients of the terminating shock wave system. In Figure 6.17b, on the other hand, the Schlieren knife edge is aligned parallel with the root chord and, thus, illustrates the spanwise density gradient integrated over a path nominally perpendicular to the upper surface of the wing. This Schlieren knife edge orientation is most effective for visualizing the vortices themselves where significant spanwise density gradients
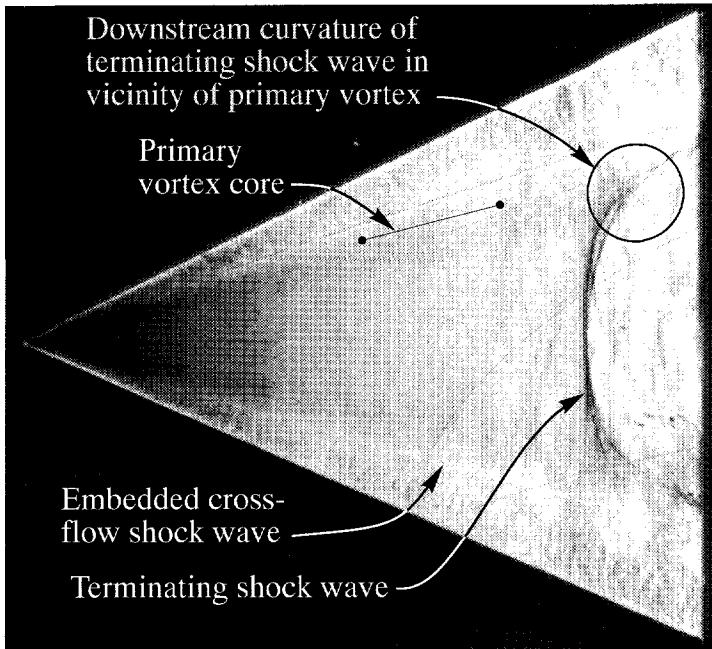
(a) Top-view SRV image, Schlieren knife edge perpendicular to root chord
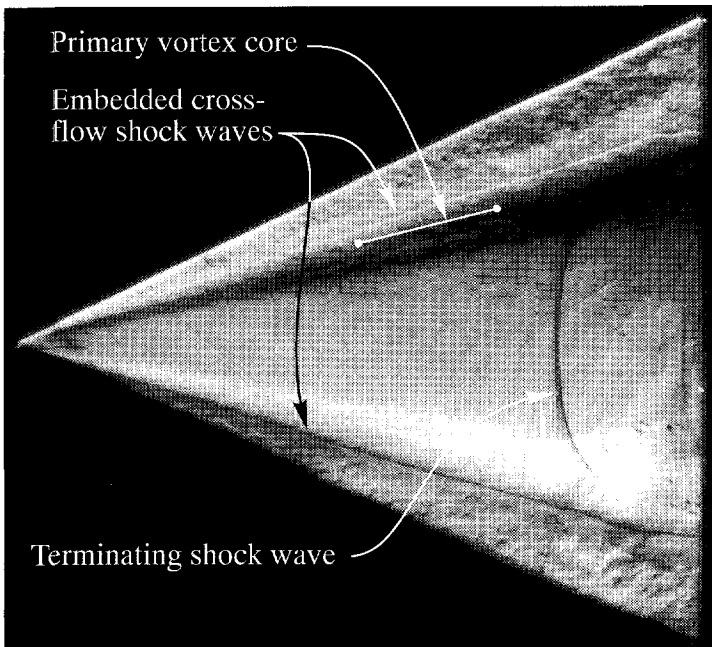
(b) Top-view SRV image, Schlieren knife edge parallel with root chord

Figure 6.17: SRV images, $M_\infty = 0.8$ and $\alpha = 15°$

are present. The primary vortex core location, determined via five-hole probe measurements, is superimposed on the images of Figure 6.17 for reference purposes. The embedded cross-flow shock wave on either side of the wing is located outboard of the primary vortex core and embedded between the primary vortex and the surface of the wing (see SRV system analysis of Chapter 5). The terminating shock wave system is noted to be unsteady with two shocks often visible above the wing (see, for example, Figure 6.10b). Neither the two SRV images of Figure 6.17 nor the side-view transmission image of Figure 6.16 are made at the same moment in time due to the physical unfeasibility of simultaneously producing the images. This makes it difficult to compare the various images directly. Based on the known function of the Schlieren system and other information over the flow field obtained from previous investigations, however, it is possible to draw some tentative conclusions regarding the structure of the shock surface present above the wing. These three images (Figures 6.16, 6.17a and 6.17b) are selected for reference due to the fairly comparable chord-wise location of the terminating shock wave in these images.

The projection of the terminating shock wave onto the wing surface is seen in both Figures 6.17a and 6.17b to intersect the root chord nearly perpendicularly and curve downstream in the vicinity of the primary vortex on either side of the wing. The line which is visible as the image of a shock wave in the side-view transmission image of Figure 6.16, can be associated with the foremost portion of the shock surface extending perpendicularly from the root chord on either side of the wing in Figures 6.17a and 6.17b. This association can be made because the light refraction imaged by a Schlieren system is known to be a function of both the extent of the density gradient along its path as well as the magnitude of the gradient (see Section 5.1). The section of the shock surface extending in the spanwise direction perpendicular to the root chord is oriented nearly parallel with the transmission light bundle and can, therefore, be expected to be more clearly illustrated in the side-view Schlieren image than other regions of the terminating shock surface. The section of the shock surface in the vicinity of the wing centerline is shown in the side-view transmission image to extend from the surface of the wing, to curve upward concave to the apex and extend above the wing nearly perpendicularly with the oncoming flow until its strength decreases to such an extent that it is no longer visible.

The downstream curvature in spanwise direction of the terminating shock wave in the vicinity of the primary vortices is consistently present in all top-view visualizations of the terminating shock wave system. This curvature is more clearly visible, however, in SRV images made with the Schlieren knife edge aligned perpendicular to the root chord where the chordwise integrated-density gradient is visualized (see Figure 6.17a), than in SRV images made with the Schlieren knife edge aligned parallel with the root chord which illustrate the
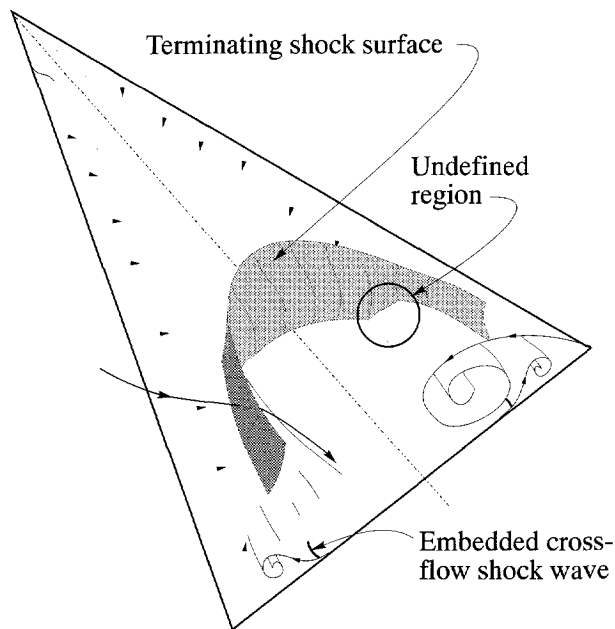
Figure 6.18: Terminating shock surface in presence of a sustained leading edge vortex system.

spanwise gradient of integrated-density (see Figure 6.17b). This difference results from the strong spanwise integrated-density gradients in the primary vortices which conceal the span-wise gradient associated with the terminating shock wave in the latter optical configuration. The fact that the terminating shock wave does not disrupt the organized vortex structure in the vicinity of the trailing edge (see Figure 6.17b), suggests that the terminating shock wave is situated above the primary vortex in this region. The presence of embedded cross-flow shock waves extending to the trailing edge, only feasible in the presence of a well organized vortex structure inducing supersonic cross-flow velocities, also attests to the undisturbed state of the vortex structure up until the trailing edge. A sketch of the possible terminating shock wave structure is shown in Figure 6.18. The geometry of the shock wave as it moves outboard and up onto the top of the vortex structure remains unclear.

It is interesting to note the similarities between the proposed terminating shock wave structure and the conical shock wave structure illustrated in region 3 of the Miller and Wood [1984] diagram for an infinite wing (see Figure 6.1). While the presence of a terminating shock wave is only possible in the case of a finite wing, the downstream curvature of the ter-minating shock wave in the vicinity of the primary vortex suggests that the terminating shock wave has a somewhat conical geometry above the vortices themselves. When $M_\infty = 0.8$ and

$\alpha = 15°$ the associated values of $M_N = 0.39$ and $\alpha_N = 32.4$ place this $M_\infty - \alpha$ combination in the proximity of region 3 in the Miller and Wood diagram. It seems likely that while no shock waves are present above the vortices along the entire length of the wing (i.e. no conical shock waves), the pressure rise associated with the trailing edge is sufficient to provoke such shock waves above the primary vortices in the vicinity of the trailing edge.

6.1.4 Trailing edge Vortices

The trailing edge vortex is an important aspect of the delta wing flow field because it strongly influences the induced drag of the wing. The trailing edge vortex is visible outboard of the primary vortex in the total pressure contour plot of Figure 6.19. The magnitude of the com-
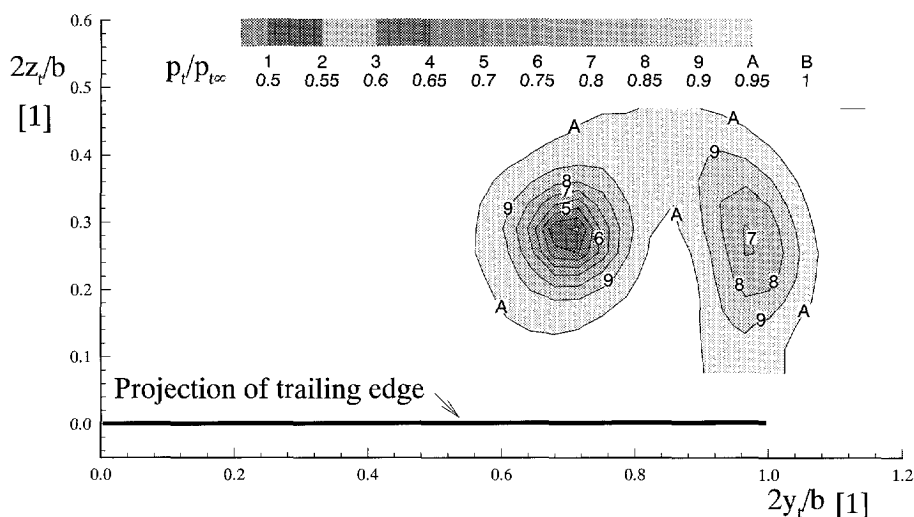
Figure 6.19: Distribution of total pressure in wing wake, $(x_t/c_r) = 0.4$, $M_\infty = 0.6$ and $\alpha = 15°$.

ponent of the vorticity along the x_t axis is positive in the primary vortex and negative for the trailing edge vortex (see Figure 6.20). The vorticity components are calculated from the five-hole probe measurement data via finite-difference calculations (see Section 6.5.2). The velocity components used in the vorticity calculations are made non dimensional by dividing them by the free stream velocity. The resulting vorticity is then multiplied by the root chord to obtain a non dimensional vorticity. The trailing edge vortices were observed by Hummel [1979], in a low speed flow field, to wrap about the primary vortex structure along a helical path as they move downstream. This same trend is visible in the current measurements.
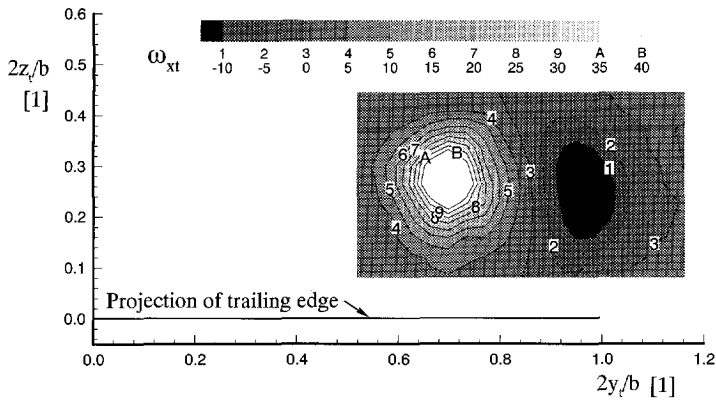
(a) $(x_t/c_r) = 0.4$
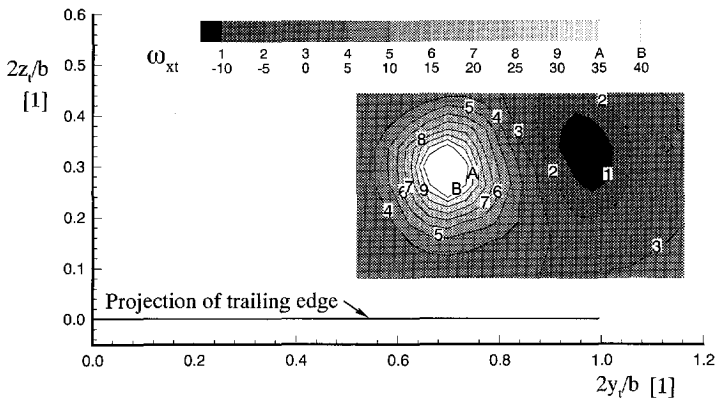
(b) $(x_t/c_r) = 0.5$

Figure 6.20: Distribution of vorticity component ω_{xt} for two different span-wise planes behind the wing at $M_\infty = 0.6$ and $\alpha = 15°$.

The trailing edge vortex is observed to move upward, around the primary vortex structure, with increasing streamwise station between $(x_t/c_r) = 0.4$ and $(x_t/c_r) = 0.5$ for all $M_\infty - \alpha$ combinations investigated (see Figure 6.20).

6.2   Conical Aspects of the Flow Field

The flow over a delta wing in the high subsonic flow regime is not truly conical due to influences such as the pressure rise in the vicinity of the trailing edge and viscous losses in the shear layer and upper surface boundary layer. The embedded cross-flow shock waves discussed in Section 6.1, however, appear nearly conical in geometry. An explanation of their conical appearance can be found by examining the spanwise pressure distribution at several chordwise stations. Comparing the pressure distributions at various chordwise stations illustrates the similarity of the spanwise pressure distribution over the length of the wing (see Figure 6.21). The similarity of the profiles is also seen to increase with increasing Mach number. Comparing the spanwise distribution with increasing chord station for the free stream Mach numbers of 0.6 and 0.8 shown in Figure 6.21, the high Mach number case is noted to have nearly identical spanwise pressure distribution between $(x_m/c_r) = 0.45$ and $(x_m/c_r) = 0.55$. Between $(x_m/c_r) = 0.6$ and $(x_m/c_r) = 0.7$ the discrepancy between the spanwise pressure distributions increases as the pressure rise associated with the presence of the trailing edge becomes apparent.

The C_p distribution along the root chord similarly illustrates a more conical behavior at higher free stream Mach number. The pressure increases continuously along the entire length of the chord when $M_\infty = 0.6$, $\alpha = 15°$ while in the case of $M_\infty = 0.8$, $\alpha = 15°$ the pressure is nearly constant between $(x_m/c_r) = 0.25$ and $(x_m/c_r) = 0.45$ and increases at a constant rate only beyond $(x_m/c_r) = 0.60$ (see Figure 6.22). This increased conicity is likely a result of the supersonic flow region present in the case of $M_\infty = 0.8$, which prevents the trailing edge and its associated pressure rise from influencing the flow in this region.

A more quantitative explanation for the conical geometry of the embedded cross-flow shock waves is the larger magnitude of the pressure gradient in the spanwise direction as compared to the chordwise direction. At $(x_m/c_r) = 0.6$ and $(y_m/y_{le}) = 0.475$ the magnitude of the spanwise gradient $|(\partial C_p/\partial y)|$ is $131.3\ m^{-1}$, while the magnitude of the chordwise gradient $|(\partial C_p/\partial x)|$ is $10.46\ m^{-1}$ when $M_\infty = 0.6$ and $\alpha = 15°$ (see Figure 6.21a). These pressure gradients have been calculated from the surface pressure data via a linear approximation. The spanwise gradient in the vicinity of the primary vortex core where the embedded cross-flow shock waves are observed is, thus, an order of magnitude larger than the corresponding chordwise pressure gradient.
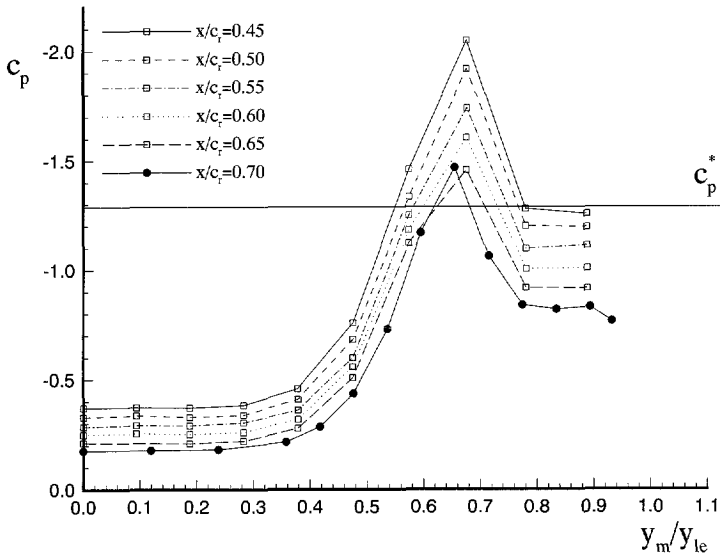
(a) $M_\infty = 0.6$
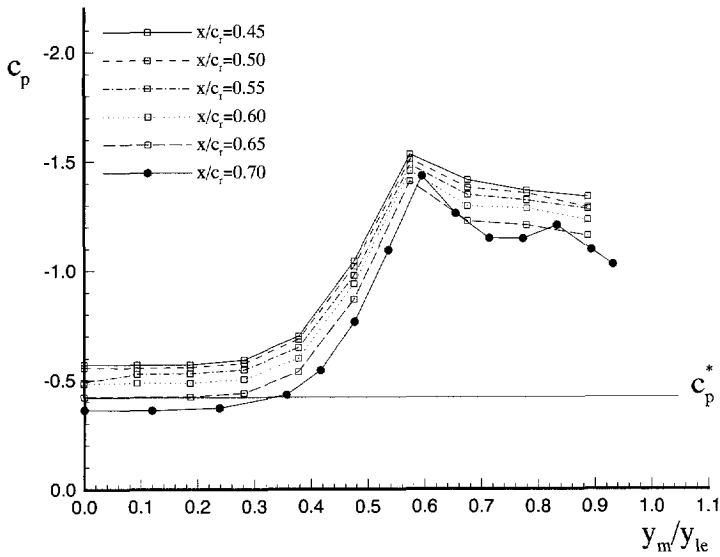
(b) $M_\infty = 0.8$

Figure 6.21: Spanwise pressure distribution at various chord-wise stations, $\alpha = 15°$.
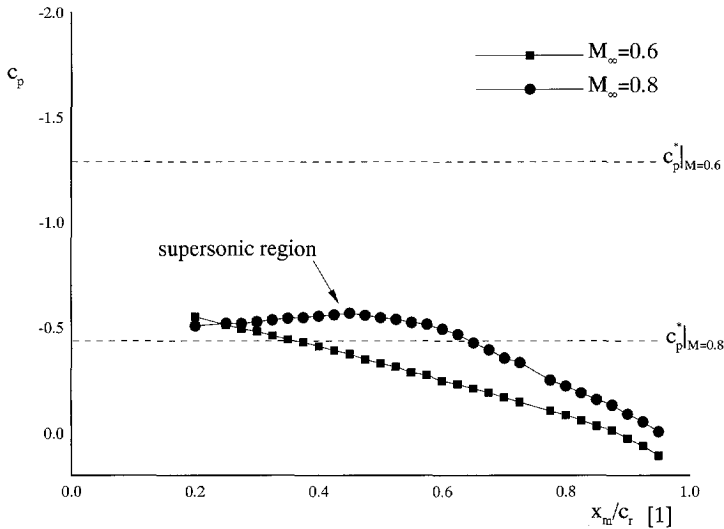
Figure 6.22: Pressure distribution along root chord at $\alpha = 15°$.

6.3   Observations in Vortex Breakdown

Vortex breakdown is defined as the abrupt termination of the organized vortex structure dis-
cussed above. Combinations of $M_\infty - \alpha$ exhibiting vortex breakdown above the wing are
indicated in bold in Table 6.6.   Symmetric vortex breakdown (SymB) above the wing is de-

M_∞	Angle of Attack			
	10°	15°	18°	20°
0.6	NB	NB	NB	**SymB**
0.7	NB	NB, TS	**AsymB, TS**	**SymB, TS**
0.8	NB, TS	NB, TS	**AsymB, TS**	**SymB, TS**

(NB: No vortex breakdown; AsymB: Asymmetric vortex breakdown; SymB: Symmetric vortex break-
down; TS: terminating shock wave system observed)

Table 6.6: The state of the leading edge vortex system for each of the $M_\infty - \alpha$ configurations con-
sidered.

fined as the abrupt termination of the organized vortex structure at the same location on either
side of the root chord. The "same location" is defined as a difference of no more than $\pm 15\%$
of the root chord between the breakdown location on either side of the root chord at a given
moment (exposure time $\approx 20\ nsec$) during the course of one test. The duration of one test,

defined by the period of time required for one rotation of the inner drum of the high speed camera, is 35 $msec$ when the photos are exposed at a rate of 2 kHz. Fluctuations of the vortex breakdown location are observed in the case of symmetric vortex breakdown. The flow field is noted to be more unsteady, however, in the case of asymmetric vortex breakdown. In the case of asymmetric vortex breakdown (AsymB) the breakdown location may be identical on either side of the root chord or differ by as much as 45% of the root chord at a given moment in the course of one experiment (again, $\Delta t < 35 \ msec$). The value of $\pm 15\%$ is selected because it seems to provide a limit between the two classes of flow. Table 6.6 also shows that $M_\infty - \alpha$ combinations exhibiting vortex breakdown exist both with and without a terminating shock wave system (TS) present.

Various visualization techniques are used to investigate vortex breakdown in the current study. The oil flow visualization technique provides an indication of the surface flow pattern associated with the breakdown, but has the disadvantage of being unable to capture the unsteady nature of vortex breakdown. The SRV technique, on the other hand, provides an *instantaneous* plan-view image of the state of the vortical flow field. The transmission flow visualization technique is also capable of capturing the unsteady behavior of vortex breakdown, but the side view perspective it provides does not allow the port and starboard vortex systems to be differentiated.

The presence of shock waves above the surface of the delta wing is difficult to confirm or refute with the oil flow technique due to the dissipating influence of the boundary layer and the unsteady nature of the terminating shock wave system. The SRV technique, on the other hand, provides a unique opportunity to observe both embedded cross-flow shock waves and the terminating shock wave system above the surface of the wing. Transmission visualization images are an important complement to the SRV visualizations in helping to define the distribution of the terminating shock wave system in space.

In the following discussion characteristics of the $M_\infty - \alpha$ combinations exhibiting vortex breakdown above the wing are discussed. The unsteady nature of the phenomenon is considered as well as the interaction of the terminating shock wave system with the vortex breakdown.

6.3.1   Asymmetric Vortex Breakdown

The unsteady nature of the flow field in the case of asymmetric vortex breakdown is illustrated in Figure 6.23. These two images, taken during one rotation of the high-speed camera ($\Delta t < 35 \ msec$), illustrate a large discrepancy in the position of vortex breakdown location on the port side of the wing. A *jump* of the vortex breakdown from one side of the wing to the other, as illustrated in Figures 6.23b and 6.24, is also observed with the video camera during one
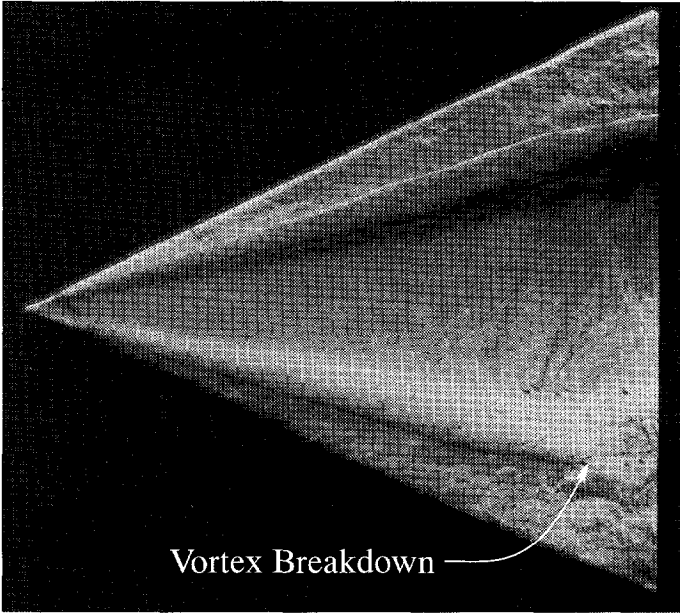
(a) Image 1
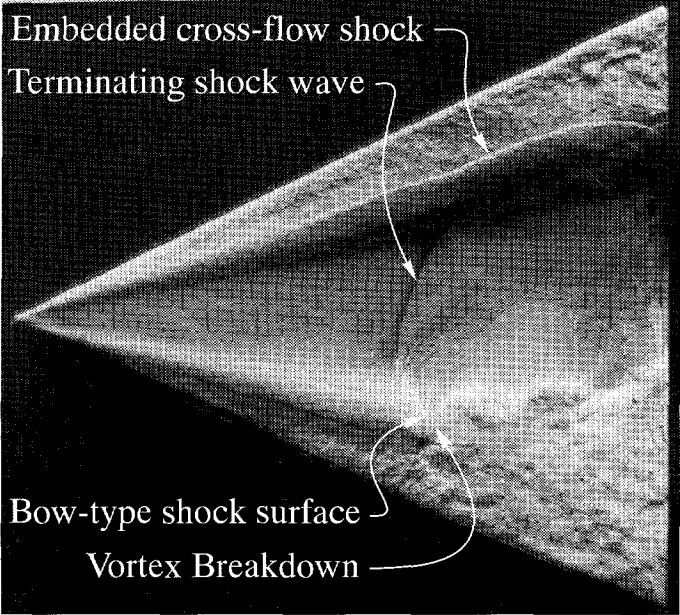
(b) Image 2

Figure 6.23: SRV images, Run 136, Schlieren knife edge parallel with root chord, $M_\infty = 0.8$, $\alpha = 18°$.
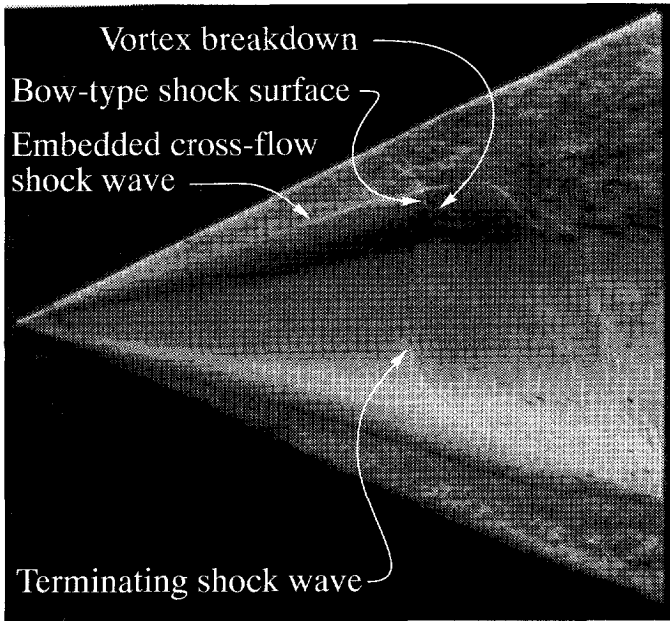
Figure 6.24: SRV image, Run 134, Schlieren knife edge parallel with root chord , $M_\infty = 0.8$, $\alpha = 18°$.

wind tunnel test ($\Delta t < 2min$). This phenomenon is not illustrated here for one particular test, however, because it is has not been recorded by the high speed camera in the course of the present study.

The average location of the breakdown on either side of the wing, the maximum discrepancy between the starboard and port breakdown locations ($\Delta bd = S_{bd} - P_{bd}$) and the difference between the average locations on either side of the wing over the course of an individual run ($\Delta t < 35\ msec$) are presented in Table 6.7 for all relevant $M_\infty - \alpha$ combinations. The term "run" refers to the exposure period of one rotation of the high speed camera. Because the high speed camera must be reloaded between exposure series, each run corresponds with an independent wind tunnel test. The data are taken exclusively from SRV images configured with the Schlieren knife edge aligned parallel with the root chord to ensure consistent determination of the vortex breakdown location. The location of a visible disruption of the organized primary vortex structure is defined as the point of vortex breakdown (see Figure 6.23b). Several tests are performed at each $M_\infty - \alpha$ combination to ensure the repeatability of the results for each configuration. Images are exposed at a rate of nominally $2\ kHz$ for a total of approximately 70 images per test, with the exception of Runs 40 and 39 which are taken at $4.5\ kHz$. Run 144 ($M_\infty = 0.7$, $\alpha = 18°$) illustrates that the asymmetric versus symmetric

Asymmetric Vortex Breakdown

M_∞	α	Run no.	Total t	S_{bd}/c_r	P_{bd}/c_r	$\left(\frac{\Delta bd_{max}}{c_r}\right)^*$	$\left(\frac{\Delta bd_{avg}}{c_r}\right)$
[1]	[°]	[1]	[msec]	[1]	[1]	[1]	[1]
0.7	18	133	34	0.71	0.75	-0.19	-0.04
0.7	18	138	35	0.99	0.73	0.36	0.26
0.7	18	144	35	0.99	0.98	0.09	0.01
0.7	18	162	35	0.70	0.99	-0.40	-0.29
0.7	18	163	35	0.70	0.99	-0.38	-0.29
0.7	18	164	36	0.69	0.99	-0.38	-0.30
0.8	18	134	35	0.72	0.98	-0.39	-0.26
0.8	18	135	35	0.72	0.98	-0.43	-0.26
0.8	18	136	35	0.97	0.72	0.36	0.25
0.8	18	137	35	0.69	0.98	-0.4	-0.29
0.8	18	142	35	0.96	0.75	0.33	0.21
0.8	18	143	36	0.98	0.7	0.42	0.28

Symmetric Vortex Breakdown

M_∞	α	Run no.	Total t	S_{bd}/c_r	P_{bd}/c_r	$\left(\frac{\Delta bd_{max}}{c_r}\right)^*$	$\left(\frac{\Delta bd_{avg}}{c_r}\right)$
[1]	[°]	[1]	[msec]	[1]	[1]	[1]	[1]
0.6	20	40	16	0.56	0.58	-0.07	-0.02
0.6	20	115	36	0.6	0.61	-0.14	-0.01
0.6	20	116	36	0.59	0.56	0.12	0.03
0.6	20	117	34	0.59	0.57	0.11	0.02
0.6	20	118	15	0.58	0.62	-0.11	-0.04
0.7	20	121	34	0.66	0.65	0.2	0.01
0.7	20	122	35	0.65	0.66	± 0.11	-0.01
0.7	20	156	35	0.63	0.67	-0.17	-0.04
0.7	20	157	35	0.63	0.67	-0.23	-0.04
0.7	20	158	34	0.63	0.66	-0.17	-0.03
0.7	20	159	35	0.60	0.65	-0.16	-0.05
0.8	20	39	5	0.64	0.64	-0.07	0.00
0.8	20	119	36	0.64	0.63	0.11	0.01
0.8	20	120	35	0.66	0.63	0.11	0.03
0.8	20	160	35	0.65	0.63	0.15	0.02
0.8	20	161	35	0.65	0.63	0.13	0.02

(S_{bd}: breakdown location on starboard side of wing, P_{bd}: breakdown location on port side of wing)

Table 6.7: Average breakdown location on either side of the wing and maximum asymmetry for various $M_\infty - \alpha$ configurations (*: the largest value of $|\Delta bd/c_r|$ has been removed as an extreme)
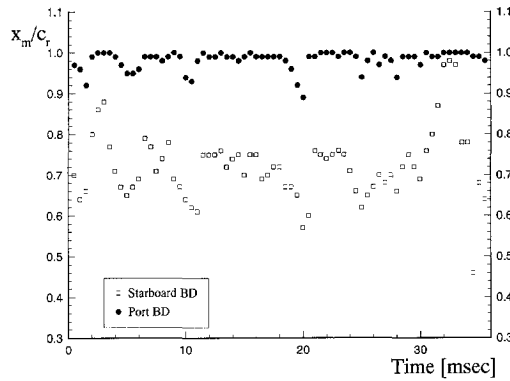
(a) Run134, predominately starboard side breakdown
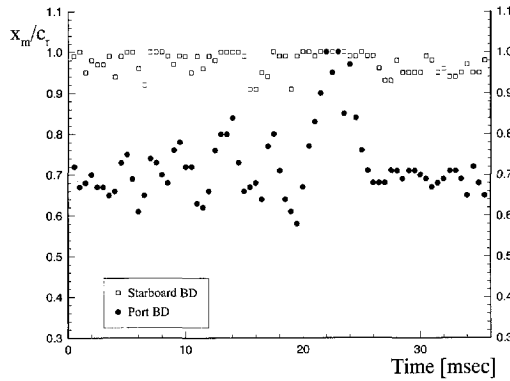
(b) Run 136, predominantly port side breakdown

Figure 6.25: Vortex breakdown location on either side of the wing, $M_\infty = 0.8$, $\alpha = 18°$.

breakdown classification criteria of $\Delta bd_{max} < 0.15c_r$ is not infallible. The maximum discrepancy in this case is only $0.09c_r$ while the other tests made at this $M_\infty - \alpha$ combination consistently satisfy the asymmetric breakdown criteria of $\Delta bd_{max} > 0.15c_r$.

Figure 6.25 illustrates the fluctuation of the vortex breakdown location on either side of the wing for two different tests at $M_\infty = 0.8$ and $\alpha = 18°$. Situations where no vortex breakdown is visible above the wing the position are indicated by $(x_m/c_r) = 1.0$. Predominantly starboard side vortex breakdown is observed in Run 134, while vortex breakdown is observed predominantly on the port side in Run 136. The vortex breakdown position fluctuations for the other asymmetric vortex breakdown case in this study, $M_\infty = 0.7$, $\alpha = 18°$, is illustrated in Figure 6.26. The fluctuations when $M_\infty = 0.7$, $\alpha = 18°$ resemble the behavior observed when $M_\infty = 0.8$ and $\alpha = 18°$ in that the vortex on one side of the wing exhibits breakdown well upstream of the trailing edge, while the vortex on the other side of the wing
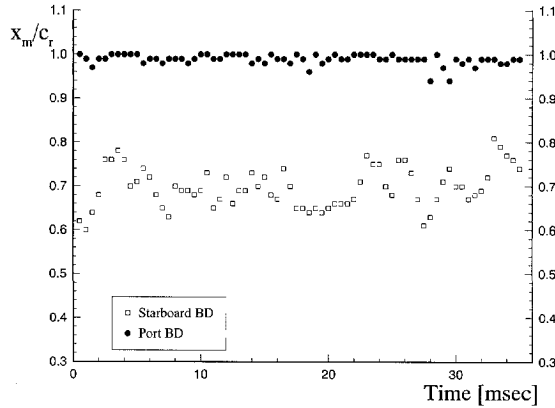
Figure 6.26: Vortex breakdown location on either side of the wing, Run 163, $M_\infty = 0.7$, $\alpha = 18°$

retains its organized structure up until the trailing edge.

The projection of the terminating shock wave observed in the transmission Schlieren visualization image of Figure 6.27a onto the upper surface of the wing is seen in Figure 6.27b. Both images are produced with a spark light source of approximately 20 $nsec$ exposure time. The highly unsteady nature of the terminating shock wave system is observed in the transmission Schlieren images as well as in the SRV images. As mentioned in Section 6.1.3, it is difficult to determine which of the SRV images correspond with a given transmission visualization image exactly due to the logistical inability to make simultaneous exposures with both systems. Yet, based on an understanding of the Schlieren system and basic knowledge of the flow field, tentative conclusions can be drawn.

The foremost and uppermost part of the shock wave, oriented approximately perpendicular to the free stream flow in Figure 6.27a, corresponds geometrically with the foremost part of the projected shock wave intersecting the root chord nearly perpendicularly in Figure 6.27b. The lower and more curved section of the shock wave in Figure 6.27a is likely associated with the section of the shock surface interacting with the vortex breakdown slightly further downstream. The shock surface near the root chord may, however, also exhibit a certain amount of curvature.

The bow-type shock wave in the vicinity of the primary vortex is likely an important mechanism in the vortex breakdown process. In a sustained delta wing vortex a jet-like profile of the axial velocity component is observed about the core of the primary vortex (see Section 1.1.2). Such a jet-like axial velocity distribution is observed above the wing in the current investigation via five-hole probe measurements at lower angle of attack and Mach number (see Section 6.5.1). The appearance of vortex breakdown has been shown in low
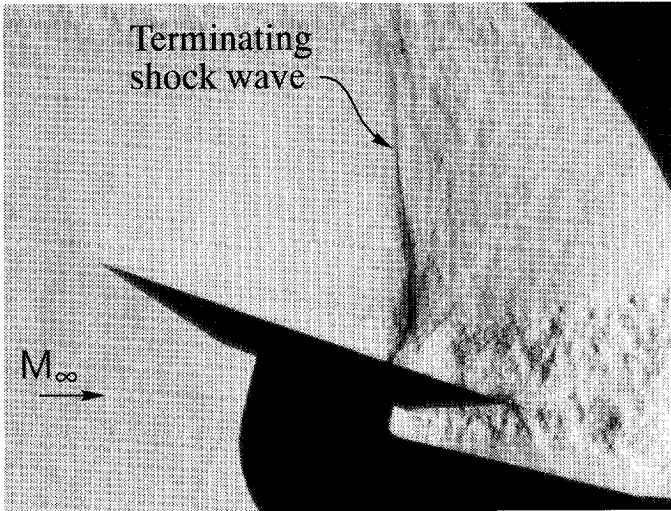
(a) Side-view transmission flow visualization, Schlieren knife edge perpendicular to free stream
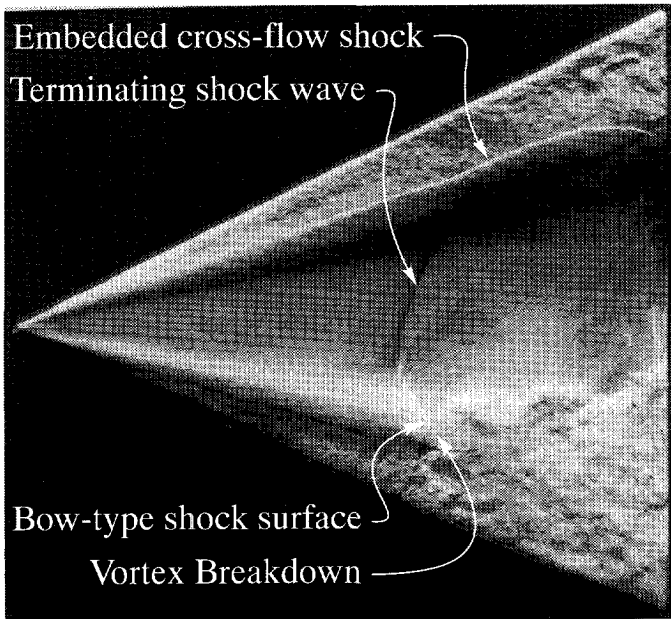
(b) Top-view SRV image, Run 136, Schlieren knife edge parallel with root chord

Figure 6.27: $M_\infty = 0.8$, $\alpha = 18°$

speed flow to be preceded by a reversal of the azimuthal vorticity component [Brown and Lopez 1990]. A reversal of the azimuthal vorticity component can be shown to correspond with a transition from a jet-like to a wake-like axial velocity profile about the vortex core in a vortical flow field (see Section 6.5.1). A jet-like axial velocity profile will correspond with a jet-like profile of the axial component of the Mach number when the total temperature of the flow is assumed constant. The presence of a shock surface, which can be approximated as a normal shock wave in the vicinity of the vortex core itself, results in a transition of the jet-like profile of the axial Mach number component to a wake-like profile downstream of shock surface. This transformation process is illustrated by the following example.

The axial component of the Mach number is assumed to have a local maximum C_0 at the axis of the primary vortex and its distribution about the axis to be defined by:

$$M_1(r) = -C_1 r^2 + C_0, \tag{6.1}$$

where $C_0 > 1$, $C_1 > 1$ and r refers to the local radial distance from the primary vortex axis. The profile of the Mach number M_2 downstream of a normal shock in the vicinity of the vortex axis can be described by the normal-shock relation:

$$M_2(r) = \sqrt{\frac{M_1(r)^2 + \frac{2}{\gamma-1}}{\frac{2\gamma}{\gamma-1}M_1(r)^2 - 1}} \tag{6.2}$$

The first and second derivatives of the axial Mach number profile beyond the normal shock wave M_2 in the radial direction can be calculated from Equations 6.1 and 6.2 at $r = 0$ to be:

$$\left(\frac{\partial M_2}{\partial r}\right)_{r=0} = 0$$

$$\left(\frac{\partial^2 M_2}{\partial r^2}\right)_{r=0} = \frac{4C_0 C_1 \left(\frac{\gamma}{\gamma-1}\left(1 + \frac{2}{\gamma-1}\right)\right)}{\sqrt{C_0^2 + \frac{2}{\gamma-1}} \cdot \left(\frac{2\gamma}{\gamma-1}C_0^2 - 1\right)^{\frac{3}{2}}} \tag{6.3}$$

The first derivative in r is, therefore, zero and the second derivative in r is positive. The axial component of the Mach number beyond the normal shock wave is, hereby, shown to exhibit a local minimum at the vortex core where $r = 0$. This local minimum is representative of a wake-like profile of the axial Mach number. A wake-like profile of axial velocity will also exist, therefore, when a constant total temperature on either side of the shock wave is assumed.

Transition of the axial Mach number profile from jet-like to wake-like via a normal shock wave suggests that a vortex breakdown process similar to that observed in the low speed flow

regime may exist in the high subsonic regime. In the low speed regime this is observed to be a gradual process which coincides with a reversal of the azimuthal vorticity component. In the presence of a shock wave the transition from jet-like to wake-like will be abrupt. Unfortunately it is not possible to examine the flow field properties in the presence of vortex breakdown above the wing in the current investigation due to probe interference affects.

The section of the shock surface extending downstream on the port side of the wing nearly parallel with the embedded cross-flow shock in Figure 6.28a is likely located above the organized vortex structure in a manner similar to the terminating shock wave discussed in Section 6.1.3. This conclusion is, again, supported by the undisturbed state of the port-side vortex and the embedded cross-flow shock wave coexisting with the terminating shock wave surface. The formation of the terminating shock surface in the vicinity of the primary vortex on the port side of the wing sketched in Figure 6.28b is strongly influenced by the presence of vortex breakdown on the starboard side of the wing. While the exact geometry of the flow beyond the point of vortex breakdown is uncertain, a loose spiral structure is visible on the starboard side of the wing in the SRV image. This less organized structure creates an obstruction for the flow moving downstream in the vicinity of the root chord. The terminating shock surface becomes necessary, therefore, to allow the supersonic flow moving over the top of the port vortex to navigate the "obstruction" of vortex breakdown on the starboard side of the wing and the impending trailing edge pressure rise.

6.3.2   Symmetric Vortex Breakdown

Symmetric vortex breakdown is observed at $\alpha = 20°$ for all three free stream Mach numbers investigated. Figure 6.29 illustrates the variation in vortex breakdown location over the course of one test with the high speed camera ($\Delta t < 35\ msec$) for each of the symmetric vortex breakdown configurations. The vortex breakdown position on either side of the wing, while not fluctuating completely in phase, are more similar to each other over the course of these runs than the asymmetric vortex breakdown fluctuations illustrated in Figures 6.25 and 6.26

The three $M_\infty - \alpha$ combinations where symmetric vortex breakdown is observed in this investigation represent significantly different flow fields. No terminating shock wave system is visible in the SRV images when $M_\infty = 0.6$ (see Figure 6.30), while at $M_\infty = 0.7$ and $M_\infty = 0.8$ a terminating shock wave system is clearly visible in the SRV images (see Figures 6.31 and 6.32, respectively). The presence of the terminating shock wave system, or lack thereof, is observed to have significant consequences for the flow field exhibiting vortex breakdown. The SRV image of Figure 6.30b when $M_\infty = 0.6$ illustrates strong spanwise gradients, indicative of an organized vortex structure, downstream of the point of vortex
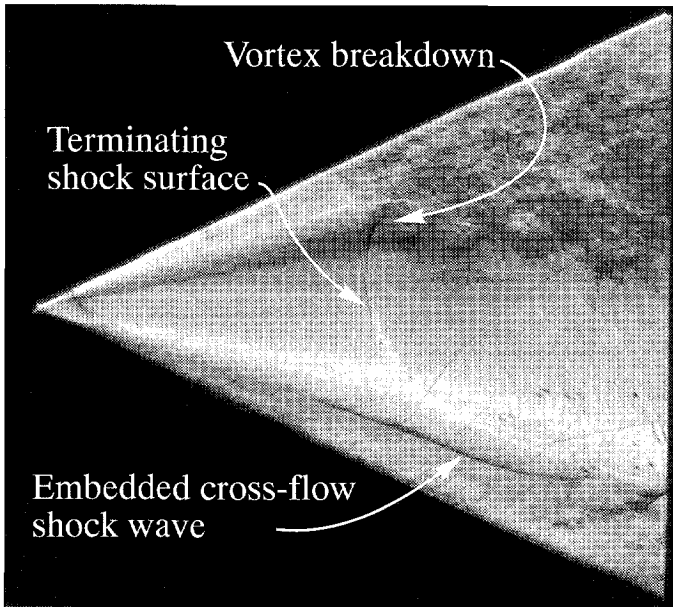
(a) SRV image, Run 134, Schlieren knife edge parallel with root chord, $M_\infty = 0.8, \alpha = 18°$.
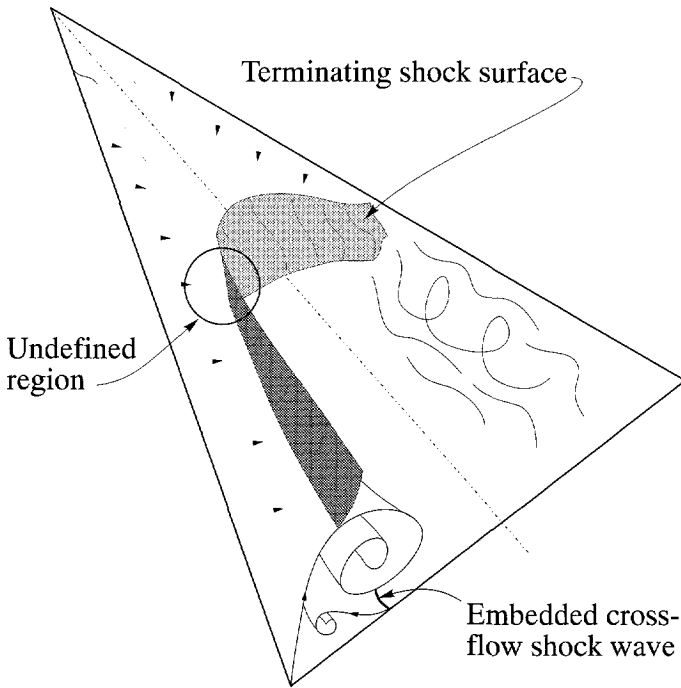
(b) Concept sketch of three dimensional shock structure

Figure 6.28: Asymmetric vortex breakdown and terminating shock wave.
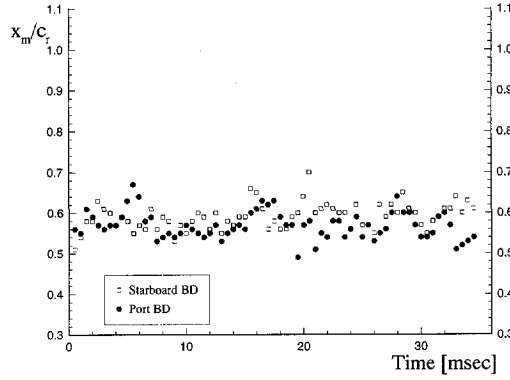
(a) $M_\infty = 0.6$, Run117
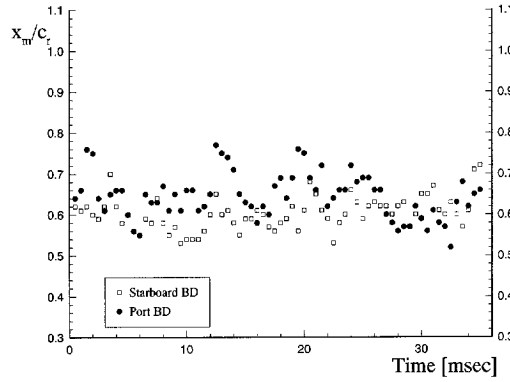
(b) $M_\infty = 0.7$, Run159
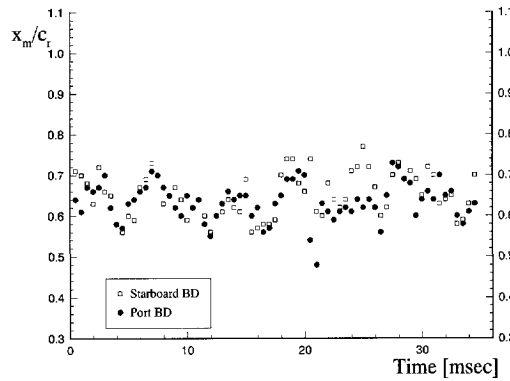
(c) $M_\infty = 0.8$, Run160

Figure 6.29: Vortex breakdown location on either side of the wing, $\alpha = 20°$
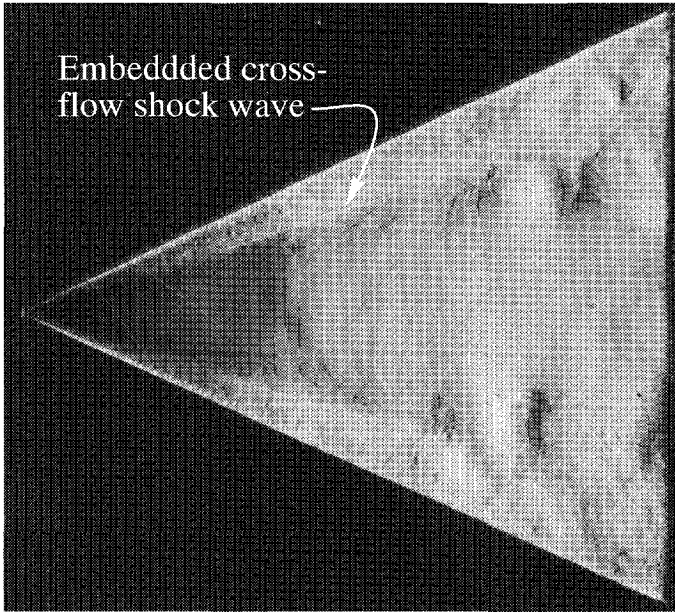
(a) Schlieren image perpendicular to the root chord
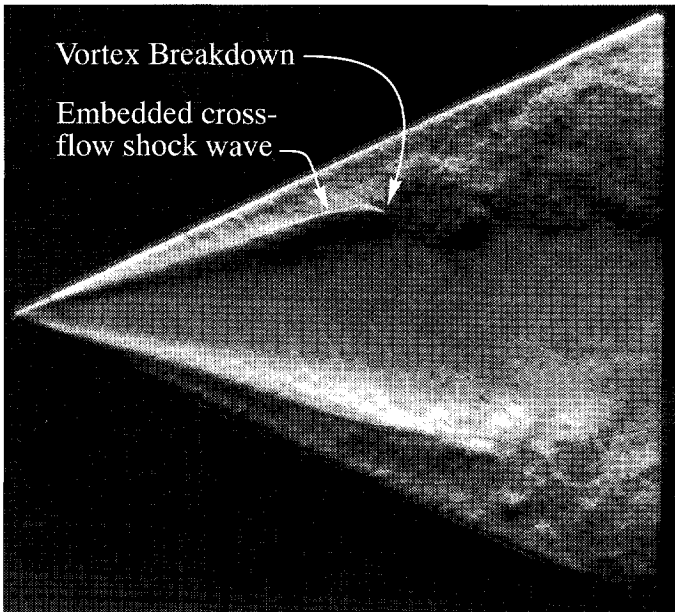
(b) Schlieren knife edge parallel with the root chord

Figure 6.30: SRV images, $M_\infty = 0.6$, $\alpha = 20°$.
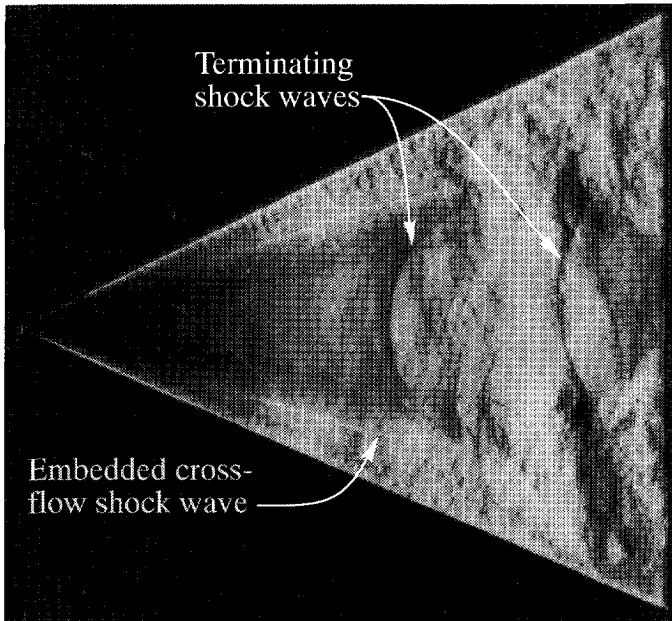
(a) Schlieren image perpendicular to the root chord
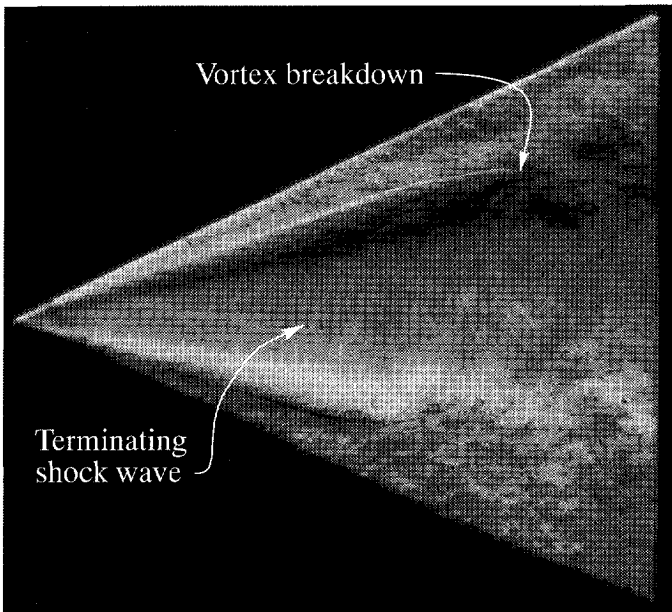
(b) Schlieren knife edge parallel with the root chord

Figure 6.31: SRV images, $M_\infty = 0.7$, $\alpha = 20°$.
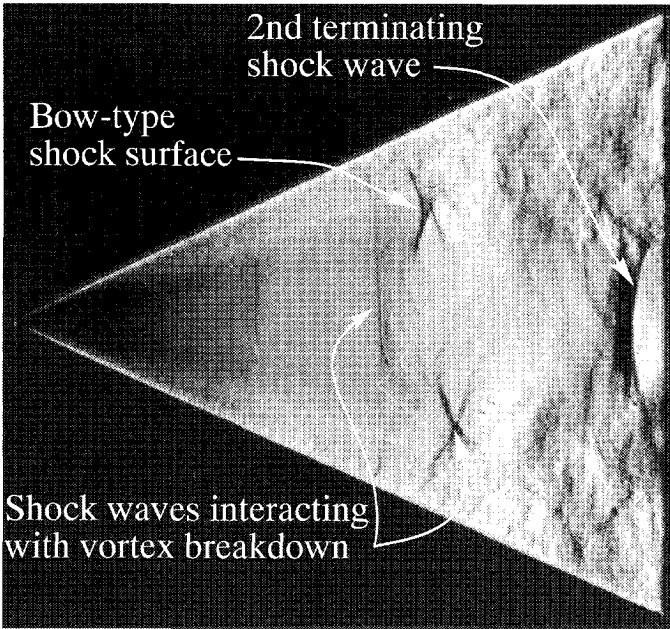
(a) Schlieren image perpendicular to the root chord
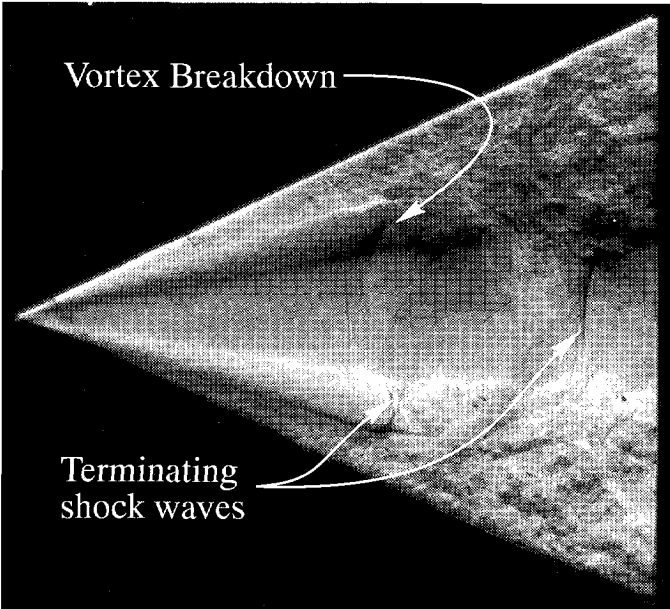
(b) Schlieren knife edge parallel with the root chord

Figure 6.32: SRV images, $M_\infty = 0.8$, $\alpha = 20°$.
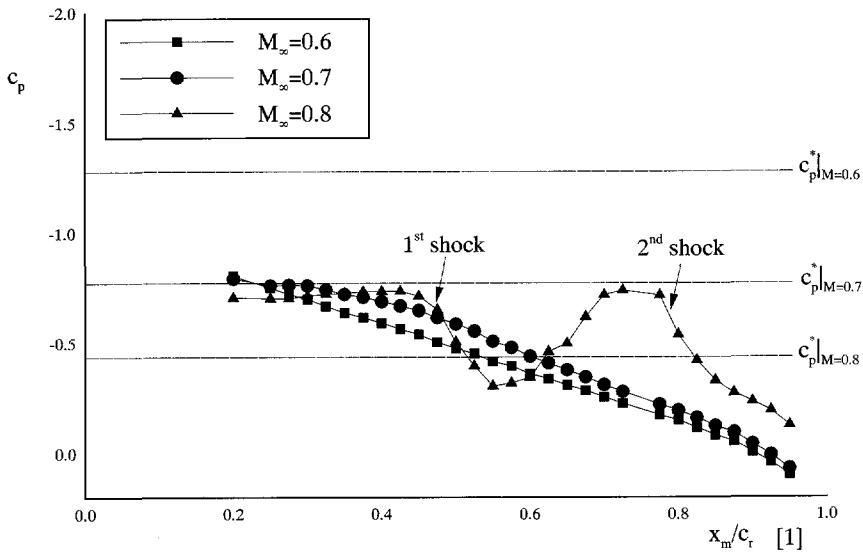
Figure 6.33: Pressure distribution along root chord when $\alpha = 20°$ at various free stream Mach numbers.

breakdown. When $M_\infty = 0.7$ and 0.8, on the other hand, a less organized flow structure is observed downstream of vortex breakdown (see Figures 6.31b and 6.32b). A strong second terminating shock wave is observed intersecting the root chord downstream of vortex breakdown in the SRV images of Figure 6.31a and Figures 6.32a and 6.32b. This second shock wave is attributed to the acceleration of the flow field downstream of the initial shock wave due to the "throat" effect resulting from the presence of vortex breakdown on either side of the wing. The acceleration of the flow along the root chord to supersonic speed downstream of the initial terminating shock wave is visible in the surface pressure measurements for the case of $M_\infty = 0.8$, but not when $M_\infty = 0.7$ (see Figure 6.33). In the case of $M_\infty = 0.8$, the supersonic flow compresses via the first shock wave, accelerates through the breakdown region until a second terminating shock wave, located at approximately $(x_m/c_r) = 0.8$, decelerates the flow as it approaches the trailing edge. The "smeared-out" appearance of the two shock waves in the surface pressure measurements is due to the inability of the average pressure measurements to capture unsteady shock fluctuations. The average surface measurements are found, however, to be repeatable.

While a terminating shock wave system is visible in the SRV images of Figure 6.31, a nearly continuous compression along the root chord is observed for the case $M_\infty = 0.7$ in Figure 6.33. This suggests that the terminating shock wave system is not as strong in the

case of $M_\infty = 0.7$ as the case of $M_\infty = 0.8$. The value of C_p on the root chord in the case of $M_\infty = 0.7$ is, indeed, noted to be less than the relevant sonic value of C_p^* only at 20% of the root chord and to rise steadily downstream of this point. The unsteady nature of the terminating shock wave system also makes it difficult to capture the shock waves in the average surface pressure measurements.

The contrast between the various symmetric vortex breakdown configurations is also apparent in the side-view transmission images of Figure 6.34. These images are obtained with the Schlieren knife edge aligned parallel with the free stream to illustrate the density gradient perpendicular to the free stream integrated over the width of the test section. In the cases of $M_\infty = 0.6$ and 0.7, the side view image indicates only a slight broadening of the vortex structure and lifting and from the wing upper surface beyond 50% of the root chord. When $M_\infty = 0.8$, on the other hand, a large scale disruption of the flow field beyond the point of vortex breakdown is visible. In Figure 6.35 side-view transmission Schlieren images are shown for the cases $M_\infty = 0.7$ and 0.8 with the knife edge aligned perpendicular to the free stream. These images, thus, illustrate the gradient of the density parallel with the free stream integrated over the width of the test section. In the case of $M_\infty = 0.8$ distinct shock waves are visible as well as a region of expansion beyond the initial terminating shock wave. When $M_\infty = 0.7$, on the other hand, these regions are less distinct. This, again, is likely a consequence of the unsteady nature of the shock wave system and decreased shock strength in the case of $M_\infty = 0.7$.

The surface pressure distributions of the various symmetric vortex breakdown configurations also illustrate that the flow field is significantly more disrupted in the case of $M_\infty = 0.8$ than when $M_\infty = 0.6$ and 0.7 at $\alpha = 20°$ (see Figure 6.36) . When $M_\infty = 0.6$ and 0.7, a fairly geometrically conical structure is maintained up until the end of the measurement grid. In the case of $M_\infty = 0.8$ this conical structure ends at $(x_m/c_r) = 0.5$. This phenomenon is more clearly illustrated by the spanwise pressure distribution in the vicinity of the trailing edge $(0.78 \leq (x_m/c_r) \leq 0.93)$ shown in Figure 6.37 for these same $M_\infty - \alpha$ combinations. These pressures are measured using surface pressure model 2 (see Figure 2.4). A significant spanwise gradient $(\partial C_p/\partial y_m)$ is, indeed, observed up until $(x_m/c_r) = 0.93$ for the two lower Mach numbers. When $M_\infty = 0.8$, on the other hand, the value of C_p is noted to remain nearly constant between $(y_m/y_{le}) = 0.38$ and 0.78.

(a) $M_\infty = 0.6$

(b) $M_\infty = 0.7$

Vortex Breakdown
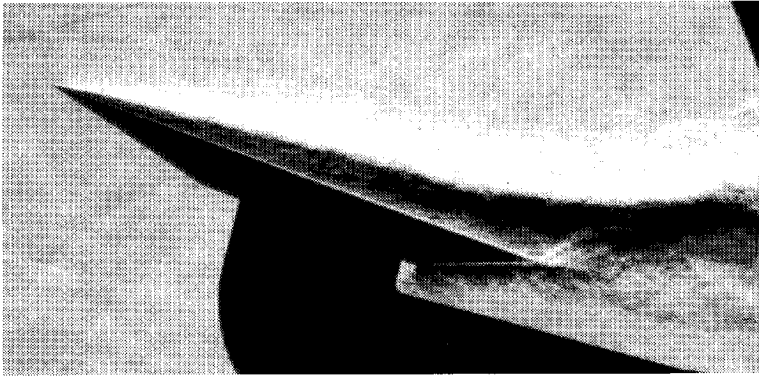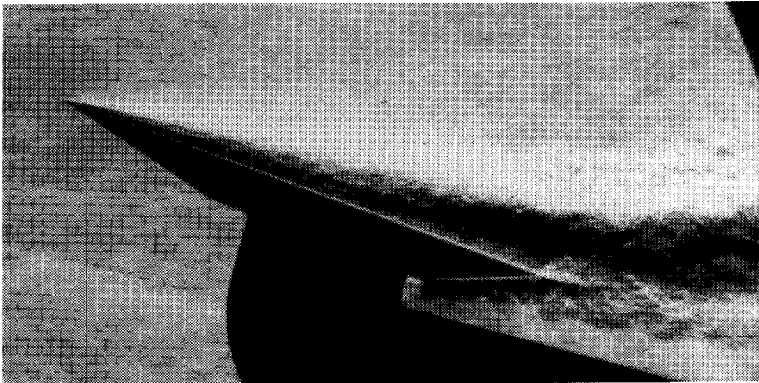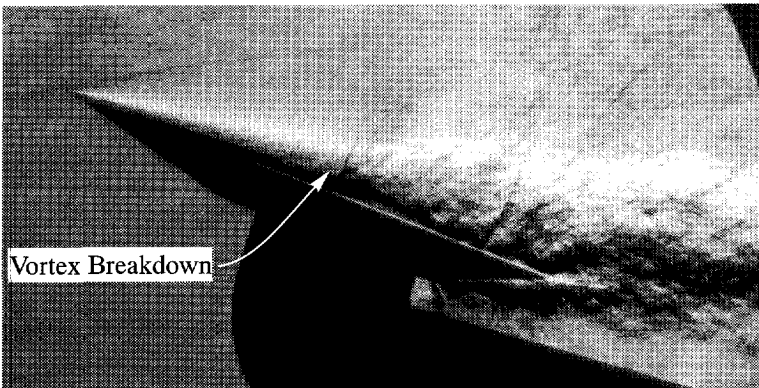
(c) $M_\infty = 0.8$

Figure 6.34: Side-view transmission Schlieren images with Schlieren knife edge parallel with the free stream, $\alpha = 20°$.

(a) $M_\infty = 0.7$

Region of expansion

Shock wave interacting
with primary vortices

Second terminating
shock wave
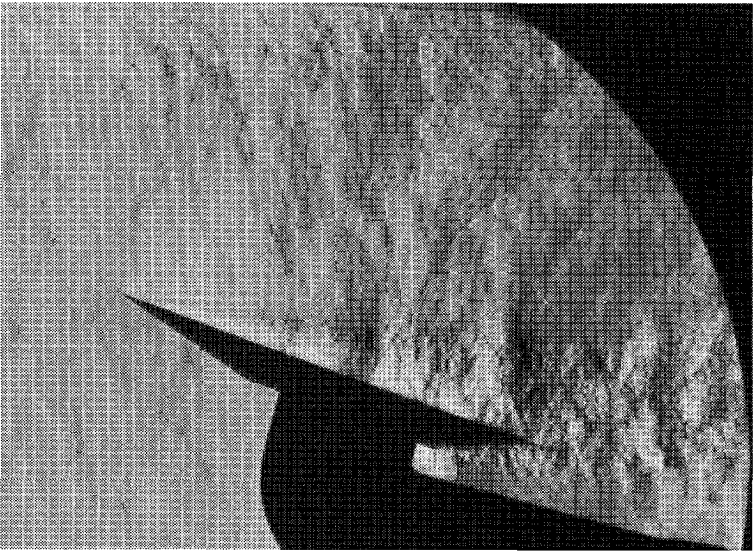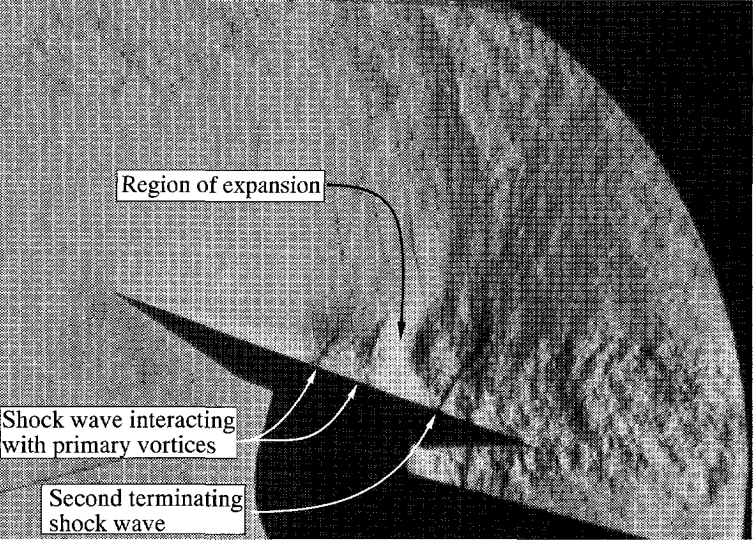
(b) $M_\infty = 0.8$

Figure 6.35: Side-view transmission Schlieren images with Schlieren knife edge perpendicular to the free stream, $\alpha = 20°$.
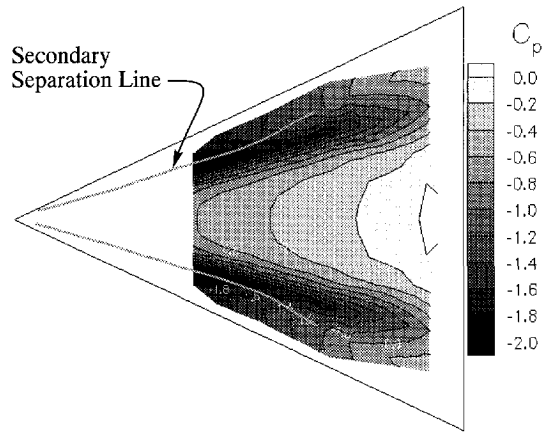
(a) $M_\infty = 0.6$
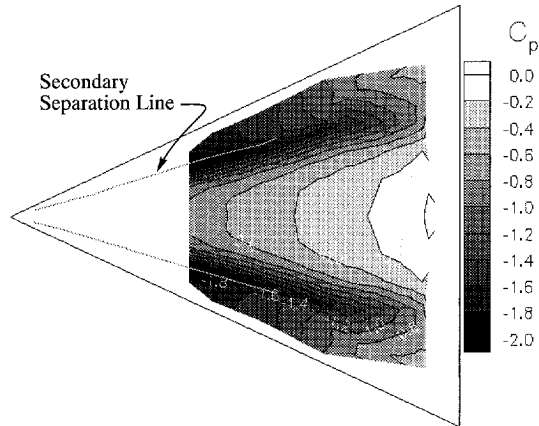
(b) $M_\infty = 0.7$
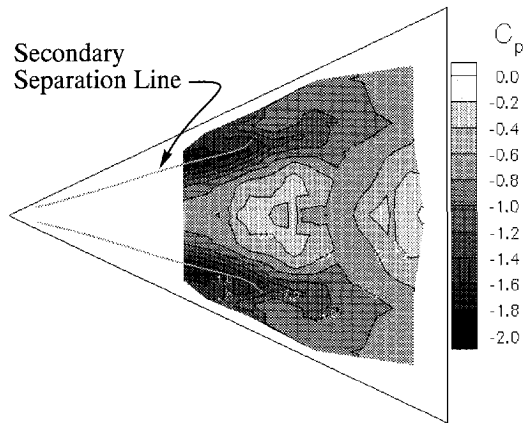
(c) $M_\infty = 0.8$

Figure 6.36: Surface pressure distributions, $\alpha = 20°$.
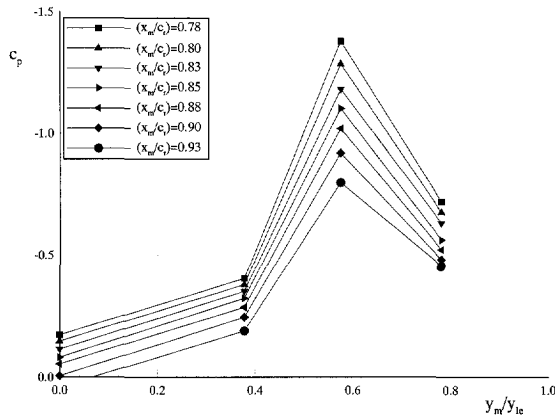
(a) $M_\infty = 0.6$
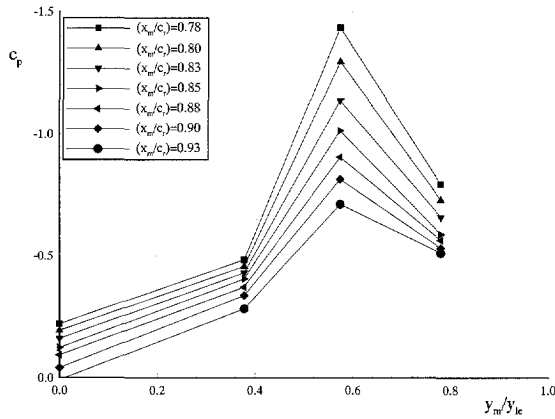
(b) $M_\infty = 0.7$
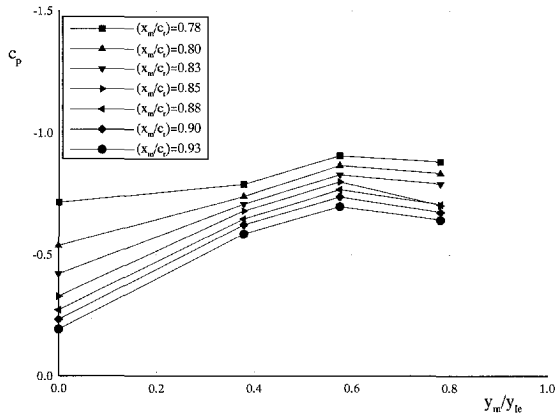
(c) $M_\infty = 0.8$

Figure 6.37: Spanwise surface pressure distributions, $\alpha = 20°$.

6.4   Vortex "Lift"

In order to investigate the effects of the vortex breakdown and compressibility on wing per-
formance, an average surface pressure coefficient $\overline{-C_p}$ is defined. This quantity is deter-
mined by summing the product of the average $-C_p$ value and the cell area of each of the
cells shown in Figure 3.6, and then dividing that sum by the total surface area of the mea-
surement grid. The grid surface covers 61% of the total wing upper surface and spans be-
tween approximately 40% and 90% of the root chord. While this analysis does not provide a
true measurement of lift, it does provide some indication of the influence of the state of the
vortical flow field on the wing performance.

The variation of $\overline{-C_p}$ with angle of attack is shown in Figure 6.38 when $M_\infty = 0.6$ and
0.8 . An estimation of the "lift" slope at zero incidence is obtained via a linear extrapolation
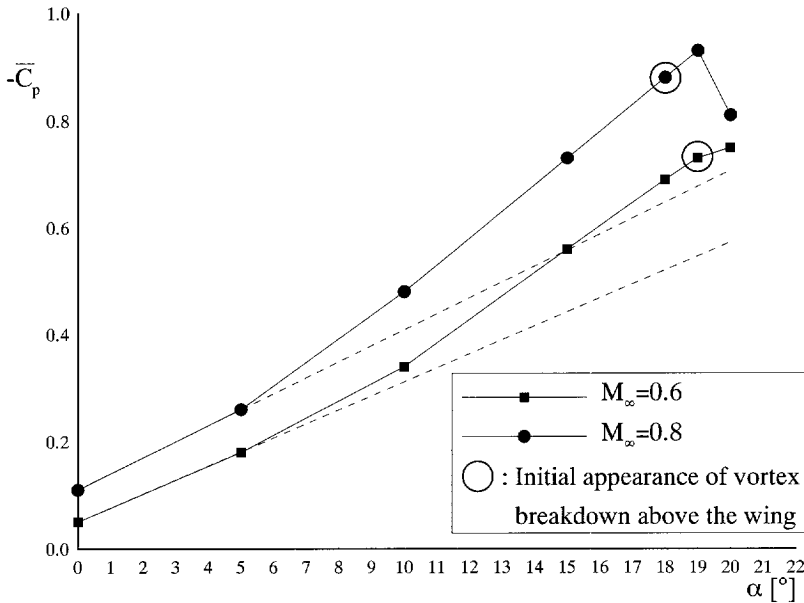
Figure 6.38: Variation of average surface pressure coefficient $\overline{-C_p}$ with angle of attack and free
stream Mach number.

of the value of $\overline{-C_p}$ at the two smallest values of α for both free stream Mach numbers for
reference purposes. The "lift" associated with the vortical flow field is noted to exceed the
linear estimation in all cases.

The angle of attack at which vortex breakdown initially appears above the wing is also
indicated in Figure 6.38. It is interesting to note that in the case of $M_\infty = 0.6$, the value

of $\overline{-C_p}$ continues to increase with angle of attack beyond the initial appearance of vortex breakdown above the wing. The slope is noted to decrease, however, between 19° and 20°. In the case of $M_\infty = 0.8$, on the other hand, a significant decrease of the $\overline{-C_p}$ value occurs between 19° and 20°. A similar trend of increasing lift with angle of attack beyond the initial appearance of vortex breakdown above the wing was also observed in the force balance measurements of Erickson et. al. [1989]. These measurements, conducted on a sharp leading edge delta wing with the free stream Mach numbers of 0.4, 0.6, 0.8, 0.85 and 0.90, illustrated a decrease in magnitude of the positive $c_l - \alpha$ slope when $M_\infty = 0.6$ when vortex breakdown appeared above the wing and a reversal of the slope in the higher Mach number cases. This difference in trend for the lower and higher Mach number cases was attributed by Erickson to the presence of a strong terminating shock wave system in the higher Mach number cases. This is consistent with the current study in that a strong terminating shock wave system is present in the case of $M_\infty = 0.8$, while no terminating shock wave system is observed when $M_\infty = 0.6$ (see Section 6.3.2).

6.5 Vorticity Dynamics and Vortex Breakdown

The axial velocity distribution and cross-flow vorticity components in the vicinity of the primary vortex core are examined in order to investigate the applicability of the vorticity dynamics theory on vortex breakdown in the high subsonic flow regime. According to this theory a reversal of the azimuthal or in-plane vorticity component will precede vortex breakdown itself. As mentioned in Section 1.2.2, previous experimental and theoretical work with both axisymmetric vortex flows and delta wings in low speed flow illustrate the importance of vorticity dynamics in vortex breakdown. In the current investigation an experimental and numerical study of the development with increasing streamwise station of the axial velocity distribution and azimuthal vorticity distribution about the primary vortex core is carried out to determine if this theory is also applicable for vortical flow about delta wings in the high subsonic flow regime. A transition from a jet-like to wake-like axial velocity distribution near the center of the vortex core is shown below to coincide with a reversal of the azimuthal vorticity component. The experimental data presented is obtained via five-hole probe measurements while the numerical data is obtained via three-dimensional Euler method calculations. The $M_\infty - \alpha$ combination selected for this investigation is $M_\infty = 0.6$ and $\alpha = 10°$. This $M_\infty - \alpha$ combination is selected because, as shown in Chapter 4, it exhibits the least distortion due to probe/flow-field interference effects.

6.5.1 Axial and Cross-flow Velocity Components

The trajectory of the vortex core above the wing is noted in Section 6.1.1 to be approximately conical in nature. For this reason a local right handed Cartesian reference system x_c, y_c, z_c, with the origin at P_c, is introduced to illustrate the axial and cross-flow velocity components above the wing (see Figure 6.39). In this reference system, the x_c axis coincides with the
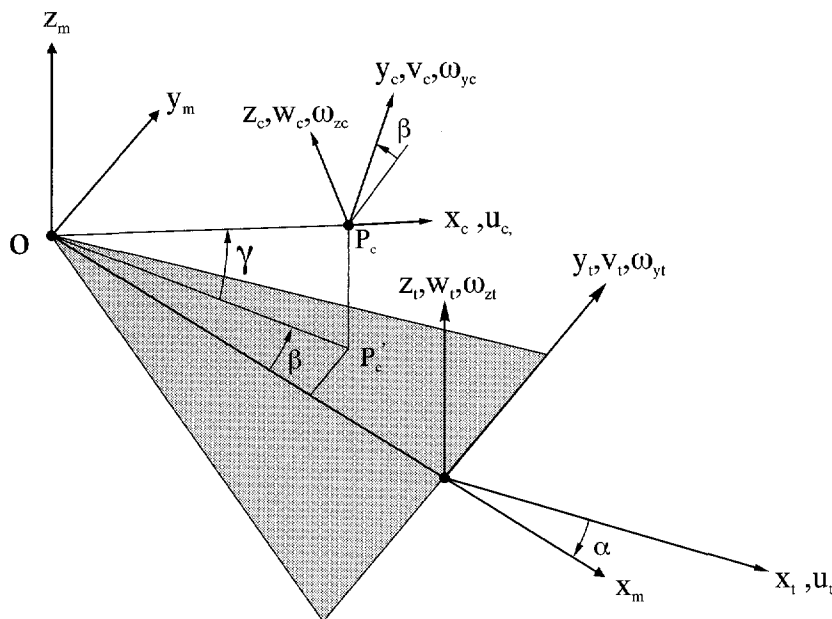
Figure 6.39: Illustration of relevant axial and cross-flow velocity components above (u_c, v_c, w_c) and behind (u_t, v_t, w_t) the wing.

conical ray OP_c and the y_c axis, perpendicular to the axial ray x_c, is parallel with the upper surface of the wing. The point P_c is the location of minimum total pressure in the five-hole probe measurement plane, or the approximate location of the axis of the primary vortex core (see Section 2.3.2). This is the same coordinate system discussed in Section 4.5. The relevant cross-flow velocity components v_c, w_c above the wing are, thus, contained in the plane perpendicular to the conical ray OP_c. The axial velocity component above the wing is aligned with the conical ray OP_c.

The trajectory of the axis of the primary vortex behind the wing, in contrast, is approximately parallel with the wind tunnel axis. A right handed Cartesian coordinate system x_t, y_t, z_t is introduced behind the wing, therefore, where the x_t axis is aligned with the tunnel axis and the y_t is parallel with the trailing edge of the wing (see Figure 6.39). This coordinate system is used to illustrate the axial and cross-flow velocity components behind the wing. Behind

the wing the axial component is defined parallel with the tunnel centerline or the free stream flow direction. The cross-flow velocity components behind the wing, v_t and w_t, are aligned with the axes y_t and z_t, respectively.

Experimentally obtained contour plots of the axial velocity component in the vicinity of the primary vortex core for one measurement plane above the wing $((x_m/c_r) = 0.7)$ and one in its wake $((x_t/c_r) = 0.5)$ are shown in Figure 6.40. The comparable numerical results are presented in Figure 6.41. The superimposed vector fields in each of these plots represent the cross-flow velocity components as defined above. The location of minimum total pressure is also indicated on these plots by a circle surrounding the relevant grid point. The orientation of the cross-flow velocity vectors about this point, both above and behind the wing, supports the definition of $(p_t)_{min}$ as the primary vortex core location in this investigation. The axial velocity u_c in the vicinity of the vortex core above the wing is in the downstream direction and jet-like, or exhibiting a maximum in the vicinity of the vortex core exceeding the free stream value. This is observed in both experimental and numerical results.

In contrast with the measurements above the wing, a local minimum of the axial velocity component exists in the vicinity of the primary vortex core in the experimental measurement plane located behind the wing (see Figure 6.40b). A similar situation is observed in the numerically calculated distribution of the axial velocity illustrated in Figure 6.41b. The velocity distribution about the primary vortex core behind the wing is wake-like as it exhibits a local axial velocity minimum, less than the free stream value, in the vicinity of the vortex core. The difference between the axial velocity distributions above and behind the wing is indicative of a transition from a jet-like to a wake-like velocity profile with increasing streamwise station. In contrast, the direction in which the vortical flow moves about the primary vortex core is counter-clockwise in both the measurement plane above the wing and in its wake for both the experimental and numerical cases. The flow direction is indicated by the orientation of the superimposed cross-flow velocity components in Figures 6.40 and 6.41. The sustained cross-flow velocity flow field implies that despite the transition from a jet-like to a wake-like axial velocity distribution about primary vortex core, the primary vortex continues to exist in the wake of the wing.

The observed transition of the axial velocity profile from jet-like to wake-like with increasing streamwise station supports the vorticity theory of vortex breakdown. Recalling the
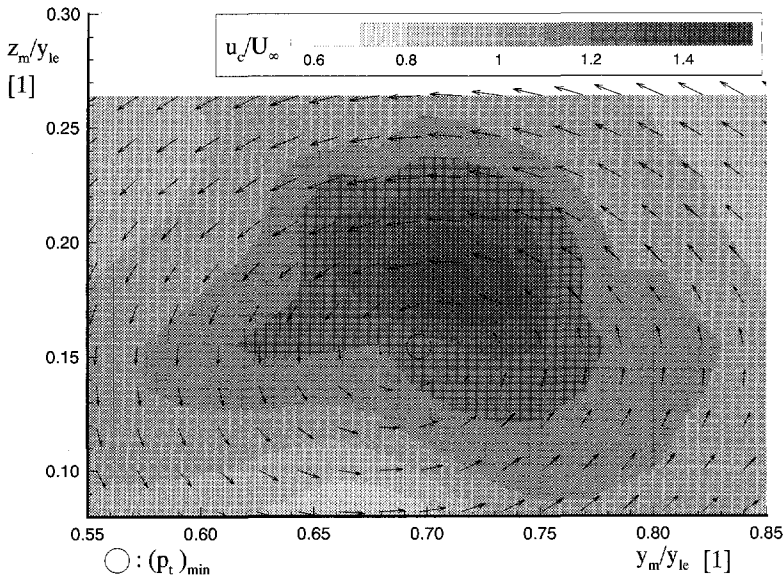
(a) Above wing, $(x_m/c_r) = 0.7$
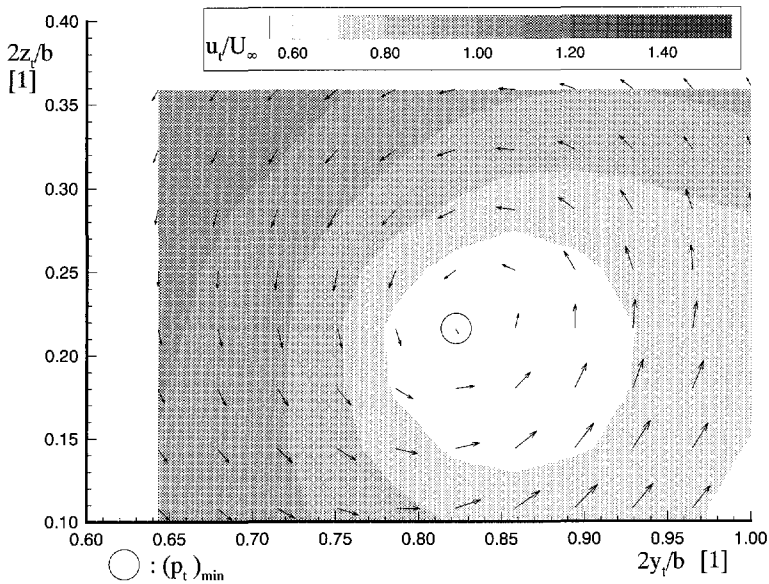
(b) Wake of wing, $(x_t/c_r) = 0.5$

Figure 6.40: Experimental axial velocity distribution about the primary vortex core with superimposed cross-flow direction $((v_c, w_c)$ above the wing and (v_t, w_t) behind the wing, $M_\infty = 0.6$ and $\alpha = 10°$.

(a) Above wing, $(x_m/c_r) = 0.7$

(b) Wake of wing, $(x_t/c_r) = 0.5$
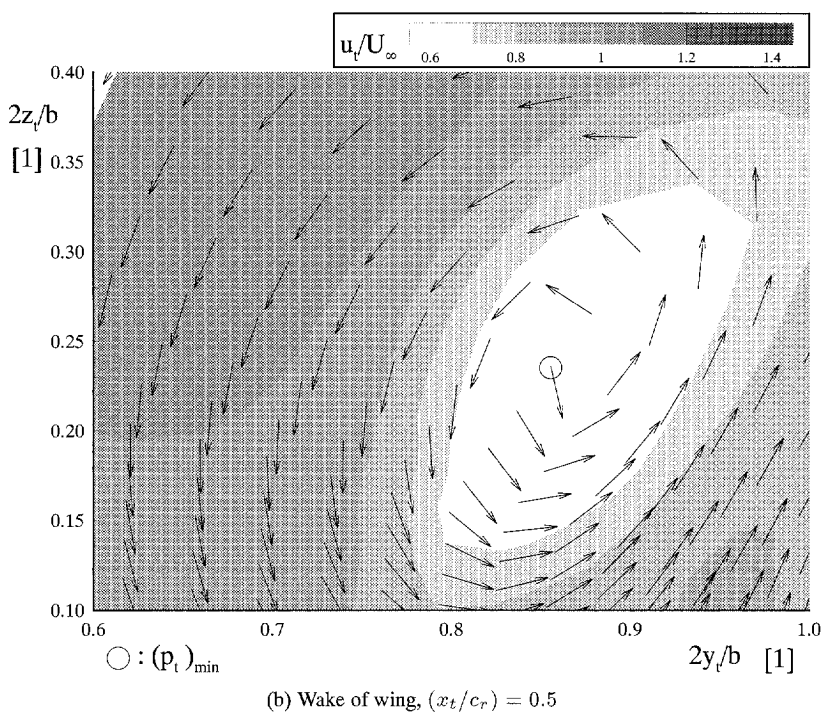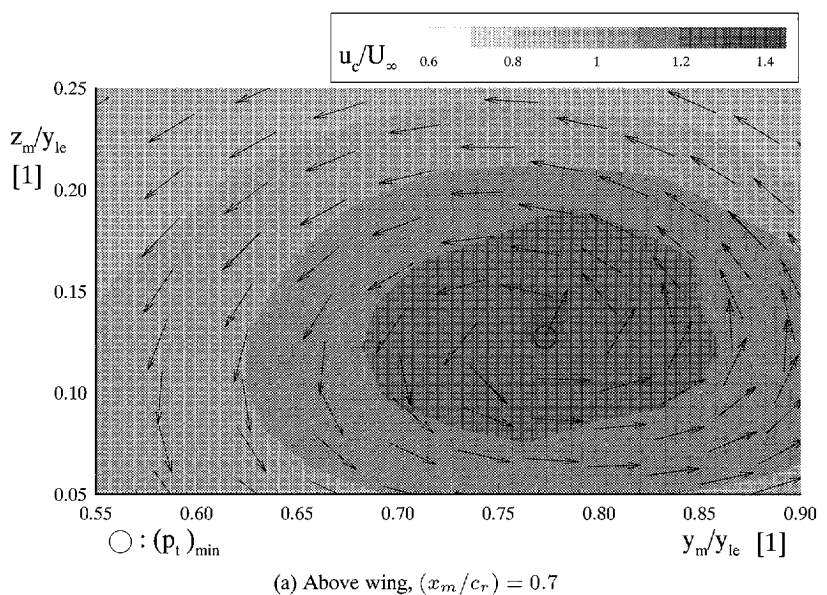
Figure 6.41: Numerical axial velocity distribution about the primary vortex core with superimposed cross-flow direction $((v_c\,,\,w_c)$ above the wing and $(v_t\,,\,w_t)$ behind the wing, $M_\infty = 0.6$ and $\alpha = 10°$.

definition of the cylindrical vorticity components from Chapter 1:

$$\omega_r = \left(\frac{1}{r} \frac{\partial v_x}{\partial \phi} - \frac{\partial v_\phi}{\partial x} \right)$$
$$\omega_\phi = \left(\frac{\partial v_r}{\partial x} - \frac{\partial v_x}{\partial r} \right) \tag{6.4}$$
$$\omega_x = \left(-\frac{1}{r} \frac{\partial v_r}{\partial \phi} + \frac{v_\phi}{r} + \frac{\partial v_\phi}{\partial r} \right)$$

it is possible to illustrate how the transition from a jet-like to a wake like profile will lead to the reversal of the azimuthal vorticity component ω_ϕ. The orientation of these various components relative to the vortex axis x is illustrated in Figure 6.42. The transition from jet-like
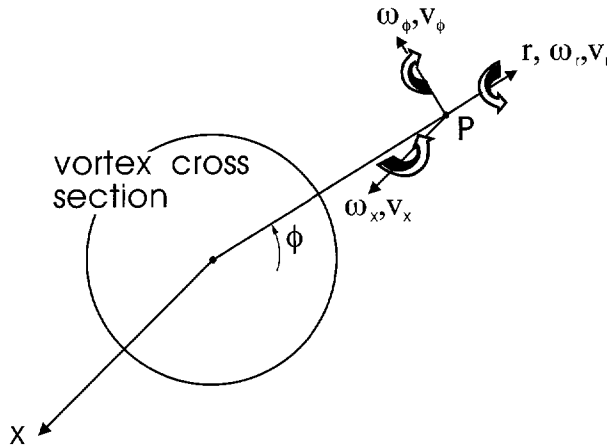
Figure 6.42: Cylindrical coordinate system and relevant vorticity components

to a wake-like profile will, by definition, change the term $\left(\frac{\partial v_x}{\partial r} \right)$ from positive to negative in the vortex core. Because $\left(\frac{\partial}{\partial x} \right) << \left(\frac{\partial}{\partial r} \right)$ can be assumed for a vortex prior to vortex breakdown, this reversal of $\left(\frac{\partial v_x}{\partial r} \right)$ will result in a reversal in sign of the azimuthal vorticity component. Thus, the transition of the axial velocity distribution from jet-like above the wing to wake-like behind the wing is associated with a reversal of the azimuthal vorticity component ω_ϕ.

6.5.2 Cross-flow Vorticity

The three vorticity components ω_i , ω_j and ω_k are calculated for both the experimental and numerical investigations via finite-difference calculations. The unit vectors $\hat{i}$, $\hat{j}$ and $\hat{k}$ are aligned with x, y and z axes of the model fixed coordinate system m and tunnel fixed coordinate system t for the measurement planes above the wing and in its wake, respectively (see

Figure 6.39). These components are conventionally defined as:

$$\omega_i = \left(\frac{\partial w}{\partial y} - \frac{\partial v}{\partial z} \right) \tag{6.5}$$

$$\omega_j = \left(\frac{\partial u}{\partial z} - \frac{\partial w}{\partial x} \right) \tag{6.6}$$

$$\omega_k = \left(\frac{\partial v}{\partial x} - \frac{\partial u}{\partial y} \right) \tag{6.7}$$

The determination of the vorticity vector for the numerical simulation results requires no further assumptions above or behind the wing. The experimental measurements, on the other hand, are made at a single x station locally and require, therefore, the use of certain assumptions regarding $(\partial/\partial x)$ in order to calculate the ω_j and ω_k vorticity components. For the measurement planes above the wing a conical flow assumption is made such that,

$$\frac{\partial}{\partial x_m} = -\eta \frac{\partial}{\partial y_m} - \zeta \frac{\partial}{\partial z_m} \tag{6.8}$$

where $\eta = (y_m/x_m)$ and $\zeta = (z_m/x_m)$. For the measurement planes behind the wing a "two-dimensional" flow has been assumed such that

$$\frac{\partial}{\partial x_t} = 0 \tag{6.9}$$

The nearly constant primary vortex core location above the wing in conical coordinates and in Cartesian coordinates behind the wing support the approximation of the flow as conical above the wing and "two-dimensional" behind the wing (see Section 6.1.1).

Substituting the conical variables η and ζ into the vorticity Equations 6.6 and 6.7 yields:

$$\omega_j = \frac{1}{x_m} \left(\frac{\partial u}{\partial \zeta} + \eta \frac{\partial w}{\partial \eta} + \zeta \frac{\partial w}{\partial \zeta} \right) \tag{6.10}$$

$$\omega_k = -\frac{1}{x_m} \left(\eta \frac{\partial v}{\partial \eta} + \zeta \frac{\partial v}{\partial \zeta} + \frac{\partial u}{\partial \eta} \right) \tag{6.11}$$

The accuracy of the conical assumption above the wing is examined by making additional measurements in a plane at $(x_m/c_r) = 0.72$ and calculating the ω_{yc} and ω_{zc} vorticity com-

ponents for $(x_m/c_r) = 0.71$. The vorticity components ω_{yc} and ω_{zc}, parallel with the y_c and z_c axes of Figure 6.39, respectively, are calculated via a geometric transformation from the Cartesian vorticity components ω_i, ω_j and ω_k to be:

$$\omega_{yc} = -\omega_i \sin \beta + \omega_j \cos \beta \tag{6.12}$$

and

$$\omega_{zc} = -\sin \gamma (\omega_i \cos \beta + \omega_j \sin \beta) + \omega_k \cos \gamma \tag{6.13}$$

when

$$\tan \beta = \left(\frac{y_m}{x_m} \right)_{core} \tag{6.14}$$

and

$$\tan \gamma = \left(\frac{z_m}{\sqrt{x_m^2 + y_m^2}} \right)_{core} \tag{6.15}$$

The distribution of the in-plane vorticity components at $(x_m/c_r) = 0.71$ is shown together with those calculated via the conical flow assumption at $(x/c_r) = 0.70$ in Figures 6.43 and 6.44. These results appear to agree well with each other. Both the conical and two-plane calculations exhibit high gradients of negative ω_{yc} and ω_{zc} in the shear layer emanating from the leading edge. The only notable discrepancies in the contours of the two methods of vorticity calculation occur in the proximity of low vorticity (i.e. $\omega_{yc} \approx 0$ or $\omega_{zc} \approx 0$).

The two-dimensional flow-field assumption is considered reasonable behind the wing due to the lack of significant streamwise pressure gradients and the absence of the wing leading edge and its associated vorticity generation in the wake. The observed tendency of the vortex to realign itself with the free stream flow beyond the trailing edge further supports its two-dimensional behavior behind the wing. Based on the two-dimensional flow assumption the gradients $\left(\frac{\partial}{\partial x} \right)$ are approximated as zero and the vorticity components become:

$$\omega_j = \left(\frac{\partial u}{\partial z} \right) \tag{6.16}$$

$$\omega_k = \left(-\frac{\partial u}{\partial y} \right) \tag{6.17}$$
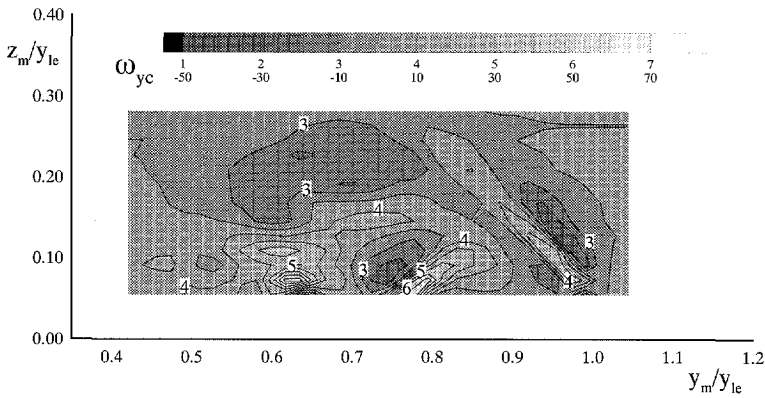
(a) Two-plane calculation of ω_{yc}, $(x_m/c_r) = 0.71$
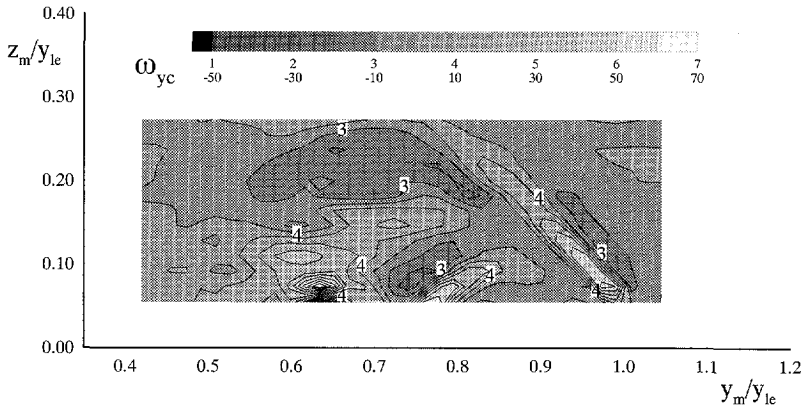
(b) Calculation of ω_{yc} via conical flow approximation, $(x_m/c_r) = 0.7$

Figure 6.43: Comparison of (ω_{yc}) distribution above wing calculated directly using two measurement planes and via conical flow assumption, $M_\infty = 0.8$ and $\alpha = 10°$.

The cross-flow vorticity vector field superimposed on a contour plot of the total pressure for a measurement plane above $((x_m/c_r) = 0.7)$ and behind the wing $((x_t/c_r) = 0.5)$ is shown in Figures 6.45 and 6.46 for the experimental and numerical studies, respectively. The vorticity vectors for the plane above the wing represent the components ω_{yc} and ω_{zc} which are parallel with the y_c and z_c axis of Figure 6.39, respectively. In both the experimental and numerical results the cross-flow vorticity vectors above the wing are oriented in the same direction about the vortex core as the corresponding cross-flow velocity vectors shown in Figures 6.40a and 6.41a. The orientation of the cross-flow vorticity vectors about the vortex core in the same direction as the sense of the circulation is, per definition, indicative of a positive azimuthal vorticity in the vicinity of the vortex core (see Figure 6.42).
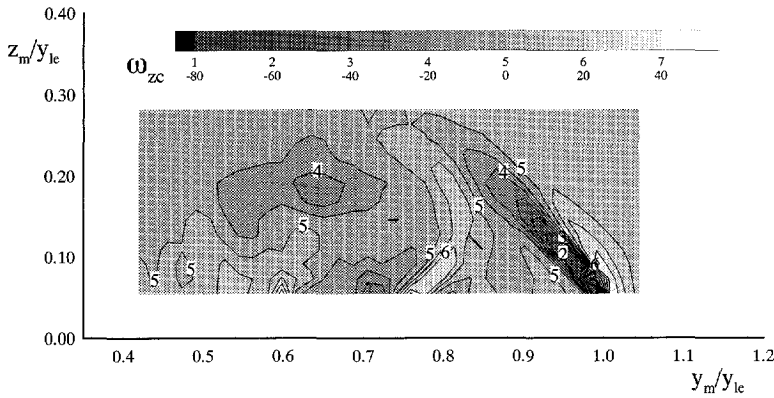
(a) Two-plane calculation of ω_{zc}, $(x_m/c_r) = 0.71$
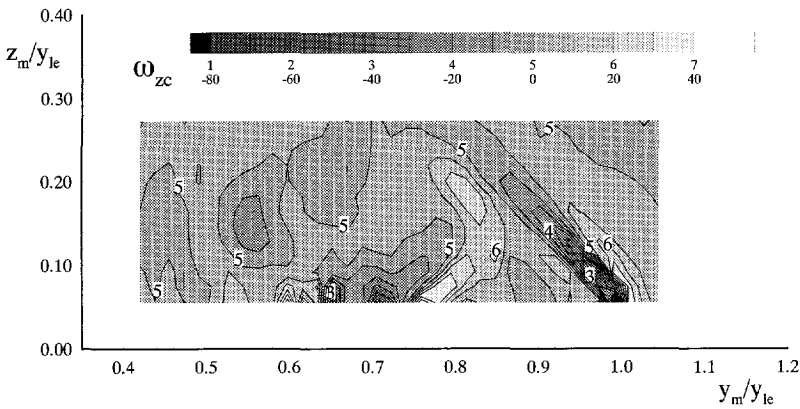
(b) Calculation of ω_{zc} via conical flow approximation, $(x_m/c_r) = 0.7$

Figure 6.44: Comparison of (ω_{zc}) distribution above wing calculated directly using two measurement planes and via conical flow assumption, $M_\infty = 0.8$ and $\alpha = 10°$.

In contrast, the in-plane vorticity vector field behind the wing, illustrated in Figures 6.45b and 6.46b for the experimental and numerical studies, respectively, is indicative of a negative azimuthal vorticity. The vorticity components represented by these vectors are illustrated in Figure 6.39 as the Cartesian components ω_{yt} and ω_{zt} parallel with the y_t and z_t axes, respectively. The corresponding cross-flow velocity components, illustrated in Figures 6.40b and 6.41b are oriented in a direction opposite to that of the in-plane vorticity vectors. This reversal of the azimuthal vorticity component with increasing streamwise station is consistent with as the transition of the axial velocity distribution near the core from a jet-like to wake-like discussed above.

The transition of axial velocity profile from jet-like to wake-like, as well as the reversal of
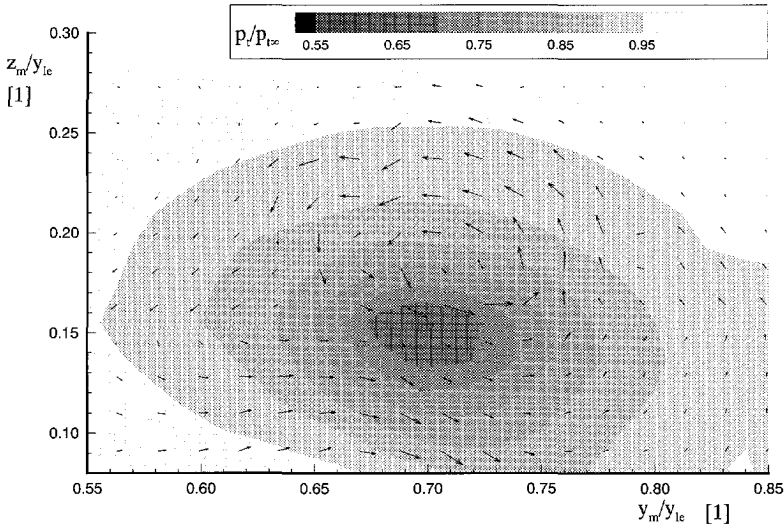
(a) Above wing, $(x_m/c_r) = 0.7$
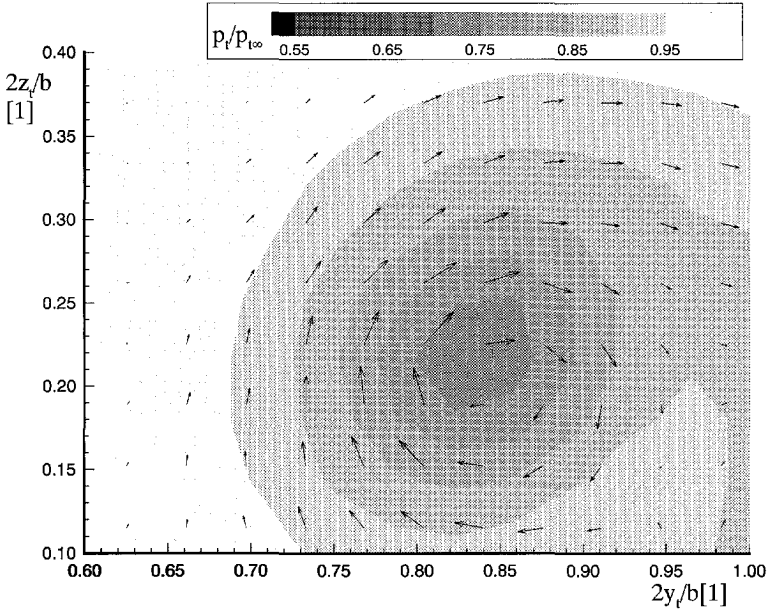
(b) Wake of wing, $(x_t/c_r) = 0.5$

Figure 6.45: Experimental total pressure distribution about primary vortex core with superimposed cross-flow vorticity direction $(\omega_{yc}, \omega_{zc})$ above the wing and $(\omega_{yt}, \omega_{zt})$ behind the wing, $M_\infty = 0.6$ and $\alpha = 10°$.
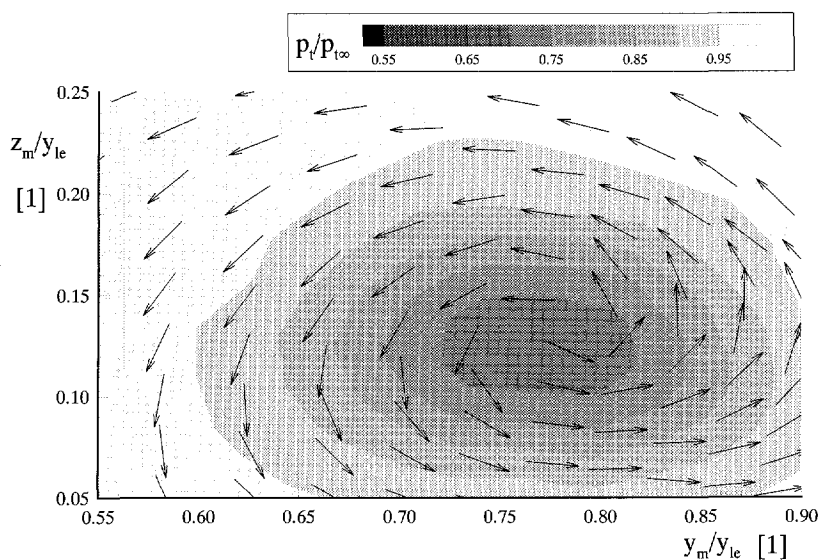
(a) Above wing, $(x_m/c_r) = 0.7$
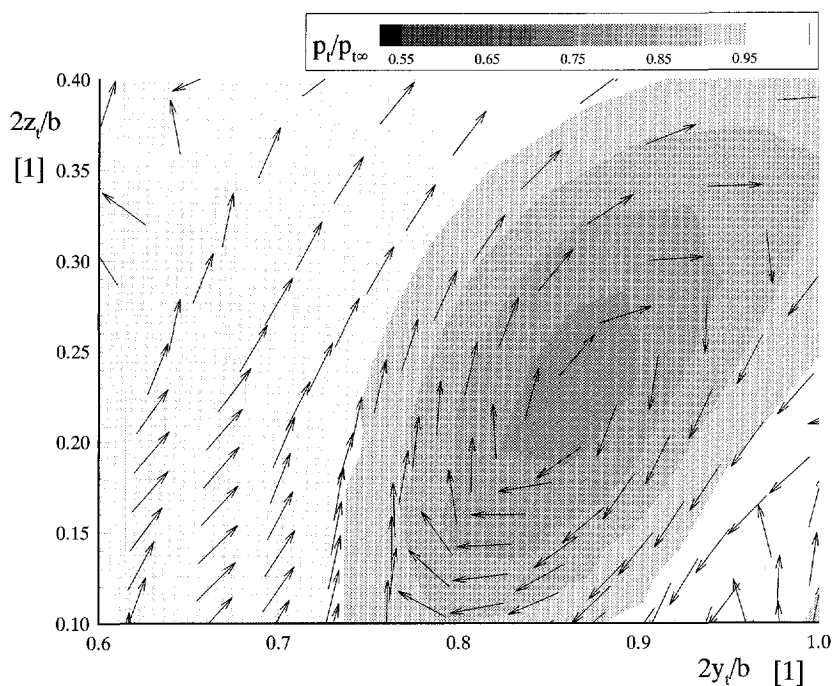
(b) Wake of wing, $(x_t/c_r) = 0.5$

Figure 6.46: Numerical total pressure distribution about primary vortex core with superimposed cross-flow vorticity direction $(\omega_{yc}, \omega_{zc})$ above the wing and $(\omega_{yt}, \omega_{zt})$ behind the wing, $M_\infty = 0.6$ and $\alpha = 10°$.

the orientation of the azimuthal vorticity component from a positive value above the wing to negative value behind the wing, support the vorticity dynamics theory on vortex breakdown. It is not possible to trace the development of the vortex up until the point of vortex breakdown with neither the five-hole probe measurements nor the Euler method calculations due to interference problems and solution breakdown, respectively. However, because a typical feature of vortex breakdown is a stagnation of the axial velocity at the vortex core, transition from a jet-like to wake-like profile can also be considered indicative of a process leading to vortex breakdown behind the delta wing. Thus, the current results are consistent with the theory of Brown and Lopez [1990] that the reversal of the azimuthal vorticity component from a positive to a negative value is a precursor to the occurrence of vortex breakdown.

7

Conclusions and Future Prospects

7.1 Major Conclusions

Vortex flow and vortex breakdown over a delta wing in a high subsonic free stream are investigated in this study using a variety of experimental techniques. The results obtained with the newly developed SRV technique, in particular, provide new insight into these complex flow fields. The presence of the embedded cross-flow shock wave and its influence on the secondary vortex separation is established via a combination of oil flow visualizations and SRV images. The presence of the shock wave is shown to effect the mode of secondary separation taking place. The mode of separation, viscous or shock-induced, is important for determining which parameters are likely to have the strongest effect on the separation location and, thereby, the flow geometry.

New information on the terminating shock wave system and its influence on vortex breakdown in the high subsonic flow regime is obtained via application of the SRV technique in combination with the side-view transmission flow visualization system. Both asymmetric and symmetric breakdown geometries are observed in the SRV images. The flow field is noted to be most unsteady in the asymmetric breakdown case. The terminating shock wave system is found to significantly influence the form of vortex breakdown as well as its associated surface pressure distribution.

Comparison of five-hole probe measurements behind the wing with those above the wing illustrates a reversal of the azimuthal vorticity component from positive above the wing to negative in the wing wake. Transition of the axial velocity profile from jet-like above the wing to wake-like behind the wing in the vicinity of the vortex core, a phenomenon shown to be consistent with the reversal of the azimuthal vorticity component, is also observed. Reversal of the azimuthal vorticity component is compatible with the theory that such a reversal

175

will precede vortex breakdown itself which was developed for an incompressible axisymmetric vortex by Brown and Lopez [1990].

7.2   Future Prospects

While the SRV technique in combination with the surface pressure measurements yields interesting information regarding the influence of vortex breakdown on the wing performance, investigations at higher angles of attack appear necessary to reach the catastrophic performance losses commonly associated with vortex breakdown. In the current study significant performance loss (i.e. reduced vortex lift) is observed only in the case of $M_\infty = 0.8$, $\alpha = 20°$. It is not possible to examine higher angles of attack in the current study due to blockage effects in the wind tunnel. Further investigation with the same model in a larger wind tunnel would allow a larger angle of attack to be tested.

A more complete definition of the three-dimensional terminating shock wave above the delta wing could be obtained through application of a conical Schlieren system [Love and Grigsby 1953]. This is not feasible in the current investigation, however, due to size limitations of the test section which prohibit the construction of such an optical system inside the wind tunnel.

It is possible to examine the frequency of the terminating shock wave fluctuations and vortex breakdown using the SRV system configured with the high speed camera. This option is not pursued in the current study because the TST-27 wind tunnel is calibrated only for steady flow conditions. Any flow fluctuations in the wind tunnel would certainly influence the unsteady behavior of the vortical flow field. The unsteady aspects of the vortex breakdown are important, however, as flow fluctuations can lead to fatigue of aircraft components located in the path of the vortex. Unsteady pressure fluctuation measurements would be an useful complement to an unsteady flow visualization study. In the current investigation only average surface pressures are considered. While simultaneous surface pressure measurements and visualizations would be preferred, this is problematic as the presence of instrumentation on the surface of the mirrored delta wing would decrease the effectiveness of the SRV system.

While the five-hole probe measurements are found to be consistent with the information obtained via other measurement techniques in this study (see Chapter 4), the absolute accuracy of the measurements in the flow field remain uncertain. In order to gain a better understanding of flow interference effects resulting from the presence of the five-hole probe in the vortical flow field, it would be useful to conduct the five-hole probe measurements above the mirror delta wing and to use the SRV system to observe these measurements. The top-view perspective provided by the SRV technique would allow the status of the vortex system to

be more clearly defined than with side-view observations of the measurements. Side-view observations of the probe/vortex interactions are obscured by the presence of the organized vortex structure on the opposite side of the wing during the measurements. This information would allow a more accurate interpretation of the viability of the five-hole probe measurement data.

In order to examine the influence of the presence of gradients in the flow field on the measurement accuracy, it would be useful to either conduct measurements with this same probe above a larger delta wing under the same flow conditions or to make measurements with a smaller probe above this same delta wing.

The interaction of the embedded cross-flow shock wave with the secondary separation could be better understood given additional information on the status of the upper surface boundary layer upstream of this interaction. An understanding of this interaction is interesting as the position of the secondary separation influences the trajectory of the primary vortex. However, the large spanwise pressure gradients present above the delta render traditional "quick-look" methods of boundary layer investigation based on the variation of skin friction (i.e. surface sublimation and fluorescent oil surface flow visualizations) ineffective. Indeed, preliminary fluorescent oil surface flow studies conducted in the course of the current investigation yielded inconclusive results. Two possible methods which could be applied to investigate the status of the upper surface boundary layer include the application of individual disturbances in the boundary layer to examine their influence (i.e. negligible in the case of an established turbulent boundary layer) or thin-film measurements of high frequency flow fluctuations.

The SRV technique, while providing a revolutionary new perspective on the compressible vortical flow field above a delta wing, is presently limited to the examination of noncambered wings. A preliminary investigation was conducted in the course of the present study to examine the possibility of applying "highway-sign" paint to a curved surface. This paint, typically used in road signs, reflects light back along its incident path. This same concept was successfully applied by Settles et al. [1995] using 3M retroreflective highway-sign material type 3970-G in a large scale Schlieren system. This paint was not effective in the SRV system, however, due to the insufficient amount of returning light it provided. This may well be a problem of scale and deserves further investigation. Another possible method to capture the light reflected by a cambered model surface would be the use of a lens designed for the specific model upper surface which would capture the reflected light and transform it into a parallel light bundle.

While the possibility of applying the SRV system to a cambered wing is attractive for practical applications, it is unlikely necessary for the investigation of the fundamental vortex

breakdown problem. The fundamentals of the problem such as vortex formation, the presence of an adverse pressure gradient, shock wave formation and boundary layer interactions are present in the case of the noncambered wing. A more extensive parametric study in combination with complementary flow field measurements, including supersonic free stream Mach numbers, would provide new insight in the development and behavior of vortex breakdown above a delta wing.

References

Agrawal, S., Barnett, R.M., and Robinson, B.A. (1991) "Investigation of Vortex Breakdown on a Delta Wing Using Euler and Navier-Stokes Equations," Technical report, AGARD CP-494.

Ayoub, A. and McLachlan, B.G. (1987) "Slender Delta Wing at High Angles of Attack - A Flow Visualization Study," AIAA Paper 87-1230.

Backstein, S.H. and Staufenbiel, R. (1994) "Experiments on Vortex Breakdwon," In *Vortex Flows in Aeronautics, Aachen, Germany, October 12-14, 1994*. Collaborative Research Center SF25,.

Bannink, W.J. and Bakker, P.G. (1983) "Transonic Mach number determination in a blowdown wind tunnel with solid walls and a downstream throat," Report LR-402, Dept. of Aerospace Engineering, Delft University of Technology.

Bannink, W.J. and Houtman, E.M. (1987) "Experiments on the Transonic Flow over a Delta Wing at High Angles of Attack," In Elsenaar, A. and Eriksson, G., editors, *Proceedings of the Symposium on the International Vortex Flow Experiment on Euler Code Validation, Stockholm, October 1-3, 1986*, pp. 37–46.

Bannink, W.J., Houtman, E.M., and Ottochian, S.P. (1989) "Investigation of the Vortex Flow over a Sharp-edged Delta Wing in the Transonic Speed Regime," Report LR-594, Dept. of Aerospace Engineering, Delft University of Technology.

Benjamin, T.B. (1962) "Theory of the Vortex Breakdown Phenomenon," *Journal of Fluid Mechanics*, **14**:593–629.

Benjamin, T.B. (1967) "Some Developments in the Theory of Vortex Breakdown," *Journal of Fluid Mechanics*, **28**:65–84.

Boersen, S.J. and Elsenaar, A. (1987) "Tests on the AFWAL 65° Delta Wing at NLR: A Study of Vortex Flow Development Between Mach = 0.4 and 4," In Elsenaar, A. and Eriksson, G., editors, *Proceedings of the Symposium on the International Vortex Flow Experiment on Euler Code Validation, Stockholm, October 1-3, 1986*, pp. 23–36.

Brown, G.L. and Lopez, J.M. (1990) "Axisymmetric Vortex Breakdown, Part 2. Physical Mechannisms," *Journal of Fluid Mechanics*, **221**:553–576.

Brücker, Ch. and Althaus, W. (1995) "Study of vortex breakdown by particle tracking velocimetry (PTV) Part 3: Time-dependent structure and development of breakdown-modes," *Experiments in Fluids*, **18**:174–186.

Darmofal, D.L. (1993) "The Role of Vorticity Dynamics in Vortex Breakdown," AIAA Paper 93-3036.

Darmofal, D.L. and Murman, E.M. (1994) "On the Trapped Wave Nature of Axisymmetric Vortex Breakdown," AIAA Paper 94-2318.

Délery, J.M. (1985) "Shock wave/turbulent boundary layer interaction and its control," *Progress in Aerospace Sciences*, **22**:209–280.

Délery, J.M. (1994) "Aspects of Vortex Breakdown," *Progress in Aerospace Sciences*, **30**:1–59.

Délery, J., Pagan, D., and Solignac, J.L. (1987) "On the Breakdown of the Vortex Induced by a Delta-Wing," Technical report, ONERA TP-1987-105.

Earnshaw, P.B. (1961) "An experimental investigation of the structure of a leadig edge vortex," Aeronautics Research Council, London, Report no. 22,876.

Earnshaw, P.B. (1964) "Measurements of the Effects of Thickness on Vortex Breakdown Position on a Series of Sharp-Edged Delta Wings," Technical Report RAE TR-64047, RAE.

Earnshaw, P.B. and Lawford, J.A. (1964) "Low Speed Wind Tunnel Experiments on a Series of Sharp Edged Delta Wings," Aeronautics Research Council, London, RM 3424.

Ekaterinaris, J.A. and Schiff, L.B. (1990a) "Numerical Simulation of the Effects of Variation of Angle of Attack and Sweep Angle on Vortex Breakdown over Delta Wings," AIAA Paper 90-3000.

Ekaterinaris, J.A. and Schiff, L.B. (1990b) "Vortical Flows over Delta Wings and Numerical Prediction of Vortex Breakdown," AIAA Paper 90-0102.

Elle, B.J. (1958) "An investigation at low speed of the flow near the apex of thin delta wings with sharp leading edges," Aeronautics Research Council, London, RM 3176.

Elsenaar, A. (1987) "How it all Started: The International Vortex Flow Experiment on Euler Code Validation in Retrospect," In Elsenaar, A. and Eriksson, G., editors, *Proceedings of the Symposium on the International Vortex Flow Experiment on Euler Code Validation, Stockholm, October 1-3, 1986*, pp. 17–19.

Elsenaar, A., Hjelmberg, L., Bütefisch, K.A., and Bannink, W.J. (1988) "The International Vortex Flow Experiment," Validation of Computational Fluid Dynamics, AGARD CP-437, Paper 9.

Elsenaar, A. and Hoeijmakers, H.W.M. (1991) "An Experimental Study of the Flow over a Sharp-Edged Delta Wing at Subsonic and Transonic Speeds," Technical report, AGARD CP-494.

Erickson, G.E. (1982) "Water-tunnel Studies of Leading-Edge Vortices," *Journal of Aircraft*, **19**:442–448.

Erickson, G.E. (1991) "Wind Tunnel Investigation of the Interaction and Breakdown Characteristics of Slender-Wing Vortices at Subsonic, Transonic and Supersonic Speeds," NASA TP 3114.

Erickson, G.E. (1995) "High Angle-of-Attack Aerodynamics," *Annual Review of Fluid Mechanics*, **27**:45–88.

Erickson, G.E., Schreiner, J.A., and Rogers, L.W. (1989) "On the Structure, Interaction and Breakdown characteristics of Slender Wing Vortices at Subsonic, Transonic and Supersonic Speeds," AIAA Paper 89-3345.

Escudier, M. (1988) "Vortex Breakdown: observations and explanations," *Progress in Aerospace Sciences*, **25**:189–229.

Escudier, M.P. and Zehnder, N. (1982) "Vortex-flow Regimes," *Journal of Fluid Mechanics*, **115**:105–121.

Everett, K.N., Gerner, A.A., and Durston, D.A. (1985) "Seven-Hole Cone Probes for High Angle Flow Measurement: Theory and Calibration," *AIAA Journal*, **21**(7):992–998.

Falatyn, P.D. (1987) "Measurements in the Vortical Flow over a Delta-Wing at High Speed," Project Report no. 1987-17, von Karman Institute for Fluid Dynamics, Rhode St. Genèse, Belgium.

Fujii, K. and Schiff, L.B. (1989) "Numerical Simulation of Vortical Flows over Strake-Delta Wing," *AIAA Journal*, **27**:1153–1162.

GadelHak, M. and Blackwelder, R.F. (1985) "The Discrete Vortices from a Delta Wing," *AIAA Journal*, **23**(6).

Gartshore, I.S. (1962) "Recent Work in Swirling Incompressible Flow," LR 343, NLR, Canada.

Gartshore, I.S. (1963) "Some Numerical Solutions for the Viscous Core of an Irrotational Vortex," LR 378, NLR, Canada.

Hall, M.G. (1961) "A theory for the core of a leading-edge vortex," *Journal of Fluid Mechanics*, **11**:209–228.

Hall, M.G. (1967) "A New Approach to Vortex Breakdown," In *Heat Transfer and Fluid Mechanics Institute, Univ. of California, San Diego, California*, pp. 319–340.

Hall, M.G. (1972) "Vortex Breakdown," *Annual Review of Fluid Mechanics*, **4**:195–218.

Hartwich, P.M., Hsu, C.H., Luckring, J.M., and Liu, C.H. (1988) "Numerical Study of the Vortex Burst Phenomenon for Delta Wings," AIAA Paper 88-0505.

Hemsch, M.J. and Luckring, J.M. (1990) "Connection between leading-edge sweep, vortex lift, and vortex strength for delta wings," *Journal of Aircraft*, **27**:473–475.

Hitzel, S.M., Wagner, B., and Liecher, S. (1987) "Euler-Simulation of the Vortex-Flow-Experiment, A Critical Consideration," In Elsenaar, A. and Eriksson, G., editors, *Proceedings of the Symposium on the International Vortex Flow Experiment on Euler Code Validation, Stockholm, October 1-3, 1986*, pp. 281–288.

Hitzel, S.M. (1988) "Wing Vortex Flows up into Vortex-Breakdown, A Numerical Simulation," AIAA Paper 88-2518-CP.

Hitzel, S.M. and Schmidt, W. (1984) "Slender Wings with Leading-Edge Vortex Separation: A Challenge for Panel Methods and Euler Solvers," *Journal of Aircraft*, **21**:751–759.

Holder, D.W. and North, R.J. (1963) "Schlieren Methods," Notes on Applied Science 31, National Physical Laboratory, London.

Houtman, E.M. and Bannink, W.J. (1987) "Experimental Investigation of the Transonic Flow at the Leeward Side of a Delta Wing at High Incidence," Report LR-518, Dept. of Aerospace Engineering, Delft University of Technology.

Houtman, E.M. and Bannink, W.J. (1989) "The Calibration and Measuring Procedure of a Five-hole Hemispherical Head Probe in Compressible Flow," Report LR-585, Dept. of Aerospace Engineering, Delft University of Technology.

Houtman, E.M. and Bannink, W.J. (1991) "Experimental and Numerical Investigation of the Vortex Flow over a Delta Wing at Transonic Speed," Vortex Flow Aerodynamics, AGARD CP-494, Paper 5.

Hummel, D. (1979) "On the Vortex Formation over a Slender Wing at Large Angles of Incidence," Technical report, AGARD CP-247.

Jones, J.P. (1960) "The Breakdown of Vortices in Separated Flow," Technical Report U.S.A.A. 140, University Southampton.

Kandil, O.A. and Chuang, A.H. (1988) "Unsteady Vortex-Dominated Flows around Maneuvering Wings over a Wide Range of Mach Numbers," AIAA Paper 88-0317.

Kegelman, J. and Roos, F. (1989) "Effects of Leading-Edge Shape and Vortex Burst on the Flowfield of a 70 Degree Sweep Delta Wing," AIAA Paper 89-0086.

Lambourne, N.C. and Bryer, D.W. (1961) "The Bursting of Leading-Edge Vortices-Some Observations and Discussion of the Phenomenon," Aeronautics Research Council, London, Report no. 3282.

Lanen, T. and Houtman, E.M. (1992) "Comparison of Interferometric Measurements with 3-D Euler Computations for Circular Cones in Supersonic Flow," AIAA Paper 92-2691 CP.

Leibovich, S. (1978) "The Structure of Vortex Breakdown," *Annual Review of Fluid Mechanics*, **10**:221–246.

Liepmann, H.W. and Roshko, A. (1957) *"Elements of Gas Dynamics,"* John Wiley and Sons, Inc., London.

Love, E.S. and Grigsby, C.E. (1953) "A new Shadowgraph Technique for the Observation of Conical Flow Phenomena in Supersonic Flow and Preliminary Results Obtained for a Triangular Wing," Technical Report NACA TN 2950, NACA, Washington D.C.

Lowson, M.V. (1988) "The Three Dimensional Vortex Sheet Structure on Delta Wings," In *Fluid Dynamics of Three-Dimensional Turbulent Shear Flow and Transition*. AGARD CP-438.

Ludwieg, H. (1961) "Contribution to the Explanation of the Instability of Vortex Cores Above Lifting Delta Wings," Technical Report AVA/61 A01, Aero. Versuchsantalt, Gottingen.

Maeder, T. (1995) "Experimental Investigation of the Transonic Flow above a Delta Wing," Master's thesis, Faculty of Mechanical Engineering, Swiss Federal Institute of Technology, Zürich, Switzerland (Research conducted at the Delft University of Technology, High Speed Aerodynamics Laboratory).

McKernan, J.F. and Nelson, R.C. (1983) "An Investigaion of the Breakdown of the Leading Edge Vortices on a Delta-Wing at high angle of attack," AIAA Paper 83-2114.

Merzkirch, W. (1987) *"Flow Visualization,"* Academic Press, London.

Miller, D.S. and Wood, R.M. (1984) "Leeside Flows over Delta Wings at Supersonic Speeds," *Journal of Aircraft*, **21**(9):680–686.

Muylaert, J.M. (1980) "Effect of Compressibility on Vortex Bursting on Slender Delta Wings," Project Report 1980-21, von Karman Institute For Fluid Dynamics, Rhode St. Genèse, Belgium.

Naarding, S.H.J. and Verhaagen, N.G. (1988) "Experimental and Numberical Investigation of the Vortex Flow Over a Sharp Edged Delta Wing with and without Sideslip," Report LR-573, Dept. of Aerospace Engineering, Delft University of Technology.

Nelson, R.C. and Visser, K.D. (1991) "Breaking Down the Delta Wing Vortex, The Role of Vorticity in the Breakdown Process," Technical report, AGARD CP-494.

Oledal, M. (1994) "A Five Hole Probe Exploration of the Transonic Vortical Flow Field Above a Delta Wing," Master's thesis, Faculty of Mechanical Engineering, Norwegian Institute of Technology, Trondheim, Norway (Research conducted at the Delft University of Technology, High Speed Aerodynamics Laboratory).

Payne, F.M. (1987) *"The Structure of Leading Edge Vortex Flows Including Vortex Breakdown,"* PhD thesis, Department of Aerospace Engineering, University of Notre Dame, Notre Dame, Indiana, USA.

Payne, F.M. and Nelson, R.C. (1985) "An Experimental Investigation of Vortex Breakdown on Delta Wings," In *Vortex Flow Aerodynamics, NASA CP-2416*, pp. 135–161.

Payne, F.M., Ng, T.T., and Nelson, R.C. (1987) "Experimental Study of the Velocity Field on a Delta Wing," AIAA Paper 87-1231.

Peckham, D.H. (1958) "Low-speed wind-tunnel tests on a series of uncambered slender pointed wings with sharp edges," Aeronautics Research Council, London, RM 3186.

Peckham, D.H. and Atkinson, S.A. (1957) "Preliminary Results of Low Speed Wind Tunnel Tests on a Gothic Wing of Aspect Ratio 1.0," Aeronautics Research Council, London, Report no. CP-508.

Polhamus, E.C. (1966) "A Concept of the Vortex Lift of Sharp-Edge Delta Wings based on a Leading-Edge-Suction analogy," Technical Report NASA TN D-3767, NASA, Washington D.C.

Randall, J.D. and Liebovich, S. (1973) "The critical state: a trapped wave model of vortex breakdown," *Journal of Fluid Mechanics*, **58**:495–515.

Reynolds, G.A. and Abtahi (1989) "Three-Dimensional Vortex Development, Breakdown, and Control," AIAA Paper 89-0998.

Rizzetta, D.P. and Shang, J.S. (1984) "Numerical Simulation of Leading Edge Vortical Flows," AIAA Paper 84-1544.

Roe, P.L. (1981) "Approximate Riemann Solvers, Parameter Vectors and Difference Schemes," *Journal of Comp. Physics*, **43**:357–372.

Roos, F.W. and Kegelman, J.T. (1990) "An Experimental Investigation of Sweep-Angle Influence on Delta-Wing Flows," AIAA Paper 90-0383.

Schrader, K.F., Reynolds, G.A., and Novak, C.J. (1988) "Effects of mach Number and Reynolds Number on Leading-Edge Vortices at High Angle of Attack," AIAA Paper 88-0122.

Settles, G.S., Hackett, E.E., Miller, J.D., and Weinstein, L.M. (1995) "Full-Scale Schlieren Flow Visualization," In Crowder, J., editor, *Proceedings of the Seventh International Symposium on Flow Visualization, Seattle, Washington, September 11-14, 1995*, pp. 2–13.

Skow, A.M. and Erickson, G.E. (1982) "Modern Fighter Aircraft Design For High-Angle-of-Attack Maneuvering," Technical report, AGARD LS-121.

Squire, H.B. (1960) "Analysis of the vortex breakdown phenomenon, Part 1," Aeronautics Department Report 102, Imperial College of Science and Technology.

Squire, L.C., Jones, J.G., and Stanbrook, A. (1961) "An experimental investigation of some plane and cambered 65° Delta Wings at Mach Numbers from 0.7 to 2.0," Aeronautics Research Council, London, RM 3305.

Stanbrook, A. and Squire, L.C. (1964) "Possible types of flow at Swept leading edges," *Aeronautical Quarterly*, **15**:72–82.

Thomas, J.L., Taylor, S.L., and Anderson, W.K. (1987) "Navier-Stokes Computations of Vortical Flows over Low Aspect Ratio Wings," AIAA Paper 87-0207.

van Oort, H. (1986) "Ontwerp van een transsone meetplaats voor the TST-27 windtunnel," Graduation Thesis, Delft University of Technology, Department of Aerospace Engineering.

Vest, C.M. (1979) *"Holographic Interferometry,"* John Wiley and Sons, Inc., New York.

Voerman, G.J. (1976) "Determination of the Velocity Vector and the Total Pressure with a calibrated Fixed-Attitude Five-hole Probe, Part A: Calibration of the Probe," Report LR-236, Dept. of Aerospace Engineering, Delft University of Technology.

Vorropoulos, G. and Wendt, J.F. (1983) "Compressibility Effects on Delta Wing Flow Fields," Technical report, AGARD CP-342.

Washburn, A.E. (1992) "Effects of External Influences on Subsonic Delta Wing Vortices," AIAA Paper 92-4033.

Washburn, A.E. and Visser, K.D. (1994a) "Evolution of Vortical Structures in the Shear Layer of Delta Wings," AIAA Paper 94-2317.

Washburn, A.E. and Visser, K.D. (1994b) "Transition behavior on Flat Plate Delta Wings," AIAA Paper 94-1950-CP.

Weatherill, N.P. (1990) "Grid Generation," Technical report, LS1990-6, von Karman Institute for Fluid Dynamics, Rhode St. Genèse, Belgium.

Weimer, M., Hofhaus, J., Althaus, W., and Krause, E. (1994) "Simulation of Vortex Breakdown," In *Vortex Flows in Aeronautics, Aachen, Germany, October 12-14, 1994*. Collaborative Research Center SFB25,.

Weinberg, E. (1992) "Effect of Tunnel Walls on Vortex Breakdown Location Over Delta Wings," *AIAA Journal*, **30**(6):1584–1586.

Wentz, W.H. Jr. (1987) "Vortex-Fin Interaction on a Fighter Aircraft," AIAA Paper 87-2474.

Wentz, W.H. Jr. and Kohlman, D.L. (1971) "Vortex Breakdown on Slender Sharp-Edged Wings," *Journal of Aircraft*, **8**:156–161.

Werlé, H. (1954) "Quelques résultats expérimentaux sur les ailes en flèches, aux faibles vitesses, obtenus en tunnel hydrodynamique," *La Recherche Aéronautique*, **41**.

Werlé, H. (1960) La Recherch Aéronautique, Volume 74.

Williams, W.D. (1993) "Hypersonic Flow-Field Measurements: Nonintrusive," Technical report, LS1993-3, von Karman Institute for Fluid Dynamics, Rhode St. Genèse, Belgium.

List of Figures

189

Overview of Figures

Overview of Figures at various M_∞ and α

M_∞	α	Figure	Description
0.6	10	4.16	Total pressure distribution, $(x_m/c_r) = 0.7$
		4.17	Total pressure distributions and cross-flow velocity direction at $(x_m/c_r) = 0.7$
		4.18	Spanwise surface pressure distributions at $(x_m/c_r) = 0.7$
		4.20	Static pressure measurements on surface and above the wing at $(x_m/c_r) = 0.7$
		5.11	Numerical simulated-SRV Image
		5.18	Spanwise distribution of integrated-density and integrated-density gradient
		5.20	Experimental density distribution at $(x_m/c_r) = 0.70$
		5.22	SRV image and associated pixel levels at $(x_m/c_r) = 0.7$
		6.4	Total pressure distribution when $(x_m/c_r) = 0.7$
		6.5	Total pressure distribution when $(x_t/c_r) = 0.5$
		6.9	Spanwise distribution of c_p, $(x_m/c_r) = 0.70$
		6.11	Oil flow surface visualization image
		6.15	Spanwise pressure distribution at $(x_m/c_r) = 0.7$
		6.40	Experimental axial velocity distribution and cross-flow direction
		6.41	Numerical axial velocity distribution and cross-flow direction
		6.45	Experimental total pressure distribution and cross-flow vorticity direction
		6.46	Numerical total pressure distribution and cross-flow vorticity direction
0.6	15	5.19	Spanwise distribution of integrated-density and integrated-density gradient
		5.20	Experimental density distribution at $(x_m/c_r) = 0.70$
		5.23	SRV image and associated pixel levels at $(x_m/c_r) = 0.7$
		6.2	Oil surface flow visualization
		6.3	Surface pressure distribution
		6.7	Side-view transmission Schlieren image
		6.9	Spanwise distribution of c_p, $(x_m/c_r) = 0.70$
		6.13	Oil and SRV flow visualization images
		6.15	Spanwise pressure distribution at $(x_m/c_r) = 0.7$
		6.19	Total pressure distribution when $(x_t/c_r) = 0.4$

195

M_∞	α	Figure	Description
0.6	15	6.20	Distributions of the axial vorticity component behind the wing
		6.21	Spanwise pressure distribution at various chord-wise stations
		6.22	Pressure distribution along root chord
0.6	18	6.9	Spanwise distribution of c_p, $(x_m/c_r) = 0.70$
0.6	20	6.3	Surface pressure distribution
		6.9	Spanwise distribution of c_p, $(x_m/c_r) = 0.70$
		6.29	Vortex breakdown location on either side of the wing
		6.30	SRV images
		6.33	Pressure distribution along root chord
		6.34	Side-view Schlieren image, knife edge parallel with free stream
		6.36	Surface pressure distribution
		6.37	Spanwise surface pressure distribution at various x_m stations
0.7	10	-	-
0.7	15	-	-
0.7	18	6.26	Vortex breakdown location on either side of the wing
0.7	20	6.29	Vortex breakdown location on either side of the wing
		6.31	SRV images
		6.33	Pressure distribution along root chord
		6.34	Side-view Schlieren image, knife edge parallel with free stream
		6.35	Side-view Schlieren image, knife edge perpendicular to free stream
		6.36	Surface pressure distribution
		6.37	Spanwise surface pressure distribution at various x_m stations
0.8	10	4.16	Total pressure distribution, $(x_m/c_r) = 0.7$
		4.17	Total pressure distributions and cross-flow velocity direction at $(x_m/c_r) = 0.7$
		4.18	Spanwise surface pressure distributions at $(x_m/c_r) = 0.7$
		4.19	Side-view transmission Schlieren image
		4.21	Static pressure measurements on surface and above the wing at $(x_m/c_r) = 0.7$
		5.12	Numerical simulated-SRV Image
		6.4	Total pressure distribution when $(x_m/c_r) = 0.7$
		6.5	Total pressure distribution when $(x_t/c_r) = 0.5$
		6.15	Spanwise pressure distribution at $(x_m/c_r) = 0.7$
		6.43	Distribution of ω_{yc} at $(x_m/c_r) = 0.71$ and $(x_m/c_r) = 0.70$
		6.44	Distribution of ω_{zc} at $(x_m/c_r) = 0.71$ and $(x_m/c_r) = 0.70$
0.8	15	4.16	Total pressure distribution, $(x_m/c_r) = 0.7$
		4.17	Total pressure distributions and cross-flow velocity direction at $(x_m/c_r) = 0.7$
		4.18	Spanwise surface pressure distributions at $(x_m/c_r) = 0.7$
		4.22	Static pressure measurements on surface and above the wing at $(x_m/c_r) = 0.7$

M_∞	α	Figure	Description
0.8	15	5.4	SRV image, Schlieren knife edge parallel with the free stream
		5.9	Numerically calculated density distribution in cross-flow plane $(x_m/c_r) = 0.7$
		5.13	Numerical simulated-SRV Image
		5.14	Numerically calculated conical Mach number when $(x_m/c_r) = 0.7$
		5.16	Experimental density distribution when $(x_m/c_r) = 0.7$
		5.17	Experimental total pressure distribution when $(x_m/c_r) = 0.7$
		5.20	Experimental density distribution at $(x_m/c_r) = 0.70$
		5.21	Spanwise distribution of integrated-density and integrated-density gradient
		5.24	SRV image and associated pixel levels at $(x_m/c_r) = 0.7$
		6.10	Oil and SRV flow visualizations
		6.15	Spanwise pressure distribution at $(x_m/c_r) = 0.7$
		6.16	Side-view transmission Schlieren image
		6.17	SRV images
		6.21	Spanwise pressure distribution at various chord-wise stations
		6.22	Pressure distribution along root chord
0.8	18	6.23	SRV images
		6.24	SRV image
		6.25	Vortex breakdown location on either side of the wing
		6.27	Side-view and SRV flow visualization images
		6.28	SRV image
0.8	20	5.5	SRV image, Schlieren knife edge aligned perpendicular to the root chord
		6.29	Vortex breakdown location on either side of the wing
		6.32	SRV images
		6.33	Pressure distribution along root chord
		6.34	Side-view Schlieren image, knife edge parallel with free stream
		6.35	Side-view Schlieren image, knife edge perpendicular to free stream
		6.36	Surface pressure distribution
		6.37	Spanwise surface pressure distribution at various x_m stations

List of Tables

SUMMARY

Vortex Flow and Vortex Breakdown Above a Delta Wing in High Subsonic Flow: an experimental investigation

by

Sharon R. Donohoe

An experimental investigation is carried out of the vortical flow field above a noncambered, 65° sweep, sharp leading edge delta wing in the high subsonic/transonic flow regime. Configurations of M_∞ (0.6, 0.7, and 0.8) and α (10°, 15°, 18° and 20°) are considered which exhibit a sustained organized vortex system over the entire length of the wing, as well as configurations which exhibit vortex breakdown above the wing. All experiments are performed in the TST-27 transonic/supersonic wind tunnel located in the High Speed Aerodynamics Laboratory of the Department of Aerospace Engineering of the Delft University of Technology in the Netherlands. The TST-27 wind tunnel is a "blow-down" type wind tunnel with a test section 28 cm wide and with a height varying from 25 cm to 27 cm depending on the Mach number.

A variety of experimental measurement techniques and flow visualization techniques are employed in this investigation. Measurement techniques employed include surface pressure measurements and five-hole probe flow field surveys. Conventional flow visualization techniques applied include oil surface flow visualizations and side-view transmission flow field visualizations. In addition to these two "conventional" visualization techniques, the Surface Reflective Visualization (SRV) system is developed, validated and applied in the scope of the current investigation. The SRV technique is, in fact, a derivative of a double-pass Schlieren system with the definitive characteristic that the upper surface of the model is itself a flat mirror and a component of the optical system. The SRV system, thus, provides a top-view image of the flow field above the lee-side of the delta wing. This top-view image is particularly useful in providing new information on the complex three-dimensional flow field above a delta wing exhibiting vortex breakdown in the high subsonic flow regime.

The presence of the embedded cross-flow shock wave and its influence on the secondary separation is established via a combination of oil flow visualizations and SRV images. Three different types of secondary separation are observed. The presence of the embedded cross-flow shock wave is shown to influence the secondary separation. Understanding the mechanism of secondary separation, viscous or shock-induced, is important for determining which

parameters are likely to have the strongest effect on the separation location and, thereby, the flow geometry.

New information on the terminating shock wave system and its influence on vortex break-down in the high subsonic flow regime is obtained via application of the SRV technique in combination with the side-view transmission flow visualization system. Both asymmetric and symmetric breakdown geometries are observed in the SRV images. The flow field is noted to be most unsteady in the asymmetric breakdown case. The terminating shock wave system is found to significantly influence the form of vortex breakdown as well as its associated surface pressure distribution.

Comparison of five-hole probe measurements behind the wing with those above the wing illustrates a reversal of the azimuthal vorticity component from positive above the wing to negative in the wing wake. Transition of the axial velocity profile from jet-like above the wing to wake-like behind the wing in the vicinity of the vortex core, a phenomenon shown to be consistent with the reversal of the azimuthal vorticity component, is also observed. Reversal of the azimuthal vorticity component is compatible with the theory, developed for the case of an incompressible and axisymmetric vortex, that such a reversal will precede vortex breakdown itself.

SAMENVATTING

Wervelstroming en wervel "breakdown" boven een deltavleugel in hoog-subsone stroming: een experimenteel onderzoek

door

Sharon R. Donohoe

De wervelstroming boven een vlakke delta vleugel met $50°$ pijlhoek is experimenteel onderzocht in het hoog-subsone/transsone snelheidsgebied bij getallen van Mach: $M_\infty = 0.6$, 0.7, en 0.8 en invalshoeken $\alpha = 10°$, $15°$, $18°$ en $20°$. Configuraties zijn beschouwd die over de gehele lengte van de vleugel een blijvend georganiseerd wervelsysteem vertonen, als ook configuraties waarbij wervel "breakdown" optreedt. Alle experimenten zijn uitgevoerd in de TST-27 transsone/supersone windtunnel van het Hoge Snelheids Laboratorium van de Faculteit Luchtvaart-en Ruimtevaarttechniek aan de Technische Universiteit Delft. De TST-27 windtunnel is van het "blow-down"type met een meetplaats van $28\ cm$ breedte en een variërende hoogte tussen $25\ cm$ en $27\ cm$, afhankelijk van het getal van Mach.

In dit onderzoek zijn verschillende experimentele meetmethoden en stromingsvisualisatietechnieken toegepast. Oppervlaktedrukmetingen zijn uitgevoerd en het stromingsveld is onderzocht met behulp van een vijf-gats richtingbuis. Onder de gebruikte conventionele visualisatietechnieken vallen de toepassing van een oliefilm op het modeloppervlak en van het optische zijaanzicht van het stromingsveld door middel van Schlieren opnamen. Naast deze twee "conventionele" visualisatietechnieken is in het kader van dit onderzoek het "Surface Reflective Visualization" (SRV) systeem ontwikkeld, beproefd en toegepast. De SRV techniek is in feite afgeleid van een "double-pass" Schlierensysteem met de speciale eigenschap dat de bovenkant van het model een vlakke spiegel is die een onderdeel van het optische systeem vormt. Op deze manier biedt het SRV systeem een bovenaanzicht van het stromingsveld aan de lijzijde van de deltavleugel. Dit bovenaanzicht is met name geschikt om bij hoog-subsone snelheden nieuwe informatie te verkrijgen over het complexe drie-dimensionale stromingsveld boven de deltavleugel wanneer wervel "breakdown" optreedt.

De aanwezigheid van een ingebedde schokgolf, ontstaan door supersone dwarsstroming, en de invloed ervan op de secundaire loslating wordt vastgesteld door een combinatie van oliestromingspatronen en SRV beelden. Het blijkt dat er drie verschillende soorten secundaire loslating voorkomen. Ook wordt duidelijk dat de wijze waarop de secundaire loslating plaatsvindt wordt beïnvloed door de aanwezigheid van de schokgolf. Of deze loslating al-

leen door viskeuse effecten optreedt of geïnduceerd door de schokgolf plaatsvindt, daarvoor is het belangrijk om te bepalen welke parameters in feite het sterkste effect op de plaats van loslating hebben en daardoor op de geometrie van de stroming.

Nieuwe informatie over het afsluitende schokgolfsysteem en de invloed ervan op wervel "breakdown" in het subsone stromingsgebied, is verkregen door toepassing van de SRV techniek in combinatie met Schlieren opnamen in zijaanzicht. Zowel symmetrische als asymmetrische "breakdown" wordt waargenomen met de SRV beelden. Het stromingsveld blijkt zeer instabiel te zijn in het geval van asymmetrische "breakdown". Het afsluitende schokgolfsysteem beïnvloedt in belangrijke mate zowel de vorm van de wervel "breakdown" als de bijbehorende oppervlaktedrukverdeling.

Een vergelijking tussen de meetresultaten van de vijf-gats richtingsbuis achter en boven de vleugel illustreert de tekenomkering van de tangentiële component van de rotatie vector van positief boven de vleugel naar negatief in het zog van de vleugel. Ook treedt in de omgeving van de wervelkern in het axiale snelheidsprofiel een overgang op van straal- achtig (jet-like) boven de vleugel naar zog-achtig (wake-like) achter de vleugel. Dit verschijnsel is in overeenstemming met de omkering van de tangentiële component van de rotatie vector. Omkering van deze component volgt uit de theorie die stelt dat zo'n omkering voorafgaat aan de eigenlijke wervel "breakdown". Deze theorie die ontwikkeld is voor niet-samendrukbare symmetrische wervels blijkt volgens deze studie ook van toepassing te zijn op samendrukbare asymmetrische wervels.

Acknowledgements

I would like to take a moment to thank the numerous people who, through their technical and/or moral support, were of great importance in allowing this dissertation to become a reality:

- I would first like to acknowledge Mr. Cor Nebbeling. Mr. Nebbeling, a former researcher at the High Speed Aerodynamics Laboratory, originally conceived the idea of the surface reflective visualization (SRV) technique presented in this dissertation. I am very appreciative of the excellent technical support of the optical and experimental measurement systems provided by Mr. Frits Donker Duyvis and Mr. Eric de Keizer, respectively. The early-morning efforts of Mr. Nico Lam and Mr. Peter Duyndam in filling of the wind tunnel pressure vessel are also greatly appreciated.

- I would like to thank Mr. Marcus Oledal for his great enthusiasm in performing and analyzing the 5-hole probe measurements [Oledal 1994]. Similarly, I would like to thank Mr. Thierry Maeder for his extensive work on the surface pressure measurements and general data analysis [Maeder 1995].

- I would like to thank Mr. Roland Boon for his efforts in developing the fast ray tracing algorithm used in the numerical analysis of the SRV system. I would also like to thank Mr. Bert Houtman for many useful discussions regarding both delta wing flow fields and the mysteries of LaTeX.

- I would like to thank my supervisors, Mr. Bannink and Professor Bakker, for their enthusiastic guidance throughout the course of this project. I would also like to thank my co-workers Brenda, Bas, Theo, Erwin and Juup for both their camaraderie and useful advice.

- I would like to thank Ms. Pauli Paap for the very friendly welcome to the TU Delft she gave me in the summer of 1991 during my IAETE technical internship.

- I would like to thank Erik, Dick, Douwe, Jan, Nabil, Petra, Rose, Shibani, Tore and the ladies of Ariston *Dames 3* for their friendship and many good laughs during my time here in Delft. I hope to see you all one day in Seattle!

- I would, of course, also like to thank my parents, Cathleen, Chrissy and Dee Dee for their long distance love and support throughout my stay in the Netherlands: **e-mail is great!** And, finally, I would like to thank Pjot for helping me to "just do it" and complete this dissertation.

<div align="right">

Sharon R. Donohoe

Delft, the Netherlands

1 April 1996

</div>

Publications

The following conference papers and articles were published based on the research contained in this dissertation:

- S.R. Donohoe and W.J. Bannink, "The Utilization of a Surface Reflective Visualization System in the Study of Transonic Flow over a Delta Wing", paper presentation at the AGARD symposium on Wall Interference, Support Interference and Flow Field Measurements, Brussels, Belgium, October 1993.

- S.R. Donohoe and W.J. Bannink, "The Utilization of a Surface Reflective Visualization System in the Study of Transonic Flow over a Delta Wing", Wall Interference, Support Interference and Flow Field Measurements, AGARD CP- 535, paper 8, 1994.

- S.R. Donohoe, E.M. Houtman and W.J. Bannink, "A High Speed Surface Reflective Visualization System for the study of Vortex Breakdown over a Delta Wing", invited lecture presentation at the 18th AIAA Aerospace Ground Testing Conference, Colorado Springs, Colorado, AIAA paper 94-2480, June 1994.

- S.R. Donohoe, E.M. Houtman and W.J. Bannink, "Vorticity Field of a Delta Wing in High Subsonic Flow", paper presentation at the 2nd International Conference on Experimental Fluid Mechanics, Torino, Italy, July 1994.

- S.R. Donohoe and W.J. Bannink, "Surface Reflective Flow Visualizations of Shock Wave/Vortex Interactions above a Delta Wing", paper presentation at the 7th International Symposium on Flow Visualization, Seattle, Washington, September 1995.

- S.R. Donohoe, E.M. Houtman and W.J. Bannink, "Surface Reflective Visualization System Study of Vortical Flow over a Delta Wing", AIAA Journal of Aircraft, Volume 32, No. 6, page 1359, November 1, 1995.

Curriculum Vitae

Sharon Rose Donohoe

born 25 August, 1966 in Santa Barbara, California, United States of America

1980-1984 Diploma received from Dos Pueblos High School, Goleta, California, United States of America.

1986-1989 Bachelor of Science *cum laude* received from the Aeronautical Engineering Department of the California Polytechnic State University at San Luis Obispo, California, United States of America.

1989-1990 Diploma received from the Department of Aeronautics and Astronautics, von Karman Institute of Fluid Dynamics, Rhode St. Genèse, Belgium.

1990-1991 Master of Science in Engineering received under the Department of Aeronautics and Astronautics of Stanford University, Stanford, California, United States of America.

1992-1996 Research assistant and doctoral candidate at the High Speed Aerodynamics Laboratory of the Aerospace Engineering Department of Delft University of Technology, Delft, the Netherlands.